

# **Nanostructured Iron-based Compounds as Sulfur Host Material for Lithium-Sulfur Batteries**

---

**Dongjiu XIE**

**Univ.-Diss.**

**zur Erlangung des akademischen Grades  
"doctor rerum naturalium"  
(Dr. rer. nat.)  
in der Wissenschaftsdisziplin "Materialwissenschaft"**

**eingereicht an der  
Mathematisch-Naturwissenschaftlichen Fakultät  
Institut für Chemie  
der Universität Potsdam**

Ort und Tag der Disputation: Golm, Potsdam, 28/09/2023

Unless otherwise indicated, this work is licensed under a Creative Commons License Attribution – NonCommercial – NoDerivatives 4.0 International.

This does not apply to quoted content and works based on other permissions.

To view a copy of this licence visit:

<https://creativecommons.org/licenses/by-nc-nd/4.0>

Hauptbetreuerin\* Prof. Dr. Yan Lu

Betreuer\*: Prof. Dr. Andreas Taubert

Gutachter\*: Prof. Dr. Martin Oschatz

Published online on the

Publication Server of the University of Potsdam:

<https://doi.org/10.25932/publishup-61036>

<https://nbn-resolving.org/urn:nbn:de:kobv:517-opus4-610369>

*I dream my painting and then I paint my dream*

—*Vincent Willem van Gogh*





*To My Family & Friends*



## Abstract

The present thesis focuses on the synthesis of nanostructured iron-based compounds by using  $\beta$ -FeOOH nanospindles and poly(ionic liquid)s (PILs) vesicles as hard and soft templates, respectively, to suppress the shuttle effect of lithium polysulfides (LiPSs) in Li-S batteries. Three types of composites with different nanostructures (mesoporous nanospindle, yolk-shell nanospindle, and nanocapsule) have been synthesized and applied as sulfur host material for Li-S batteries. Their interactions with LiPSs and effects on the electrochemical performance of Li-S batteries have been systematically studied.

In the first part of the thesis, carbon-coated mesoporous  $\text{Fe}_3\text{O}_4$  ( $\text{C@M-Fe}_3\text{O}_4$ ) nanospindles have been synthesized to suppress the shuttle effect of LiPSs. First,  $\beta$ -FeOOH nanospindles have been synthesized via the hydrolysis of iron (III) chloride in aqueous solution and after silica coating and subsequent calcination, mesoporous  $\text{Fe}_2\text{O}_3$  ( $\text{M-Fe}_2\text{O}_3$ ) have been obtained inside the confined silica layer through pyrolysis of  $\beta$ -FeOOH. After the removal of the silica layer, electron tomography (ET) has been applied to rebuild the 3D structure of the  $\text{M-Fe}_2\text{O}_3$  nanospindles. After coating a thin layer of polydopamine (PDA) as carbon source, the PDA-coated  $\text{M-Fe}_2\text{O}_3$  particles have been calcinated to synthesize  $\text{C@M-Fe}_3\text{O}_4$  nanospindles. With the chemisorption of  $\text{Fe}_3\text{O}_4$  and confinement of mesoporous structure to anchor LiPSs, the composite  $\text{C@M-Fe}_3\text{O}_4/\text{S}$  electrode delivers a remaining capacity of  $507.7 \text{ mAh g}^{-1}$  at 1 C after 600 cycles.

In the second part of the thesis, a series of iron-based compounds ( $\text{Fe}_3\text{O}_4$ ,  $\text{FeS}_2$ , and  $\text{FeS}$ ) with the same yolk-shell nanospindle morphology have been synthesized, which allows for the direct comparison of the effects of compositions on the electrochemical performance of Li-S batteries. The  $\text{Fe}_3\text{O}_4$ -carbon yolk-shell nanospindles have been synthesized by using the  $\beta$ -FeOOH nanospindles as hard template. Afterwards,  $\text{Fe}_3\text{O}_4$ -carbon yolk-shell nanospindles have been used as precursors to obtain iron sulfides ( $\text{FeS}$  and  $\text{FeS}_2$ )-carbon yolk-shell nanospindles through sulfidation at different temperatures. Using the three types of yolk-shell nanospindles as sulfur host, the effects of compositions on interactions with LiPSs and electrochemical performance in Li-S batteries have been systematically investigated and compared. Benefiting from the chemisorption and catalytic effect of  $\text{FeS}_2$  particles and the physical confinement of the carbon shell, the  $\text{FeS}_2\text{-C/S}$  electrode exhibits the best electrochemical performance with an initial specific discharge capacity of  $877.6 \text{ mAh g}^{-1}$  at 0.5 C and a retention ratio of 86.7% after 350 cycles.

In the third part, PILs vesicles have been used as soft template to synthesize carbon nanocapsules embedded with iron nitride particles to immobilize and catalyze LiPSs in Li-S batteries. First, 3-n-decyl-1-vinylimidazolium bromide has been used as monomer to synthesize PILs nanovesicles by free radical polymerization. Assisted by PDA coating route and ion exchange, PIL nanovesicles have been successfully applied as soft template in morphology-maintaining carbonization to prepare carbon nanocapsules embedded with iron nitride nanoparticles ( $\text{Fe}_x\text{N@C}$ ). The well-dispersed iron nitride nanoparticles effectively catalyze the conversion of LiPSs to  $\text{Li}_2\text{S}$ , owing to their high electrical conductivity and strong chemical binding to LiPSs. The constructed  $\text{Fe}_x\text{N@C/S}$  cathode demonstrates a high initial discharge capacity of  $1085.0 \text{ mAh g}^{-1}$  at  $0.5 \text{ C}$  with a remaining value of  $930.0 \text{ mAh g}^{-1}$  after 200 cycles.

The results in the present thesis demonstrate the facile synthetic routes of nanostructured iron-based compounds with controllable morphologies and compositions using soft and hard colloidal templates, which can be applied as sulfur host to suppress the shuttle behavior of LiPSs. The synthesis approaches developed in this thesis are also applicable to fabricating other transition metal-based compounds with porous nanostructures for other applications.

**Keywords:** Sulfur host, Li-S batteries, Iron-based compounds, Nanospindles, Vesicles, Nanocapsules, Poly(ionic liquid)s, Electron tomography, Cryo-electron microscopy

## Zusammenfassung

Die vorliegende Arbeit beschreibt die Synthese von nanostrukturierten Verbindungen auf Eisenbasis unter Verwendung von  $\beta$ -FeOOH-Nanospindeln und Vesikeln aus Poly(ionischen Flüssigkeiten) (PILs) als harte bzw. weiche Vorlagen, um den Shuttle-Effekt von Lithiumpolysulfiden (LiPSs) in Li-S-Batterien zu unterdrücken. Drei Arten von Verbundstoffen mit unterschiedlichen Nanostrukturen (mesoporöse Nanospindel, Dotterschalen-Nanospindel und Nanokapsel) wurden synthetisiert und als Schwefel-Wirtsmaterial für Li-S-Batterien eingesetzt. Ihre Wechselwirkungen mit LiPS und ihre Auswirkungen auf die elektrochemische Leistung von Li-S-Batterien wurden systematisch untersucht.

Im ersten Teil der Arbeit wurden kohlenstoffbeschichtete mesoporöse  $\text{Fe}_3\text{O}_4$  ( $\text{C@M-Fe}_3\text{O}_4$ ) Nanospindeln synthetisiert, um den Shuttle-Effekt von LiPSs zu unterdrücken. Zunächst wurden  $\beta$ -FeOOH-Nanospindeln durch Hydrolyse von Eisen(III)-chlorid in wässriger Lösung synthetisiert. Nach der Beschichtung mit Siliziumdioxid und anschließender Kalzinierung wurde mesoporöses  $\text{Fe}_2\text{O}_3$  ( $\text{M-Fe}_2\text{O}_3$ ) innerhalb der begrenzten Siliziumdioxidschicht durch Pyrolyse von  $\beta$ -FeOOH erhalten. Nach der Entfernung der Siliziumdioxidschicht wurde Elektronentomographie (ET) eingesetzt, um die 3D-Struktur der  $\text{M-Fe}_2\text{O}_3$ -Nanospindeln zu rekonstruieren. Nach der Beschichtung mit einer dünnen Schicht Polydopamin (PDA) als Kohlenstoffquelle wurden die PDA-beschichteten  $\text{M-Fe}_2\text{O}_3$ -Partikel kalziniert, um  $\text{C@M-Fe}_3\text{O}_4$ -Nanospindeln zu synthetisieren. Durch die Chemisorption von  $\text{Fe}_3\text{O}_4$  und die Einschließung der mesoporösen Struktur zur Verankerung der LiPSs liefert die zusammengesetzte  $\text{C@M-Fe}_3\text{O}_4/\text{S}$ -Elektrode nach 600 Zyklen eine Restkapazität von  $507,7 \text{ mAh g}^{-1}$  bei 1 C.

Im zweiten Teil der Arbeit wurde eine Reihe von eisenbasierten Verbindungen ( $\text{Fe}_3\text{O}_4$ ,  $\text{FeS}_2$ , und  $\text{FeS}$ ) mit der gleichen Dotterschalen-Nanospindel-Morphologie synthetisiert, was einen direkten Vergleich der Auswirkungen der Zusammensetzungen auf die elektrochemische Leistung von Li-S-Batterien ermöglicht. Die  $\text{Fe}_3\text{O}_4$ -Kohlenstoff-Dotterschalen-Nanospindeln wurden unter Verwendung der  $\beta$ -FeOOH-Nanospindeln als harte Vorlage synthetisiert. Anschließend wurden  $\text{Fe}_3\text{O}_4$ -Kohlenstoff-Dotterschalen-Nanospindeln als Vorläufer verwendet, um Eisensulfide ( $\text{FeS}$  und  $\text{FeS}_2$ ) - Kohlenstoff-Dotterschalen-Nanospindeln durch Sulfidierung bei verschiedenen Temperaturen zu erhalten. Durch Verwendung der drei Arten von Dotterschalen-Nanospindeln als Schwefelwirt wurden die Auswirkungen der

Zusammensetzungen auf die Wechselwirkungen mit LiPS und die elektrochemische Leistung in Li-S-Batterien systematisch untersucht und verglichen. Die FeS<sub>2</sub>-C/S-Elektrode, die von der Chemisorption und der katalytischen Wirkung der FeS<sub>2</sub>-Teilchen und dem physikalischen Einschluss der Kohlenstoffschale profitiert, zeigt die beste elektrochemische Leistung mit einer anfänglichen spezifischen Entladekapazität von 877,6 mAh g<sup>-1</sup> bei 0,5 C und einem Kapazitätserhalt von 86,7 % nach 350 Zyklen.

Im dritten Teil wurden PILs-Vesikel als weiche Vorlage verwendet, um Kohlenstoff-Nanokapseln zu synthetisieren, die mit Eisennitridpartikeln durchsetzt sind, um LiPSs in Li-S-Batterien zu immobilisieren und deren Umwandlung zu katalysieren. Zunächst wurde 3-n-Decyl-1-Vinylimidazoliumbromid als Monomer für die Synthese von PIL-Nanovesikeln durch radikalische Polymerisation verwendet. Mit Hilfe der PDA-Beschichtung und des Ionenaustauschs wurden die PIL-Nanomoleküle erfolgreich als weiche Vorlage bei der morphologieerhaltenden Karbonisierung eingesetzt, um Kohlenstoff-Nanokapseln mit eingebetteten Eisennitrid-Nanopartikeln (Fe<sub>x</sub>N@C) herzustellen. Die gut dispergierten Eisennitrid-Nanopartikel katalysieren die Umwandlung von LiPS in Li<sub>2</sub>S aufgrund ihrer hohen elektrischen Leitfähigkeit und starken chemischen Bindung an LiPS effektiv. Die konstruierte Fe<sub>x</sub>N@C/S-Kathode zeigt eine hohe anfängliche Entladekapazität von 1085,0 mAh g<sup>-1</sup> bei 0,5 C mit einer verbleibenden Kapazität von 930,0 mAh g<sup>-1</sup> nach 200 Zyklen.

Die Ergebnisse dieser Arbeit zeigen, dass sich nanostrukturierte eisenbasierte Verbindungen mit kontrollierbarer Morphologie und Zusammensetzung leicht synthetisieren lassen, indem weiche und harte kolloidale Template verwendet werden, die als Schwefelwirt eingesetzt werden können, um das Shuttle-Verhalten von LiPS zu unterdrücken. Die in dieser Arbeit entwickelten Syntheseansätze sind auch für die Herstellung anderer Verbindungen auf Übergangsmetallbasis mit porösen Nanostrukturen für andere Anwendungen einsetzbar.

**Schlüsselwörter:** Schwefelwirt, Li-S-Batterien, Verbindungen auf Eisenbasis, Nanospindeln, Vesikel, Nanokapseln, Poly(ionische Flüssigkeiten), Elektronentomographie, Kryoelektronenmikroskopie

## Table of contents

Abstract.....	I
Zusammenfassung.....	III
<b>1. Introduction.....</b>	<b>1</b>
<b>1.1 Challenges in Li-S batteries.....</b>	<b>2</b>
1.1.1 Sulfur cathode.....	2
1.1.2 Lithium anode.....	4
1.1.3 Electrolyte.....	6
<b>1.2 Sulfur host design.....</b>	<b>8</b>
1.2.1 Physicochemical properties of sulfur and polysulfide.....	8
1.2.2 Designing sulfur host based on carbon with physical confinement of LiPSs ...	10
1.2.3 Designing polar sulfur host with chemical adsorption of LiPSs .....	12
<b>1.3 Objectives.....</b>	<b>14</b>
<b>2. Theory .....</b>	<b>19</b>
<b>2.1 Working principle of Li-S batteries.....</b>	<b>19</b>
2.1.1 Electrochemical thermodynamics.....	19
2.1.2 Electrochemical kinetics.....	21
<b>2.2 Template methods for the synthesis of nanostructured sulfur host .....</b>	<b>24</b>
2.2.1 Hard template method .....	24
2.2.2 Soft template method.....	26
<b>2.3 Interactions of iron-based compounds with LiPSs .....</b>	<b>28</b>
2.3.1 Iron oxides.....	28
2.3.2 Iron sulfides.....	30
2.3.3 Iron nitrides .....	32
<b>3. Carbon-coated Mesoporous Fe<sub>3</sub>O<sub>4</sub> Nanospindles with Interconnected Porosities as Polysulfide Mediators for Li-S Batteries .....</b>	<b>35</b>

<b>3.1 Synthesis of mesoporous Fe<sub>2</sub>O<sub>3</sub> nanospindle</b> .....	38
<b>3.2 Synthesis and characterization of C@M-Fe<sub>3</sub>O<sub>4</sub> and M-Carbon nanospindles</b> .....	40
<b>3.3 Interactions of mesoporous C@M-Fe<sub>3</sub>O<sub>4</sub> with polysulfides</b> .....	43
<b>3.3.1 LiPS adsorption test</b> .....	43
<b>3.3.2 Symmetrical cell</b> .....	44
<b>3.3.3 Li<sub>2</sub>S precipitation test</b> .....	45
<b>3.4 Electrochemical performance of C@M-Fe<sub>3</sub>O<sub>4</sub> as sulfur host for Li-S batteries</b> ....	47
<b>4. Yolk-Shelled Iron Sulfides-Carbon Nanospindles as Efficient Sulfur Host Materials for Li-S Batteries</b> .....	53
<b>4. 1 Synthesis and characterization of yolk-shell nanospindles</b> .....	55
<b>4.1.1 Fe<sub>3</sub>O<sub>4</sub>-carbon yolk-shell nanospindles</b> .....	55
<b>4.1.2 Iron sulfides-carbon yolk-shell nanospindles</b> .....	58
<b>4.2 Interactions of yolk-shell particles with LiPSs</b> .....	61
<b>4.2.1 LiPSs adsorption test</b> .....	62
<b>4.2.2 Investigation of catalytic effects</b> .....	62
<b>4.3 Electrochemical performance</b> .....	64
<b>5. Poly(ionic liquid) Nanovesicle-Templated Carbon Nanocapsules Functionalized with Uniform Iron Nitride Nanoparticles as Catalytic Sulfur Hosts for Li-S Batteries</b> .....	69
<b>5.1 Synthesis and characterization of Fe<sub>x</sub>N@C nanocapsules</b> .....	71
<b>5.1.1 Synthesis and characterization of PILs vesicle template</b> .....	71
<b>5.1.2 Synthesis and characterization of Fe<sub>x</sub>N@C and N-Carbon nanocapsules</b> .....	72
<b>5.2 Interaction of Fe<sub>x</sub>N@C particles with polysulfides</b> .....	79
<b>5.2.1 LiPSs adsorption test</b> .....	79
<b>5.2.2 Investigation of catalytic effects</b> .....	80
<b>5.3 Electrochemical performance</b> .....	81
<b>6. Summary and Outlook</b> .....	85
<b>7. Experimental Part and Methods</b> .....	87



<b>7.1 Chemicals and Materials</b> .....	87
<b>7.2 Material Synthesis Procedure</b> .....	88
<b>7.2.1 Synthesis of FeOOH nanospindles</b> .....	88
<b>7.2.2 Synthesis of polydopamine (PDA)-coated FeOOH nanospindles</b> .....	88
<b>7.2.3 Synthesis of SiO<sub>2</sub>-coated FeOOH nanospindles</b> .....	88
<b>7.2.4 Synthesis of mesoporous Fe<sub>2</sub>O<sub>3</sub> nanospindles</b> .....	88
<b>7.2.5 Synthesis of carbon-coated mesoporous Fe<sub>3</sub>O<sub>4</sub> nanospindles and mesoporous carbon nanospindles</b> .....	88
<b>7.2.6 Synthesis of Fe<sub>3</sub>O<sub>4</sub>-C yolk-shell nanoparticles</b> .....	89
<b>7.2.7 Synthesis of FeS<sub>2</sub>-C and FeS-C yolk-shell nanoparticles</b> .....	89
<b>7.2.8 Synthesis of hollow PIL nanocapsules</b> .....	90
<b>7.2.9 Synthesis of polydopamine-coated PILs nanovesicles (PDA@PILs)</b> .....	90
<b>7.2.10 Synthesis of carbon nanocapsules functionalized with iron nitride nanoparticles</b> .....	90
<b>7.2.11 Synthesis of nanovesicle-templated hollow carbon nanocapsules and bulk carbon particles</b> .....	91
<b>7.2.12 LiPSs adsorption tests</b> .....	91
<b>7.3 Electrochemical Measurement</b> .....	91
<b>7.3.1 Preparation of the sulfur/host material composites</b> .....	91
<b>7.3.2 Electrode preparation and coin cell assembly</b> .....	91
<b>7.3.3 Cyclic voltammetry, galvanostatic charge-discharge, and electrochemical impedance spectroscopy</b> .....	92
<b>7.3.4 Kinetics of Li<sub>2</sub>S precipitation and dissolution in the host materials</b> .....	94
<b>7.3.5 Kinetic evaluation of polysulfide conversion</b> .....	95
<b>7.4 Material Characterization</b> .....	95
<b>7.4.1 Powder X-ray diffraction (PXRD)</b> .....	95
<b>7.4.2 X-ray photoelectron spectroscopy (XPS)</b> .....	96

<b>7.4.3 Raman spectroscopy</b> .....	97
<b>7.4.4 Ultraviolet-visible (UV-vis) spectroscopy</b> .....	98
<b>7.4.5 Electron microscopy (EM)</b> .....	99
<b>7.4.6 Electron tomography</b> .....	102
<b>7.4.7 N<sub>2</sub> adsorption/desorption test</b> .....	103
<b>7.4.8 Thermogravimetric analysis (TGA)</b> .....	105
<b>Bibliography</b> .....	107
<b>List of Figures</b> .....	123
<b>List of Tables</b> .....	129
<b>List of Abbreviations</b> .....	131
<b>List of Publications</b> .....	135
<b>Acknowledgement</b> .....	139
<b>Declaration</b> .....	141

## 1. Introduction

Over the last decades, wide usage of nonrenewable fossil fuels (such as coal, gas, and fossil oil) as dominant power sources has released a massive amount of greenhouse gas ( $\text{CO}_2$ ) into the atmosphere, causing global warming. One of the most obvious damages of global warming is the increase in extreme weather events. To create a  $\text{CO}_2$ -neutral world for the next generations, scientists and engineers have devoted lots of effort to harnessing and storing renewable and clean energy sources (*e.g.*, tide, solar power, and wind) as a replacement.<sup>[1]</sup>

However, we could not effectively utilize green energy sources without appropriate energy storage technologies because most of them are intermittent. Thus, it is highly demanded to develop advanced battery systems, which are efficient, reliable, low-cost, and environmentally friendly to store energy on a large scale. Based on intercalation chemistry, the first commercialized lithium (Li)-ion battery was successfully made by Sony Group Corp. with  $\text{LiCoO}_2$  as cathode and graphite as anode in 1991 (Figure 1.1a).<sup>[2]</sup> Since then, Li-ion batteries have been widely applied in portable electric devices because, without memory effects, they have a long lifetime and high energy density. In the past three decades, Li-ion battery technology has been explored greatly with the inventions of new cathode materials, such as  $\text{LiFePO}_4$ ,<sup>[3]</sup>  $\text{LiMn}_{1.5}\text{Ni}_{0.5}\text{O}_4$ ,<sup>[4]</sup>  $\text{LiNi}_{0.80}\text{Co}_{0.15}\text{Al}_{0.05}\text{O}_2$  (NCA),<sup>[5]</sup> and  $\text{LiNi}_x\text{Mn}_y\text{Co}_z\text{O}_2$  (NCM),<sup>[6]</sup> to dominate the market of cell phones and electric vehicles. However, Li-ion batteries with NCM or NCA as cathodes are expensive due to the usage of cobalt and nickel elements. Notably, owing to the aggressive surface reaction with the organic carbonate electrolyte at a deep charge state, Li-ion batteries are flammable and extremely sensitive to high temperatures, leading to thermal runaways or even explosions.<sup>[7]</sup>

With the booming of the electric vehicle market, the increasing need for new energy-storage devices has prompted the development and exploration of next-generation batteries to extend

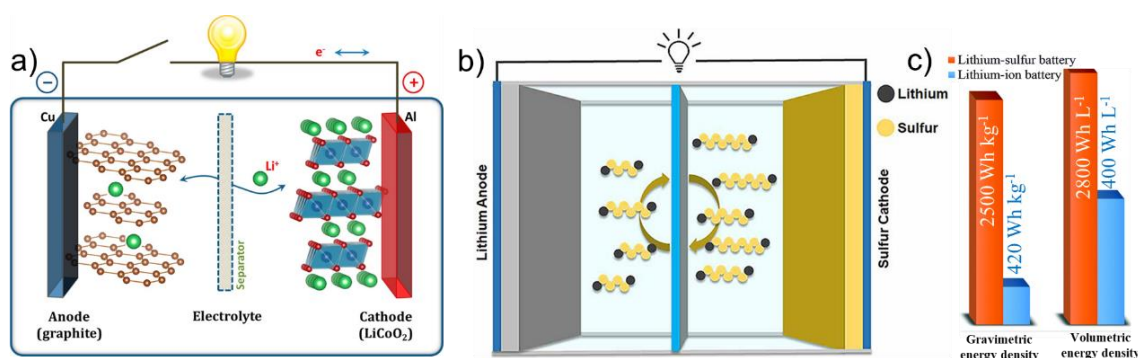


**Figure 1.1** Comparison of the components in Li-ion (a) and Li-S (b) batteries;<sup>[2, 8]</sup> (c) theoretical energy densities of Li-S battery and Li-ion battery.<sup>[9]</sup>

the range (130 miles for NCM and 45 miles for LiFePO<sub>4</sub>) and improve the safety of electric vehicles.<sup>[10]</sup> The limited energy density (420 Wh kg<sup>-1</sup> theoretically) of Li-ion batteries could not meet the needs of long-range electric vehicles and drones.<sup>[9]</sup> As a post Li-ion battery candidate, lithium-sulfur (Li-S) batteries with abundant sulfur as cathode have a theoretical specific capacity of 1675 mAh g<sup>-1</sup>, which is much higher than 274 mAh g<sup>-1</sup> of LiCoO<sub>2</sub>.<sup>[11]</sup> Coupled with Li metal as anode (Figure 1.1b), an ideally discharged Li-S battery could possess a theoretical energy density of 2800 Wh L<sup>-1</sup> or 2500 Wh kg<sup>-1</sup> (Figure 1.1c), which is much higher than those of commercial Li-ion batteries.<sup>[12]</sup> Unlike the high-cost elements (Co, Ni, and Mn) in Li-ion batteries, sulfur is widely spread, inexpensive, and environmentally benign. With these attractive advantages, Li-S battery system is regarded as one of the strongest competitors for future battery systems.

## 1. 1 Challenges in Li-S batteries

Despite all these merits, the real application of Li-S battery on a large scale is still hindered by several severe problems (*e.g.*, shuttle effect, flooded electrolyte, and lithium dendrite growth) in its sulfur cathode, electrolyte, and lithium anode, respectively.<sup>[9, 13]</sup> As a result, the scientific community and industry have explored a variety of strategies and techniques to address these serious issues, enhancing the electrochemical performance of Li-S batteries.<sup>[14]</sup> In this context, the challenges in different parts of Li-S batteries are discussed in the following parts.

### 1.1.1 Sulfur cathode

In 1962, elemental sulfur was first introduced by Ulam and Herbert as the electrode material in Li-S batteries and they proposed the redox reaction as  $2\text{Li} + \text{S} \leftrightarrow \text{Li}_2\text{S}$ .<sup>[15]</sup> Owing to its earth's abundance (the 17<sup>th</sup> richest element), cheap price, and less toxicity, sulfur as cathode could largely reduce the cost of battery production, contributing to green battery technology development. However, the usage of sulfur is plagued with several challenges, hindering its commercialization and application. The first one is related to the poor electronic conductivities of the discharged product Li<sub>2</sub>S and S cathode. The electrical conductivity of S is around  $5 \times 10^{-30}$  S cm<sup>-1</sup>,<sup>[16]</sup> while that of Li<sub>2</sub>S is  $\sim 1 \times 10^{-13}$  S cm<sup>-1</sup>.<sup>[17]</sup> Moreover, the bulk Li<sub>2</sub>S is a poor lithium ion conductor with an ionic conductivity of  $\sim 10^{-9}$  S cm<sup>-1</sup>.<sup>[17]</sup> Under this scenario, if the active sites on the cathode are completely blocked by Li<sub>2</sub>S particles, further lithiation process is impeded with rapid voltage decay. Consequently, the full conversion from sulfur to Li<sub>2</sub>S is difficult to reach, leading to low sulfur utilization. Owing to the large difference in the densities

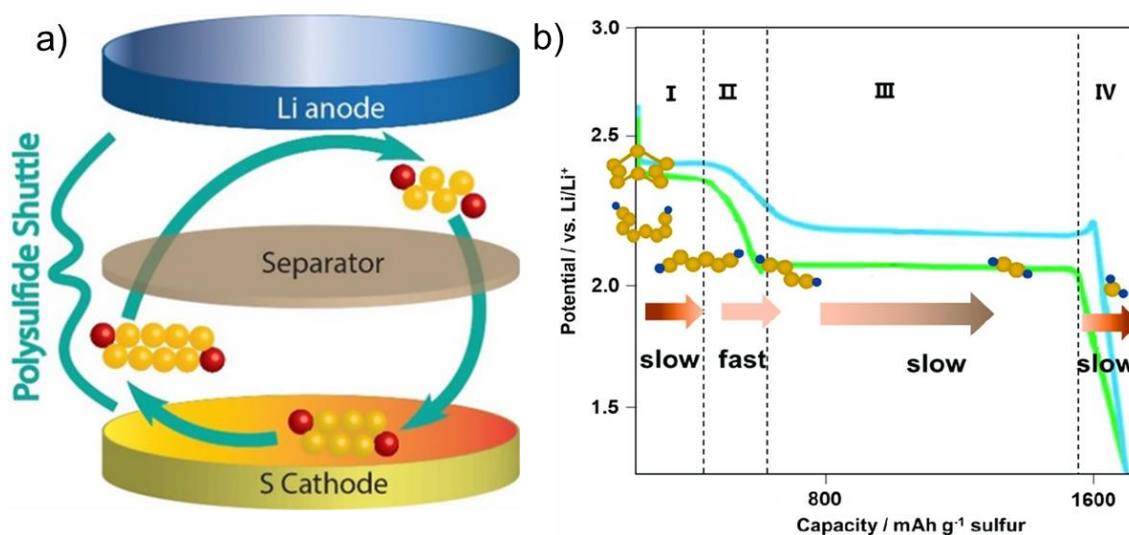


**Figure 1.2** (a) Polysulfide shuttle effect in a Li-S battery;<sup>[18]</sup> (b) typical voltage profiles of a Li-S battery during the discharge-charge process.<sup>[19]</sup>

of  $\text{Li}_2\text{S}$  ( $1.66 \text{ g cm}^{-3}$ ) and  $\text{S}$  ( $2.03 \text{ g cm}^{-3}$ ),<sup>[12]</sup> there is a volume variation of  $\sim 80\%$  in the sulfur cathode during the charging and discharging process. The large volume expansion and shrinkage will lead to fractures, pulverization, or even detachment of cathode materials from the current collector, resulting in rapid capacity decay.

Moreover, the well-known “shuttle effect” induced by lithium polysulfides (LiPSs) is the most significant problem in Li-S batteries. LiPSs are the  $\text{Li}_2\text{S}_n$  ( $n = 4-8$ ) intermediates produced by the reduction reaction from sulfur to  $\text{Li}_2\text{S}$ . LiPSs have high solubilities in the ether-based electrolyte. As demonstrated in Figure 1.2a, the produced long-chain LiPSs in the cathode during the discharging can cross the separator and diffuse to the lithium anode side due to the concentration difference between the anode and cathode.<sup>[18]</sup> Then, long-chain LiPS molecules are reduced by lithium into short-chain ones at the anode side. The produced short-chain LiPS species with high concentration at the anode side will further diffuse back to the cathode side and then get oxidized by sulfur to generate high-order LiPSs again. This unique parasitic process takes place continuously along cycling, resulting in an internal “shuttle” behavior between the lithium anode and sulfur cathode. Inevitably, the shuttle effect of LiPSs will lead to active material loss, an increase in impedance, poor Coulombic efficiency along cycling, as well as the passivation of lithium anode. Besides, LiPSs could continuously corrode the lithium chip during cycling. Previously, Qie *et al.* investigated the degradation mechanism of Li anode in Li-S batteries by using carbon nanofibers (CNFs) as sulfur host and  $1 \text{ M Li}_2\text{S}_6$  dissolved in the blank electrolyte as a sulfur source.<sup>[20]</sup> They found that after cycling, the thickness of the

lithium chip was largely decreased to 120  $\mu\text{m}$  from the initial 250  $\mu\text{m}$ , suggesting a large amount of lithium metal was consumed by the LiPSs after cycling.

Another main challenge in Li-S batteries is the sluggish redox reaction between the high-order LiPSs in the electrolyte and solid  $\text{Li}_2\text{S}_2/\text{Li}_2\text{S}$  during charging and discharging (Figure 1.2b) due to poor  $\text{Li}^+/\text{e}^-$  transportation.<sup>[19, 21]</sup> Anchoring LiPSs in the cathode side without promoted redox reaction kinetics doesn't ensure to deliver a high capacity for sulfur because the liquid-to-solid conversion reaction from  $\text{Li}_2\text{S}_4$  to  $\text{Li}_2\text{S}$  contributes about 75% to the theoretical capacity of sulfur.<sup>[22]</sup> Essentially, the liquid-to-solid conversion reaction is significantly suppressed by a high nucleation barrier of  $\text{Li}_2\text{S}$  on the surfaces of host materials. Therefore, understanding the reduction reaction from LiPSs to  $\text{Li}_2\text{S}$  in terms of thermodynamics and kinetics is important to develop sulfur hosts with abundant electroactive sites for boosting the reduction kinetics.<sup>[21]</sup> In short, it is necessary to develop a multifunctional host material that can confine LiPSs and simultaneously accelerate the transformation process between LiPSs and  $\text{Li}_2\text{S}$ .

### 1.1.2 Lithium anode

Lithium (Li) is the lightest alkali metal with a density of  $0.534 \text{ g cm}^{-3}$  for solid metallic Li. It is considered a “Holy Grail” electrode due to its lowest electrochemical potential, low gravimetric density, and high theoretical capacity ( $3860 \text{ mAh g}^{-1}$ ).<sup>[14c]</sup> Using metallic Li as anode is indispensable for achieving high-energy-density batteries (Li-S,<sup>[23]</sup> Li-O<sub>2</sub>,<sup>[24]</sup> and all-solid-state Li-ion batteries<sup>[25]</sup>). However, the safety issue of lithium metal as electrode is a serious concern because of its high chemical reactivity. Moreover, Li metal with ultralow potential is usually unstable with electrolytes (*e.g.*, solid electrolytes and organic liquid electrolytes) applied in different batteries.<sup>[14c]</sup> In addition, the Li dendrite formed during the repeated stripping/deposition process could penetrate the separator membrane, leading to a short circuit with serious thermal runaway.<sup>[26]</sup>

Similarly, Li dendrite growth is unavoidable in Li-S battery systems without further treatment or modification. In general, the dendrite formation is induced by two factors: one is the non-uniform distribution of current density on the surface of electrode; another is the concentration difference of lithium ions at the interfaces of the electrode and electrolyte.<sup>[27]</sup> The bottom of the lithium dendrites tends to strip first owing to its higher reactivity than the plated lithium. It quickly dissolves in the local region and separates from the lithium anode during the stripping process, forming “dead” Li disconnected from the conductive substrate without capacity contribution to battery.<sup>[28]</sup> This phenomenon decreases the efficiency and cycling performance

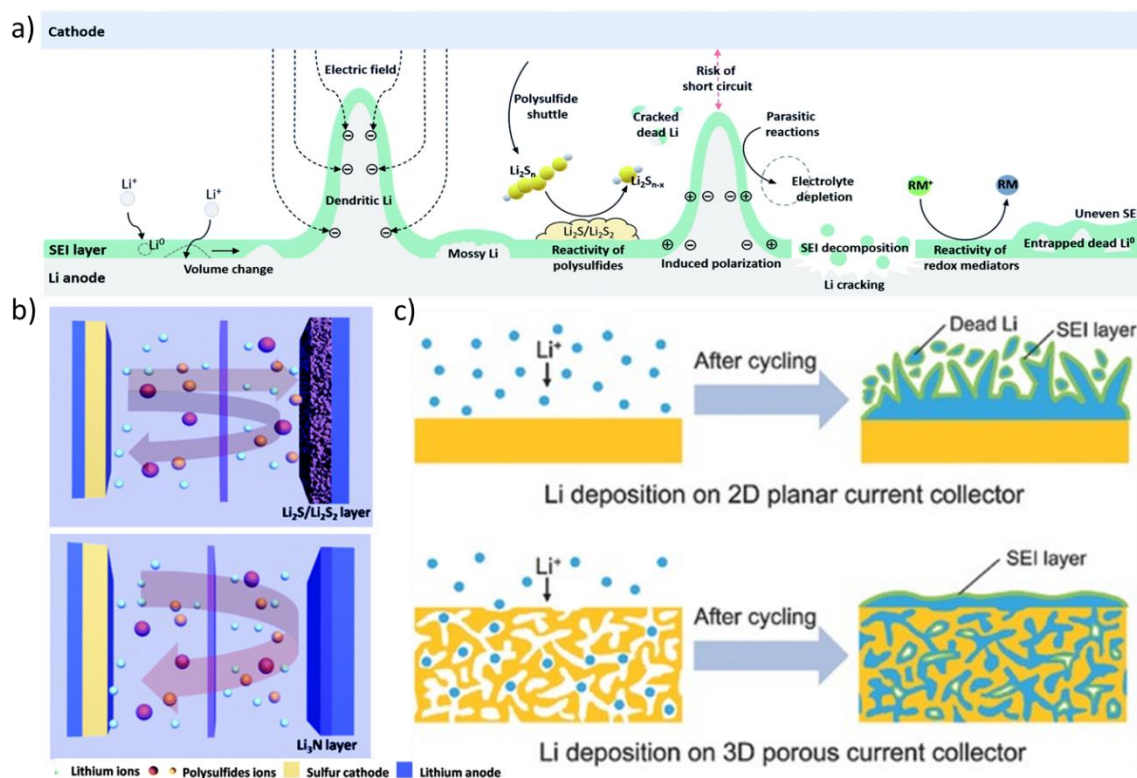


**Figure 1.3** (a) Scheme of the degradation of Li metal anode in Li-S batteries;<sup>[29]</sup> (b) Li-S batteries without/with  $\text{Li}_3\text{N}$  layer;<sup>[30]</sup> (c) Li deposition in a conventional 2D planar and a 3D porous current collector, respectively.<sup>[31]</sup>

of the battery with lithium anode. Moreover, it was proven both experimentally and theoretically that at high charge rates, the onset time of dendrite growth was highly related to the local consumption of the electrolyte at the electrode surface.<sup>[32]</sup>

Notably, the presence of LiPSs in Li-S batteries leads to a much more complicated scenario than that in lithium-ion batteries, as illustrated in Figure 1.3a.<sup>[29]</sup> To hinder the serious parasitic reactions between Li and LiPSs and the growth of lithium dendrite, there are two main strategies proposed: one is coating a physical layer on the lithium chip and another is designing a nanostructured current collector. As shown in Figure 1.3b, Ma *et al.* introduced a physical protection layer of lithium nitride ( $\text{Li}_3\text{N}$ ) on the lithium anode surface through the chemical reaction between nitrogen gas and lithium.<sup>[30]</sup> With a high ionic conductivity, the constructed  $\text{Li}_3\text{N}$  layer could suppress the side reactions between the lithium anode and electrolyte without hindering the lithium ion migration. Meanwhile, the undesired corrosive reactions between LiPSs and lithium were suppressed, contributing to the homogeneous deposition and stripping of lithium with improved safety. Since the nucleation and growth of lithium dendrite highly relies on the plating substrate, alternatively, designing current collectors for Li has been considered as an efficient method to control Li plating/stripping with depressed lithium

dendrite growth, as demonstrated in Figure 1.3c.<sup>[31]</sup> Ideal current collectors for lithium plating/stripping should lower the absolute local current density and provide robust mechanical support and suitable space for the huge volume change of lithium. Thus, different kinds of nanostructured lithiophilic hosts or current collectors with hierarchical pores or voids have been designed, such as porous carbon materials,<sup>[33]</sup> copper,<sup>[31]</sup> nickel,<sup>[34]</sup> and titanium.<sup>[35]</sup>

### 1.1.3 Electrolyte

The electrolyte conducts the ionic component of the electrochemical reactions between the anode and the cathode without premitting the flow of electrons.<sup>[2]</sup> With a high lithium ionic conductivity of  $10 \text{ mS cm}^{-1}$  at room temperature, liquid electrolytes enable efficient contact with porous electrodes, which further allows for rapid and effective transport of lithium ions. In addition, the electrolyte's electrochemical window should be wider than that of electrode materials. As illustrated in Figure 1.4, the electrochemical window of a liquid electrolyte is the energy difference between its highest occupied molecular orbital (HOMO) and the lowest unoccupied molecular orbital (LUMO).<sup>[2]</sup> If the chemical potential of an anode ( $\mu_A$ ) is higher than the LUMO of the electrolyte, it will reduce the electrolyte until the side reaction at the anode-electrolyte interfaces becomes blocked by forming a passivating solid electrolyte interphase (SEI) layer; likewise, the chemical potential of a cathode ( $\mu_C$ ) below the HOMO will oxidize the electrolyte inducing a passivating SEI layer at the interface.<sup>[2]</sup>

Generally, the liquid electrolyte for Li-S batteries consists of organic solvents, Li salts, and additives. Apart from some general requirements for electrolytes, it is worth noting that electrolyte components (such as solvent and salt) in Li-S batteries should exhibit good chemical stability to polysulfides due to their strong nucleophilic reactivity. Generally, carbonate-based solvents (*e.g.*, diethyl carbonate (DC) and ethylene carbonate (EC)) are not considered as candidates, because they can easily react with polysulfides to form thioether and sulfonium functionalities.<sup>[36]</sup> Owing to a high electrochemical and chemical stability, ether-based solvents (*e.g.*, 1,2-dimethoxyethane (DME), 1,3-dioxolane (DOL)) have been widely applied as candidate solvents for electrolytes in Li-S batteries.<sup>[10]</sup> The cyclic DOL was shown to be a suitable component since it could form a flexible SEI layer after reduction, which is made of oligomers with -OLi edge groups and -ROLi (R stands for alkyl) species.<sup>[37]</sup> The variations in the morphology of deposited lithium upon the charging-discharging process could be accommodated by the formed flexible SEI layer. But DOL has a limited solubility for LiPSs, leading to a sluggish reaction kinetics in the reduction reaction from sulfur to LiPSs. In the



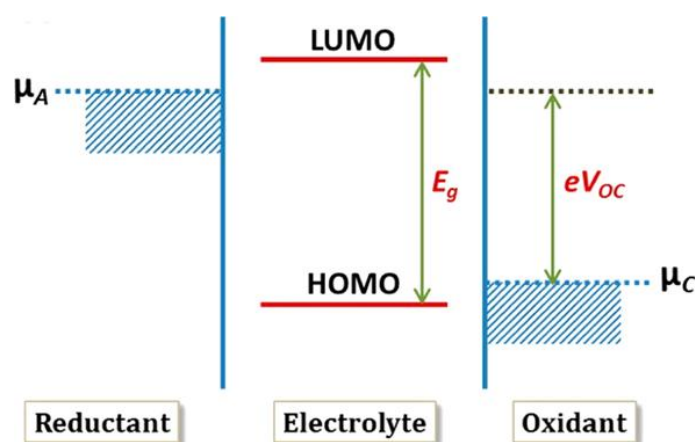


**Figure 1.4** Relative energies of the electrolyte window  $E_g$  and the electrode electrochemical potentials  $\mu_A$  and  $\mu_C$ .<sup>[2]</sup>

meantime, DME solvent possesses a high solvation ability for LiPSs, but it is more unstable with lithium than DOL.<sup>[38]</sup> As a result, with synergistic properties, a mixed solution of DME and DOL as a solvent for electrolyte can contribute to better electrochemical performance of Li-S batteries than a single solvent. In addition, the DME/DOL electrolyte with a low viscosity is beneficial to high-performance Li-S batteries at low temperatures. Owing to the above merits, the mixed solvent of DOL and DME is usually used to dissolve lithium salts as electrolyte for Li-S batteries.

Another important ingredient in electrolytes for Li-S batteries is lithium salts, which provide mobile lithium ions. The variation of the coordinated anions in lithium salts attributes to different physicochemical and electrochemical properties, such as the dissociation process in a specific solvent. Besides, it is also important to consider the compatibilities of lithium salts with polysulfides in case of any side reactions. For instance, although lithium hexafluorophosphate ( $\text{LiPF}_6$ ) has been widely used as lithium salt in electrolytes for Li-ion batteries, it is not chosen as lithium salt for Li-S battery systems because of the following side reactions:<sup>[39]</sup>



Similar reactions are also found in the lithium tetrafluoroborate ( $\text{LiBF}_4$ ). Moreover, since the crowded coordination anions (*e.g.*,  $\text{AsF}_6^-$ ,  $\text{PF}_6^-$ , and  $\text{BF}_4^-$ ) are Lewis acids, they can easily initiate the chain scission of solvent molecules, such as linear DME.<sup>[40]</sup> Currently, the most popular lithium salt applied in liquid electrolytes for Li-S batteries is lithium bis(trifluoromethanesulfonyl)imide ( $\text{LiTFSI}$ ) owing to its good dissociation ability, high ionic conductivity, excellent thermal stability, and good compatibility with LiPSs and ether-based solvents.<sup>[11]</sup> For instance, with the same mixed solvent DME/DOL for Li-S batteries, the

electrolyte dissolved with LiTFSI showed better stability than the one with bis(fluorosulfonyl) imide (LiFSI) because the weak N-S bond in the FSI<sup>-</sup> anion could be easily broken and react with LiPSs to generate lithium sulfate (Li<sub>2</sub>SO<sub>x</sub>).<sup>[41]</sup>

Besides lithium salts, modification of electrolytes with a trace amount of additives is considered as one of the efficient methods to improve the safety and cycling performance of Li-S batteries.<sup>[42]</sup> The additives can help to construct a robust and flexible SEI layer to hinder the growth of lithium dendrite and suppress the shuttle behavior and dissolution of polysulfide. In Li-S batteries, the great research progress of additives is the introduction of lithium nitrate (LiNO<sub>3</sub>) to electrolyte, which remarkably diminishes the possible reduction of LiPSs by lithium anode.<sup>[43]</sup> After discharging process, lithium nitride could form a stable SEI layer on the Li, mitigating the shuttle effect of LiPSs. Aurbach *et al.* investigated the chemical information on the surface of Li anode in the electrolytes with/without LiNO<sub>3</sub>.<sup>[43b]</sup> It was found that the additive LiNO<sub>3</sub> could be reduced to insoluble Li<sub>x</sub>NO<sub>y</sub> species, while the Li<sub>2</sub>S<sub>n</sub> could be oxidized to Li<sub>x</sub>SO<sub>y</sub> species. Both Li<sub>x</sub>NO<sub>y</sub> and Li<sub>x</sub>SO<sub>y</sub> components can suppress the side reactions of lithium anode with LiPSs.<sup>[43b]</sup> In short, the mixed DME/DOL solution dissolved with LiTFSI salt and a desired amount of LiNO<sub>3</sub> as additive has become the most popular electrolyte for Li-S batteries.

## 1.2 Sulfur host design

Over the last twenty years, great efforts have been made to improve the electrochemical performance of Li-S batteries via different strategies to suppress the shuttle behavior of LiPSs by blocking their transportation paths, such as sulfur host design,<sup>[13, 44]</sup> modification of separator,<sup>[45]</sup> and lithium protection.<sup>[27]</sup> It is believed that anchoring the LiPSs with sulfur host materials is much more effective than other methods to achieve high-performance Li-S batteries. Under a comprehensive consideration of good electrical conductivity, mitigation of the shuttle effect, accommodation of volume expansion, and improvement of safety, rational sulfur host design is highly demanded to mitigate or solve those issues simultaneously.<sup>[13]</sup> In addition, for practical applications, the cost and scalability of host materials should also be addressed.

### 1.2.1 Physicochemical properties of sulfur and polysulfide

Understanding the physicochemical properties of sulfur and polysulfides is of great significance for designing an effective sulfur host. Sulfur exists in the form of cyclo-S<sub>8</sub> with a

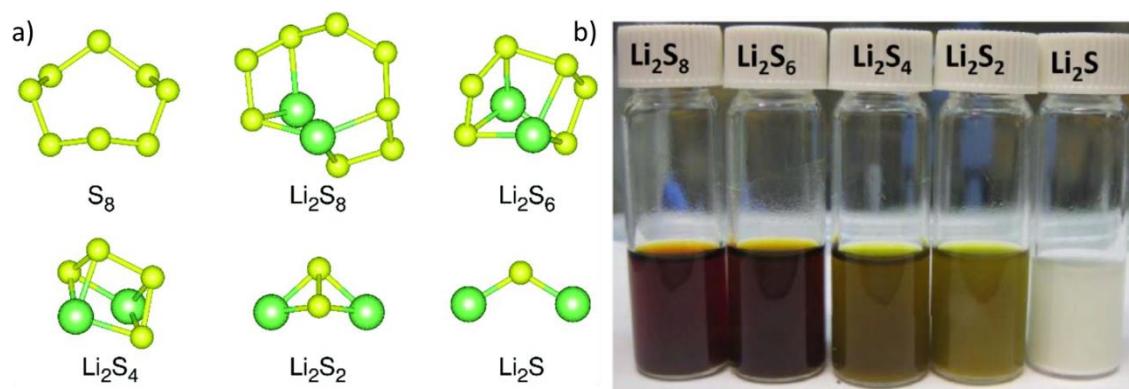


**Figure 1.5** (a) The molecular structures of S<sub>8</sub> and Li<sub>2</sub>S<sub>n</sub> (n = 8, 6, 4, 2, and 1), where the green and yellow balls represent the Li and S atoms, respectively;<sup>[46]</sup> (b) different Li<sub>2</sub>S<sub>n</sub> dissolved in DOL/DME solvents.<sup>[47]</sup>

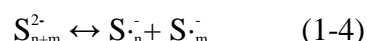
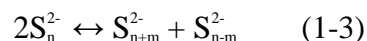
crown-shaped ring structure under ambient environments,<sup>[48]</sup> and its calculated S-S-S angle and S-S bond length are 109.3° and 2.06 Å, respectively.<sup>[49]</sup> The most common sulfur on earth is orthorhombic  $\alpha$ -S. When heated to 95.6 °C,  $\alpha$ -S transforms to its  $\beta$ -phase and then melts at 119.6 °C and converts to  $\lambda$ -S.<sup>[50]</sup> In the melting state, most S<sub>8</sub> rings are in liquid equilibrium with other sulfur rings with different sulfur numbers, controlling the viscosity of liquid sulfur.<sup>[50]</sup> A minimum viscosity of sulfur with low-molecular rings reaches around 155 °C, which is used for melt-diffusion infiltration of sulfur into porous host materials. Interestingly, when the temperature is over 159 °C, S<sub>8</sub> rings can form linear sulfenyl diradical by the thermal scission, initiating the ring-opening polymerization (ROP) of S<sub>8</sub> rings into a high-molecular-weight linear polysulfane.<sup>[48]</sup> With this unique property, free-radical copolymerization between sulfur and organic monomers can be realized only by heating the sulfur above the ground temperature for the ROP. With increasing temperature, sulfur obtains a maximum viscosity in the range of 186 to 188 °C. Sulfur reaches its boiling point at 445 °C and starts to evaporate. Based on this particularity of sulfur, thermogravimetric analysis (TGA) has been widely applied to determine the specific sulfur content inside a host/sulfur composite material. Due to its high chemical reactivity, sulfur can be also used as sulfur source to synthesize metal sulfides. In the meantime, sulfur is highly soluble in carbon disulfide (CS<sub>2</sub>) with a solubility of 24 wt. % at room temperature.<sup>[51]</sup> Thus, a solution-based infiltration method has been used to impregnate sulfur into porous host materials as cathode for Li-S batteries.

Apart from sulfur, the physicochemistry nature of polysulfides is another consideration for rational sulfur host design to mitigate the shuttle effect. Essentially, polysulfides contain multiple sulfur atoms, which are linked with each other by covalent bonds. Sulfur atoms with a high S-S binding energy (265 kJ mol<sup>-1</sup>) prefer to form rings and homoatomic chains.<sup>[52]</sup> The

existing states of polysulfides are complicated and ever-changing, including the oxidization state, charge number, steric configuration, and cluster level.<sup>[53]</sup> Generally, polysulfide anions exist in high-temperature melts or solutions with two dominant forms (the singly charged radical monoanion and dianion) via the chemical equilibrium.



Furthermore, owing to their similar Gibbs free energies, polysulfide anions are present with each other in comproportionation or disproportionation equilibria.<sup>[39]</sup>



Individual polysulfide equilibria are extremely difficult to isolate and be characterized spectroscopically and analytically due to their complexity.<sup>[53]</sup> Unlike the chair-like or cyclic structure in Figure 1.5a, computational calculation results showed that polysulfide anions were thermodynamically stable in the form of a chain-like cluster in solutions.<sup>[46]</sup> Additionally, due to the high reactivity of the outer-shell electrons, the terminal sulfur (charge of 1-) atoms in the polysulfide molecule exhibit high chemical reactivity, as evidenced by their high sensitivity to moisture and air.<sup>[53-54]</sup> Moreover, the long-chain polysulfides are highly soluble in ether-based solvents, as demonstrated in Figure 1.5b.<sup>[47]</sup> It's important to note that the stability of polysulfides is highly dependent on the solvents. In aqueous solutions, the most stable polysulfide molecules are  $S_4^{2-}$  and  $S_5^{2-}$ ,<sup>[55]</sup> while in polar non-aqueous solutions like tetrahydrofuran, long-chain  $S_6^{2-}$  and  $S_8^{2-}$  exhibit better stability.<sup>[56]</sup> The wide range of sulfur atom numbers in polysulfides leads to a large variation in the molecular polarities. In other words, the solubility of LiPSs highly relies on the properties of the used solvent. Therefore, it's challenging to find a universal solvent with high solubilities for all polysulfide anions.

### 1.2.2 Designing sulfur host based on carbon with physical confinement of LiPSs

To mitigate the poor electrical conductivities of sulfur and  $Li_2S_2/Li_2S$ , a conductive host or matrix is required for an improved electron transport process in the electrochemical redox reaction. Nanostructured carbon-based materials with a high specific surface area have been widely explored as sulfur host materials due to their excellent electrical conductivity and sufficient pore volume.<sup>[14a, 57]</sup> The pores or void spaces inside the carbon materials can anchor LiPS molecules through van der Waals' force. The porous structure or hollow space can efficiently suppress the volume variation induced by the redox reaction from sulfur to  $Li_2S$  during discharge. In 1989, Peled *et al.* used porous carbon to enhance the electron contact

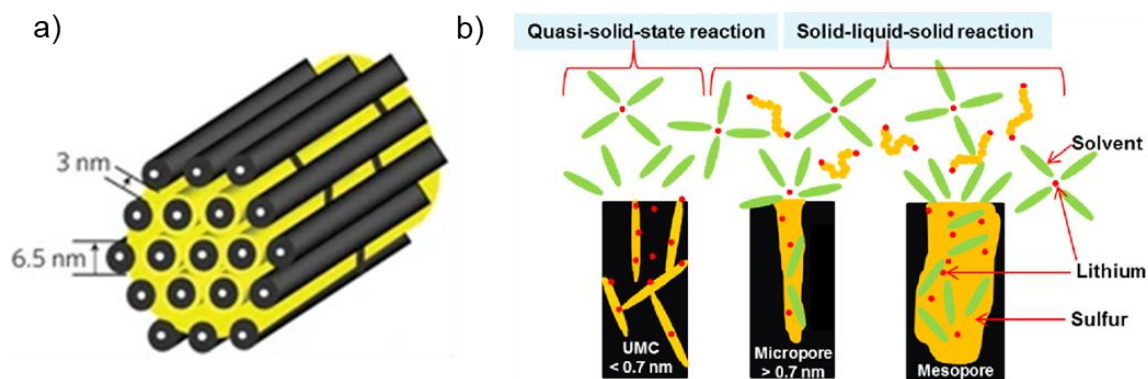


**Figure 1.6** (a) A schematic diagram of the sulfur (yellow) confined in CMK-3 through melting impregnation;<sup>[58]</sup> (b) illustration of the difference in solvent accessibility by sulfur in carbon pores of varying size (ultramicroporous carbon (UMC), microporous and mesoporous carbon) in carbon/sulfur composites.<sup>[59]</sup>

efficiency of sulfur cathode in Li-S batteries with an improved energy density.<sup>[37]</sup> In 2009, significant progress in Li-S batteries was made by Nazar's group. As shown in Figure 1.6a, they first introduced the ordered conductive mesoporous carbon framework (CMK-3) as sulfur host and greatly improved the capacity of sulfur with good cycling stability.<sup>[58]</sup> This is because the CMK-3 structure could work as an electronic conduit to the encapsulated sulfur and confine the polysulfides formed during charging-discharging process at the same time. Later on, various strategies have been developed to synthesize nanostructured carbon materials as sulfur host materials with functionalities of high electrical conductivity and efficient confinement to LiPSs.<sup>[58]</sup>

According to the geometric structures, carbon-based materials as a sulfur host can be classified as porous/hollow carbon spheres (0D), carbon nanotubes/fibers (1D), graphene or nanoflakes (2D), and hierarchical/free-standing structures (3D). Although many carbon materials with unique nanostructures have been developed, systematic research on the geometric structures of sulfur hosts is rarely investigated.<sup>[60]</sup> During the charging-discharging process, the accumulated sulfur species dimensionally block electron transportation, suppressing the further activation of sulfur species. Formerly, Qi *et al.* systematically studied the failure mechanism of Li-S batteries through carbon materials with different geometric structures: elaborately designed 3D carbon structure, 2D carbon flake (CF), 1D carbon nanotube (CNT), and 0D Ketjenblack (KB) spheres.<sup>[60]</sup> The results showed that the precipitation of sulfur-related species after the discharge process resulted in large contact resistance in the batteries with low dimensional hosts, while small resistance was observed in the 3D sulfur host.<sup>[60]</sup> Moreover, the 3D sulfur host exhibited faster conversion reaction kinetics from liquid LiPSs to solid Li<sub>2</sub>S, hence mitigating the shuttle effect of polysulfides.<sup>[60]</sup>

Apart from the geometric structures, carbon-based materials confine LiPSs mainly through their pores because of their nonpolar nature. Porous carbon materials as sulfur host can be classified into macroporous (>50 nm), mesoporous (2-50 nm), and microporous (<2 nm) carbon, respectively, based on different pore sizes.<sup>[23]</sup> Specifically, microporous carbon materials with fine pore size are considered as a suitable host material for suppressing the shuttle effect since the pore size in microporous carbon is close to that of polysulfide molecules.<sup>[61]</sup> But the microporous carbon materials have poor contact with liquid electrolyte, leading to sluggish quasi-solid-state reactions, as demonstrated in Figure 1.6b.<sup>[59]</sup> Mesoporous carbon materials as sulfur host enable sufficient contact of host material with electrolyte, have more available paths for lithium ion diffusion, and allow for a high sulfur loading in the cathode. Macroporous carbon materials as sulfur host materials are rarely applied since the pore size is too large to efficiently immobilize polysulfides. Therefore, microporous and/or mesoporous carbon materials are widely designed and synthesized as sulfur host materials for Li-S batteries.<sup>[23]</sup>

### 1.2.3 Designing polar sulfur host with chemical adsorption of LiPSs

It is well-known that LiPSs are polar molecules, while carbon-based host materials (such as CNT and graphene) are nonpolar. As a result, the nonpolar surfaces of carbon materials have a poor interaction with  $\text{Li}_2\text{S}_n$  species. Under the strong electric field and concentration gradient between the cathode and anode, carbon materials can not efficiently anchor polysulfides with the poor van der Waals' force, causing the serious shuttle effect.<sup>[62]</sup> Thus, alternatively, polar metal-based compounds have been proposed to suppress the shuttle effect because of their stronger chemical bonding with LiPSs.

Most recently, nanostructured metal-based compounds were investigated to trap polysulfides owing to their abundant active sites and catalytic properties, which could suppress the shuttle effect.<sup>[63]</sup> According to the different electrical conductivities, as demonstrated in Figure 1.7, they can be classified as conductors (*e.g.*  $\text{Ti}_4\text{O}_7$ , FeS, and VN), semimetals (*e.g.*  $\text{TiS}_2$  and  $\text{VS}_2$ ), semiconductors (*e.g.*  $\text{TiO}_2$  and  $\text{MnO}_2$ ), and insulators (*e.g.*  $\text{Al}_2\text{O}_3$  and metal hydroxides). This variety raises an important question of whether the electrochemical kinetics of the redox reaction from polysulfide to  $\text{Li}_2\text{S}$  is controlled by the conductivity of polar host materials.<sup>[64]</sup> There are two main factors (adsorption and nucleation) that dominate the interfacial electrochemical kinetics of  $\text{Li}_2\text{S}$  deposition from LiPSs in electrolyte.<sup>[63-64]</sup> First, to avoid the active material loss, efficient adsorption to LiPSs should be made in the host material by

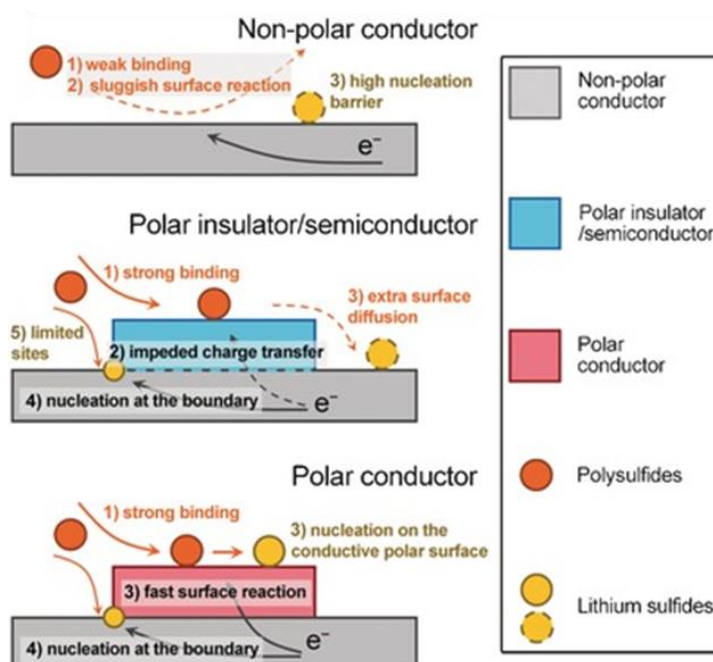


**Figure 1.7** Illustration of the working mechanism of different conductors as sulfur host materials.<sup>[64]</sup>

abundant binding sites. Moreover, facilitated charge transfer at the liquid/solid interfaces should be guaranteed for the redox reaction.<sup>[63]</sup> As non-polar hosts, carbon materials are doomed to be poor at binding LiPSs, leading to a low utilization of sulfur. Furthermore, the nucleation barrier caused by the surface energy difference between deposited  $\text{Li}_2\text{S}$  nuclei and the host plays a crucial role in the growth of  $\text{Li}_2\text{S}$  particles. For a semiconductor or polar insulator host such as  $\text{Al}_2\text{O}_3/\text{TiO}_2$ , although it has the suitable chemical affinity required for LiPSs, the direct conversion on the surface of the polar host material is depressed due to the low electrical conductivity. As a result, nucleation of  $\text{Li}_2\text{S}$  particles can only take place at the “triple-phase” sites of the insulating host, liquid electrolyte, and conductive agent. In other words, the active site density in the insulating host is slightly low. Therefore, a polar conductive host is required to fully meet the requirements for both effective charge transport and sufficient binding of LiPSs. Such a polar conductive host can improve the electrochemical kinetics since the sulfur reduction reactions can easily occur at abundant “triple-phase” sites.

However, compared with the nanostructured carbon materials, most polar metal-based compounds as sulfur host materials suffer from a low specific surface area, which leads to few exposed active sites for LiPSs adsorption.<sup>[44]</sup> Moreover, the low utilization efficiency of host materials causes a decreasing gravimetric energy density of Li-S batteries. For small or fine nanoparticles, they tend to be merged into larger ones during heat treatment. It is worth noting that metal-based compounds (*e.g.*, sulfides and nitrides) with a high specific surface area are

unstable when they are exposed to air, weakening their reaction activity and possible catalytic properties. To address these issues, composites with carbon materials have been applied to suppress the oxidation and particle size growth of metal-based compounds during heat treatment. Thus, designing and synthesizing the composites of carbon materials and metal-based compounds as sulfur host materials is considered as an efficient way to confine LiPSs through the combination of physical confinement and chemisorption.

As mentioned above, the sluggish sulfur reduction reaction (SRR) kinetics from LiPSs to  $\text{Li}_2\text{S}$  in the cathode side results in an inadequate utilization of sulfur, which in turn aggravates the polysulfide shuttle since the confined polysulfides will inevitably diffuse to the anode side owing to the large concentration gradients between cathode and anode. In other words, the widely applied confinement strategies with the sole functionality of adsorption to LiPS could not fundamentally resolve the shuttle effect problem without promoting the SRR kinetics. Ideally, to achieve full utilization of sulfur cathodes, it is necessary to design a host material with multiple functionalities, which can both immobilize LiPSs and accelerate the conversion kinetics of SRR. It was found that promoting charge transfer and/or decreasing the reaction energy barrier of sulfur cathodes could effectively improve the SRR kinetics with rationally designed host materials.<sup>[21]</sup>

Besides, for real applications of Li-S batteries, it is essential to synthesize sulfur host materials in a large scale at a low cost. So far, developing a scalable synthesis method with low cost has become a challenging and indispensable proposition for the wide application of Li-S batteries. To address these challenges, colloidal synthesis routes have been chosen to synthesize sulfur host materials because of the simple procedures, mild conditions, uniformity, and mass production. In this thesis, colloidal  $\beta\text{-FeOOH}$  nanospindles and imidazole-based poly(ionic liquid)s particles have been used as template to synthesize nanostructured iron-carbon composite as sulfur host for Li-S batteries because they are low-cost and easily synthesized in gram scale. Owing to the polarity, good electrical conductivity, and low cost, iron-based compounds (oxide, sulfide, and nitride) have been integrated into carbon materials with different nanostructures to suppress the shuttle effect of LiPSs and promote the SRR kinetics.

### 1.3 Objectives

The main objective of this thesis is the synthesis of iron-based compounds with different nanostructures, characterization, and their application as sulfur hosts for Li-S batteries. The nanostructured iron-based compounds could offer void space for sulfur loading, suppress the



shuttle effect of LiPSs, and provide active sites to facilitate the electrochemical conversion process, contributing to improved electrochemical performance.

The first work aims to synthesize carbon-coated mesoporous iron oxide ( $\text{Fe}_3\text{O}_4$ ) nanospindles, which can be used as sulfur host materials and provide a polar surface to confine LiPSs in Li-S batteries. The investigation is carried out as follows:

- ✚ The colloidal  $\beta$ - $\text{FeOOH}$  particles with a nanospindle morphology have been synthesized via the hydrolysis of  $\text{FeCl}_3$  in an aqueous solution. After coating a condensed layer of  $\text{SiO}_2$ , porous  $\text{Fe}_2\text{O}_3$  nanospindles ( $\text{M-Fe}_2\text{O}_3$ ) have been produced within the  $\text{SiO}_2$ -coated layer after thermal pyrolysis. The  $\text{M-Fe}_2\text{O}_3$  particles have been applied as template to obtain the carbon-coated mesoporous iron oxide ( $\text{C@M-Fe}_3\text{O}_4$ ) particles through PDA coating and following calcination.
- ✚ To follow the morphology and phase transformation of the target samples in each step, transmission electron microscopy (TEM) images, scanning electron microscopy (SEM) images, and X-ray diffraction (XRD) patterns have been collected. Moreover, the  $\text{N}_2$  adsorption/desorption measurement and electron tomography (ET) have been conducted to analyze the pore features of the porous samples. The spectra of C 1s, N 1s, and Fe 2p of the carbon-coated mesoporous iron oxide ( $\text{M-Fe}_3\text{O}_4$ ) have been collected by X-ray photoelectron spectroscopy (XPS) to reveal the chemical state.
- ✚ To study the adsorption ability of the samples to LiPSs: first, the LiPS was synthesized through the chemical reaction between  $\text{Li}_2\text{S}$  and sulfur in a solvent at  $80^\circ\text{C}$ . Then, visualized adsorption tests along with UV-*vis* spectroscopy measurements have been conducted. To evaluate the effects of  $\text{M-Fe}_3\text{O}_4$  nanoparticles on liquid-to-liquid and liquid-to-solid conversion reactions, the cyclic voltammetry (CV) curves of symmetric cells and  $\text{Li}_2\text{S}$  precipitation tests have been carried out.
- ✚ The  $\text{C@M-Fe}_3\text{O}_4/\text{S}$  composite was prepared by the melting diffusion method and the specific content of sulfur in the composite was determined by thermogravimetric analysis (TGA). The electrochemical performance of Li-S batteries with the  $\text{C@M-Fe}_3\text{O}_4/\text{S}$  cathode has been investigated in 2032-type coin cells. The CV curves, rate capability, electrochemical impedance spectroscopy (EIS), and cycling performance have been collected.

The second work aims to study the effect of compositions of iron-based compounds ( $\text{Fe}_3\text{O}_4$ ,  $\text{FeS}$ , and  $\text{FeS}_2$ ) with the same yolk-shell morphology on the electrochemical performance

(capacity, cycling stability, and rate capability) of Li-S batteries. The investigation has been carried out as follows:

- ✚ To get a yolk-shell nanostructure, a thin layer of PDA has been coated on  $\beta$ -FeOOH particles. With the optimization of the calcination condition under an argon atmosphere, the Fe<sub>3</sub>O<sub>4</sub>-C yolk-shell nanostructure has been achieved. To increase the void space in the shell, partial Fe<sub>3</sub>O<sub>4</sub> particles have been etched off with an optimized etching condition. Then, the collected Fe<sub>3</sub>O<sub>4</sub>-C yolk-shell particles mixed with sulfur have been used to synthesize FeS-C and FeS<sub>2</sub>-C yolk-shell particles at different temperatures.
- ✚ The iron-based yolk-shell particles have been systematically characterized with TEM, SEM, N<sub>2</sub> adsorption-desorption isotherms, Raman spectra, XRD, and XPS. The visualized adsorption test of Fe<sub>3</sub>O<sub>4</sub>-C, FeS-C, and FeS<sub>2</sub>-C yolk-shell particles in the LiPS solution has been conducted to evaluate their adsorption abilities to LiPSs.
- ✚ To reveal the effects of the composition of different iron-based compounds on liquid-to-liquid and liquid-to-solid conversion reactions, the CV curves of symmetric cells and Li<sub>2</sub>S precipitation test have been collected, respectively. The electrochemical performance of the three iron-based cathodes (Fe<sub>3</sub>O<sub>4</sub>-C/S, FeS-C/S, and FeS<sub>2</sub>-C/S) has been investigated in 2032-type coin cells by measuring the CV curves, rate capability, electrochemical impedance spectroscopy (EIS), and cycling stability.

The third work aims to synthesize hollow carbon capsules embedded with ultrafine iron nitride particles (Fe<sub>x</sub>N@C), which can provide void space to confine polysulfides and facilitate Li<sub>2</sub>S precipitation in Li-S batteries. The investigation has been carried out as follows:

- ✚ 3-n-decyl-1-vinylimidazolium bromide has been used to synthesize PILs vesicles via free radical polymerization in an aqueous solution and the PILs vesicles as soft template have been synthesized to obtain hollow carbon capsules embedded with ultrafine iron nitride particles. After PDA coating and followed by ion exchange, ferricyanide anions were introduced into the PILs vesicles. With melamine as the nitrogen source, hollow carbon capsules embedded with ultrafine iron nitride particles have been successfully fabricated after calcination in the tubular furnace under argon. The effects of PDA coating, ion-exchange process, calcination temperature, and usage of melamine on the morphologies of the final samples have been studied.
- ✚ The cryogenic electron microscopy (cryo-EM) images, TEM, and SEM images of the PILs vesicles were collected. The iron-based particles have been characterized with TEM images

and XRD patterns. The carbon nanocapsules embedded with iron nitrides have been comprehensively investigated by TEM, SEM, N<sub>2</sub> adsorption-desorption, TGA, XPS, and XRD techniques to have a comprehensive understanding of the morphology, crystal structure, porosity, and chemical state information.

- ✚ To reveal the adsorption ability and mechanism of the Fe<sub>x</sub>N@C particles to LiPSs, visualized adsorption tests of LiPSs solution have been conducted and the Fe 2p spectra of the Fe<sub>x</sub>N@C particles after the adsorption test have been measured to study the interactions between iron nitride and LiPSs.
- ✚ The catalytic effects of Fe<sub>x</sub>N@C particles on sulfur reduction reaction have been demonstrated with the CV curves of symmetric cells and Li<sub>2</sub>S precipitation tests. The electrochemical performance of the Fe<sub>x</sub>N@C/S electrode has been systematically investigated. After cycling, TEM images of the Fe<sub>x</sub>N@C particles used in the Fe<sub>x</sub>N@C/S electrode have been taken to reveal the nanostructure evaluation of the host material.



## 2. Theory

### 2.1 Working principle of Li-S batteries

#### 2.1.1 Electrochemical thermodynamics

The redox potential of an electrode material is determined by the Gibbs free energy change between the reactants and products of the electrochemical reaction:

$$E = -\Delta G/nF \quad (2-1)$$

where  $E$  represents the redox potential of the electrode material,  $F$  refers to the Faraday constant,  $\Delta G$  represents the Gibbs free energy change of the electrochemical reaction, and  $n$  is the number of charge during the electrochemical reaction, respectively.<sup>[65]</sup> The transformation from sulfur to  $\text{Li}_2\text{S}$  in Li-S batteries is a two-electron conversion reaction rather than an intercalation mechanism. The whole electrochemical reaction in Li-S batteries can be formulated as follows:



The free reaction enthalpy  $\Delta_r G^0(\text{Li/S})$  for this reaction is  $-432.6 \text{ kJ mol}^{-1}$  at  $25^\circ\text{C}$ , from which the theoretical cell potential ( $E^0$ ) is calculated to be  $2.24 \text{ V}$ .<sup>[66]</sup> Due to the electrochemical polarization and resistance, the real charge voltage of a battery is slightly higher than the theoretical one.<sup>[66b]</sup> The open circuit voltage ( $V$ ) between the cathode and anode is also the same as the difference in the chemical potential of electrons in the anode and the cathode according to the Nernst equation:

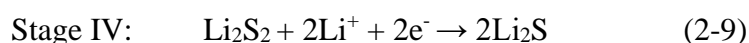
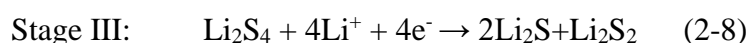
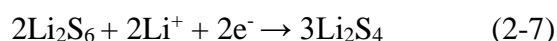
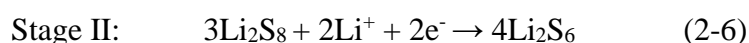
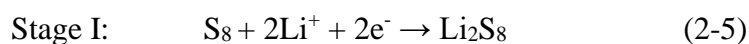
$$V = \frac{\mu_A - \mu_C}{e} \quad (2-3)$$

where  $\mu_C$  and  $\mu_A$  stand for the chemical potential of electrons in the cathode and anode, respectively.<sup>[67]</sup> When lithium is applied as the reference electrode in a battery, the lithium chemical potential within the electrode determines the voltage profile of an electrode material. Under this condition, the voltage curves of a working electrode along cycling could provide direct information about the thermodynamic properties, such as phase transformations of electrode material with lithium accommodation and the Li chemical potential, which has characteristic signatures in the voltage curves.<sup>[67]</sup> This is because any variations in the chemistry or crystal structure of the electrode material will induce the change in its Li-chemical potential, Gibbs free energy, and hence the voltage.

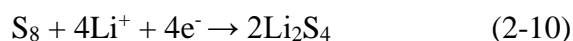
Except for voltage, the capacity of electrode material is also highly related to the energy density of the battery. For an electrode material, based on Faraday's law, the theoretical capacity can be calculated by the following equation:

$$Q = nF/(3600 \times M_w) \quad (2-4)$$

where  $F$  refers to the Faraday constant,  $n$  is the number of transferred electrons during the redox reaction, and  $M_w$  is the molecular weight of the electrode, respectively. According to Equation (2-4), the calculated theoretical capacity of S is 1675 mAh g<sup>-1</sup>. A typical Li-S battery has a similar sandwich structure with metallic lithium as the anode, composite sulfur as the cathode, a porous membrane as a separator, and lithium salts dissolved in ether-based solvents as the electrolyte. The voltage of a Li-S battery is proportional to the difference between the electrochemical potentials of the S cathode and Li anode, contributing an average working voltage of ~2.1 V (vs. Li/Li<sup>+</sup>).<sup>[68]</sup> Differing from the “solid-to-solid” phase conversion in Li-ion batteries, the sulfur cathode follows a multistep “solid-liquid-solid” electrochemical reaction since the polysulfide intermediates are dissolved in the liquid electrolyte. As demonstrated in Figure 1.2b, the detailed reactions can be described as follows:



At the beginning of the discharge curve, the dissolved sulfur in the electrolyte is reduced to long-chain Li<sub>2</sub>S<sub>8</sub>. Since LiPSs are highly soluble in the electrolyte, this step is a solid-liquid reaction. Subsequently, long-chain Li<sub>2</sub>S<sub>8</sub> molecules are reduced to lower-order ones (Li<sub>2</sub>S<sub>6</sub> and Li<sub>2</sub>S<sub>4</sub>), involving a liquid-liquid reaction (single phase). This high plateau around 2.3 V of the discharge curve is caused by the conversion reactions from sulfur to polysulfide, which have a contribution of 25% to the whole sulfur capacity. The overall reaction and corresponding Nernst equation are:



$$E_H = E_H^\ominus + \frac{RT}{n_{\text{HF}}} \ln \frac{[\text{S}_{8(l)}]}{[\text{S}_4^{2-}]^2} \quad (2-11)$$

where  $E_H$  represents the cell potential high plateau,  $E_H^\ominus$  is the standard cell potential at the high plateau, and  $[\text{S}_{8(l)}]$  and  $[\text{S}_4^{2-}]$  are sulfur and polysulfide S<sub>4</sub><sup>2-</sup> concentrations dissolved in the electrolyte, respectively. Because sulfur is almost at its saturated concentration and polysulfide S<sub>4</sub><sup>2-</sup> concentration increases, the voltage at the high plateau decreases with the increasing depth of discharge according to Equation (2-11). In the low plateau region at ~2.1 V, the polysulfide

$\text{Li}_2\text{S}_4$  is further converted to solid  $\text{Li}_2\text{S}_2/\text{Li}_2\text{S}$ , which precipitates from the electrolyte (liquid-solid reaction). The corresponding Nernst equation is

$$E_L = E_L^\ominus + \frac{RT}{n_L F} \ln \frac{[\text{S}_4^{2-}]}{[\text{S}_2^{2-}]^2 [\text{S}_2^{2-}]} \quad (2-12)$$

where  $E_L$  is the cell potential at the low plateau,  $E_L^\ominus$  represents the standard cell potential at the low plateau, and  $[\text{S}_2^{2-}]$  and  $[\text{S}_4^{2-}]$  are  $\text{Li}_2\text{S}$  and  $\text{Li}_2\text{S}_2$  concentrations in the electrolyte, respectively. Because both  $\text{Li}_2\text{S}$  and  $\text{Li}_2\text{S}_2$  have extremely low solubility in the electrolyte, their concentrations are considered constant. On the other hand, the polysulfide  $\text{S}_4^{2-}$  concentration decreases slowly due to the slow kinetic reactions from the liquid phase to the non-conductive solid  $\text{Li}_2\text{S}_2/\text{Li}_2\text{S}$ . Therefore, the voltage in the discharge curve exhibits a long plateau around 2.1 V. Once the electrode is largely covered by the insulated discharge products ( $\text{Li}_2\text{S}_2/\text{Li}_2\text{S}$ ), the charge transfer processes are suppressed, leading to increased resistance and a quick drop of cell voltage. The last sloping tail (region IV in Figure 1.2b) is attributed to the sluggish solid-to-solid conversion reaction from  $\text{Li}_2\text{S}_2$  to  $\text{Li}_2\text{S}$ . When it is charging back, the discharge product  $\text{Li}_2\text{S}$  will be oxidized to LiPSs and finally S.

### 2.1.2 Electrochemical kinetics

As the rate capability of energy release/storage, power density ( $P_{\text{batt}}$ ) is a kinetic indicator to show the current rate ability of a battery. It can be defined as:

$$P_{\text{batt}} = \frac{QV_{\text{op}}}{t} = \frac{V_{\text{op}}^2}{R_{\text{int}}} \quad (2-13)$$

where  $V_{\text{op}}$  represents the operating voltage,  $R_{\text{int}}$  stands for the internal resistance,  $Q$  is the reversible capacity, and  $t$  is the time, respectively.<sup>[69]</sup> The internal resistance is the sum of electronic, ionic, and interfacial resistance (electrode/current collector, electrolyte/electrode, and conductive additive) in a battery. To normalize the battery capacity, the charge-discharge current density of a battery is usually expressed as a C-rate. It is defined that a 1 C rate represents the applied current that can charge or discharge a battery to its theoretical capacity in 1 hour.<sup>[69]</sup> It means that the time for discharging/charging to the theoretical capacity is decreased to 1/n hour when the C-rate increased to n C.<sup>[69]</sup>

The electrochemical redox reaction kinetics are slightly different from the bulk chemical reactions. Firstly, the electrochemical reactions at the electrode interfaces start in a 2D rather than in a 3D way. And there is a potential drop at the electrode due to the electrical double layer, which could make a difference in the electrochemical reaction. Compared to the equilibrium voltage, the kinetics of the electrochemical redox reactions results in a voltage

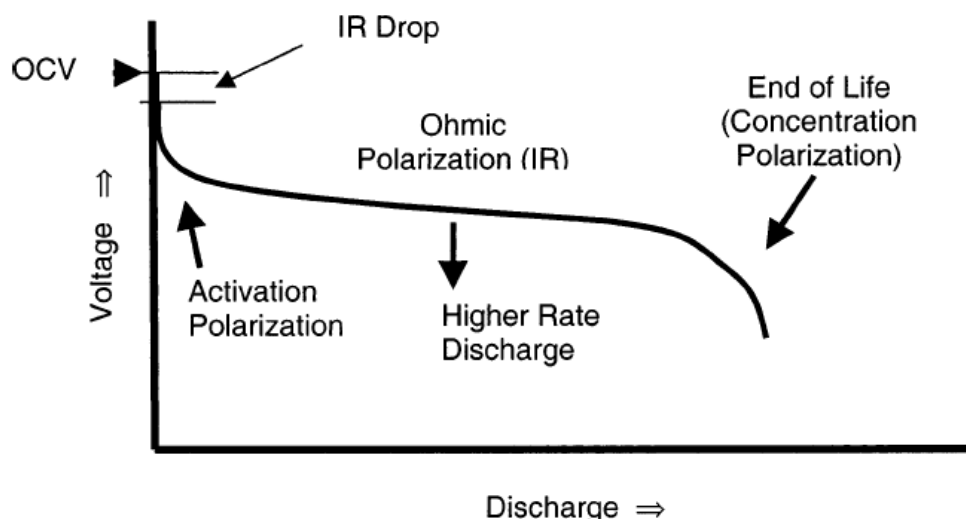


**Figure 2.1** The influence of the various types of polarization on the discharge curve of a battery.<sup>[65]</sup>

polarization during the charging-discharging process. In general, the electrochemical reaction kinetics of the electrode material is determined by the following factors (Figure 2.1): I) activation polarization, which is related to the charge-transfer of the electrode material during the electrochemical redox reactions; II) ohmic polarization, which originates from the resistance of single cell components (electrode materials, binder, conductive agent, etc.) and the contact problems; III) concentration polarization, which is caused by the mass transport limitation during battery cycling.<sup>[65]</sup> The overall voltage polarization ( $\eta$ ) is calculated by

$$\eta = V_{ocv} - V_{op} \quad (2-14)$$

where  $V_{op}$  is the operating voltage and  $V_{ocv}$  stands for the open circuit voltage.<sup>[65]</sup>

For a redox reaction determined by the charge-transfer process, the current flow ( $I$ ) can be described by the as:

$$I = I_0 [\exp(\alpha F \eta / RT) - \exp((1-\alpha) \eta F / RT)] \quad (2-15)$$

$$I_0 = k_0 F A \quad (2-16)$$

where  $k_0$  represents the reaction rate constant for the redox reaction,  $I_0$  is the exchange current density,  $T$  is the Kelvin temperature,  $A$  stands for the reactant activity, and  $\alpha$  is the transfer coefficient, respectively.<sup>[65]</sup> Therefore, the reaction kinetics is controlled by the activity of the electrode materials, the reaction rate constant, and the potential drop. It is worth noting that caused by activation polarization, the potential drop follows the Tafel equation:

$$\eta = a - b \log(I/I_0) \quad (2-17)$$

where  $a$  and  $b$  are constants.<sup>[69]</sup> The voltage polarization under the effect of ohmic resistance ( $R_{ohm}$ ) follows Ohm's law:



$$\eta = IR_{ohm} \quad (2-18)$$

During battery cycling, the concentration of the active materials at the interfaces between electrolyte and electrode is changing, limiting the mass transport abilities. With limited diffusion in the electrolyte, the voltage polarization caused by concentration difference can be calculated by

$$\eta = (RT/n)\ln(C/C_0) \quad (2-19)$$

where  $C_0$  is the concentration of active species in the bulk of the solution and  $C$  is the concentration of active species at the electrode surface.<sup>[65]</sup>

Ohmic polarization, electrochemical polarization, and concentration polarization widely exist in general redox reactions in Li-S batteries. The kinetics of a Li-S battery is primarily limited by electrochemical polarization and concentration polarization. Electrochemical polarization relies on the improved charge transfer process to boost the kinetics of the redox reaction. The diffusion time ( $\tau$ ) for the lithium ion diffusion in electrode materials can be calculated by

$$\tau = \lambda^2/D_i \quad (2-20)$$

where  $D_i$  is the diffusivity of lithium ions in the bulk or surface and  $\lambda$  is the diffusion length.<sup>[69-70]</sup> Therefore, it is reasonable to improve the electrochemical kinetics of sulfur cathode by decreasing the particle size of sulfur to shorten the diffusion length and/or doping with alien atoms to improve the conductivity of sulfur.

As mentioned above, sulfur undergoes a “solid-liquid-solid” phase conversion during discharging. To understand the kinetics in each step, the discharge process of sulfur can be divided into four parts according to the phase state of sulfur and the corresponding electrochemical reactions.<sup>[19]</sup> I) solid-liquid conversion: it needs a low-viscosity electrolyte with high solubility to polysulfides for fast kinetic performance; II) liquid-liquid conversion: in this intermediate stage, the liquid-liquid reaction has fast kinetics because polysulfides are soluble in the electrolyte; III) liquid-solid conversion and IV) solid-solid conversion: due to the insulation properties of solid  $\text{Li}_2\text{S}_2$  and  $\text{Li}_2\text{S}$ , step III and step IV are kinetically sluggish, leading to high voltage polarization.<sup>[19]</sup> Accelerating the conversion reaction from  $\text{Li}_2\text{S}_4$  in electrolyte to solid  $\text{Li}_2\text{S}$  is important to achieve the full utilization and maximize the capacity of sulfur in Li-S batteries because it has a 75% contribution to the theoretical capacity of sulfur. It was revealed that during the electrochemical deposition process,  $\text{Li}_2\text{S}$  particles precipitated in a 2D island nucleation and growth way at the “triple-phase” interfaces between the  $\text{Li}_2\text{S}_2/\text{Li}_2\text{S}$  particles, liquid electrolyte, and conductive agents.<sup>[22]</sup> Furthermore, the applied

current density plays a crucial role in the  $\text{Li}_2\text{S}$  growth process. A high current density along with a high overpotential will generate a high nuclei density, leading to a continuous coating of many small  $\text{Li}_2\text{S}$  crystallites, while a low current density produces a few larger  $\text{Li}_2\text{S}$  precipitates.<sup>[71]</sup> It is worth mentioning that the  $\text{Li}_2\text{S}$  deposition kinetics is also impacted by the electrolyte/sulfur (E/S) ratio in the battery.<sup>[19, 72]</sup> With a low E/S ratio condition (i.e., a high polysulfide concentration),  $\text{Li}_2\text{S}$  deposition becomes noticeably sluggish with island nucleation and its growth rate is 75% slower than that with excessive electrolyte.<sup>[73]</sup> Therefore, for Li-S batteries with lean electrolyte, the slow electrodeposition kinetics of  $\text{Li}_2\text{S}$  results in significantly high polarization, low capacity, and poor rate capability.

## 2.2 Template methods for the synthesis of nanostructured sulfur host

Compared to bulk counterparts, nanostructured metal-based compounds manifest superior electrochemical properties due to their abundant active sites, showing great potential in a variety of electrochemical fields, such as supercapacitors, batteries, and water splitting. Over the past decades, the template method is considered as one of the most effective ways to precisely control the size, morphology, composition, or spatial arrangement of nanoparticles. A so-called “template” is a “gauge, pattern or mold used as a guide to the form of a piece being made”. Generally, there are three main steps in the synthesis route for nanostructured materials with the template method: firstly, preparation or synthesis of the templates; afterward, compositing or merging the target materials and the templates; finally, removing the template. The template can be optionally removed by dissolution, calcination, or etching according to the nature of the target materials. Most of the time, templates can be identified as “hard” and “soft” ones. Soft templates are usually in a fluid-like state (such as vesicle or micelle), whereas a hard template is generally a solid-state particle with a distinctive morphology or nanostructure.

### 2.2.1 Hard template method

With hard templates, nanocasting and nanocoating have been widely explored to synthesize nanostructured host materials for Li-S batteries. A representative nanocasting route is impregnating desirable precursors within the pore channels or voids of hard templates. Shape-reversed templated nanostructure could be produced after the solidification or calcination and consequently etching off the hard template. With a simple synthesis procedure and controllable pore size and shape, nanocasting method has been applied to synthesize mesoporous host materials for Li-S batteries. Silica spheres and ordered mesoporous silica are popular as hard templates to obtain porous or hollow metal-based compounds or carbon materials. For instance,

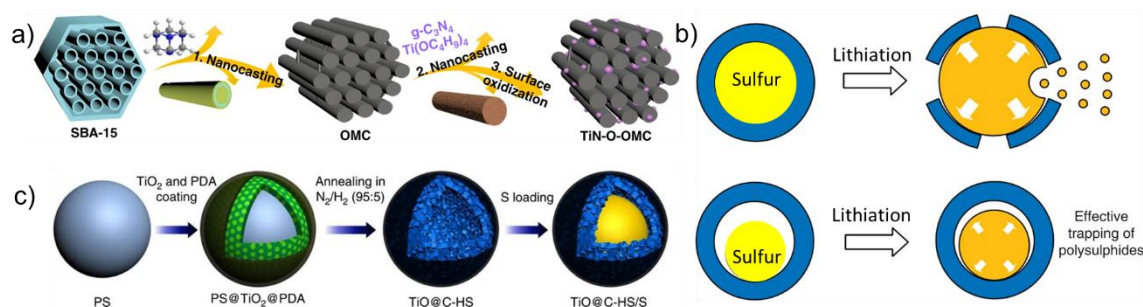


**Figure 2.2** (a) Schematic illustration for the fabrication of TiN-O-OMC particles;<sup>[74]</sup> (b) schematic lithiation process of core-shell sulfur-TiO<sub>2</sub> and yolk-shell sulfur-TiO<sub>2</sub> spherical particles;<sup>[75]</sup> (c) schematic illustration of the synthesis process of the TiO@C-HS/S composite.<sup>[76]</sup>

using nanocasting method, Hoffman *et al.* synthesized silicon carbide-derived carbon with silica nanospheres as the template.<sup>[77]</sup> The outstanding pore volume in the porous carbon allowed for high sulfur loadings (80 wt.%) and carbide-derived carbon/sulfur composites showed an initial capacity of 1165 mAh g<sup>-1</sup> at 0.1 C with good cycling stability. Similarly, with a two-time nanocasting process, Wang *et al.* designed an ordered mesoporous carbon (OMC) matrix embedded with partially oxidized TiN (TiN-O) nanoparticles as a sulfur host material for Li-S batteries.<sup>[74]</sup> As demonstrated in Figure 2.2a, ordered carbon substrate was first synthesized using silica SBA-15 as hard template and hexamethylenetetramine as precursor.<sup>[74]</sup> Afterward, TiO<sub>2</sub> nanoparticles were introduced into the OMC matrix by the hydrolysis of tetrabutyl titanate and followed by a nitridation process.

Nanocoating on the hard template has been widely applied to synthesize core-shell, yolk-shell, or hollow nanoparticles with suitable void space for high sulfur loading. For a nanocoating process, the target materials or precursors can be closely deposited on the surface of template particles during the polymerization or hydrolysis process via chemical or electrostatic interactions. The typical applied materials for the coating layer are polydopamine,<sup>[78]</sup> resorcinol-formaldehyde resin,<sup>[79]</sup> and TiO<sub>2</sub><sup>[80]</sup> because of their low cost and easy synthesis procedures. In Li-S batteries, especially, Li<sub>2</sub>S and sulfur nanospheres can also be used as templates to synthesize core-shell or yolk-shell nanostructures since they can work as a sulfur source for cathode without a post-loading process.<sup>[75, 81]</sup> The shell layer over the sulfur nanospheres is usually made of polar metal oxides or conductive polymers to accommodate the volume expansion and confine polysulfides. It was demonstrated by Cui *et al.* that a yolk-shell sulfur-TiO<sub>2</sub> nanospheres with internal void space could mitigate the volume expansion along cycling and the polar TiO<sub>2</sub> shell also minimized polysulfide dissolution (Figure 2.2b).<sup>[75]</sup> The sulfur-TiO<sub>2</sub> yolk-shell cathode showed an initial specific capacity of 1030 mAh g<sup>-1</sup> at 0.5 C

with good cycling stability over 1000 cycles. Apart from the yolk-shell nanostructure, hollow nanoparticles can work efficiently as sulfur host to confine polysulfides with an elaborate design. There are two major benefits in the polar hollow nanostructures: 1) the polar shell can anchor the LiPSs near the shell, preventing the leakage of the internal deep-seated LiPSs during cycling; 2) hollow materials with the large void spaces not only mitigate the volumetric changes of sulfur but also allow for high sulfur loading.<sup>[76]</sup> Using polystyrene (PS) spheres as the template (Figure 2.2c), titanium monoxide@carbon hollow nanospheres were constructed by Li *et al.* and used as sulfur host material.<sup>[76]</sup> With the strong adsorption ability and high conductivity of TiO to LiPSs, the TiO@C/S electrode showed good cycling stability over 500 cycles.<sup>[76]</sup>

### 2.2.2 Soft template method

Although the hard template method is straightforward for the synthesis of the nanostructured sulfur host materials, etching off the hard templates is time-consuming and sometimes requires a harsh environment, such as HF solution. On the contrary, soft template method usually permits the facile removal of the template *via* calcination or washing.<sup>[82]</sup> Usually, soft templates are made of micelles or vesicles, emulsions, and gas bubbles. The desired materials or their precursors can be coated on the surface of the soft template through polymerization and precipitation with well-defined sizes and shapes.<sup>[83]</sup> Thus, soft templates have been extensively applied to synthesize mesoporous or hollow materials as electrodes in batteries and supercapacitors.<sup>[84]</sup>

As a typical soft template, micelles are made by self-assembly of amphiphilic molecules, which are usually block copolymers or surfactants with hydrophilic and hydrophobic groups.<sup>[85]</sup> Micelles are colloidal stable with a core-shell architecture and their size is around in the range of 5-100 nm. The most crucial step in the soft-templating process is micelle formation. The Krafft temperature, also known as the minimum temperature for surfactant dissolution, and the critical micelle concentration (CMC) of surfactant are equally important for the micelle formation.<sup>[84b]</sup> Once these conditions are met, the surfactant molecules are naturally self-assembled into various-shaped micelles, which are determined by the packing parameter ( $g$ ). The packing parameter  $g$  can be calculated by the following equation,

$$g = v_0 / (a_e l_0) \quad (2-21)$$

where  $a_e$  is the equilibrium area of the head group,  $v_0$  stands for the hydrophobic tail volume, and  $l_0$  is the tail length, respectively.<sup>[86]</sup> A large value of  $g$  will increase the curvature of the

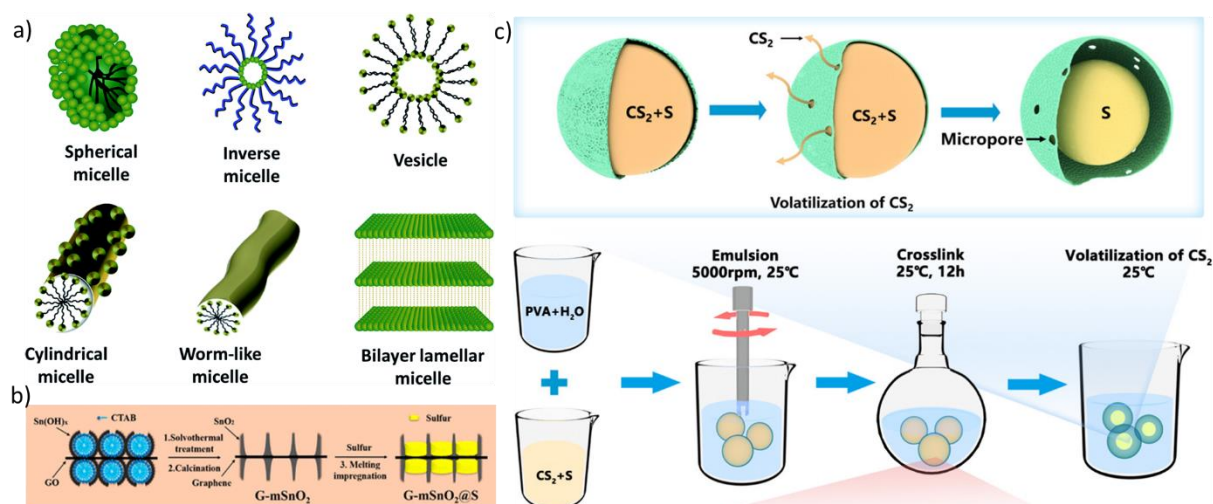


**Figure 2.3** (a) Schematic representation of different-shaped micelles ranging from spherical micelles ( $g \leq 1/3$ ) to bilayer lamellar micelles ( $g = 1$ );<sup>[84b]</sup> (b) illustration of synthesis routes for G-mSnO<sub>2</sub> and G-mSnO<sub>2</sub>@S composites with the micelles of CTAB as template;<sup>[87]</sup> (c) schematic illustration of the fabrication of S@polyvinyl alcohol (PVA) particles.<sup>[88]</sup>

interface between the solution and micelle with the formation of different shaped micelles (such as disc-like, spherical, and rod-like).<sup>[86, 89]</sup> When  $g$  is  $>1$ , reverse micelles are formed. As a result, the packing parameter could be an indicator of both the packing shape and the micelle shape. Figure 2.3a depicts the representative micelles with different packing numbers.<sup>[84b]</sup> After being subjected to appropriate chemical reactions, these micelles with different shapes can be applied as soft templates to obtain various nanostructures. Using the micelle of hexadecyltrimethylammonium bromide (CTAB) as a soft template, Liu *et al.* designed a hybrid nanostructure with mesoporous SnO<sub>2</sub>-coated graphene (G-mSnO<sub>2</sub>), as seen in Figure 2.3b.<sup>[87]</sup> They found that the fabricated mesoporous SnO<sub>2</sub> could promote the redox kinetics of LiPSs with the suppressed shuttle effect. The designed G-mSnO<sub>2</sub>@S electrode exhibited a reversible capacity of 1380 mA h g<sup>-1</sup> at 0.1 C over 200 cycles.<sup>[87]</sup> Similarly, using the micelle of di-block poly(ethylene oxide)-*b*-polystyrene (PEO-*b*-PS) copolymer as soft template, nitrogen-doped mesoporous carbon nanosheets loaded with manganese oxide (MnO) clusters were prepared and used as sulfur host for Li-S batteries to improve the electrochemical performance.<sup>[90]</sup>

Besides the micelles, emulsion has been widely used as soft templates to synthesize hollow, porous, and hierarchical nanostructures.<sup>[85]</sup> An emulsion typically consists of two immiscible phases: a droplet phase and a continuous phase, where one is dispersed within the other as droplets.<sup>[91]</sup> In an oil-in-water (O/W) emulsion, water serves as the continuous phase and organic solvent serves as the droplet phase.<sup>[92]</sup> To express how many droplets exist in an emulsion, the volume ratio or the percentage of the droplet phase to the continuous phase is

often applied. An emulsion is referred to as a high internal phase emulsion (HIPE) when the droplets are closely packed with a volume percentage over 74%.<sup>[93]</sup> To create an emulsion, a suitable surfactant is typically needed to stabilize the droplets in the continuous phase.<sup>[94]</sup> Occasionally, a co-surfactant or co-solvent may be added to increase the stability of the emulsion.<sup>[92]</sup> In Li-S batteries, a variety of porous or yolk-shell materials have been produced using both W/O and O/W emulsions as templates. For instance, Zhou *et al.* synthesized S@polyvinyl alcohol (PVA) yolk-shell particles using a self-emulsification technique (Figure 2.3c).<sup>[88]</sup> With a lot of active hydroxyl groups, PVA chains could work as surfactant to disperse S/CS<sub>2</sub> in water.<sup>[88]</sup> In addition, the hydroxyl groups could form a strong shell when they are cross-linked by glutaraldehyde. After the elimination of the CS<sub>2</sub> solvent, yolk-shell S@PVA particles can be collected. Furthermore, the number of pores inside the shell can be altered by improving the CS<sub>2</sub> evaporation rate.<sup>[88]</sup>

## 2.3 Interactions of iron-based compounds with LiPSs

Fe-based compounds (oxides, sulfides, and nitrides) have been widely used in different components (sulfur hosts,<sup>[95]</sup> interlayer,<sup>[96]</sup> or catalysts<sup>[97]</sup>) of Li-S batteries due to their good adsorption ability to LiPSs, low-cost, excellent stability, and low lithiation voltage.<sup>[98]</sup> The introduction of Fe-based compounds as sulfur hosts can inhibit the shuttling of polysulfide by chemical adsorption and facilitate the sulfur reduction reactions, achieving improved electrochemical performance.

### 2.3.1 Iron oxides

Owing to natural abundance, high chemical stability, nontoxicity, and environmental friendliness, iron oxides (hematite Fe<sub>2</sub>O<sub>3</sub> and magnetite Fe<sub>3</sub>O<sub>4</sub>) as sulfur host material have great potential for real massive application. Essentially, the difference in electronegativity between oxygen and iron atoms in the iron oxides induces a strong surface polarity, which effectively interacts with polar LiPS species. As a desulfurization sorbent, hematite Fe<sub>2</sub>O<sub>3</sub> has received some interest in Li-S batteries. It has a rhombohedrally centered hexagonal crystal structure with a space group of *R-3C*, consisting of densely arranged Fe<sup>3+</sup> ions in octahedral sites coordinated with hexagonal closest-packed oxygen atoms. According to the theoretical work by Balbuena *et al.*, the calculated adsorption energies of LiPSs on the (0001) plane of Fe<sub>2</sub>O<sub>3</sub> are greater than those of MnO<sub>2</sub> and MoS<sub>2</sub>.<sup>[99]</sup> However, just like most of the other metal oxides, Fe<sub>2</sub>O<sub>3</sub> has poor electrical conductivity, hindering its applications in the electrochemical fields.<sup>[100]</sup> Many methods have been developed to improve the electrical conductivity and LiPS

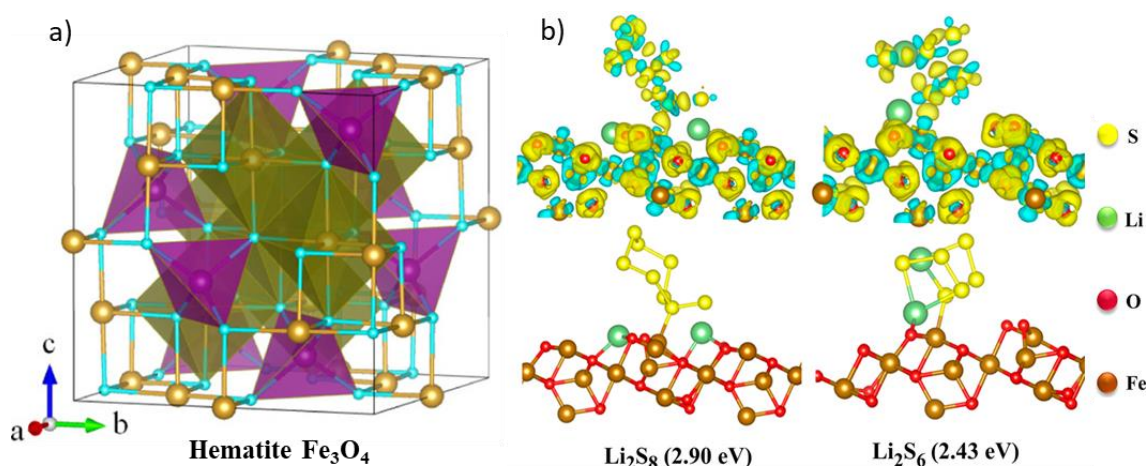


**Figure 2.4** (a) Crystal structure of hematite  $\text{Fe}_3\text{O}_4$ ;<sup>[101]</sup> (b) the calculated binding energy and optimized configurations of  $\text{Li}_2\text{S}_8$  and  $\text{Li}_2\text{S}_6$  on  $\text{Fe}_3\text{O}_4$  (311).<sup>[102]</sup>

adsorption ability of  $\text{Fe}_2\text{O}_3$ , such as creating rich oxygen vacancies,<sup>[100]</sup> regulating surface structure,<sup>[103]</sup> and compositing with carbon materials.<sup>[104]</sup> It was found that the high-index faceted  $\text{Fe}_2\text{O}_3$  particles with abundant unsaturated coordinated Fe sites could be applied as the active centers to boost the chemisorption for LiPSs, accelerate polysulfide conversion, and enhance the decomposition kinetics of  $\text{Li}_2\text{S}$ .<sup>[103]</sup> Unlike  $\text{Fe}_2\text{O}_3$ , the magnetite  $\text{Fe}_3\text{O}_4$  shows a spinel structure with a space group  $Fd-3m$ , where  $\text{Fe}^{3+}$  locates at the tetrahedral (Td) positions and the octahedral (Oh) sites are occupied by equal amounts of  $\text{Fe}^{3+}$  and  $\text{Fe}^{2+}$  (Figure 2.4a).<sup>[101]</sup> The electrical conductivity of  $\text{Fe}_3\text{O}_4$  is significantly higher than that of  $\text{Fe}_2\text{O}_3$ , which is ascribed to the inherent electron exchange between the  $\text{Fe}^{2+}$  and  $\text{Fe}^{3+}$  centers in  $\text{Fe}_3\text{O}_4$ .<sup>[105]</sup> With the DFT calculation shown in Figure 2.4b,  $\text{Li}_2\text{S}_8$  and  $\text{Li}_2\text{S}_6$  molecules can be anchored on the facet (311) of  $\text{Fe}_3\text{O}_4$  with a binding energy of 2.90 and 2.43 eV, respectively.<sup>[58]</sup> Meanwhile, highly conductive  $\text{Fe}_3\text{O}_4$  particles are beneficial for the charge transfer process during cycling. The yolk-shelled carbon- $\text{Fe}_3\text{O}_4$  (YSC@ $\text{Fe}_3\text{O}_4$ ) particle with a nanobox shape was designed as sulfur host, aiming to immobilize the polysulfide intermediates through a combination of physical confinement of carbon shell and chemisorption of  $\text{Fe}_3\text{O}_4$  core.<sup>[106]</sup> With synergistic effects in the core-shell particles, the S/YSC@ $\text{Fe}_3\text{O}_4$  cathode with sulfur content (80 wt.%) and high areal sulfur loading ( $5.5 \text{ mg cm}^{-2}$ ) showed high capacity, good cycling stability, and excellent rate performance.

Without any templates, iron oxide nanoparticles have been synthesized by one-step hydrothermal and precipitation methods as polysulfide mediators for Li-S batteries. For instance, porous  $\text{Fe}_3\text{O}_4$  nanospheres were obtained by Zhang *et al.* through a hydrothermal method and used as sulfur host to mitigate the shuttle effects of LiPSs through chemical

interactions.<sup>[107]</sup> However, using the hydrothermal or precipitation method, it is challenging to control the morphology and particle size of iron oxide particles, leading to low utilization efficiency. Besides, iron-based compounds with different nanostructures have been used as self-sacrifice template for synthesizing iron oxides, such as  $\beta$ -FeOOH nanospindles, iron-based metal-organic frameworks (such as MIL-53 and MIL-88), and Prussian blue analogues. After further modification and calcination, composite Fe<sub>3</sub>O<sub>4</sub>/carbon particles could be achieved with the remaining morphologies of their templates. For example, a 3D ternary Fe<sub>3</sub>O<sub>4</sub>/porous carbon/graphene aerogel was prepared by Ding *et al.* with graphite oxide and Fe-MOF (MIL-88) as precursors, which was applied as a multifunctional sulfur host and promoted the reaction kinetics from LiPSs to Li<sub>2</sub>S. With self-sacrifice template, further post modification procedures (such as coating and calcination process) are usually required to increase the conductivity or suppress the particle growth before application as sulfur host materials.

### 2.3.2 Iron sulfides

Based on the Hard and Soft Acid and Base theory, transition metal sulfides (TMSs) usually show higher electrical conductivities than their metal oxide counterparts due to the more covalent nature endowed by soft basic S<sup>2-</sup>/S<sub>2</sub><sup>2-</sup> ions.<sup>[108]</sup> In addition, the interactions between soft-base S<sup>2-</sup>/S<sub>2</sub><sup>2-</sup> anions and soft-acid transition metal (TM) cations endow TM atoms with a high valence electron density in sulfides, permitting TM as active sites for anchoring polysulfides.<sup>[108]</sup> Owing to these merits, TMSs held huge potential as efficient sulfur hosts to mitigate the shuttle effect of LiPSs. Furthermore, the combination of metal d-orbital and the unsaturated sulfur atom could yield an effective *d*-band structure at the edge or interfacial sites of metal sulfides,<sup>[21]</sup> which is close to the *d*-band of Pt, imparting catalytic characteristics for the sulfur reduction reactions.<sup>[109]</sup>

Generally, sulfurphilic iron sulfides (pyrite FeS<sub>2</sub> and troilite FeS) could be applied to promote the polysulfide conversion by chemical adsorption to restrain polysulfide migration.<sup>[95b, 110]</sup> Meanwhile, iron sulfides are metallic or semimetallic with higher electrical conductivity than iron oxides, reducing the nuclear energy barrier of Li<sub>2</sub>S by rapid surface charge transfer. As a common byproduct of coal production, FeS<sub>2</sub> is particularly attractive to confine LiPSs in Li-S batteries due to its low toxicity, earth abundance, and low cost.<sup>[111]</sup> As shown in Figure 2.5a, pyrite FeS<sub>2</sub> has a NaCl-type structure, in which the Fe atoms occupy the corners and face centers and two S atoms with a S<sub>2</sub><sup>2-</sup> dumbbell-shape are positioned at the midpoints of cube edges and the center of the cube.<sup>[112]</sup> The symmetric cubic crystal structure and strong S-S



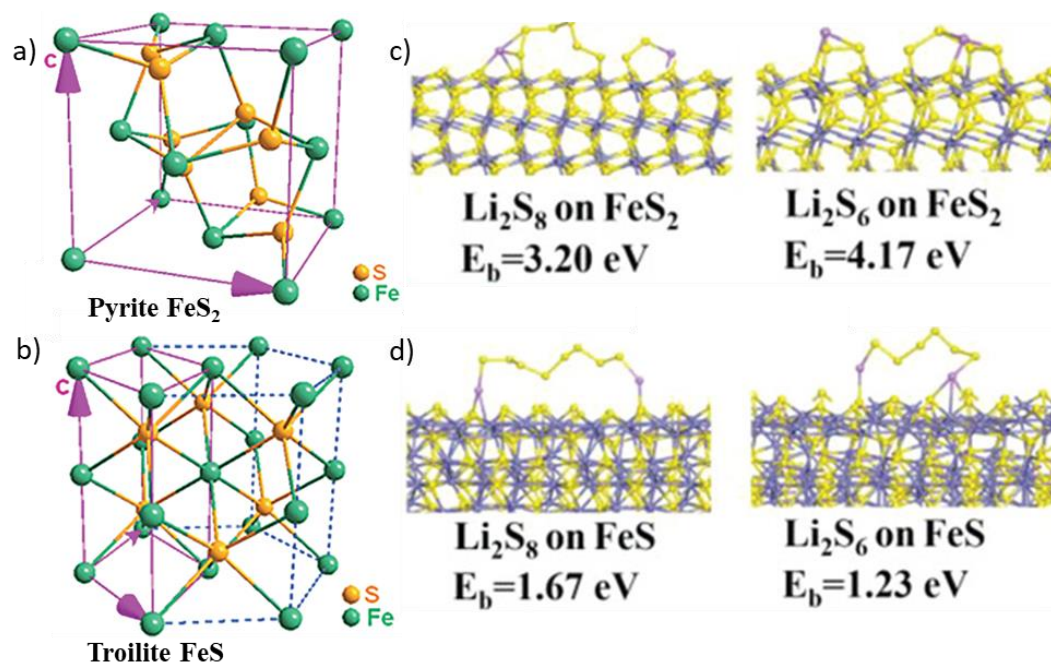


**Figure 2.5** Crystalline structures of (a) pyrite FeS<sub>2</sub> and (b) troilite FeS;<sup>[112]</sup> the optimized geometries and binding energies of Li<sub>2</sub>S<sub>6</sub> and Li<sub>2</sub>S<sub>8</sub> on the surfaces of (c) FeS<sub>2</sub> and (d) FeS.<sup>[95b]</sup>

bond render pyrite FeS<sub>2</sub> quite stable under ambient conditions. As the most stable form of FeS, troilite FeS has a hexagonal structure based on the NiAs structure with the space group of *P*-62c, as demonstrated in Figure 2.5b.<sup>[112]</sup> In the NiAs structure, Fe<sup>2+</sup> and S<sup>2-</sup> ions are located in c-planes alternatively and each Fe atom has an octahedral coordination with six sulfur atoms.<sup>[113]</sup> Interestingly, the short cation-cation site distances (<3.0 Å) permit the Fe-Fe interaction through the overlap of 3d orbital, contributing to its high electronic conductivity.<sup>[113]</sup>

The experimental adsorption test results along with the theoretical calculations revealed that the sulfur atoms of iron sulfides could strongly anchor the polysulfide species through the interactions with Li atoms of LiPSs.<sup>[95b, 111, 114]</sup> Theoretical calculation results (Figure 2.5c and 5d) indicated that the binding energies for adsorption onto FeS were lower than those for adsorption onto FeS<sub>2</sub> surface, suggesting that FeS<sub>2</sub> exhibited a better adsorption ability for LiPSs than FeS.<sup>[95b]</sup> Additionally, it was revealed that Li<sub>2</sub>S<sub>6</sub> and Li<sub>2</sub>S<sub>8</sub> prefer to decompose into two shorter chain segments on the surface of FeS<sub>2</sub>.<sup>[22]</sup> This indicated that FeS<sub>2</sub> particles could strongly catalyze the reduction reaction of long-chain LiPSs. Thus, monodispersed FeS<sub>2</sub> nanoclusters (sub-10 nm) were embedded into a nitrogen-doped porous carbon by Sun *et al.*,<sup>[95a]</sup> which exhibited strong confinement to LiPSs. The presence of FeS<sub>2</sub> particles in host material contributed to the high utilization of sulfur with a low E/S ratio for Li-S batteries.

Iron-based sulfides could be obtained in different temperature range through various synthesis routes, *e.g.*, the chemical reaction of iron salts with sodium sulfide at room temperature and sulfidation at high temperature with sulfur species (elemental sulfur, H<sub>2</sub>S, and thio-based molecules). With ball-milling the mixture of sodium sulfide nonahydrate, sublimed sulfur, and ferric chloride at room temperature, a multifunctional FeS<sub>2</sub>/FeS/S composite was achieved and used as a high-tap-density cathode for Li-S batteries. Through a one-step hydrothermal method, a flower-like composite of FeMoO<sub>4</sub>/FeS<sub>2</sub>/Mo<sub>2</sub>S<sub>3</sub> was synthesized by Chen *et al.* and applied as sulfur host for Li-S batteries.<sup>[115]</sup> Owing to the high electrical conductivity of iron sulfide, the catalytic effect of Mo<sub>2</sub>S<sub>3</sub>, and the high adsorption ability of FeMoO<sub>4</sub> to LiPSs, the flower-like composite with high sulfur loading maintained a capacity of 421 mAh g<sup>-1</sup> after 300 cycles at 10 C. To improve the reduction kinetics of polysulfide, ZnS-FeS heterostructures were encapsulated in N-doped carbon by in-situ sulfuration method.<sup>[116]</sup> Using the heterostructure of ZnS-FeS, the assembled cathode showed an excellent rate capability with a discharge capacity of 718 mA h g<sup>-1</sup> at 4 C.

### 2.3.3 Iron nitrides

Transition metal nitrides have been widely applied and investigated in electrochemical fields, such as supercapacitors, water splitting, and Li-ion batteries due to their high electrical conductivities.<sup>[117]</sup> Recently, metal nitrides have been explored and investigated as sulfur hosts for Li-S batteries due to their strong adsorption ability to LiPSs and electrical conductivity.<sup>[14b, 118]</sup> Mosavati *et al.* demonstrated that the tungsten nitride (WN) particles could immobilize LiPSs through the S-W-N bonds, which efficiently promoted the redox reaction kinetics.<sup>[118]</sup> Moreover, transition metal nitrides have similar electronic structures of noble metals since the *d*-band of metal atoms could be shrunk by N atoms with an increased *d* electron density, making metal nitrides potential catalysts for sulfur reduction reaction.<sup>[119]</sup> Among different metal nitrides, iron nitrides also attract some interest in Li-S batteries due to their good chemical stability, high electronic conductivities, and polar Fe-N bonds. Depending on the nitrogen concentration, there exists a series of iron nitrides, seen in Figure 2.6a.<sup>[120]</sup> Usually, iron nitrides comprise an orthorhombic  $\zeta$ -Fe<sub>2</sub>N, a face-centered cubic  $\gamma'$ -Fe<sub>4</sub>N, a close-packed hexagonal phase  $\varepsilon$ -Fe<sub>3</sub>N<sub>1+x</sub> ( $-0.40 < x < 0.48$ ), and a body-centered tetragonal phase  $\alpha''$ -Fe<sub>16</sub>N<sub>2</sub>. According to Jack's structural model in Figure 2.6b,<sup>[121]</sup>  $\varepsilon$ -Fe<sub>3</sub>N<sub>1+x</sub> ( $x \leq 0$ ) exhibits a well-ordered structure with space group *P*6<sub>3</sub>22 and the octahedral interstices (2c site) are occupied by the N atoms. While the disorder in  $\varepsilon$ -Fe<sub>3</sub>N<sub>1+x</sub> ( $0 < x < 0.48$ ) with space group *P*312 is caused by excess N

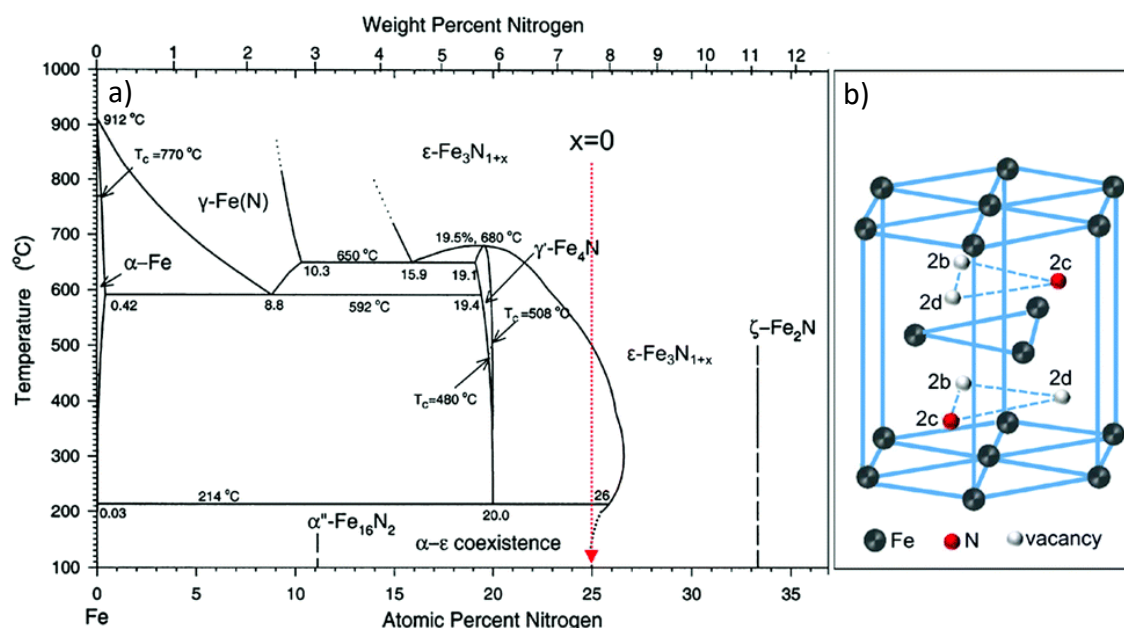


**Figure 2.6** (a) Phase diagram of the Fe-N binary system, where the red arrow show the stoichiometric  $\epsilon\text{-Fe}_3\text{N}$ ;<sup>[120]</sup> (b) crystal structure of the stoichiometric  $\epsilon\text{-Fe}_3\text{N}$ .<sup>[120]</sup>

atoms occupied at octahedral interstices (2b site).<sup>[120]</sup>

Based on the DFT calculations, the obtained binding energies on the (011) surface of  $\text{Fe}_2\text{N}$  for  $\text{Li}_2\text{S}_6$  and  $\text{Li}_2\text{S}_8$  are -5.21 and -2.96 eV, respectively.<sup>[102]</sup> Another work also showed that the (111) crystal facet of  $\text{Fe}_3\text{N}$  exhibited a binding energy of -3.34 eV with  $\text{Li}_2\text{S}_6$ .<sup>[122]</sup> Those results indicate there is a strong interaction between iron nitrides and LiPS molecules, which mitigates the shuttle effect. Sun *et al.* have designed yolk-shelled  $\text{Fe}_2\text{N}@C$  nanoboxes with an etching and nitridation process, in which  $\text{Fe}_2\text{N}$  particles provided strong chemisorption to LiPSs and facilitated the redox reaction and the carbon shell physically immobilized LiPSs and permitted the fast electron/ion transport.<sup>[102]</sup> Through DFT calculation, it was found that the state density at the Fermi level could be improved by  $\text{Co}_{0.547}\text{N}/\text{Fe}_3\text{N}$  heterostructures, enhancing the adsorption ability to LiPSs.<sup>[122]</sup> As a result, the combination of adsorptive  $\text{Co}_{0.547}\text{N}$  and high catalytic activity  $\text{Fe}_3\text{N}$  in the abundant heterojunctions could work efficiently as a sulfur host with excellent electrochemical performance.<sup>[122]</sup>

Generally, metal nitrides can be synthesized through the heat treatment of the corresponding metal oxides in the presence of ammonia gas. Using this strategy, yolk-shelled  $\text{Fe}_2\text{N}@C$  nanoboxes were obtained through the nitridation of the yolk-shelled  $\text{Fe}_3\text{O}_4$ -nanoboxes under  $\text{NH}_3$  flow at 500 °C. According to the phase diagram of the binary Fe-N system, iron nitrides with different nitrogen content exist in different temperature ranges. With increasing the temperature for the nitridation process to 650 °C, nitrogen-doped graphene loaded with

nanosized Fe<sub>4</sub>N particles was achieved by calcination of the Fe<sub>2</sub>O<sub>3</sub>@graphene oxide composite. Another way to synthesize metal nitrides is by heating nitrogen-rich organic molecules (such as urea,<sup>[123]</sup> melamine,<sup>[124]</sup> and cyanamide<sup>[125]</sup>) with the presence of metal ions under nitrogen atmosphere at high temperatures since these organic molecules could produce NH<sub>3</sub> gas during the decomposition process. For instance, using the Fe@carbon nano-necklaces as precursors, Fe<sub>3</sub>N@carbon was obtained by annealing process in the presence of urea at 500 °C for 1 h in N<sub>2</sub> atmosphere.<sup>[126]</sup>

### 3. Carbon-coated Mesoporous Fe<sub>3</sub>O<sub>4</sub> Nanospindles with Interconnected Porosities as Polysulfide Mediators for Li-S Batteries\*

So far, enormous efforts have been devoted to addressing the shuttle effect of LiPSs, mainly by constructing advanced sulfur host materials. Recently, polar metal-based compounds have attracted much attention as they can anchor LiPSs to the particle surface through chemisorption.<sup>[127]</sup> Previously, Wu *et al.* revealed that the adsorption amount of LiPSs by metal-based compounds (such as FeS and MnO<sub>2</sub>) was much higher than that of carbon black with an equal surface area.<sup>[128]</sup> However, the adsorption capability of sulfur host materials to LiPSs is also limited by the number of their active sites. To further boost the LiPS adsorption ability and increase the utilization efficiency of transition metal-based compounds, various methods have been developed to enhance the active site number and adsorption capability, such as doping,<sup>[129]</sup> creating vacancies,<sup>[130]</sup> heterostructures,<sup>[131]</sup> and nanostructure engineering.<sup>[83, 106]</sup>

In particular, nanostructured transition metal compounds with pores or voids could both physically confine and chemically bond with LiPSs, which could efficiently mitigate the shuttle effect of LiPSs in Li-S batteries. For instance, Evers *et al.* demonstrated that mesoporous TiO<sub>2</sub> as sulfur host material could enhance the cycling performance of Li-S batteries due to the increased active sites.<sup>[132]</sup> For this purpose, researchers have designed and synthesized various transition metal-based compounds with different nanostructures, such as yolk-shell structures,<sup>[102, 133]</sup> hollow spheres,<sup>[134]</sup> cubes,<sup>[135]</sup> nanotubes or fibers,<sup>[136]</sup> and polyhedrons.<sup>[137]</sup> The formation of pores or voids inside transition metal-based compounds depends on the properties and availabilities of porogens, which usually need hard or soft templates.<sup>[138]</sup> With hard templates, various pore structures could be made by precisely controlling the shape and size of the template particles.<sup>[83]</sup> Highly ordered mesoporous SiO<sub>2</sub> (for example, SBA-15 and MCM-48) are commonly used to synthesize mesoporous metal oxides by impregnating a guest precursor into the porous templates.<sup>[138b]</sup> After calcination, the hard template silica can be selectively removed using alkaline or hydrofluoric acid solutions. However, the synthesis and removal process of hard templates is usually time-consuming. In the soft template methods,

\*This chapter is adapted from my manuscript in submission: Dongjiu Xie, Yaolin Xu, Eneli Härk, Zdravko Kochovski, Xuefeng Pan, Xia Zhang, Johannes Schmidt, and Yan Lu “Carbon-coated Mesoporous Fe<sub>3</sub>O<sub>4</sub> Nanospindles with Interconnected Porosities as Polysulfide Mediators for Li-S Batteries”, *Materials Today Energy*, **2023**, 36, 101344.

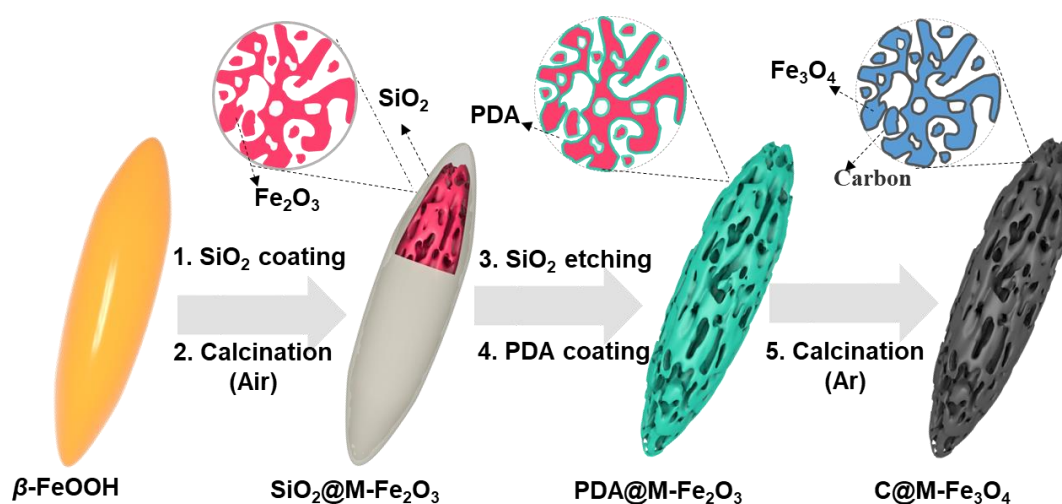


**Figure 3.1** Schematic synthesis route of the C@M-Fe<sub>3</sub>O<sub>4</sub> nanopindles.

block copolymers or surfactants are usually employed to produce porous or hollow particles due to the feasibility to be removed.<sup>[83, 139]</sup> Unlike the solid template method, cooperative assembly or interactions between precursors and soft templates are generally involved through weak electrostatic interactions or hydrogen bonds.<sup>[138b]</sup> Besides, the self-sacrifice template method is widely used to obtain porous metal-based compounds through the precursors' pyrolysis, reduction or conversion reactions.<sup>[140]</sup> However, during the heat treatment, pores and voids inside nanoparticles tend to be merged and aggregated, leading to a low specific surface area. To control the dispersity, porosity, particle size, and internal cavity induced by templates, space-confined pyrolysis within a protective shell has been developed.<sup>[141]</sup> Piao *et al.* developed water-dispersible and uniform Fe<sub>3</sub>O<sub>4</sub> and Fe<sub>2</sub>O<sub>3</sub> nanocapsules using the spindle-shaped FeOOH as a template after a “wrap-bake-peel” route that includes silica coating, calcination, and removal of the coating layer.<sup>[141c]</sup> It is expected that transition metal-based compounds with smaller particle size and higher porosity can promote their interactions with LiPSs to suppress the shuttle effects.

With the advantages of environmental benignity, low cost, and good electrical conductivity, polar Fe<sub>3</sub>O<sub>4</sub> attracts significant attention as sulfur host material in Li-S batteries. To further enhance the ability to confine LiPSs, various types of nanostructured Fe<sub>3</sub>O<sub>4</sub> and its composites have been synthesized, such as yolk-shell nanoboxes,<sup>[106]</sup> microrods,<sup>[142]</sup> carbon/Fe<sub>3</sub>O<sub>4</sub> tubes.<sup>[143]</sup> For instance, Yao *et al.* successfully prepared long porous Fe<sub>3</sub>O<sub>4</sub>@C rods (1D-Fe<sub>3</sub>O<sub>4</sub>@C) under a magnetic field.<sup>[143]</sup> Due to its ferromagnetic properties, the 1D-Fe<sub>3</sub>O<sub>4</sub>@C composite could anchor LiPSs through the Lorentz force. Utilization of carbonaceous materials in the composites can improve the electrical conductivity of the sulfur host material, facilitating

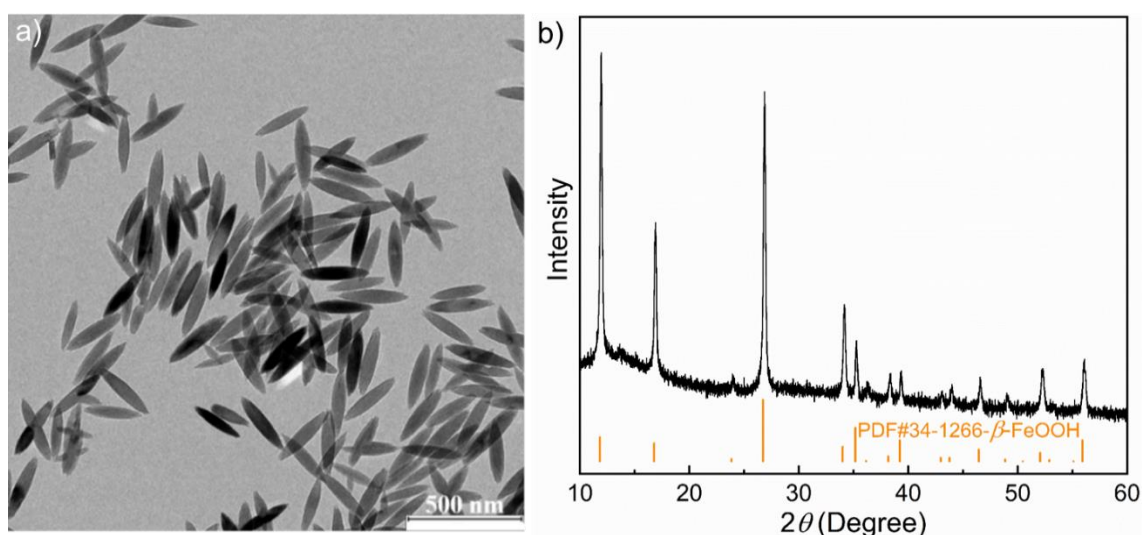
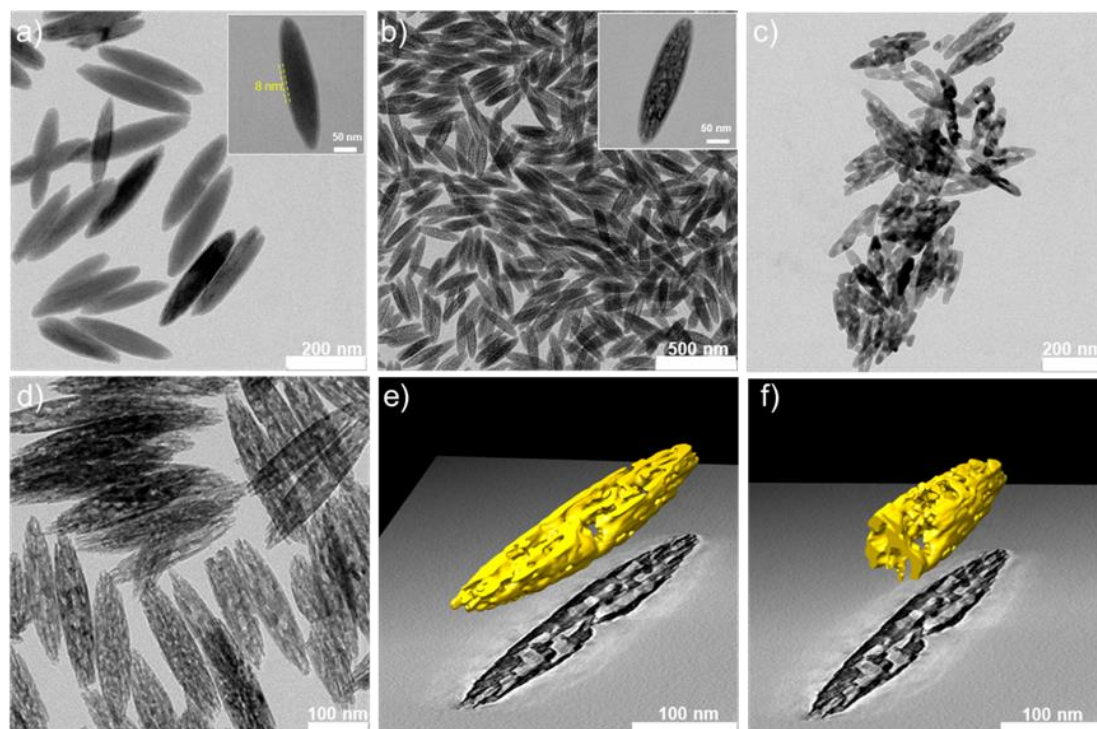


Figure 3.2 (a) TEM image and (b) XRD pattern of  $\beta$ -FeOOH particles.

the conversion of LiPSs onsite. However, their capability of confining LiPSs is inferior because of the deficient interactions between polar LiPS molecules and non-polar carbon. Moreover, although these  $\text{Fe}_3\text{O}_4$ /carbon composite materials have high specific surface area, the pores or voids primarily contribute from the poorly LiPS-confining carbon material other than  $\text{Fe}_3\text{O}_4$ , leading to limited efficacy in suppressing the shuttle effects of LiPSs.

In this chapter, carbon-coated mesoporous  $\text{Fe}_3\text{O}_4$  nanospindles ( $\text{C@M-Fe}_3\text{O}_4$ ) with interconnected pore structures have been synthesized using porous  $\text{M-Fe}_2\text{O}_3$  particles as template, as shown in Figure 3.1. Firstly, using the space-confined pyrolysis method, porous  $\text{Fe}_2\text{O}_3$  colloidal particles have been prepared by calcinating the  $\text{SiO}_2$ -coated  $\text{FeOOH}$  ( $\text{SiO}_2@\text{FeOOH}$ ) and followed by removal of  $\text{SiO}_2$ . After coating of a polydopamine (PDA) layer and followed by calcination, the mesopores inside the template nanoparticles are maintained in the obtained  $\text{C@M-Fe}_3\text{O}_4$  particles. Using them as sulfur host, the Li-S batteries with the  $\text{C@M-Fe}_3\text{O}_4/\text{S}$  cathode deliver an initial discharge capacity of  $952.1 \text{ mAh g}^{-1}$  at 1 C with good cycling performance. The developed synthesis routes in this work can be extended for the synthesis of other mesoporous metal-based compounds through the corresponding sacrificial templates, which can be used in other applications.





**Figure 3.3** TEM images of (a)  $\text{SiO}_2@\text{FeOOH}$ , (b)  $\text{SiO}_2@\text{M-Fe}_2\text{O}_3$ , (c)  $\text{FeOOH}$  after calcination at  $500\text{ }^\circ\text{C}$ , and (d) mesoporous  $\text{M-Fe}_2\text{O}_3$  nanospindles; TEM images of a single  $\text{M-Fe}_2\text{O}_3$  particle with the insets of the cross-sectional views in the parallel (e) and perpendicular directions (f), respectively.

### 3.1 Synthesis of mesoporous $\text{Fe}_2\text{O}_3$ ( $\text{M-Fe}_2\text{O}_3$ ) nanospindle

$\text{FeOOH}$  nanoparticles were chosen as templates since they can be easily synthesized with a low cost in a large scale. According to the previous work,<sup>[144]</sup> colloidal  $\beta\text{-FeOOH}$  particles with uniform size and morphology can be obtained by hydrolysis of  $\text{FeCl}_3$  in an aqueous solution in the presence of hexadecyltrimethylammonium bromide (CTAB) under a mild condition. As shown in Figure 3.2a, the collected  $\text{FeOOH}$  nanoparticles exhibit a nanospindle shape with a smooth surface. The  $\text{FeOOH}$  nanoparticles are monodispersed with a length of  $\sim 250\text{ nm}$  and a width of  $\sim 50\text{ nm}$ . The corresponding XRD pattern in Figure 3.2b well matched with the standard peaks of  $\beta\text{-FeOOH}$  (PDF#34-1266). To introduce a confined space for  $\text{FeOOH}$  particles during the thermal decomposition, a condensed layer of silica was introduced through the hydrolysis of tetraethyl orthosilicate (TEOS). As demonstrated in Figure 3.3a, a thin  $\text{SiO}_2$  layer was uniformly coated on the  $\text{FeOOH}$  particles with a thickness of  $\sim 8\text{ nm}$ . After the heat treatment of the  $\text{SiO}_2$ -coated  $\text{FeOOH}$  particles ( $\text{SiO}_2@\text{FeOOH}$ ) at  $500\text{ }^\circ\text{C}$  in air, highly porous  $\text{M-Fe}_2\text{O}_3$  particles (Figure 3.3b) were produced inside the  $\text{SiO}_2$  shell after the loss of  $\text{H}_2\text{O}$ . On the contrary, without the confinement of the silica layer, bare  $\text{FeOOH}$  particles were converted into agglomerated  $\text{Fe}_2\text{O}_3$  rods with few pores (Figure 3.3c). This result indicates that the silica shells could block the aggregation of the core  $\text{Fe}_2\text{O}_3$  particles and prevent the



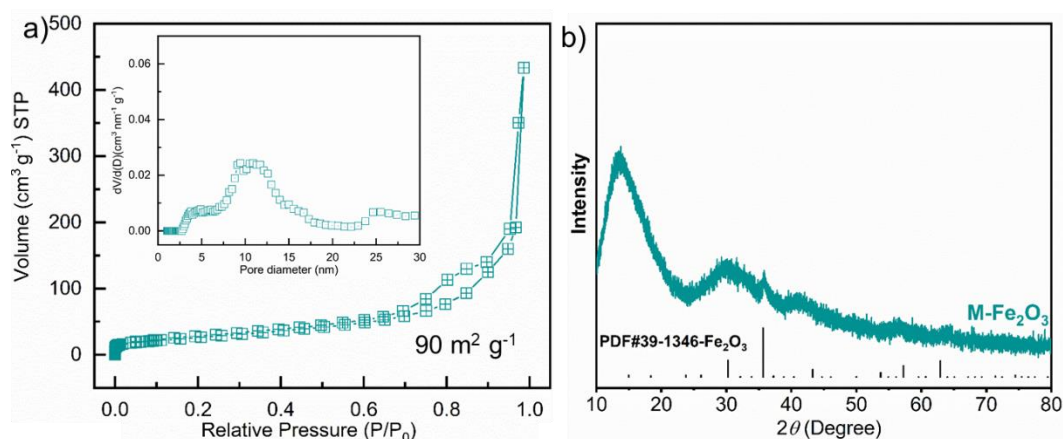


**Figure 3.4** (a)  $N_2$  adsorption-desorption isotherms of the  $M\text{-Fe}_2\text{O}_3$  particles with the corresponding pore size distribution (inset); (b) XRD pattern of the  $M\text{-Fe}_2\text{O}_3$  particles.

amalgamation of the pores generated during the decomposition process. After the removal of the  $\text{SiO}_2$  layer with  $\text{NaOH}$  solution, the porous  $\text{Fe}_2\text{O}_3$  particles still keep the nanospindle morphology without pulverization into small particles, as depicted in Figure 3.3d. Since the nanostructure information along the electron beam direction is doomed to be superimposed over other ones, the structural features provided by the standard TEM images are minimal and inconclusive. Therefore, electron tomography (ET) has been used to rebuild the 3D structure from a series of two-dimensional micrograph images and reveal the inner structural details. These images were recorded every one or two degrees about a tilt axis.<sup>[145]</sup> Figure 3.3e and 3f show the reconstructed 3D images of a single  $M\text{-Fe}_2\text{O}_3$  particle, which are sliced in parallel and perpendicular directions, respectively. It is found that the  $\text{Fe}_2\text{O}_3$  particles are highly porous and exhibit 3D channels interconnected from the surface to the center. With large void space, a highly porous nanostructure as sulfur host is beneficial for high sulfur loading and polysulfide confinement.

To further reveal the pore structure of  $M\text{-Fe}_2\text{O}_3$  particles,  $N_2$  adsorption-desorption measurement has been conducted and the collected isotherms are shown in Figure 3.4a. A distinct hysteresis loop can be observed, which is a characteristic type-IV isotherm, indicating the existence of mesopores in the  $M\text{-Fe}_2\text{O}_3$  sample. According to the Barrett-Joyner-Halenda (BJH) method,<sup>[146]</sup> the corresponding pore size distribution is calculated and shown in the inset of Figure 3.4a, suggesting the existence of multiple hierarchical mesopores with pore sizes ranging from 5 to 15 nm. Based on the Brunauer-Emmett-Teller (BET) model,<sup>[147]</sup> the calculated specific surface area is around  $90 \text{ m}^2 \text{ g}^{-1}$ . Moreover, the bumpy background and weak crystalline peak in the XRD pattern of the  $M\text{-Fe}_2\text{O}_3$  sample (Figure 3.4b) indicate the poor crystallization of  $\text{Fe}_2\text{O}_3$  due to the confinement of the  $\text{SiO}_2$  layer. In brief, through a space-

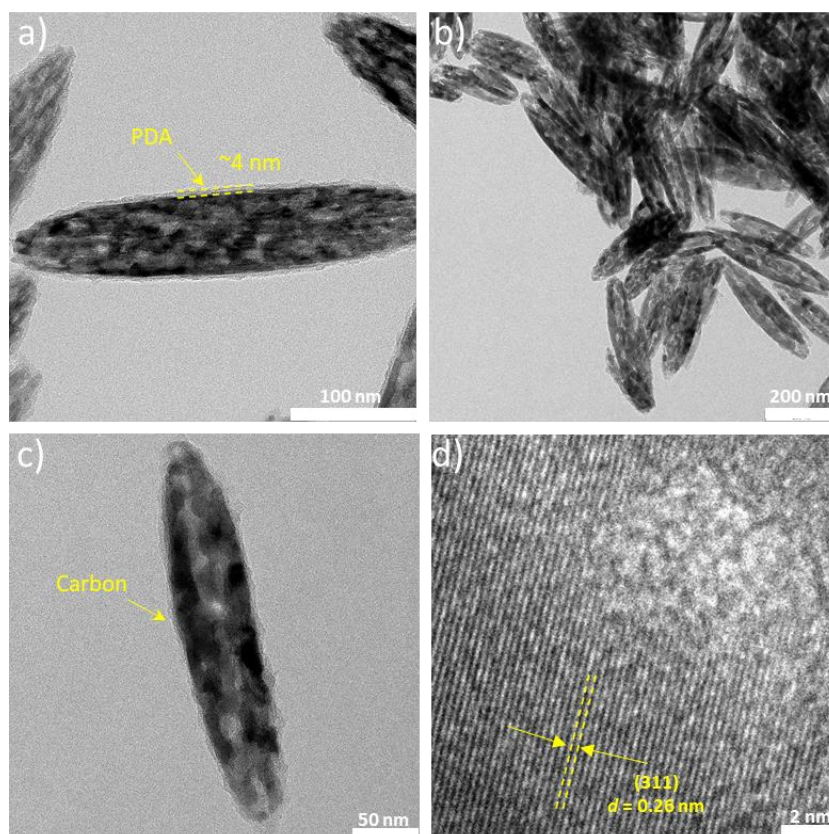


**Figure 3.5** TEM images of the PDA@M-Fe<sub>2</sub>O<sub>3</sub> (a) and C@M-Fe<sub>3</sub>O<sub>4</sub> (b, c) nanospindles; (d) HR-TEM image of a randomly selected C@M-Fe<sub>3</sub>O<sub>4</sub> particle.

confined pyrolysis method, the synthesized M-Fe<sub>2</sub>O<sub>3</sub> particles exhibit a porous nanospindle morphology with interconnected 3D channels.

### 3.2 Synthesis and characterization of C@M-Fe<sub>3</sub>O<sub>4</sub> and M-Carbon nanospindles

To obtain the carbon-coated Fe<sub>3</sub>O<sub>4</sub> nanoparticles (C@M-Fe<sub>3</sub>O<sub>4</sub>), a thin PDA layer was deposited on the mesoporous Fe<sub>2</sub>O<sub>3</sub> particles' surface as the carbon source through the polymerization of dopamine monomer. As shown in Figure 3.5a, the PDA layer exhibits a thickness of ~4 nm. After calcination in argon, the porous nanospindle morphology is still preserved, ascribing to the confinement of the carbon layer, as shown in Figures 3.5 b and 5c. In addition, the lattice fringes of the Fe<sub>3</sub>O<sub>4</sub> particle are observed under HR-TEM images (Figure 3.5d). The measured interplanar *d*-spacing is around 0.26 nm, corresponding to the (311) plane of magnetite Fe<sub>3</sub>O<sub>4</sub>.<sup>[148]</sup> After the heat treatment of the PDA@M-Fe<sub>2</sub>O<sub>3</sub> sample in argon, the collected XRD pattern of sample C@M-Fe<sub>3</sub>O<sub>4</sub> is shown in Figure 3.6a, which is in good agreement with the standard magnetite Fe<sub>3</sub>O<sub>4</sub> phase (PDF#75-0033). The five peaks at  $2\theta = 62.6, 56.9, 43.1, 35.5,$  and  $30.1^\circ$  are attributed to the (440), (511), (400), (311), and (220) planes

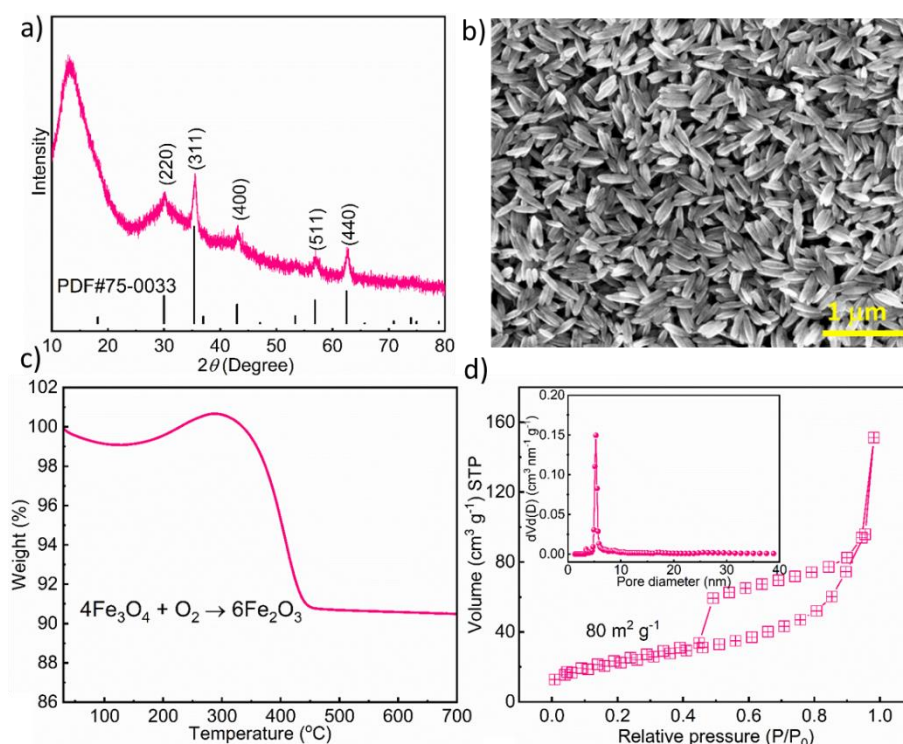


**Figure 3.6** (a) XRD pattern and (b) SEM image of the C@M-Fe<sub>3</sub>O<sub>4</sub> particles; (c) TGA curve of the C@M-Fe<sub>3</sub>O<sub>4</sub> particles under synthetic air; (d) N<sub>2</sub> adsorption-desorption isotherms of the C@M-Fe<sub>3</sub>O<sub>4</sub> particles with the inset of the corresponding pore size distribution.

of the magnetite Fe<sub>3</sub>O<sub>4</sub> phase, respectively. This indicates that the porous Fe<sub>2</sub>O<sub>3</sub> particle was fully converted into Fe<sub>3</sub>O<sub>4</sub> after calcination. The SEM image in Figure 3.6b shows the overview of the surface morphology of the C@M-Fe<sub>3</sub>O<sub>4</sub> particles, which is consistent with the TEM results. To determine the content of Fe<sub>3</sub>O<sub>4</sub> in the composite C@M-Fe<sub>3</sub>O<sub>4</sub> particles, TGA curve of the C@M-Fe<sub>3</sub>O<sub>4</sub> particles in synthetic air has been collected and plotted in Figure 3.6c. In the range of 100-200 °C, the weight loss comes from the adsorbed water in the sample and the increased weight around 300 °C is contributed by the oxidation of Fe<sub>3</sub>O<sub>4</sub> into Fe<sub>2</sub>O<sub>3</sub>. Afterward, a large weight loss is observed around 400 °C, which is due to the oxidation of carbon. The calculated specific content of Fe<sub>3</sub>O<sub>4</sub> in the composite C@M-Fe<sub>3</sub>O<sub>4</sub> is 87.5 wt.%, which is based on the residual Fe<sub>2</sub>O<sub>3</sub>.

The N<sub>2</sub> adsorption-desorption isotherms of the C@M-Fe<sub>3</sub>O<sub>4</sub> particles in Figure 3.6d also exhibit a hysteresis loop, a characteristic type-IV isotherm of mesoporous materials. As shown in the inset of Figure 3.6d, the pore diameter inside the C@M-Fe<sub>3</sub>O<sub>4</sub> particles is centred at 5 nm calculated by the BJH model. According to the BET model, the calculated specific surface area is around 80 m<sup>2</sup> g<sup>-1</sup>, which is slightly lower than that of the template M-Fe<sub>2</sub>O<sub>3</sub> particles. This is because the coalescence of some mesopores during the calcination process could cause

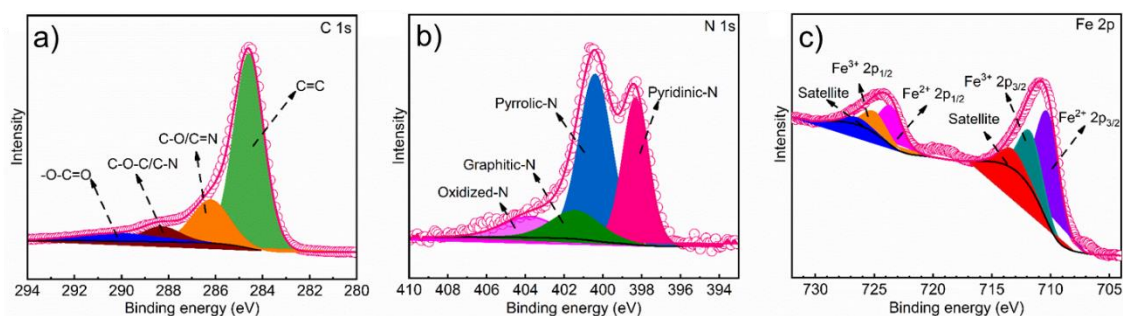


**Figure 3.7** The high-resolution XPS spectra of (a) C 1s, (b) N 1s, and (c) Fe 2p regions of the C@M-Fe<sub>3</sub>O<sub>4</sub> nanopindles.

a decreased specific surface area for the C@M-Fe<sub>3</sub>O<sub>4</sub> particles.

Furthermore, X-ray photoelectron spectroscopy (XPS) was applied to reveal the chemical bonding information of the C@M-Fe<sub>3</sub>O<sub>4</sub> sample. The high-resolution C 1s spectrum in Figure 3.7a shows four prominent peaks positioned at around 290.2, 284.6, 288.4, and 286.2 eV, which could be induced by -O-C=O, C=C, C-O-C/C-N, and C=N/C-O, respectively<sup>[149]</sup>. Additionally, the N 1s spectrum has been also collected, which is derived from the PDA precursor. As presented in Figure 3.7b, the deconvoluted four peaks at 403.2, 401.1, 400.2, and 398.1 eV are contributed by the oxidized N species, graphitic, pyrrolic, and pyridinic inside the C@M-Fe<sub>3</sub>O<sub>4</sub> sample, respectively.<sup>[150]</sup> It was reported that the doped nitrogen in the carbon matrix could enhance the electrical conductivity of carbon and provide more active sites for LiPSs adsorption.<sup>[151]</sup> Due to the energy splitting of the Fe 2p level, two broad peaks at 724.3 and 710.7 eV are detected in the Fe 2p spectrum (Figure 3.7c), which are assigned to Fe 2p<sub>1/2</sub> and Fe 2p<sub>3/2</sub> states, respectively. Specifically, the deconvoluted peaks at 724.8 eV and 711.8 eV are assigned to the Fe 2p<sub>1/2</sub> and Fe 2p<sub>3/2</sub> of Fe<sup>3+</sup>, respectively; while the peaks belonging to the Fe 2p<sub>1/2</sub> and Fe 2p<sub>3/2</sub> of Fe<sup>2+</sup> are located at 723.7 and 710.5 eV, respectively.<sup>[152]</sup> It is worth noting that the two satellite peaks are observed at 713.5 and 726.7 eV.

In addition, a reference sample, mesoporous carbon (M-Carbon) nanopindles have been prepared by etching Fe<sub>3</sub>O<sub>4</sub> particles from the composite C@M-Fe<sub>3</sub>O<sub>4</sub> particles in an acidic solution. Figure 3.8a shows the TEM image of the collected carbon particles after the removal of Fe<sub>3</sub>O<sub>4</sub>. Mesoporous structures are present inside the carbon nanopindles, proving the 3D nanostructure of the Fe<sub>3</sub>O<sub>4</sub> particles indirectly. Figure 3.8b provides N<sub>2</sub> adsorption-desorption isotherms of the M-Carbon particles with a large hysteresis loop, which is a typical type-IV isotherm of mesoporous materials. The calculated BET-specific surface area of the M-Carbon sample is 284 m<sup>2</sup> g<sup>-1</sup>, which is much higher than that of the C@M-Fe<sub>3</sub>O<sub>4</sub> sample. Based on



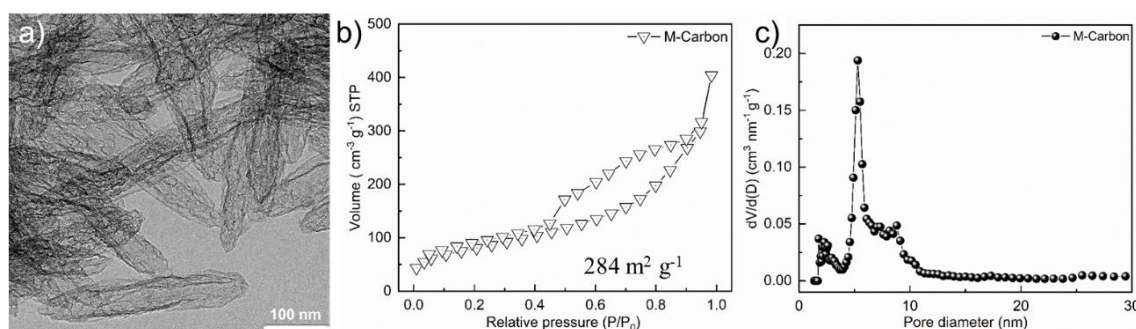


**Figure 3.8** (a) TEM image of the M-Carbon particles; (b)  $N_2$  adsorption-desorption isotherms of the M-Carbon particles with the corresponding pore size distribution (c).

the BJH model, the diameter of the mesopores inside M-Carbon is centered at 6 nm (Figure 3.8c).

### 3.3 Interactions of mesoporous C@M- $Fe_3O_4$ with polysulfides

#### 3.3.1 LiPS adsorption test

The adsorption capabilities of the host materials to LiPSs play a crucial role in suppressing the shuttle effect in Li-S batteries. Accordingly, a static adsorption test was conducted inside the glove box. The host material powders (M-Carbon, M- $Fe_2O_3$ , and C@M- $Fe_3O_4$ ) with an equal BET-specific surface area of  $1 \text{ m}^2$  were added into three vials with 3 mL of  $Li_2S_8$  (2 mM) dissolved in the mixed solution of DOL/DME (v/v = 1/1), respectively. After aging for 4 hours, the color of the three supernatants faded from the original yellow as shown in Figure 3.9a. These results indicate that most of the LiPSs molecules are adsorbed on the surface of the mesoporous host materials. Interestingly, the color of the supernatant in the vial with C@M- $Fe_3O_4$  particles is bleached, while the supernatants inside the vials with M- $Fe_2O_3$  and M-Carbon particles are still slightly yellow. This indicates that the C@M- $Fe_3O_4$  nanoparticles exhibit the strongest adsorption capability to LiPSs than the other two counterparts. Furthermore, the supernatants were centrifuged and sealed in quartz cylinders under argon for UV-*vis* spectroscopy measurement. As shown in Figure 3.9b, the UV-*vis* absorption spectrum of the supernatant of the C@M- $Fe_3O_4$  sample shows the lowest intensity among the three samples, which is consistent with the visualized adsorption results. The good adsorption ability of the C@M- $Fe_3O_4$  particles to LiPSs may be originated from the combination of the physical confinement and chemisorption in the mesoporous composite nanostructure. The M-Carbon sample shows the weakest adsorption ability to LiPSs due to the inferior interaction between polar LiPSs and nonpolar carbon materials.

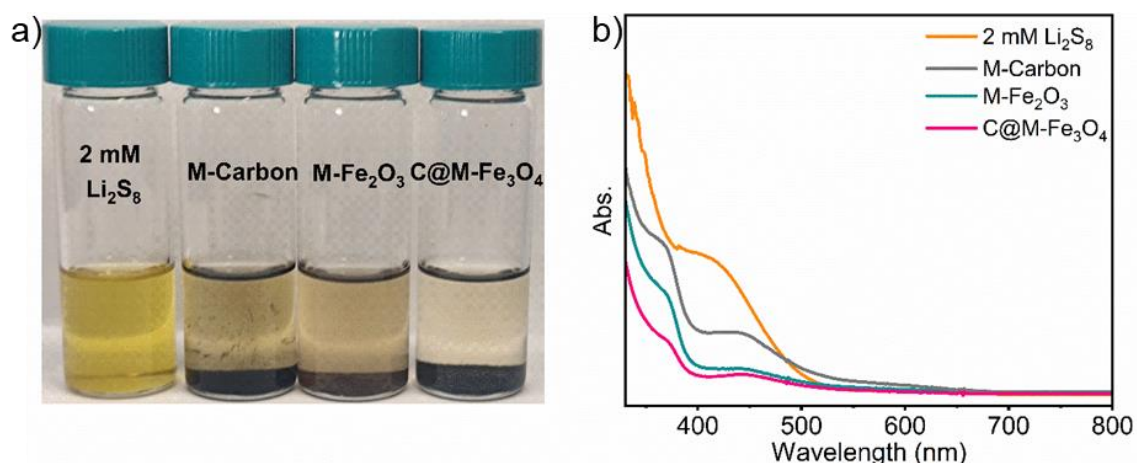


**Figure 3.9** (a) Static adsorption of  $\text{Li}_2\text{S}_8$  solution (2 mM) with different host materials (M-Carbon, M- $\text{Fe}_2\text{O}_3$ , and C@M- $\text{Fe}_3\text{O}_4$ ) and the corresponding UV-*vis* spectra (b) of the supernatants in the vials.

### 3.3.2 Symmetrical cell

Cyclic voltammetry (CV) curves of the symmetrical cells have been collected to study the effects of the C@M- $\text{Fe}_3\text{O}_4$  particles on the conversion reaction among LiPSs during cycling. The symmetrical cells were assembled according to the previous report by applying the host material particles both as counter and working electrodes and the  $\text{Li}_2\text{S}_6$  dissolved in the mixture solution of DOL/DME (v/v = 1/1) was used as the electrolyte.<sup>[153]</sup> To study the kinetics of the polysulfide conversion reactions on different electrodes (M-Carbon, M- $\text{Fe}_2\text{O}_3$ , and C@M- $\text{Fe}_3\text{O}_4$ ), the constructed symmetrical cells were scanned at  $10 \text{ mV s}^{-1}$  in the range of -0.8 to 0.8 V. As shown in Figure 3.10, the CV curve of the symmetrical cell with the C@M- $\text{Fe}_3\text{O}_4$  electrodes exhibited the highest current density among them, compared with the M- $\text{Fe}_2\text{O}_3$  and M-Carbon electrodes, suggesting the promoted kinetics in the liquid-liquid conversion reaction of LiPSs.<sup>[153]</sup> Essentially, the poor interaction between nonpolar carbon and polar LiPSs molecules slows down the electron transfer process during the LiPSs conversion reaction, leading to the lowest current value in CV curves of the M-Carbon electrode. Although the polar M- $\text{Fe}_2\text{O}_3$  particles could chemically anchor LiPSs molecules, their inferior electrical conductivity hinders the electron transfer from the confined LiPSs to the conductive agents in the symmetrical cell. It was previously proposed that the “triple-phase” interfaces among the host particles, conductive agents, and electrolyte could facilitate the kinetic behaviors of soluble LiPSs since they provided good electrical conductivity and strong chemisorption for LiPSs during the sulfur redox reaction.<sup>[154]</sup> Only a few “triple-phase” interfaces of the  $\text{Fe}_2\text{O}_3$ , conductive substrate, and the liquid  $\text{Li}_2\text{S}_6$  solution in the M- $\text{Fe}_2\text{O}_3$  electrode are active sites for the conversion reaction in the symmetrical cell. On the contrary, the designed C@M- $\text{Fe}_3\text{O}_4$

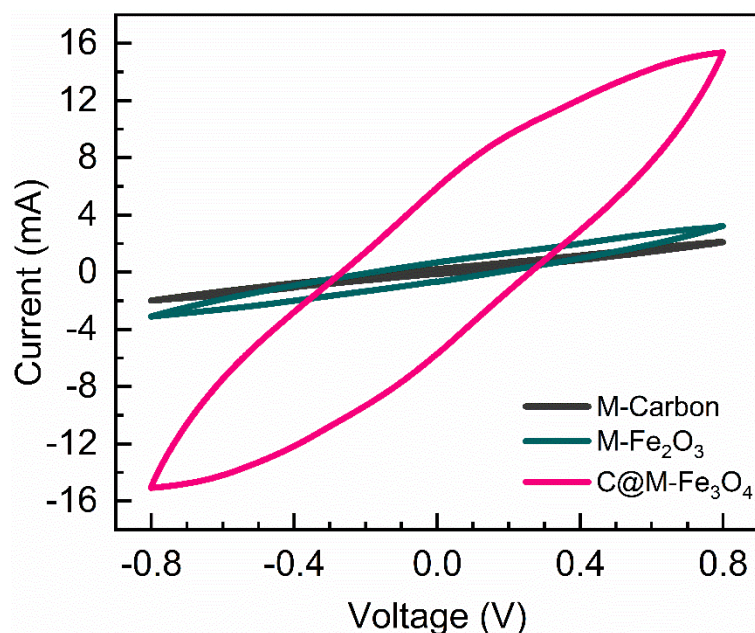


**Figure 3.10** CV curves of the symmetrical cells with different electrodes (M-Carbon, M-Fe<sub>2</sub>O<sub>3</sub>, and C@M-Fe<sub>3</sub>O<sub>4</sub>) scanned at 10 mV s<sup>-1</sup> in the range of -0.8 to 0.8 V.

electrode has rich “triple-phase” interfaces, which are made of the porous Fe<sub>3</sub>O<sub>4</sub> particles, coated-carbon layer, and the liquid Li<sub>2</sub>S<sub>6</sub> solution. The plentiful electron transfer paths in the C@M-Fe<sub>3</sub>O<sub>4</sub> electrode could facilitate the LiPSs conversion reactions, ascribing to the high current value of its symmetrical cell.

### 3.3.3 Li<sub>2</sub>S precipitation test

Ideally, the complete conversion reaction from Li<sub>2</sub>S<sub>4</sub> to Li<sub>2</sub>S could contribute to ~75% of the total theoretical capacity of sulfur. However, the reduction reaction from the soluble Li<sub>2</sub>S<sub>4</sub> molecules (liquid phase) to Li<sub>2</sub>S (solid phase) is a sluggish process, leading to a low discharge capacity of Li-S batteries.<sup>[22, 155]</sup> Therefore, a facilitated Li<sub>2</sub>S precipitation process could play a pivotal role in enhancing the capacity and rate capability of Li-S batteries. To investigate the effects of the C@M-Fe<sub>3</sub>O<sub>4</sub> particles on the liquid-solid conversion reaction, a potentiostatic nucleation test of Li<sub>2</sub>S was applied by using Li<sub>2</sub>S<sub>8</sub> solution as the catholyte. After the galvanostatically discharging step, the cells were potentiostatically discharged at 2.05 V for the Li<sub>2</sub>S precipitation. The time-dependence reduction current curves of the cells with different electrodes were collected and displayed in Figure 3.11, respectively. It is observed that after a monotonic decrease of the current in the initial stage, a characteristic peak appears, which is ascribed to the electrodeposition of Li<sub>2</sub>S.<sup>[22]</sup> Based on Faraday’s law, the deposition capacities of Li<sub>2</sub>S on the M-Carbon, M-Fe<sub>2</sub>O<sub>3</sub> and C@M-Fe<sub>3</sub>O<sub>4</sub> electrodes are 530.8 mAh g<sup>-1</sup>, 553.9 mAh g<sup>-1</sup>, and 701.3 mAh g<sup>-1</sup> respectively. Interestingly, although the deposition capacities of

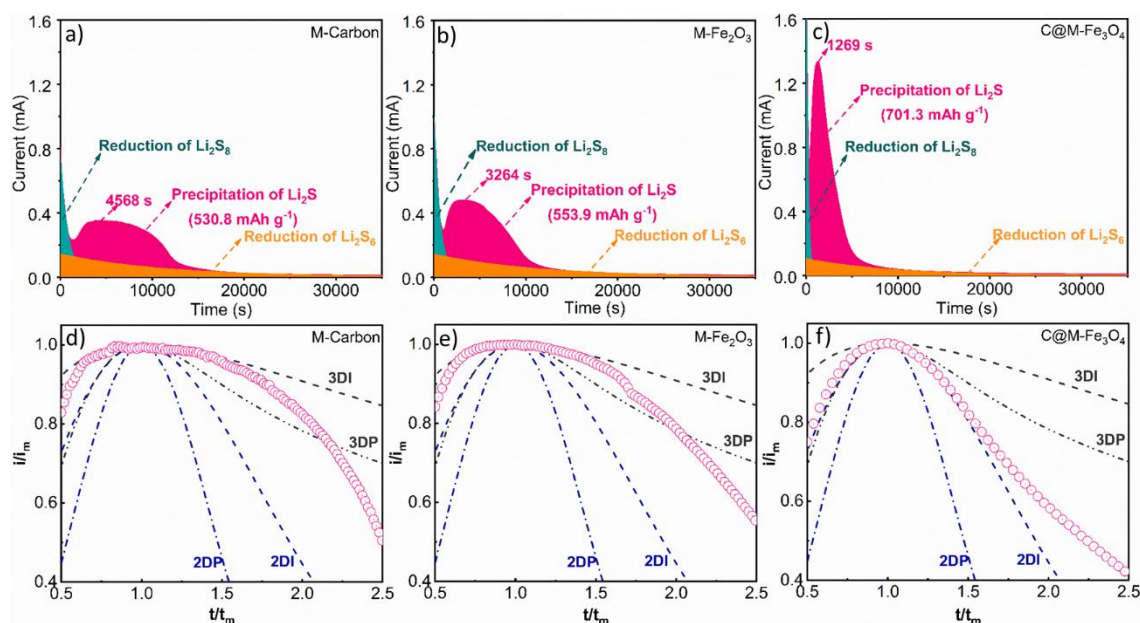


**Figure 3.11** Current-time plots of catholyte  $\text{Li}_2\text{S}_8$  potentiostatic discharged at 2.05 V (vs.  $\text{Li}/\text{Li}^+$ ) on different host materials (M-Carbon (a), M- $\text{Fe}_2\text{O}_3$  (b), and C@M- $\text{Fe}_3\text{O}_4$  (c)); (d-f) the dimensionless transient of  $\text{Li}_2\text{S}$  deposition in comparison with theoretical 2D and 3D electroplating models;  $i$ : current,  $i_m$ : peak current;  $t$ : time,  $t_m$ : time needed to achieve the peak current.

M-Carbon and M- $\text{Fe}_2\text{O}_3$  electrodes are close to each other, the M- $\text{Fe}_2\text{O}_3$  electrode needs a shorter time (3264 s) to reach the peak current than that of the M-Carbon sample (4568 s) with weak interactions with LiPSs. As demonstrated in Figure 3.11c, the cell with the C@M- $\text{Fe}_3\text{O}_4$  electrode only takes 1269 s to reach the peak current, which is much faster than those of M-Carbon and M- $\text{Fe}_2\text{O}_3$  electrodes, suggesting that the C@M- $\text{Fe}_3\text{O}_4$  particles can facilitate the conversion process from LiPSs to  $\text{Li}_2\text{S}$ .

Meanwhile, the nucleation peak of  $\text{Li}_2\text{S}$  on the C@M- $\text{Fe}_3\text{O}_4$  electrode is much sharper than those of the M-Carbon and M- $\text{Fe}_2\text{O}_3$  electrodes, implying improved conversion kinetics from LiPSs to  $\text{Li}_2\text{S}$  on the mesoporous C@M- $\text{Fe}_3\text{O}_4$  particles. To further decode the  $\text{Li}_2\text{S}$  growth behavior on the different host materials, the classical Bewick-Fleischman-Thirsk (BFT) and Scharifer-Hills (SH) models for the electrochemical deposition process were applied to fit the current-time profiles collected in the potentiostatic discharging process (Figure 3.11d to 11f).<sup>[156]</sup> The BFT models describe the 2D nucleation growth, while the SH models exploit the 3D diffusion-dominated growth. The instantaneous and progressive nucleation processes are considered in both models. The term “progressive” indicates that the nucleation rate at early stages is very small. At the same time, the initial nuclei density increases linearly with time, leading to nuclei with different sizes. If the nucleation rate is tremendous and the consumption of the nucleation site starts at very beginning stages, it is termed “instantaneous”. The 2D



**Table 3.1.** The equations corresponding to the four classic electrochemical models, respectively.<sup>[156b, c]</sup>

2D progressive (2DP)	2D instantaneous (2DI)	3D progressive (3DP)	3D instantaneous (3DI)
$\frac{i}{i_m} = \left(\frac{t}{t_m}\right) \left(\exp\left[\frac{t^2 - t_m^2}{2t_m^2}\right]\right)$	$\frac{i}{i_m} = \left(\frac{t}{t_m}\right)^2 \left(\exp\left[\frac{-2(t^3 - t_m^3)}{3t_m^3}\right]\right)$	$\frac{i^2}{i_m^2} = \frac{1.9542}{t/t_m} \{1 - \exp[-1.2564(t/t_m)]\}$	$\frac{i^2}{i_m^2} = \frac{1.2254}{t/t_m} \{1 - \exp[-2.3367(t/t_m)^2]\}^2$

instantaneous (2DI) and progressive (2DP) nucleation of the BFT model suggests a two-dimensional nucleation mechanism, in which the lattice incorporation controls the growth rate.<sup>[156b]</sup> However, the 3D instantaneous (3DI) and progressive (3DP) nucleation of the SH model indicates ion diffusion dominates the growth rate of a 3D hemispheric nucleus.<sup>[156c]</sup> The corresponding equations of the four models are provided in Table 3.1. From the fitted results in Figure 3.11d and 11e, the Li<sub>2</sub>S growth behaviors on the M-Carbon and M-Fe<sub>2</sub>O<sub>3</sub> electrodes are a hybrid model of 3DI and 3DP, implying the growth rate of Li<sub>2</sub>S particle is mainly controlled by ion diffusion.<sup>[157]</sup> However, the growth process of Li<sub>2</sub>S on the C@M-Fe<sub>3</sub>O<sub>4</sub> electrode is well-matched with the 2DI nucleation model in Figure 3.11f, in which Li<sub>2</sub>S growth is controlled by lattice bonding.<sup>[158]</sup> These results suggest that benefiting from the good electron conductivity of the coated carbon layer and the strong affinity of the porous Fe<sub>3</sub>O<sub>4</sub> particles to LiPSs, the C@M-Fe<sub>3</sub>O<sub>4</sub> particles can facilitate the growth of Li<sub>2</sub>S from the LiPSs by a 2D instantaneous nucleation mechanism.

### 3.4 Electrochemical performance of C@M-Fe<sub>3</sub>O<sub>4</sub> as sulfur host for Li-S batteries

To further study the effect of different mesoporous nanospindles on the electrochemical performance of Li-S batteries, different sulfur/host composites (M-Carbon/S, M-Fe<sub>2</sub>O<sub>3</sub>/S, and C@M-Fe<sub>3</sub>O<sub>4</sub>/S) were prepared and used as cathode for Li-S batteries. The areal sulfur loading for three cathodes is fixed to around 1.5 mg cm<sup>-2</sup>. The specific sulfur contents in these different composites were determined by the thermogravimetry analysis (TGA), which is provided in Figure 3.12. After the complete evaporation of sulfur at 500 °C, the calculated sulfur contents inside the M-Carbon/S, M-Fe<sub>2</sub>O<sub>3</sub>/S, and C@M-Fe<sub>3</sub>O<sub>4</sub>/S composites are 72.5, 72.1, and 71.8 wt.%, respectively. The CV curves of the Li-S batteries with different cathodes were scanned in the electrochemical range of 1.7-2.8 V vs. Li/Li<sup>+</sup> at 0.1 mV s<sup>-1</sup> (Figure 3.13a). The CV curves of the three electrodes exhibit a similar shape with two representative redox peaks, which originate from the multistep reduction reactions from sulfur to Li<sub>2</sub>S.<sup>[159]</sup> Specifically, the labelled C1 peak in the cathodic scan corresponds to the conversion reaction of sulfur to high-order LiPSs and the marked C2 peak is ascribed to the conversion reactions of liquid LiPSs to

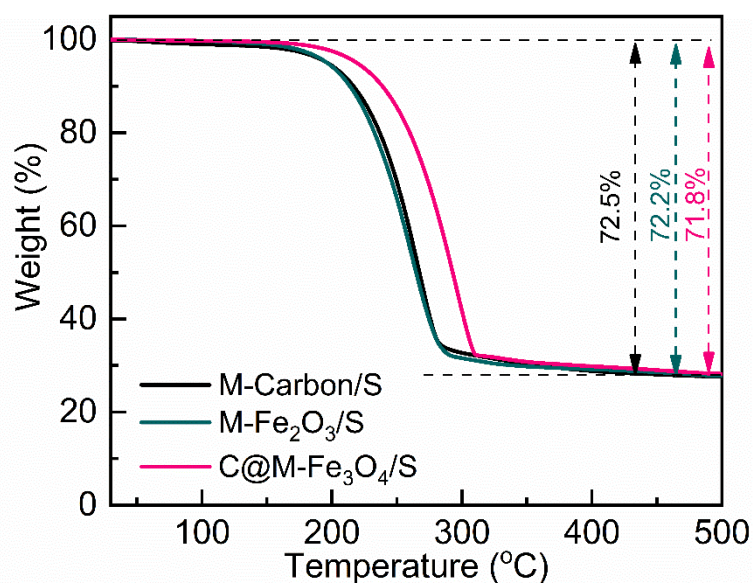


**Figure 3.12** TGA curves of the M-Carbon/S, M-Fe<sub>2</sub>O<sub>3</sub>/S, and C@M-Fe<sub>3</sub>O<sub>4</sub>/S under nitrogen atmosphere.

Li<sub>2</sub>S. In the subsequent anodic scan, two partially overlapped peaks (A1 and A2) are observed corresponding to the reverse oxidation conversion from solid Li<sub>2</sub>S to liquid polysulfide and then to S. Interestingly, compared with the other two cathodes, the C2 peak in the CV curve of the C@M-Fe<sub>3</sub>O<sub>4</sub>/S cathode exhibits the highest current density value and is slightly shifted to a higher voltage, indicating its promoted reduction kinetics from high-order LiPSs to Li<sub>2</sub>S. Figure 3.13b shows the initial galvanostatic charge-discharge profiles of three cathodes at 0.1 C. Two characteristic plateaus of Li-S batteries are observed in the discharging curves for all three cathodes. The first short plateau around 2.35 V is ascribed to the conversion reactions from sulfur to high-order LiPSs and the other long one at 2.10 V is from the conversion reaction from low-order LiPSs to Li<sub>2</sub>S, respectively.<sup>[134c]</sup> The initial specific discharge capacities of the M-Carbon/S, M-Fe<sub>2</sub>O<sub>3</sub>/S, and C@M-Fe<sub>3</sub>O<sub>4</sub>/S cathodes at 0.1 C are 1254.0, 1347.6, and 1618.0 mAh g<sup>-1</sup>, respectively. To further interpret the discharge behaviors, it is defined that Q<sub>1</sub> represents the capacity from the initial reduction from the solid S to the LiPSs and Q<sub>2</sub> corresponds to the capacity from the subsequent reduction from liquid LiPSs to solid Li<sub>2</sub>S. The calculated ratios of Q<sub>2</sub>/Q<sub>1</sub> for the M-Carbon/S electrode is 2.52, which is lower than that of C@M-Fe<sub>3</sub>O<sub>4</sub>/S (Q<sub>2</sub>/Q<sub>1</sub>: 2.91) and M-Fe<sub>2</sub>O<sub>3</sub>/S (Q<sub>2</sub>/Q<sub>1</sub>: 2.92) electrodes. This proves that the C@M-Fe<sub>3</sub>O<sub>4</sub> and M-Fe<sub>2</sub>O<sub>3</sub> particles can also effectively accelerate the polysulfide conversion to Li<sub>2</sub>S under the galvanostatic discharge process.<sup>[160]</sup>

Furthermore, the cycling performance of the Li-S batteries with the different cathodes at 0.2 C is compared and shown in Figure 3.14a. The initial discharge capacities of M-Carbon/S, M-Fe<sub>2</sub>O<sub>3</sub>/S, and C@M-Fe<sub>3</sub>O<sub>4</sub>/S cathodes are 1214.3, 1304.4, and 1597.1 mAh g<sup>-1</sup>, respectively.

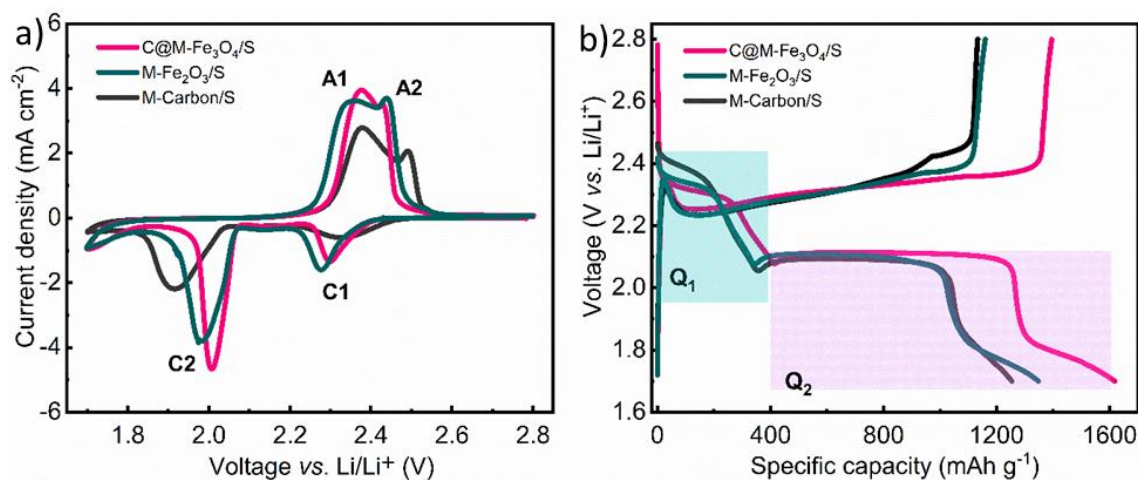


**Figure 3.13** CV profiles of the Li-S cells with C@M-Fe<sub>3</sub>O<sub>4</sub>/S, M-Fe<sub>2</sub>O<sub>3</sub>/S, and M-Carbon/S cathodes at 0.1 mV s<sup>-1</sup> in the range of 1.7-2.8 V vs. Li/Li<sup>+</sup>; (b) initial charge-discharge curves of Li-S cells with different cathodes at 0.1 C (1 C = 1675 mA g<sup>-1</sup>).

The improved capacity for the C@M-Fe<sub>3</sub>O<sub>4</sub>/S electrode is ascribed to its strong adsorption ability to LiPSs and the facilitated liquid-to-solid conversion reaction. With good adsorption of LiPSs and promoted conversion of Li<sub>2</sub>S, the cell with the C@M-Fe<sub>3</sub>O<sub>4</sub> cathode delivers the highest specific discharge capacity of 1064.3 mAh g<sup>-1</sup> after 100 cycles, which is much higher than those of M-Fe<sub>2</sub>O<sub>3</sub>/S (836.1 mAh g<sup>-1</sup>) and M-Carbon/S (741.6 mAh g<sup>-1</sup>) electrodes. The inferior cycling stability of the M-Carbon/S electrode could be a result of the poor interactions between the LiPSs and carbon. The rate capabilities of the M-Carbon/S, M-Fe<sub>2</sub>O<sub>3</sub>/S, and C@M-Fe<sub>3</sub>O<sub>4</sub>/S cathodes are assessed at different C rates (from 0.1 to 2 C) for 10 cycles, as shown in Figure 3.14b. It is found that the C@M-Fe<sub>3</sub>O<sub>4</sub>/S electrode shows better rate capabilities than the other two electrodes. Even when cycled at a high C rate ( $\geq 0.5$  C), the C@M-Fe<sub>3</sub>O<sub>4</sub>/S electrode can still deliver 890.8 mAh g<sup>-1</sup> at 1 C and 712 mAh g<sup>-1</sup> at 2 C, respectively. Without the combination of good adsorption to LiPSs and electron conductivity, the M-Carbon/S and M-Fe<sub>2</sub>O<sub>3</sub>/S electrodes show lower capacities of 688.1 and 759.1 mAh g<sup>-1</sup> at 1 C, respectively. As demonstrated in Figure 3.14c, with increasing the C rate, the plateau contributed by the reduction reaction from LiPSs to Li<sub>2</sub>S becomes shortened and shifts the lower voltage position due to the large polarization. However, the plateau is still visible even at high C rates ( $\geq 0.5$  C), suggesting a facilitated conversion reaction. Furthermore, the electrochemical impedance spectroscopy (EIS) of Li-S cells has been investigated before cycling, as shown in Figure 3.15. Judging from the semicircles of the Nyquist plots, the C@M-Fe<sub>3</sub>O<sub>4</sub>/S electrode has a lower polarization and charge transfer resistance ( $R_{ct}$ ) than that of the M-Carbon/S and M-Fe<sub>2</sub>O<sub>3</sub>/S electrodes, attributing to its good rate capability. Additionally,

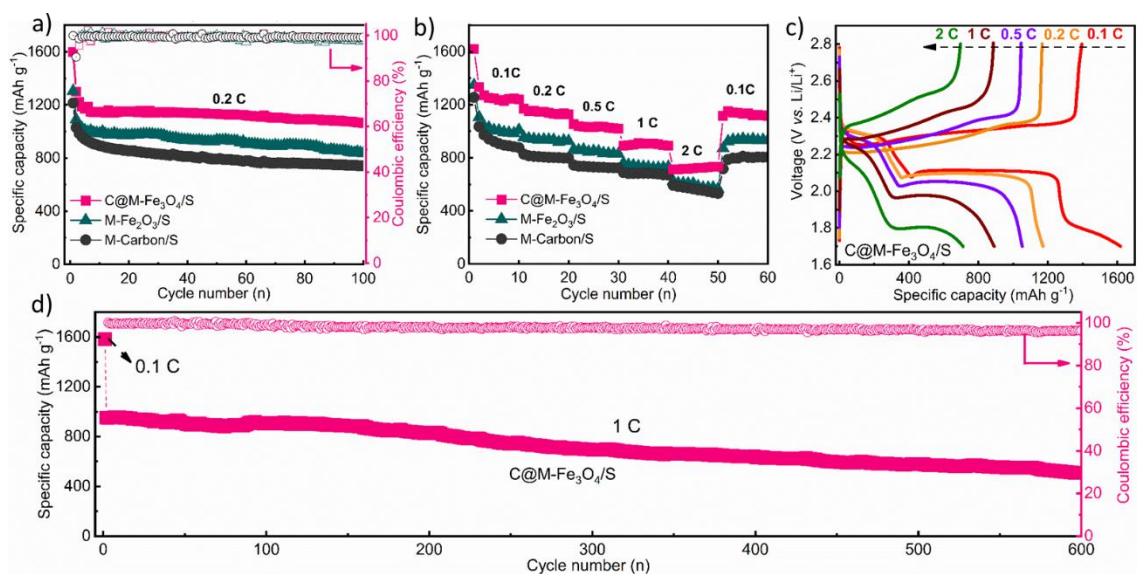


**Figure 3.14** (a) Cycling performance of the Li-S batteries with different cathodes (M-Carbon/S, M-Fe<sub>2</sub>O<sub>3</sub>/S, and C@Fe<sub>3</sub>O<sub>4</sub>/S) at 0.2 C; (b) rate capability of the Li-S batteries with different host materials; (c) the initial charge-discharge curves of the C@M-Fe<sub>3</sub>O<sub>4</sub>/S electrode at different C rates; (d) the long-term cycling performance of the Li-S cell with C@M-Fe<sub>3</sub>O<sub>4</sub>/S cathode at 1 C.

after the activation process by charging-discharging at 0.1 C for one cycle, the cycling performance of the Li-S cell with the C@M-Fe<sub>3</sub>O<sub>4</sub>/S electrode at 1 C is presented in Figure 3.14d. With a high discharge capacity of 952.1 mAh g<sup>-1</sup> at 1 C in the first cycle, the C@M-Fe<sub>3</sub>O<sub>4</sub>/S electrode maintains a capacity of 507.7 mAh g<sup>-1</sup> after 600 cycles, suggesting its good long-term cycling stability. With the synergistic effect of the unique mesoporous nanospindle structure and improved conductivity, the synthesized C@M-Fe<sub>3</sub>O<sub>4</sub> particles can efficiently suppress the shuttle effect and promote the conversion from LiPSs to Li<sub>2</sub>S.

In this chapter, the mesoporous Fe<sub>2</sub>O<sub>3</sub> nanospindles have been synthesized through a confined-space pyrolysis method and C@M-Fe<sub>3</sub>O<sub>4</sub> particles have been obtained after the PDA coating and calcination, persevering similar mesoporous structure of M-Fe<sub>2</sub>O<sub>3</sub>. Electron tomography reveals that 3D interconnected porosities are present in the M-Fe<sub>2</sub>O<sub>3</sub> particles. The porous C@M-Fe<sub>3</sub>O<sub>4</sub> particles exhibit a better confinement ability to LiPSs than M-Carbon and M-Fe<sub>2</sub>O<sub>3</sub> nanospindles, thanks to the synergistic effects of physical confinement in the mesoporous structure and the chemisorption of Fe<sub>3</sub>O<sub>4</sub> particles. Therefore, they act as an efficient sulfur host material for Li-S batteries. More importantly, it is revealed that the C@M-Fe<sub>3</sub>O<sub>4</sub> particles with abundant “triple-phase” sites could boost the conversion reactions of LiPSs and the Li<sub>2</sub>S nucleation/deposition. As a result, better electrochemical performance has been achieved by using the C@M-Fe<sub>3</sub>O<sub>4</sub>/S composite as cathode for Li-S batteries compared to the M-Carbon/S and M-Fe<sub>2</sub>O<sub>3</sub>/S electrodes. The C@M-Fe<sub>3</sub>O<sub>4</sub>/S electrode exhibits good

long-term cycling stability at 1 C with an initial discharge capacity of  $952.1 \text{ mAh g}^{-1}$  and a retained capacity of  $507.7 \text{ mAh g}^{-1}$  after 600 cycles. The proposed strategy in this work could be also applicable to synthesizing other transition metal-based compounds with 3D interconnected porosities as sulfur-host materials in Li-S batteries and for applications beyond.

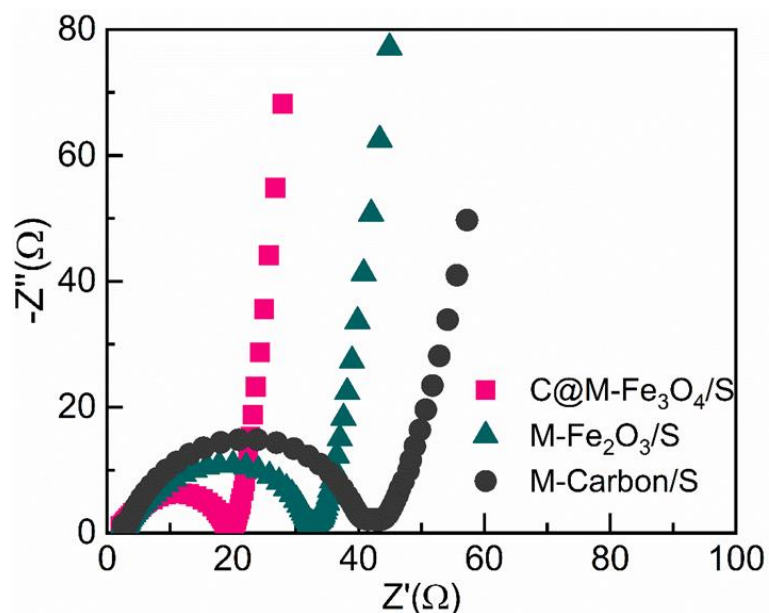


**Figure 3.15** EIS spectra of the Li-S batteries with different cathodes before cycling.



## 4. Yolk-Shelled Iron Sulfides-Carbon Nanospindles as Efficient Sulfur Host Materials for Li-S Batteries\*

To suppress the “shuttle effect”, researchers have used three main approaches according to the diffusion path of LiPSs: i) cathode design, ii) separator modification or introduction of interlayer, and iii) electrolyte optimization.<sup>[161]</sup> Among these approaches, the design and synthesis of novel cathode materials with an outstanding capability to confine LiPSs on-site is substantially efficient and important for the long-term stability of Li-S batteries. To date, many kinds of nanostructures as sulfur host materials have been synthesized, including hollow spheres,<sup>[162]</sup> tubes,<sup>[163]</sup> cubes,<sup>[102, 106, 164]</sup> and polyhedrons,<sup>[116]</sup> etc. Besides the nanostructure in chapter 3, the selection of metal-based compounds is also crucial for improving the electrochemical performance of Li-S batteries. Therefore, systematic research on the compositions is necessary to understand the effects of different metal-based compounds on the electrochemical performance of Li-S batteries.

Among various compounds, iron-based materials have attracted tremendous interest in Li-S batteries because of their nontoxicity, high adsorption ability to LiPSs, and low cost. So far, nanostructure and synthetic methods of iron-based compounds have been widely investigated in Li-S batteries.<sup>[106, 165]</sup> For instance, through the polar-polar interaction between iron oxides and LiPSs, three-dimensional Fe<sub>2</sub>O<sub>3</sub>-graphene was designed as the anchor sites for LiPSs. It was found that Fe<sub>2</sub>O<sub>3</sub> particles could restrain the shuttling of LiPSs and accelerate the transformation of the soluble LiPSs to insoluble products.<sup>[104]</sup> Besides, Zhang *et al.* found that sulfiphilic FeS<sub>2</sub> particles as additive in the sulfur cathode can improve the long-term cycling stability of Li-S batteries.<sup>[110]</sup> Also, Xi *et al.* prepared the composite of FeS<sub>2</sub>/FeS/S *via* a simple ball milling of Na<sub>2</sub>S, S, and FeCl<sub>3</sub>, revealing that FeS<sub>2</sub> exhibited a stronger adsorption ability than FeS according to their theoretical results with the specific electrochemical performance of each sulfide unidentified.<sup>[95b]</sup> Although excellent performance has been achieved, it is difficult to compare and define the optimal composition among various sulfur host materials because of the large variations in their nanostructures. This hinders the rational design of electrode materials for Li-S batteries. To address the challenge, systematic study on the chemical composition of host materials with the same nanostructure is required to optimize

\*This chapter is adapted with permission from my original work: Dongjiu Xie, Shilin Mei, Yaolin Xu, Ting Quan, Eneli Härk, Zdravko Kočovski, and Yan Lu, Efficient Sulfur Host Based on Yolk-Shell Iron Oxide/Sulfide-Carbon Nanospindles for Lithium-Sulfur Batteries, *ChemSusChem*, **2021**, 14, 1404. Published by John Wiley & Sons in Open access.



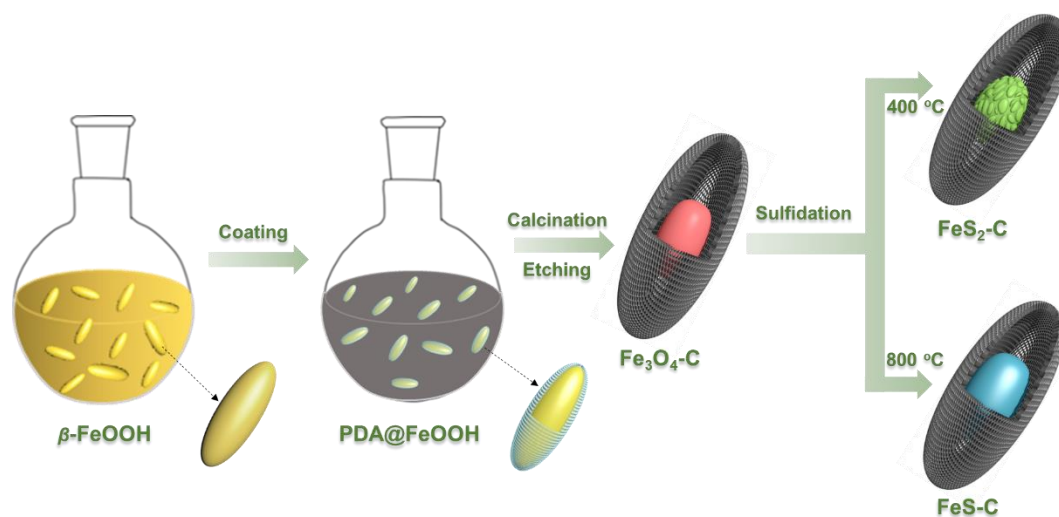


**Figure 4.1** Illustration of the synthetic routes of the yolk-shell  $\text{Fe}_3\text{O}_4\text{-C}$ ,  $\text{FeS-C}$ , and  $\text{FeS}_2\text{-C}$  nanoparticles.

the metal-based compounds for Li-S batteries. These systematic studies, however, remain underdeveloped, especially for Fe-based compounds. Cui *et al.* quantitatively compared the adsorption ability of a series of metal-based compounds to LiPSs, revealing that there is a large difference between the poor adsorption compounds and strong adsorption ones.<sup>[128]</sup> Moreover, Qian *et al.* revealed that among four types of cobalt-based compounds ( $\text{CoP}$ ,  $\text{Co}_4\text{N}$ ,  $\text{CoS}_2$ , and  $\text{Co}_3\text{O}_4$ ), the sulfur cathode with  $\text{CoP}$  as additive displayed the best rate capability for Li-S batteries due to moderate adsorption ability and superior diffusion dynamics.<sup>[166]</sup>

In this chapter, three types of yolk-shell structured iron-based compounds ( $\text{Fe}_3\text{O}_4$ ,  $\text{FeS}$ , and  $\text{FeS}_2$ ) have been encapsulated into hollow carbon nanospindles, aiming for systematical investigation on their efficiency in suppressing the LiPSs shuttling effect and electrochemical performance in Li-S batteries. The hollow carbon shell provides the physical confinement of LiPSs, while the iron-based compounds enable the chemical adsorption. The synthesis is scalable and the procedure is depicted in Figure 4.1. Firstly, the colloidal  $\text{FeOOH}$  nanospindles have been synthesized in a large scale with the hydrolysis of  $\text{FeCl}_3$  in an aqueous solution,<sup>[144]</sup> which were then coated with a thin polydopamine (PDA) layer as carbon source. Along with calcination under argon and partially etching with  $\text{HCl}$ , yolk-shell  $\text{Fe}_3\text{O}_4\text{-C}$  nanoparticles were obtained. Further calcination of the mixture of sulfur and  $\text{Fe}_3\text{O}_4\text{-C}$  particles under argon at different temperatures leads to yolk-shell  $\text{FeS}_2\text{-C}$  (at  $400\text{ }^\circ\text{C}$ ) and  $\text{FeS-C}$  (at  $800\text{ }^\circ\text{C}$ ) particles, respectively, without destroying the nanostructure. This synthetic routine allows to directly compare the specific effect of iron oxide and sulfides on the electrochemical performance of Li-S batteries. The influence of material properties (i.e., affinity to LiPSs and conductivity) on the specific capacity, cycling stability, and rate capability has been systematically studied,



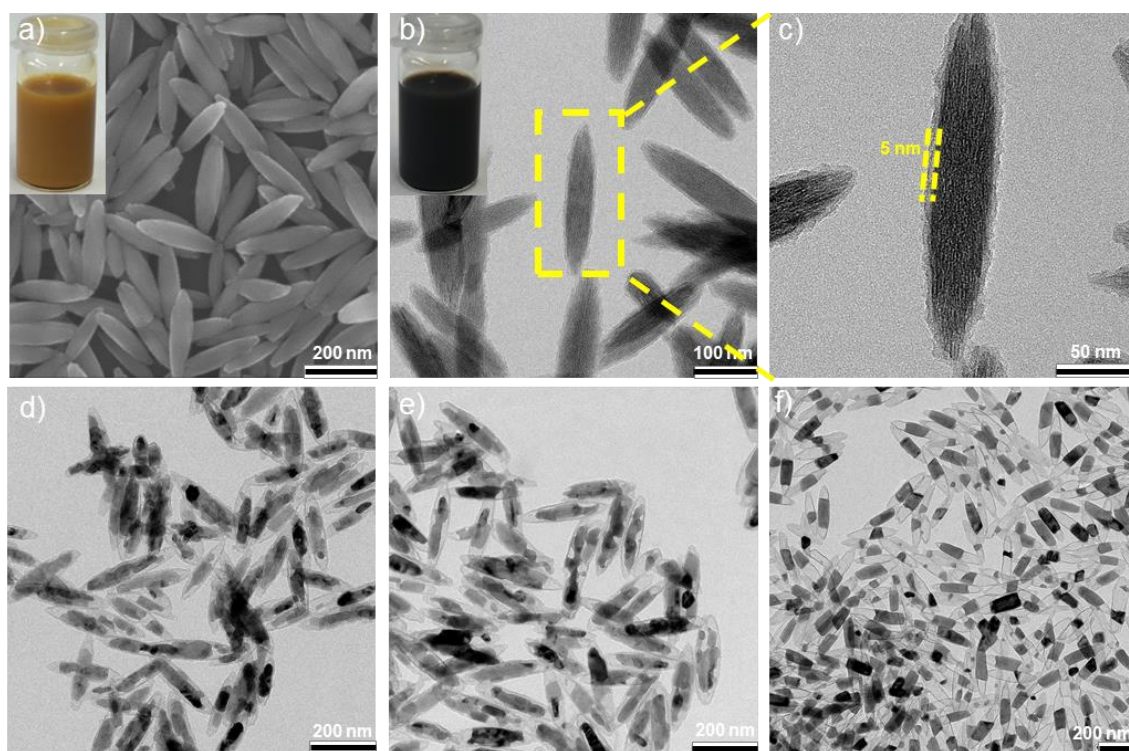


**Figure 4.2** SEM image of the FeOOH particles with the photograph of the FeOOH particles dispersed in water (a); (b, c) TEM images of the PDA-coated FeOOH (PDA@FeOOH) with the photograph of its dispersion in water; TEM images of the PDA@FeOOH particles after calcination at different temperatures (550 °C (c), 600 °C (d), and 700 °C (e)) under argon.

providing fundamental information for the rational design of efficient sulfur cathode. Besides, the synthesis of yolk-shell iron-based composite particles is simple, scalable, and broadly applicable, creating possibilities for the mass production of various functional nanomaterials for different applications.

## 4. 1 Synthesis and characterization of yolk-shell nanospindles

### 4.1.1 Fe<sub>3</sub>O<sub>4</sub>-carbon yolk-shell nanospindles

The  $\beta$ -FeOOH nanoparticles in Chapter 3 have been chosen as templates and iron source for synthesizing yolk-shell nanoparticles because they can be easily synthesized in a large scale with a simple procedure. The SEM image in Figure 4.2a shows the overview of the  $\beta$ -FeOOH nanoparticles with nanospindle morphology. Furthermore,  $\beta$ -FeOOH nanoparticles are colloidal stable in aqueous solution as demonstrated in the inset in Figure 4.2a. Afterward, a thin layer of PDA has been coated on the surface of FeOOH nanospindles through the polymerization of dopamine monomer in a tris buffer solution (pH = 8.5). PDA is often used as source for N-doped porous carbon.<sup>[22]</sup> Hetero-atom doping with nitrogen can increase the adsorption capability of carbon-based materials to LiPSs due to the increased polarity. As

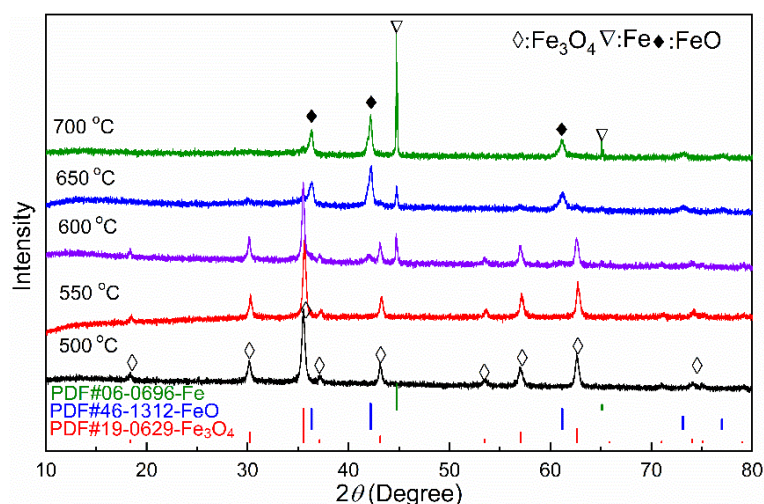


**Figure 4.3** XRD patterns of the PDA@FeOOH nanoparticles after calcination at different temperatures under argon.

shown in the inset of Figure 4.1b, the color of the FeOOH solution turns from yellow to black, indicating the successful encapsulation of PDA. The TEM image shown in Figure 4.1c confirms that a PDA layer with a thickness of 5 nm has been uniformly coated on the surface of the FeOOH nanospindle with the formation of the core-shell nanostructure.

To obtain a yolk-shell nanostructure, the PDA-coated FeOOH (PDA@FeOOH) nanoparticles were calcinated at different temperatures in a tube furnace under argon flow. The optimization temperature of the heat treatment is determined by the TEM images and XRD results of the collected products. As shown in Figure 4.2d-2f, the nanospindle shape of the composite particles remains almost unchanged after calcination, which contains an iron oxide core coated with a 5 nm carbon shell. Void spaces in the carbon shell are created due to the volume shrinkage after the decomposition of FeOOH particles into iron oxide. It is found that the inner void space of yolk-shell nanospindles expands with increasing calcination temperature, implying the phase transition of the iron oxides. XRD patterns of the collected samples after calcination have been collected to investigate the influence of calcination temperatures on the crystal phases of iron oxides. As demonstrated in Figure 4.3, iron oxide with a pure Fe<sub>3</sub>O<sub>4</sub> phase can be only obtained in the temperature range of 500-550 °C. Additional phases of FeO and Fe appear at 600 °C. Further increase of temperature to 650 °C leads to the complete decomposition of Fe<sub>3</sub>O<sub>4</sub> into a mixture of FeO and Fe phases, contributing to the increased void space inside yolk-shell nanospindles. As a result, the sample calcinated at 550 °C with a pure Fe<sub>3</sub>O<sub>4</sub> phase was used for further investigation.

Although the yolk-shell nanospindle is achieved with a pure phase of Fe<sub>3</sub>O<sub>4</sub>, as shown in

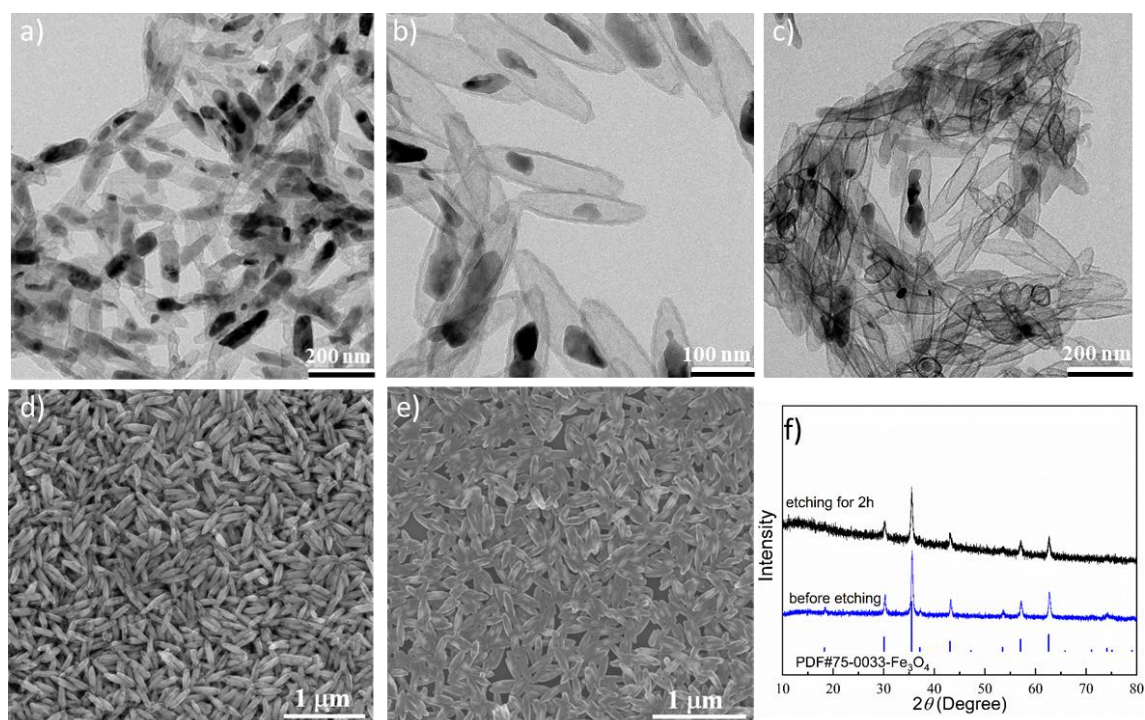


**Figure 4.4** TEM images of the yolk-shell Fe<sub>3</sub>O<sub>4</sub>-C nanopindles after etching with HCl solution for different durations ((a) 1, (b) 2, and (c) 3 h) under a mild mechanical stirring; SEM images of the yolk-shell Fe<sub>3</sub>O<sub>4</sub>-C particles before (d) and after etching for 2 h (e); XRD patterns (f) of the yolk-shell Fe<sub>3</sub>O<sub>4</sub>-C particles before and after etching for 2 h.

Figure 4.2d, the inner void space is very limited for sulfur loading. In addition, it was reported by Liu *et al.* that after the sulfidation process of yolk-shell Fe<sub>3</sub>O<sub>4</sub>-carbon nanoboxes, the large volume expansion could break the carbon shell.<sup>[167]</sup> Thus, to create extra void spaces, the obtained yolk-shell nanoparticles have been further treated with HCl solution (2 M) to etch part of the Fe<sub>3</sub>O<sub>4</sub> particles. The optimized etching time is further determined by the TEM images of the collected particles. As shown in Figure 4.4a, no obvious changes are observed in the particles after etching for 1 h, compared with the pristine in Figure 4.2d. After etching for 2 h, extra void spaces are created with the core size reduced to 30-50 nm (Figure 4.4b). Further extending the etching time to 3 h results in the removal of the Fe<sub>3</sub>O<sub>4</sub> core particles, leaving hollow carbon spindle shells (Figure 4.4c). Figure 4.4d and e show the SEM images of the yolk-shell pristine nanoparticles and etched ones, respectively. Well-defined nanopindles are detected with bright spots inside, which are ascribed to Fe<sub>3</sub>O<sub>4</sub> particles. After the partial removal of Fe<sub>3</sub>O<sub>4</sub> particles, the bright spot area is decreased as shown in Figure 4.4e. Moreover, the XRD patterns in Figure 4.4f indicate that the etching process leads to no change in the crystal phase of Fe<sub>3</sub>O<sub>4</sub> particles. Hence, the optimized etching time was determined as 2 h for further sulfidation process.



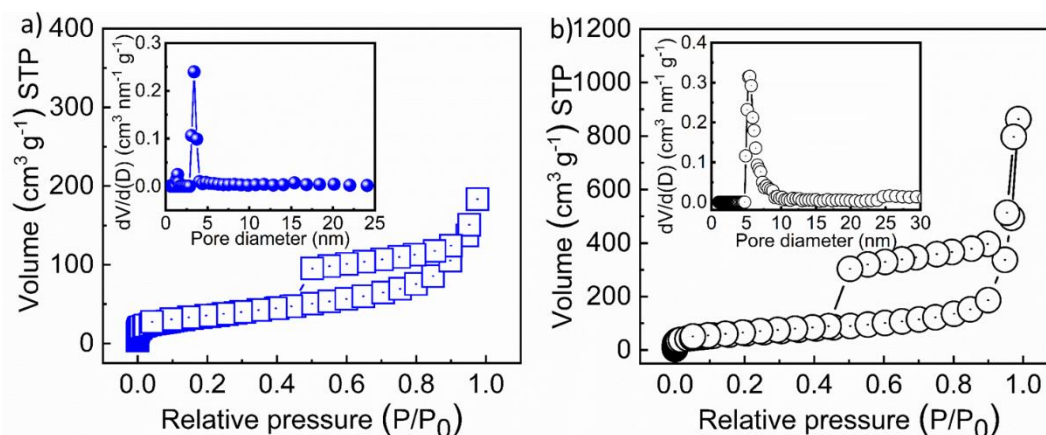


**Figure 4.5**  $N_2$  adsorption-desorption isotherms of the yolk-shell  $Fe_3O_4$ -C particles before (a) and after etching for 2h (b) with the insets of the corresponding pore size distribution.

To reveal the contribution of etching to the specific surface area,  $N_2$  adsorption-desorption isotherms of the pristine yolk-shell nanoparticles and etched ones were measured and shown in Figure 4.5. Compared with the pristine, the isotherms of the etched yolk-shell  $Fe_3O_4$ -C sample exhibit a wider hysteresis loop, which could be contributed by the increased void space inside the carbon shell. According to the BET model,<sup>[147]</sup> the calculated specific surface area of the etched  $Fe_3O_4$ -C particle is  $223.2 \text{ m}^2 \text{ g}^{-1}$ , which is higher than that of the pristine one ( $124.4 \text{ m}^2 \text{ g}^{-1}$ ). This is due to the weight loss after the etching process and decreasing particle size of  $Fe_3O_4$  particles. The diameter of the pores in the pristine particles is centered at 3 nm based on the BJH model,<sup>[146]</sup> while the diameter of pores in the etched sample is increased to 5 to 10 nm.

#### 4.1.2 Iron sulfides-carbon yolk-shell nanospindles

The etched yolk-shell  $Fe_3O_4$ -C particles have been used as precursors to synthesize iron sulfides ( $FeS$  and  $FeS_2$ ). Instead of toxic  $H_2S$  gas, the elemental sulfur powder was used as the sulfur source because sulfur has been widely applied to synthesize different iron sulfides due to its high reactivity at high temperatures.<sup>[167-168]</sup> The yolk-shell  $Fe_3O_4$ -C particles mixed with excessive sulfur were calcinated at 400 and 800 °C to generate  $FeS_2$ -C and  $FeS$ -C particles, respectively. For the  $FeS_2$ -C nanoparticles, the mechanism of sulfidation at 400 °C is listed as:



With further increasing the calcination temperature,  $FeS_2$  starts to gradually decompose into  $FeS$  and sulfur, which can be described in the following reaction:



As shown in the TEM images in Figure 4.6a and 6b, the  $FeS$ -C and  $FeS_2$ -C particles exhibit a

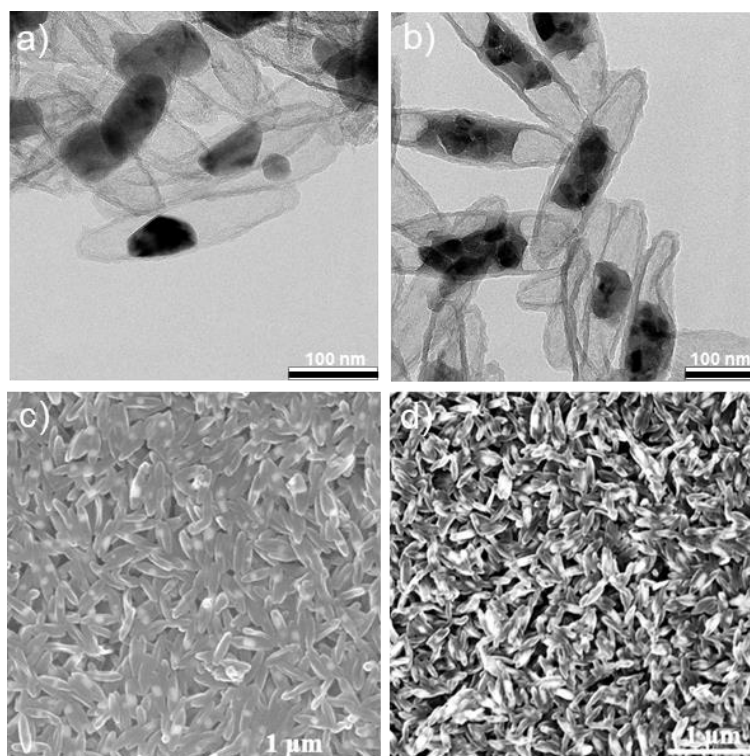


**Figure 4.6** TEM images of the FeS-C (a) and FeS<sub>2</sub>-C (b) yolk-shell nanoparticles; SEM images of the FeS-C (c) and FeS<sub>2</sub>-C (d) yolk-shell nanoparticles.

similar morphology as that of Fe<sub>3</sub>O<sub>4</sub>-C nanoparticles and there is still a large void space inside the carbon shell after the sulfidation process. Interestingly, the yolk part of the FeS<sub>2</sub>-C sample is composed of several FeS<sub>2</sub> nanoparticles with size of 20-30 nm. This could be caused by the pulverization during the sulfidation process of iron oxide particles at low temperature. On the contrary, the yolk part inside the FeS-C nanospindles is a single FeS particle because of its high sulfidation temperature. From the SEM images of the yolk-shell nanoparticles in Figure 4.6c and 6d, bright spots of iron sulfide are observed inside the intact carbon shells, ascribing to the extra void space created in the etching step.

The crystal structures of the iron sulfide particles have been further characterized by the XRD patterns (Figure 4.7a). After the sulfidation at 400 °C, the collected patterns of FeS<sub>2</sub>-C are well indexed to pyrite phase FeS<sub>2</sub> (PDF#42-1340), indicating the complete conversion of Fe<sub>3</sub>O<sub>4</sub> into FeS<sub>2</sub>. The peaks at  $2\theta = 28.4, 33.1, 37.2, 40.8, 47.5,$  and  $56.3^\circ$  are corresponding to the (111), (200), (210), (211), (220), and (311) reflections of pyrite FeS<sub>2</sub>. After sulfidation at 800 °C, troilite phase FeS (PDF#89-6926) is obtained. The five peaks at  $2\theta = 30.1, 33.9, 43.8, 53.2,$  and  $71.1^\circ$  are corresponding to the (110), (112), (114), (300), and (224) reflections of troilite FeS, respectively. To compare the differences of various iron-based compounds in the crystal structure, the ball-and-stick structure models of magnetite Fe<sub>3</sub>O<sub>4</sub>, troilite FeS, and pyrite FeS<sub>2</sub>

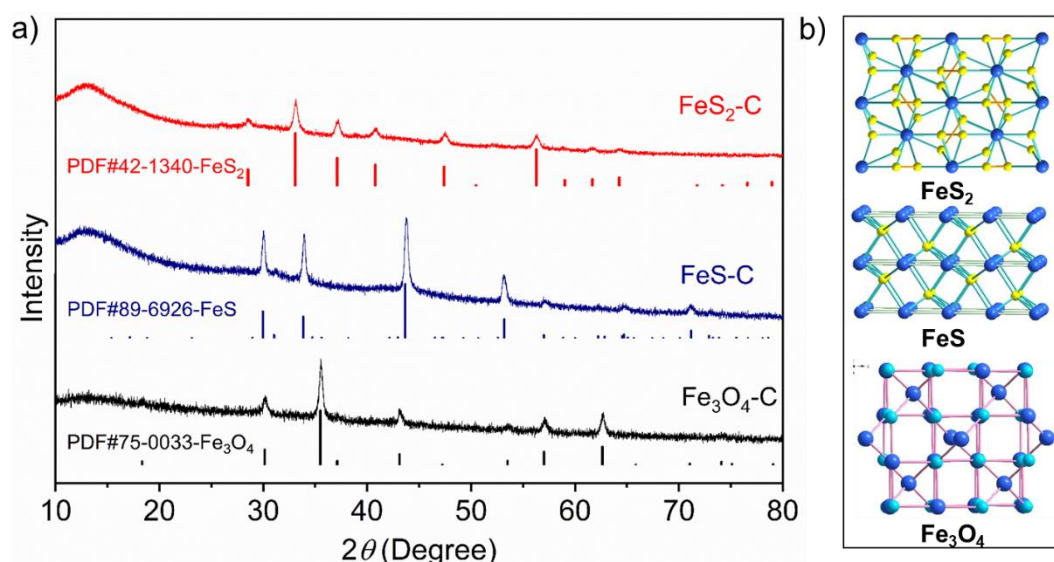


**Figure 4.7** (a) XRD patterns of  $\text{Fe}_3\text{O}_4\text{-C}$ ,  $\text{FeS-C}$ , and  $\text{FeS}_2\text{-C}$ ; (b) crystal structures of magnetite  $\text{Fe}_3\text{O}_4$ , troilite  $\text{FeS}$ , and pyrite  $\text{FeS}_2$ , respectively.

were plotted and shown in Figure 4.7b, respectively. Unlike the spinel structure of magnetite  $\text{Fe}_3\text{O}_4$ , the pyrite  $\text{FeS}_2$  consists of disulfide  $\text{S}_2^{2-}$  moieties (S-S, depicted in orange), while the sulfur atoms in troilite  $\text{FeS}$  are only bonded with iron atoms in the form of  $\text{S}^{2-}$  instead of  $\text{S}_2^{2-}$ . Metallic bonding between iron atoms (Fe-Fe, depicted in gray) exists in the crystal structure of  $\text{FeS}$ , which contributes to a higher electronic conductivity than that of pyrite  $\text{FeS}_2$  and  $\text{Fe}_3\text{O}_4$ . The difference of iron-based compounds in their crystal structure may lead to different interaction behavior with LiPSs. To further explore the bonding characteristics, X-ray photoelectron spectroscopy (XPS) and Raman spectroscopy have been performed, respectively. From the Fe 2p spectra of  $\text{Fe}_3\text{O}_4\text{-C}$ , as shown in Figure 4.8a, the peaks at 726.1 and 713.8 eV are assigned to Fe  $2p_{1/2}$  and Fe  $2p_{3/2}$  of  $\text{Fe}^{3+}$  states, respectively, while the peaks at the binding energies of 710.9 eV and 723.8 eV are ascribed to  $\text{Fe}^{2+}$  states.<sup>[106]</sup> The existence of  $\text{Fe}^{3+}$  in iron sulfides arises from the surface oxidation of  $\text{FeS}$  and  $\text{FeS}_2$  nanoparticles after exposure to air. Besides, in the XPS spectra of  $\text{FeS}_2\text{-C}$  nanoparticles, two additional peaks are observed at 707.4 and 720.7 eV, which are ascribed to the  $2p_{3/2}$  and  $2p_{1/2}$  regions of Fe in pyrite  $\text{FeS}_2$ , respectively.<sup>[169]</sup> In the high-resolution spectrum of S 2p (Figure 4.8b), the peaks at 162.6 eV and 161.4 eV correspond to  $2p_{1/2}$  and  $2p_{3/2}$  of  $\text{S}^{2-}$  in  $\text{FeS}$ , respectively. The detected polysulfide ( $\text{S}_n^{2-}$ ) and sulfate ( $\text{SO}_x$ ) in the  $\text{FeS-C}$  nanoparticles can be induced by the surface oxidation. In the S 2p spectra of the  $\text{FeS}_2\text{-C}$  sample, two characteristic peaks of the  $2p_{1/2}$  and  $2p_{3/2}$  of  $\text{S}_2^{2-}$  in  $\text{FeS}_2$  are found at 164.9 and 163.5 eV, respectively.

In the Raman spectra shown in Figure 4.8c, there are two strong bands at 1345 and 1587  $\text{cm}^{-1}$

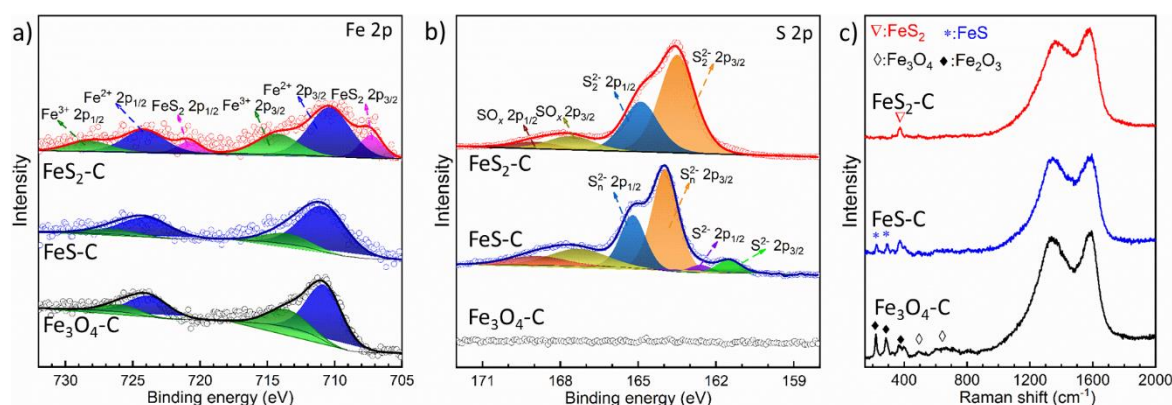


**Figure 4.8** XPS spectra of Fe 2p (a) and S 2p (b) in the Fe<sub>3</sub>O<sub>4</sub>-C, FeS-C, and FeS<sub>2</sub>-C nanoparticles; (c) Raman spectra of Fe<sub>3</sub>O<sub>4</sub>-C, FeS-C, and FeS<sub>2</sub>-C nanoparticles.

in all samples, which correspond to the D and G bands of the carbon shell, respectively. The peak at  $378.1\text{ cm}^{-1}$  in the FeS<sub>2</sub>-C sample is assigned to the A<sub>1g</sub> of FeS<sub>2</sub>, which is induced by the S-S in-phase stretching vibration.<sup>[170]</sup> In the Raman spectrum of the FeS-C sample, two characteristic peaks of FeS are observed at  $222\text{ cm}^{-1}$  and  $288\text{ cm}^{-1}$ , while the peak at around  $372\text{ cm}^{-1}$  belongs to the polysulfide S<sub>n</sub><sup>2-</sup>.<sup>[171]</sup> In the spectra of Fe<sub>3</sub>O<sub>4</sub>-C, strong peaks from Fe<sub>2</sub>O<sub>3</sub> are presented, while only weak peaks of Fe<sub>3</sub>O<sub>4</sub> are found, possibly due to the laser-induced conversion of Fe<sub>3</sub>O<sub>4</sub> into Fe<sub>2</sub>O<sub>3</sub>.<sup>[172]</sup> N<sub>2</sub> adsorption/desorption measurements have been conducted to further measure the specific surface area and pore size distribution of yolk-shell iron sulfides-carbon nanoparticles, as shown in Figure 4.9. The isotherms of FeS<sub>2</sub>-C nanoparticles are typical Type-III ones, while those of the FeS-C sample are typical Type-IV isotherms with a hysteresis loop. After sulfidation of the Fe<sub>3</sub>O<sub>4</sub>-C sample, the BET-specific surface areas of FeS-C and FeS<sub>2</sub>-C are  $162.96$  and  $134.4\text{ m}^2\text{ g}^{-1}$ , respectively, which is lower than that of the Fe<sub>3</sub>O<sub>4</sub>-C sample. This is due to the increased mass of the core particles after the sulfidation process. The pores in the FeS-C nanoparticles show a similar pore size distribution with the Fe<sub>3</sub>O<sub>4</sub>-C sample. In the FeS<sub>2</sub>-C sample, its pore diameter decreases to around 2-3 nm, because the mesopores could be blocked by the FeS<sub>2</sub> agglomerates.

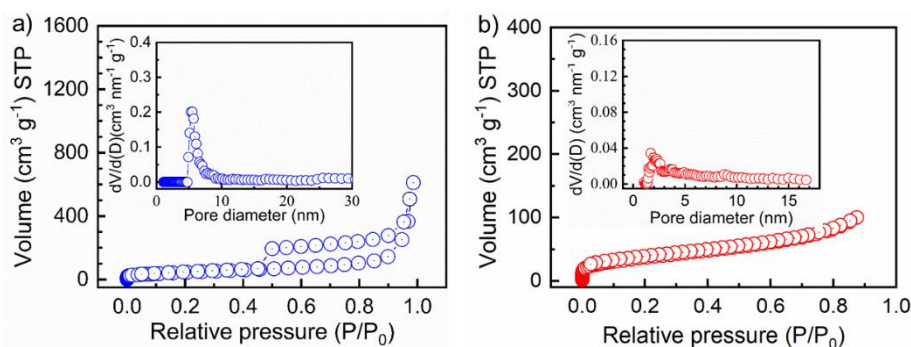


**Figure 4.9** Nitrogen adsorption/desorption isotherms of the FeS-C (a) and FeS<sub>2</sub>-C (b) nanoparticles and corresponding pore size distribution curves as insets.

## 4.2 Interactions of yolk-shell particles with LiPSs

### 4.2.1 LiPSs adsorption test

To investigate the effects of the compositions of iron-based compounds on the adsorption abilities to LiPS, visualized adsorption test has been conducted inside the glove box. The host materials with the same surface area have been applied for the adsorption of LiPSs based on the obtained BET-specific surface area.<sup>[128]</sup> Firstly, 3.5 mL of  $\text{Li}_2\text{S}_8$  solution (2 mM) in DME/DOL ( $v/v = 1/1$ ) was mixed with different host materials. As shown in the photograph of the inset in Figure 4.10, after aging for 2 h in the glove box, the color of the supernatant in the vial with  $\text{Fe}_3\text{O}_4\text{-C}$  nanoparticles slightly bleaches, suggesting its weak affinity to LiPSs. However, the color of the supernatant liquid containing  $\text{FeS}_2\text{-C}$  and  $\text{FeS-C}$  nanoparticles turns into colorless from yellow, indicating a strong adsorption capability to LiPSs in virtue of their sulfiphilic nature. Then, these supernatant solutions were centrifuged inside the glovebox and sealed in a cylindrical quartz tube for UV-*vis* measurement. As shown in Figure 4.10, for the  $\text{FeS-C}$  and  $\text{FeS}_2\text{-C}$  nanoparticles, the absorption intensities of their supernatant solutions are much lower than those of the pristine  $\text{Li}_2\text{S}_8$  solution and  $\text{Fe}_3\text{O}_4\text{-C}$  sample.

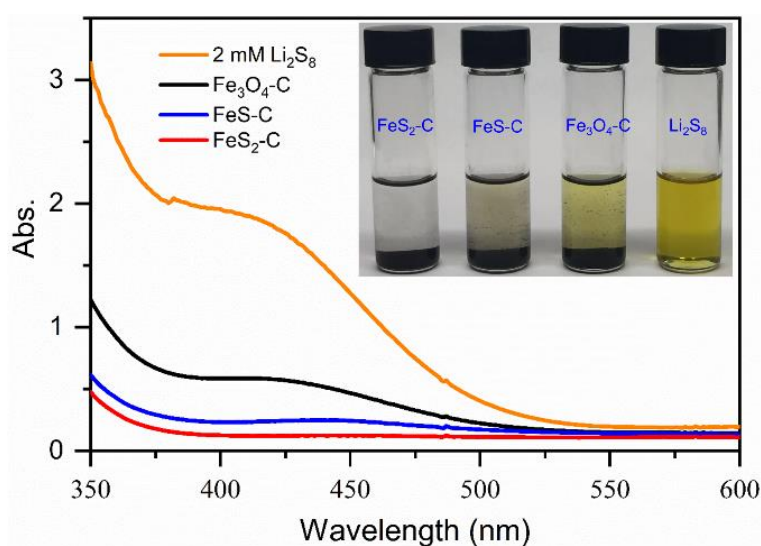


**Figure 4.10** UV-*vis* spectroscopy of 2 mM  $\text{Li}_2\text{S}_8$  in DOL/DME ( $v/v = 1/1$ ) and the solutions after the addition of  $\text{Fe}_3\text{O}_4\text{-C}$ ,  $\text{FeS-C}$ , and  $\text{FeS}_2\text{-C}$  for 2 h with the same surface area of  $2 \text{ m}^2$  based on their BET results. Inset: photographs of the vials with  $\text{Li}_2\text{S}_8$  solution and host materials.

### 4.2.2 Investigation of catalytic effects

According to the previous reports, the  $\text{Li}_2\text{S}$  precipitation and dissolution experiments have been conducted through potentiostatic discharge at 2.05 V and charge at 2.40 V to further elucidate the catalytic effects of the iron-based nanoparticles.<sup>[22, 173]</sup> For the  $\text{Li}_2\text{S}$  precipitation



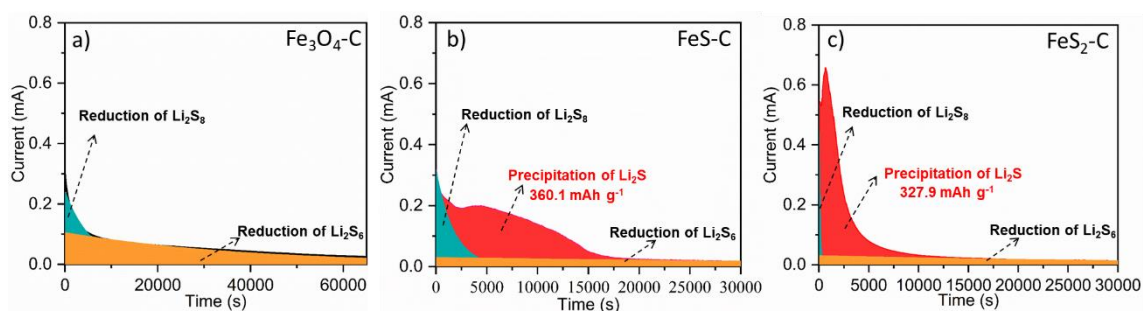


**Figure 4.11** The current-time curves of  $\text{Li}_2\text{S}_8$  solution potentiostatically discharged at 2.05 V (vs.  $\text{Li}/\text{Li}^+$ ) on different host materials:  $\text{Fe}_3\text{O}_4\text{-C}$  (a),  $\text{FeS-C}$  (b), and  $\text{FeS}_2\text{-C}$  (c).

and dissolution, the batteries were assembled by using  $\text{Li}_2\text{S}_8$  solution as the catholyte, host material as working electrode, and lithium metal as counter electrode. After the potentiostatic discharging process, the collected current-time profiles are shown in Figure 4.11. The sum of two exponential functions was first used as a fit for the background for the current versus time curve, the subtraction of which isolates the peaks. Specifically, the initial regime with monotonically decreasing current is the reduction curves for  $\text{Li}_2\text{S}_8$  in solution and the ending area with monotonically decreasing current is due to the reduction of  $\text{Li}_2\text{S}_6$  in the solution. The remaining peak in the profile is an indicator of the formation of  $\text{Li}_2\text{S}$ .<sup>[22]</sup> As demonstrated in Figure 4.11a, the  $\text{Li}_2\text{S}$  precipitation peak is absent in the current-time curve of the cell with the  $\text{Fe}_3\text{O}_4\text{-C}$  electrode, indicating no effective  $\text{Li}_2\text{S}$  precipitation on the cathode side. This phenomenon could be caused by the following two reasons: one is that because of the poor adsorption capability of the  $\text{Fe}_3\text{O}_4\text{-C}$  nanoparticles to LiPSs, a large portion of the LiPSs on the  $\text{Fe}_3\text{O}_4\text{-C}$  electrode side might have diffused to the anode side, leading to the loss of active materials; the other is that the nucleation process of  $\text{Li}_2\text{S}$  particles is sluggish on the  $\text{Fe}_3\text{O}_4\text{-C}$  electrode. Meanwhile, a well-defined peak is shown in the current-time curves of the cells with the  $\text{FeS-C}$  and  $\text{FeS}_2\text{-C}$  electrodes (Figure 4.11b and 11c), suggesting the deposition of  $\text{Li}_2\text{S}$  particles. According to Faraday's law, the precipitation capacities of  $\text{Li}_2\text{S}$  are  $360.1 \text{ mAh g}^{-1}$  and  $327.9 \text{ mAh g}^{-1}$  on the  $\text{FeS-C}$  and  $\text{FeS}_2\text{-C}$  electrodes, respectively. However, the sharp  $\text{Li}_2\text{S}$  peak of the  $\text{FeS}_2\text{-C}$  electrode appears much earlier than that of the  $\text{FeS-C}$  electrode, indicating a promoted  $\text{Li}_2\text{S}$  deposition process. In other words, the presence of  $\text{FeS}_2$  particles could improve the liquid-to-solid conversion process from LiPSs to  $\text{Li}_2\text{S}$ . For the  $\text{Li}_2\text{S}$  dissolution process, as shown in Figure 4.12a, a peak appeared in the current-time curve of the cell with the  $\text{FeS}_2\text{-C}$  electrode is much earlier and stronger than that of the  $\text{FeS-C}$  and  $\text{Fe}_3\text{O}_4\text{-C}$  electrode. This suggests that  $\text{FeS}_2$  particles significantly accelerate the solid-to-liquid conversion reaction from  $\text{Li}_2\text{S}$  to LiPSs. Besides, to investigate the effects of different iron- based compounds on

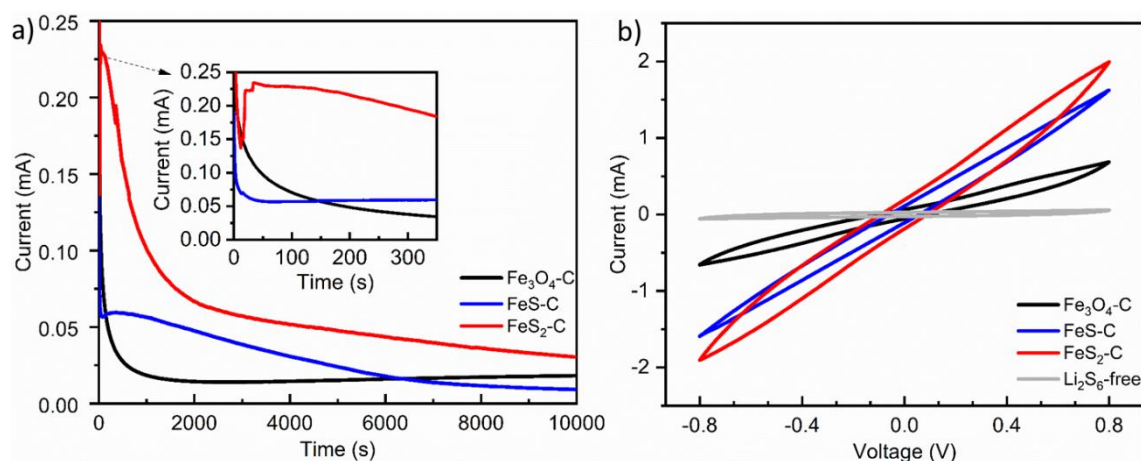


**Figure 4.12** (a) Potentiostatic charge curves of  $\text{Li}_2\text{S}_8$  solution at 2.4 V vs.  $\text{Li}/\text{Li}^+$  on different electrodes; (b) CV curves of symmetric cells with  $\text{Li}_2\text{S}_6$  solution as electrolyte scanned at  $10 \text{ mV s}^{-1}$  between -0.8 and 0.8 V.

the liquid-liquid transformation among different LiPSs, symmetric cells were assembled by using  $\text{Li}_2\text{S}_6$  solution as electrolyte and two identical electrodes both as working electrode and counter electrode. The CV curves of the symmetric cells with different electrodes ( $\text{Fe}_3\text{O}_4\text{-C}$ ,  $\text{FeS-C}$ , and  $\text{FeS}_2\text{-C}$ ) were measured at  $10 \text{ mV s}^{-1}$  in the range of -0.8 to 0.8 V. With the presence of yolk-shell particles in the symmetrical cells, there is an increased capacitive current compared to that without  $\text{Li}_2\text{S}_6$  solution (Figure 4.12b), implying the yolk-shell particles can accelerate the conversion reactions among different LiPS molecules.<sup>[153]</sup> Furthermore, iron sulfides exhibit a much higher current density than that of  $\text{Fe}_3\text{O}_4\text{-C}$  electrode, implying promoted redox kinetics between liquid-phase LiPSs. This is mainly contributed by the high electrical conductivities of iron sulfides and their strong adsorption abilities to LiPSs.

### 4.3 Electrochemical performance

To investigate the effect of the compositions of iron-based materials on the electrochemical performance of Li-S batteries, as-prepared composites ( $\text{Fe}_3\text{O}_4\text{-C/S}$ ,  $\text{FeS-C/S}$ , and  $\text{FeS}_2\text{-C/S}$ ) with the same sulfur content and areal loading (around  $1.1 \text{ mg cm}^{-2}$ ) have been used as cathode. The specific sulfur contents in these different sulfur/host composites are determined by the complete evaporation of sulfur under the thermogravimetry analysis (TGA) under nitrogen. As shown in Figure 4.13a, the calculated specific sulfur contents are 60.3, 58.5, and 61.7 wt.% for the composites  $\text{Fe}_3\text{O}_4\text{-C/S}$ ,  $\text{FeS-C/S}$ , and  $\text{FeS}_2\text{-C/S}$ , respectively. To investigate the specific electrochemical reactions inside a Li-S battery, Figure 4.13b shows the CV curves of the  $\text{Fe}_3\text{O}_4\text{-C/S}$ ,  $\text{FeS-C/S}$ , and  $\text{FeS}_2\text{-C/S}$ -based cathodes, which were scanned at  $0.1 \text{ mV s}^{-1}$  in the range of 1.7-2.8 V vs.  $\text{Li}/\text{Li}^+$ . The typical redox peaks are detected in all Li-S batteries with different host materials, which are ascribed to the multistep conversion reactions from sulfur to  $\text{Li}_2\text{S}$ .

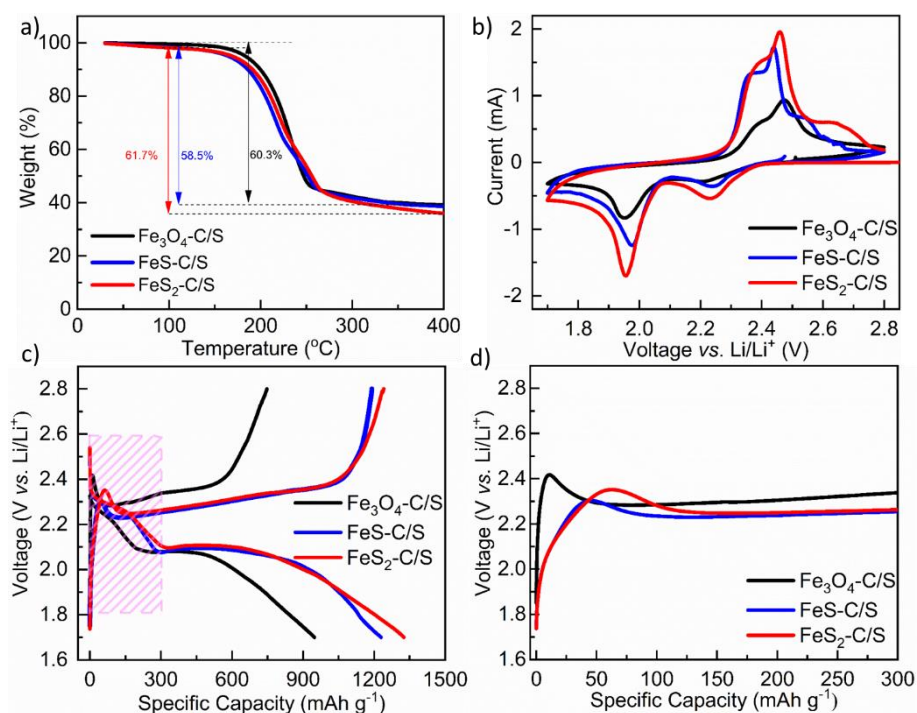


**Figure 4.13** (a) TGA curves of the composites ( $\text{Fe}_3\text{O}_4\text{-C/S}$ ,  $\text{FeS-C/S}$ , and  $\text{FeS}_2\text{-C/S}$ ) under argon; (b) CV curves scanned at  $0.1 \text{ mV s}^{-1}$ , galvanostatic charge/discharge profiles at  $0.1 \text{ C}$  (c), the enlarged rectangle region (d) of Li-S batteries with the  $\text{Fe}_3\text{O}_4\text{-C/S}$ ,  $\text{FeS-C/S}$ , and  $\text{FeS}_2\text{-C/S}$  as cathode in the range of  $1.7\text{-}2.8 \text{ V vs. Li/Li}^+$ .

Specifically, during the initial cathodic scan in the assembled coin cell with the  $\text{FeS-C/S}$  and  $\text{FeS}_2\text{-C/S}$  electrodes, the two main reduction peaks located at  $2.30$  and  $2.01 \text{ V}$  are corresponding to the conversion of sulfur to long-chain LiPSs and then lower-order sulfides ( $\text{Li}_2\text{S}_2$  and  $\text{Li}_2\text{S}$ ), respectively. In the subsequent anodic scan, the sharp oxidation peak at  $2.42 \text{ V}$  is due to the transformation of  $\text{Li}_2\text{S}$  to LiPSs and ultimately to elemental sulfur. In the second cycle, the two cathodic peaks shift to a higher potential value and the anodic peaks shift to a lower electrode potential, indicating a reduced polarization, which is believed to be the re-accommodation of sulfur after the initial activation cycle.<sup>[174]</sup> No additional peak from parasitic reactions on the host materials has been observed in the CV profiles. Compared with the iron sulfides, the  $\text{Fe}_3\text{O}_4\text{-C/S}$  cathode exhibits a much weaker peak at around  $1.95 \text{ V}$ , indicating the sluggish kinetics of the conversion reaction from long-chain LiPSs to  $\text{Li}_2\text{S}$ .<sup>[102]</sup>

The galvanostatic charge-discharge curves of the initial cycle at  $0.1 \text{ C}$  are shown in Figure 4.13c. All of them exhibit one typical charge plateau and two discharge plateaus of Li-S batteries. The two well-defined plateaus located at  $2.30$  and  $2.10 \text{ V}$  are assigned to the transformation of sulfur to long-chain LiPSs and their conversion to short-chain lithium sulfides, respectively, which is well consistent with the CV results. The initial specific discharge capacities of the  $\text{Fe}_3\text{O}_4\text{-C/S}$ ,  $\text{FeS-C/S}$ , and  $\text{FeS}_2\text{-C/S}$  electrodes at  $0.1 \text{ C}$  are  $948.1$ ,

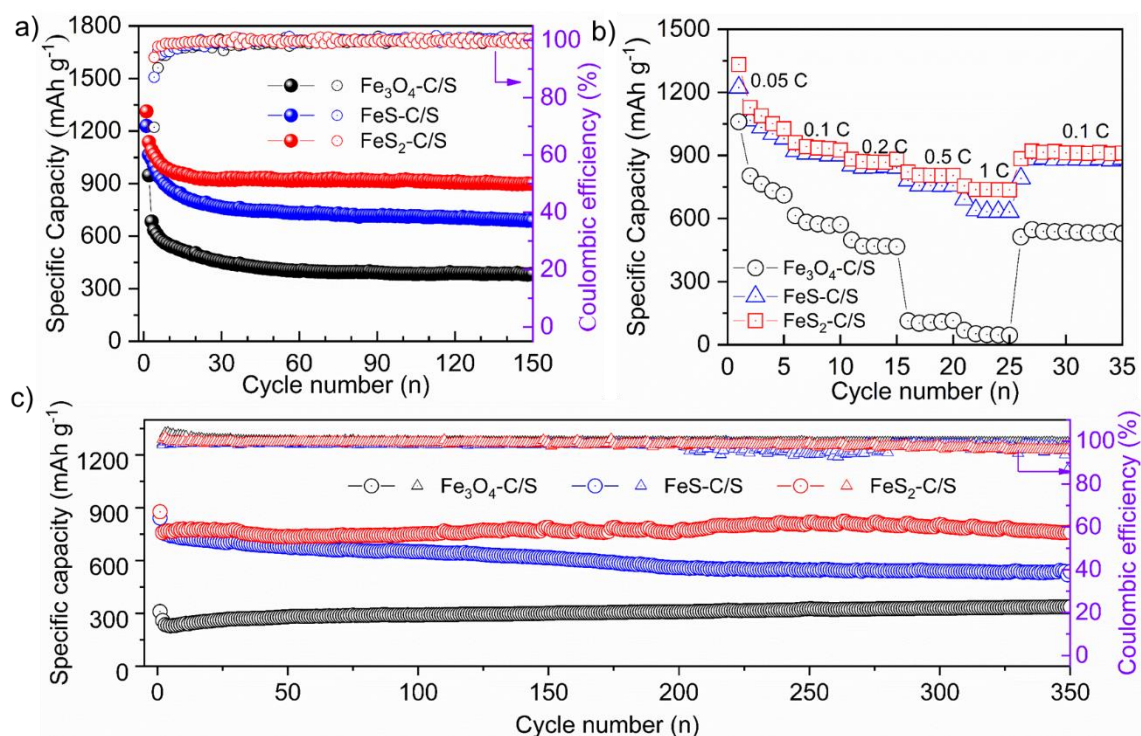


**Figure 4.14** Cycling performance at 0.2 C (a) and 0.5 C (c) and rate capability (b) of Li-S batteries with different cathodes (Fe<sub>3</sub>O<sub>4</sub>-C/S, FeS-C/S, and FeS<sub>2</sub>-C/S) in the range of 1.7-2.8 V vs. Li/Li<sup>+</sup> at room temperature.

1229.9, and 1326.4 mAh g<sup>-1</sup>, respectively. Compared to the typical voltage profile of Li-S batteries, the short discharge plateau (around 2.10 V) with a sloped tail in Figure 4.13c could be fundamentally related to the nanosizing effect of sulfur trapped within the yolk-shelled nanospindles. Increasing the surface area of sulfur results in the enhanced surface storage of Li-ions and suppressed phase transition.<sup>[175]</sup> Besides, the initial charge curves of the three electrodes inside the magenta rectangular area in Figure 4.13c are enlarged and plotted in Figure 4.13d. As demonstrated, the Fe<sub>3</sub>O<sub>4</sub>-C/S cathode shows the highest charging potential barrier to 2.42 V during the initial charging process, indicating the slowest redox kinetics of the conversion reaction from Li<sub>2</sub>S to S.<sup>[114]</sup> A lower voltage barrier is observed in iron sulfide-based cathodes due to their higher electrical conductivities than that of Fe<sub>3</sub>O<sub>4</sub>. In addition, the potential difference at half value of the initial charge capacity of the FeS-C/S and FeS<sub>2</sub>-C/S electrodes are 216.3 and 217.6 mV, respectively, which is much lower than that of the Fe<sub>3</sub>O<sub>4</sub>-C/S cathode (267.2 mV), suggesting a lowered polarization and a facilitated electrochemical redox reaction for the iron sulfide-based electrodes. The cycling performance of these cathodes has been compared and shown in Figure 4.14a. The battery with the FeS<sub>2</sub>-C/S cathode exhibits the highest specific capacity of 930 mAh g<sup>-1</sup> after 100 charge-discharge cycles, which is much higher than that of Fe<sub>3</sub>O<sub>4</sub>-C/S (385.8 mAh g<sup>-1</sup>) and FeS-C/S (718.1 mAh g<sup>-1</sup>) cathodes. The

excellent cycling stability of the FeS<sub>2</sub>-C/S electrode could originate from the better adsorption capability of FeS<sub>2</sub> to the LiPSs.

The rate capabilities of the Fe<sub>3</sub>O<sub>4</sub>-C/S, FeS-C/S, and FeS<sub>2</sub>-C/S electrodes are assessed at different discharge rates from 0.1 to 1 C, as demonstrated in Figure 4.14b. Both the FeS-C/S and FeS<sub>2</sub>-C/S electrodes show better rate capabilities than the Fe<sub>3</sub>O<sub>4</sub>-C/S cathode. Because of the poor confinement ability to LiPSs, the Fe<sub>3</sub>O<sub>4</sub>-C electrode exhibits a fast capacity decay at 0.05 C in the rate capability test, leading to a much lower retained capacity at 0.5 C than that achieved from galvanostatic cycling at the same rate (Figure 4.14b). To further interpret this phenomenon, electrochemical impedance spectroscopy (EIS) of Li-S batteries with different host materials has been investigated at open circuit voltage before cycling. As shown from the semicircles in the Nyquist plots (Figure 4.15), the Fe<sub>3</sub>O<sub>4</sub>-C/S cathode has a high polarization and charge transfer resistance ( $R_{ct}$ ), compared to the FeS-C/S and FeS<sub>2</sub>-C/S electrodes, which is responsible for its poor rate capability. The  $R_{ct}$  of the FeS-C/S cathode is, though slightly lower than, comparable to that of the FeS<sub>2</sub>-C/S cathode. The FeS<sub>2</sub>-based electrode possesses better rate capability than that of the FeS-based electrode because the FeS<sub>2</sub>-C nanoparticles have stronger catalytic effect in accelerating the nucleation process of Li<sub>2</sub>S. Besides, the FeS<sub>2</sub>-C nanoparticles show a better adsorption capability to LiPSs than that of FeS-C, leading to less sulfur loss on the cathode side and hence improved capacity.

Furthermore, the long-term cycling performance of batteries with different electrodes at 0.5 C is presented in Figure 4.13c. Both iron sulfide-based cathodes achieve much higher specific discharge capacity than that of Fe<sub>3</sub>O<sub>4</sub>. To be specific, the FeS<sub>2</sub>-C/S and FeS-C/S electrodes obtain initial specific discharge capacities of 877.6 mAh g<sup>-1</sup> and 841.9 mAh g<sup>-1</sup>, respectively, while the Fe<sub>3</sub>O<sub>4</sub>-C/S electrode only delivers an initial specific discharge capacity of 311 mAh g<sup>-1</sup>. The slight capacity increase during cycling at 0.5 C, especially for the Fe<sub>3</sub>O<sub>4</sub>-C/S electrode, is due to the activation process induced by sulfur redistribution.<sup>[176]</sup> The FeS-C/S electrode undergoes a gradual capacity fading along cycling, while the specific capacity of the FeS<sub>2</sub>-C/S electrode appears rather stable. After 350 cycles, the specific discharge capacity of the FeS-C/S electrode is only 537.8 mAh g<sup>-1</sup> with a retention ratio of 63.9%, while the FeS<sub>2</sub>-C/S electrode delivers a specific discharge capacity of 761.2 mAh g<sup>-1</sup> with a retention ratio of 86.7%. This demonstrates that a strong adsorption ability of the cathode material to LiPSs could play a crucial role in achieving long-term cycling stability.



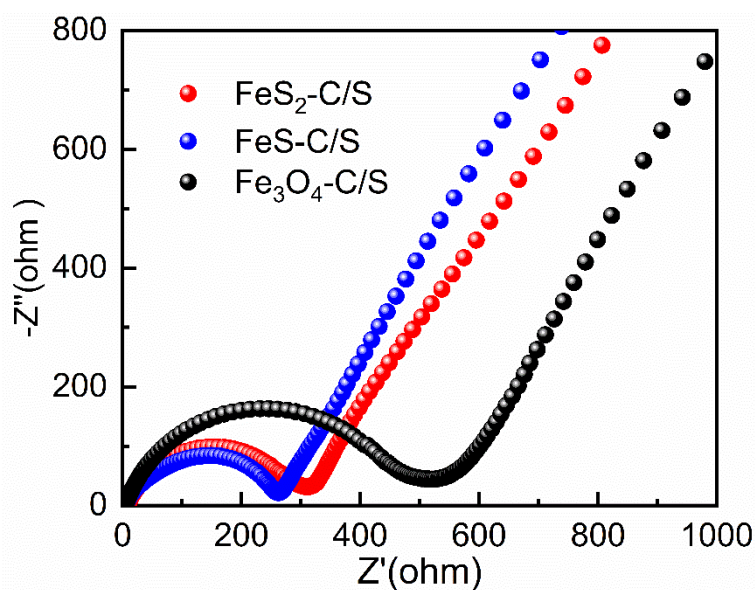


**Figure 4.15** Electrochemical impedance spectroscopy of Li-S batteries with the  $\text{Fe}_3\text{O}_4\text{-C/S}$ ,  $\text{FeS-C/S}$ , and  $\text{FeS}_2\text{-C/S}$  as cathode before cycling.

In this chapter, three iron oxide/sulfide-based sulfur host materials with the same yolk-shelled morphology have been successfully synthesized via a simple colloidal route using  $\text{FeOOH}$  nanoparticles as template. The same morphology allows for the systematic investigation of the effect of chemical composition on the electrochemical performance of Li-S batteries. The results show that the  $\text{FeS}_x$ -based cathodes exhibit higher specific capacity and better rate capability than  $\text{Fe}_3\text{O}_4$  since they possess not only stronger chemical adsorption ability to LiPSs but also higher conductivity. Moreover, it is found that the  $\text{FeS}_2$  nanoparticles could significantly accelerate the conversion of LiPSs to  $\text{Li}_2\text{S}$ . Benefiting from the synergistic chemical adsorption and catalytic effect of  $\text{FeS}_2$  as well as the physical confinement of the carbon shell to suppress the shuttle effects, the  $\text{FeS}_2\text{-C/S}$  electrode delivers an initial specific discharge capacity of  $877.6 \text{ mAh g}^{-1}$  at  $0.5 \text{ C}$  and a retention ratio of 86.7% after 350 cycles. This work provides the insights about the composition effects of sulfur host materials on the electrochemical performance of Li-S batteries other than nanostructure, which sheds light on the rational design of efficient cathode materials.

## 5. Poly(ionic liquid) Nanovesicle-Templated Carbon Nanocapsules Functionalized with Uniform Iron Nitride Nanoparticles as Catalytic Sulfur Hosts for Li-S Batteries\*

Significant progress has been made via impregnating sulfur into a vast variety of types of hollow as well as porous carbon-based nanomaterials with different morphologies, such as nanospheres,<sup>[177]</sup> nanocapsules,<sup>[178]</sup> nanotubes,<sup>[179]</sup> and nanocages.<sup>[180]</sup> However, without any modification, it is challenging for nanostructured carbon-based materials to effectively catalyze the multiple-step conversion reactions from LiPSs to Li<sub>2</sub>S. Therefore, many efforts have been made to synthesize electrocatalytic host materials with the confinement of LiPSs on-site, since the full utilization of sulfur can be realized only when the confinement and catalytic conversion of LiPSs are integrated simultaneously.<sup>[21, 114]</sup>

In chapters 3 and 4, it is demonstrated that both the mesoporous structure and composition of the host materials can play a crucial role in improving the electrochemical performance of Li-S batteries. Considering the insulating character of sulfur and polar LiPSs, the carbon/metal composites with both rationally designed nanostructure and deliberately selected composition are needed and regarded as an all-in-one sulfur host to offer physical confinement, conductive matrix, and chemical adsorption.<sup>[44, 117]</sup> To strengthen the interaction between the host materials and LiPSs guest, a wide range of metal compounds have been examined extensively as the LiPSs mediator, including metal oxides,<sup>[83, 181]</sup> nitrides,<sup>[176b, 182]</sup> sulfides,<sup>[114]</sup> carbides,<sup>[183]</sup> phosphides,<sup>[163, 176a]</sup> and selenides.<sup>[184]</sup> Among them, transition metal nitrides (TMNs) are of particular interest as electrocatalysts for the conversion of polysulfides because of their merits such as superior electrical conductivity, sufficient chemical stability, and polar metal-nitrogen (M-N) bonds.<sup>[118, 185]</sup> Some TMNs have been previously investigated as sulfur host materials in Li-S batteries, such as TiN,<sup>[186]</sup> VN,<sup>[182, 187]</sup> InN,<sup>[188]</sup> Co<sub>4</sub>N,<sup>[189]</sup> MoN,<sup>[157, 190]</sup> and WN.<sup>[191]</sup> For instance, Cui *et al.* reported a mesoporous TiN as sulfur host materials, in which the TiN-S composite cathode delivered a capacity of over 644 mAh g<sup>-1</sup> after 500 cycles at 0.5 C.<sup>[186b]</sup> Sun *et al.* developed a mesoporous VN nanorod and graphene composite, exhibiting lower polarization and faster redox reaction kinetics than that of the reduced graphene oxide cathode.<sup>[182]</sup> Unfortunately, those metal-based nitride nanoparticles often suffer from high

\*This chapter is adapted with permission from my original work: Dongjiu Xie, Yaolin Xu, Yonglei Wang, Xuefeng Pan, Eneli Härk, Zdravko Kočovski, Alberto Eljarrat, Johannes Müller, Christoph T Koch, Jiayin Yuan, Yan Lu, Poly(ionic liquid) Nanovesicle-Templated Carbon Nanocapsules Functionalized with Uniform Iron Nitride Nanoparticles as Catalytic Sulfur Host for Li-S Batteries, *ACS Nano*, **2022**, 16, 7, 10554-10565. Published by American Chemical Society in Open access.

cost, low specific surface area, low utilization of catalytic particles, and lack of voids or space to accommodate a sufficiently large amount of sulfur.

Consequently, earth-abundant and environmentally friendly iron-based nitrides have moved into the frontline of the electrochemical field due to their high electronic conductivity and catalytic activity. Sun *et al.* designed yolk-shelled Fe<sub>2</sub>N-carbon nanoboxes as sulfur host materials for Li-S batteries, and the polar iron nitride (Fe<sub>2</sub>N) core could provide strong chemical bonding and effective catalytic activity for polysulfides.<sup>[135a]</sup> Later on, Zhang *et al.* reported that phosphorus doping could boost the catalytic activity of the iron nitride (Fe<sub>4</sub>N) nanoparticles.<sup>[192]</sup> However, the particle size of these iron nitrides was too large, i.e., in the range of 30-100 nm, thus suppressing the better utilization efficiency of the catalyst. Ideally, well-dispersed sub-10 nm metal-based nanoparticles could immediately expose at least 10 times more active sites for boosting the catalytic, electronic, and kinetic performance.<sup>[154, 193]</sup> However, when synthesized from nanosized precursor particles, they typically tend to agglomerate and grow adversely into much larger ones during calcination.<sup>[193]</sup> Usually, time-consuming and complicated preparative routes are required, e.g., template-assisted selective etching fabrication or post-loading methods.

To address this challenge, polymer-metal ion complexes as the precursor to ultrafine metal nanoparticles *via* one-step calcination have been actively attempted, since the parallel polymer-to-carbon conversion could *in situ* produce a carbonaceous matrix to impede or slow down the growth kinetics of these nanoparticles.<sup>[165c, 193]</sup> In this regard, imidazolium-based poly(ionic liquid)s (PILs) with N-rich ionic liquids as repeating units have been of great interest, not only because they can form N-doped porous carbon fibers or membranes with controllable N content and conductivity but also the possible coordination with the metallic species *via* the nitrogen atoms during pyrolysis.<sup>[194]</sup> Equally important, the introduction of metal ions into PILs can be fairly easy *via* the ion-complexation or ion-exchange method. Unsurprisingly, imidazolium-based PILs could produce nanostructured carbon materials embedded with metal-containing species.<sup>[195]</sup> Chen *et al.* reported carbon nanosheets with small cobalt nanoparticles by using PIL-cobaltinitrite complex/graphene oxide as precursors, which were then used to modify the separator membrane for the Li-S battery.<sup>[195b]</sup> Nevertheless, due to a high compression and fluidity of ionic liquid species, PIL-derived carbon materials face challenges in maintaining PIL's morphology on the nanoscale. The state-of-the-art methods rely much on the time-consuming hard template (silica) coating or silica nanocasting process.<sup>[141d, 196]</sup>



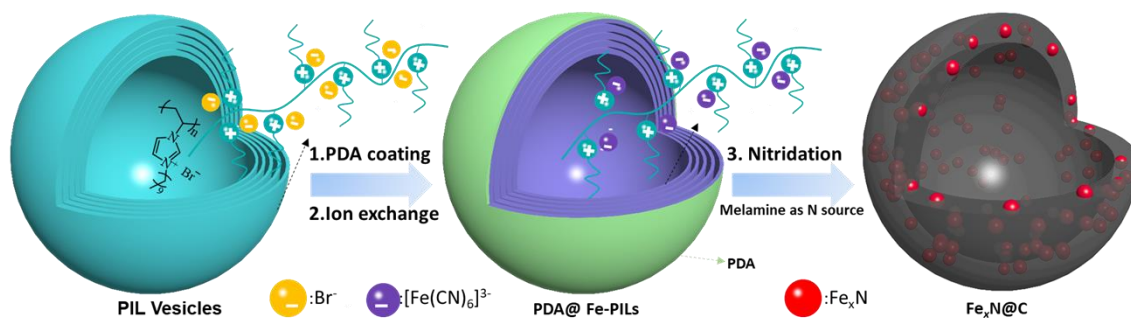


**Figure 5.1** Schematic illustration of the synthetic route to the  $\text{Fe}_x\text{N}@C$  nanocapsules.

In this chapter, with PILs nanovesicles as template, a facile synthetic route towards carbon composite nanocapsules, which are embedded with ultrafine iron nitride nanoparticles (3-5 nm in size), has been developed. Assisted by a protective polydopamine (PDA) coating in combination with an ion-exchange process to introduce the iron species, the hollow spherical morphology of PILs nanovesicles has been preserved along with pyrolysis, and successfully transferred into the functional composite product despite an inevitable dimensional shrinkage due to a large weight loss. The designed nanocomposite has been applied as an efficient sulfur host material for Li-S batteries with drastically improved electrochemical performance. The catalytic active and conductive iron nitride nanoparticles have abundant active sites to assist LiPS conversion and  $\text{Li}_2\text{S}$  nucleation during cycling. Besides, the synthetic route in this chapter could be applied to fabricate other metal compounds (nitrides, sulfides, and phosphides) with similar nanostructures for a broader range of electrochemical applications, *i.e.*, fuel cells and supercapacitors.

## 5.1 Synthesis and characterization of $\text{Fe}_x\text{N}@C$ nanocapsules

### 5.1.1 Synthesis and characterization of PILs vesicle template

The scheme in Figure 5.1 shows the synthetic route to the target composite carbon nanocapsules embedded with iron nitride nanoparticles. Firstly, poly(ionic liquid)s (PILs) nanovesicles have been synthesized by one-step radical homopolymerization of the monomer 3-*n*-decyl-1 vinylimidazolium bromide (ILM-10) in water at 75 °C using 2,2'-Azobis[2-methyl-N-(2-hydroxyethyl)propionamide] (VA-86) as initiator under nitrogen atmosphere. After purification by dialysis in water, a stable PIL colloidal dispersion was collected with a solid concentration of 10 g L<sup>-1</sup> (Figure 5.2a). Cryo-electron microscopy (cryo-EM) was used to access the true morphology of these soft PILs nanoparticles in their dispersed state. As demonstrated in Figure 5.2b, the PIL nanoparticles show a characteristic vesicular shape with

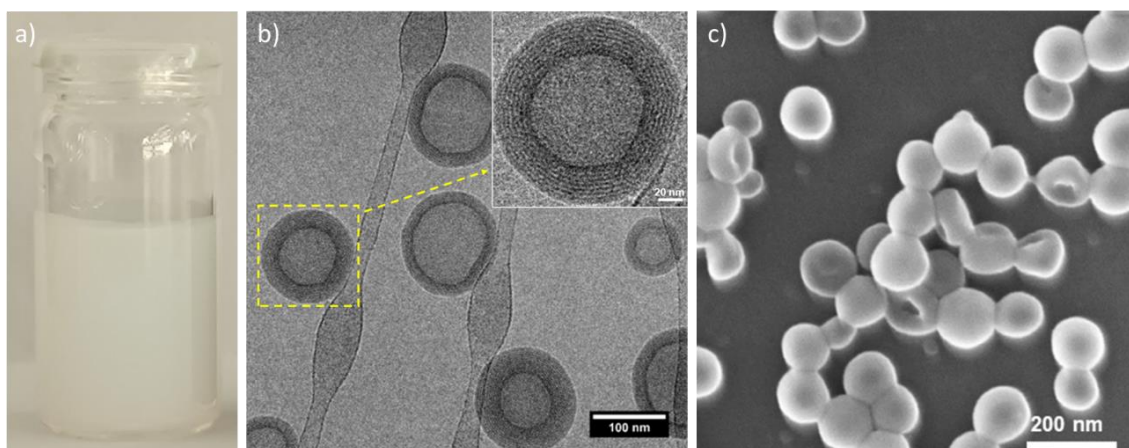


**Figure 5.2** (a) Photo of the dispersion of the PILs vesicles in water. (b) Cryo-TEM image and (c) SEM image of the PILs vesicles.

an outer diameter of  $100 \pm 10$  nm. Interestingly, several repeated lamellas are found in the wall of a single PIL nanovesicle enlarged in the inset of Figure 5.2b. Owing to a higher electron density of the  $\text{Br}^-$  ions than that of the alkyl chains, the hydrophobic alkyl chains and the charged backbones result in the alternating light and dark nanodomains, respectively.<sup>[197]</sup> The distribution of the  $\text{Br}^-$  ions (the dark lamellae) across the entire wall is beneficial for their ion exchange with ferricyanide anions. Besides, Figure 5.2c shows the SEM image of the PILs nanoparticles. It is found that after the drying process, the morphology of some PILs nanovesicles partially deviated from their original spherical shape to a bowl-like structure. According to the previous report, after the loss of the structural water component, the softness of the PILs outer layer could not withstand the capillary force exerted on the vesicles, leading to the deformation of the certain vesicles.<sup>[198]</sup>

### 5.1.2 Synthesis and characterization of $\text{Fe}_x\text{N}@C$ and N-Carbon nanocapsules

A thin protective layer of PDA was coated onto the surface of the PIL nanovesicles to avoid ionic crosslinking of the PILs nanovesicles by ferricyanide anions during the ion-exchange process. Besides, the presence of the PDA layer could help preserve the original morphology of PILs during calcination since the fluidic fragmentation intermediates of PILs during carbonization may cause the amalgamation of individual PILs nanovesicles together to forfeit their nanoscopic morphology.<sup>[199]</sup> As shown in the inset of Figure 5.3a, the color of the PDA@PILs dispersion turned dark after the deposition of a PDA layer in a Tris buffer (pH = 8.5) solution. To evaluate the effects of PDA coating on the structure of PILs particles, the cryo-TEM image of the PDA@PILs particles was collected and shown in Figure 5.3a. It is found that the multilamellar pattern in the wall of the PDA@PILs nanovesicle remains the same as

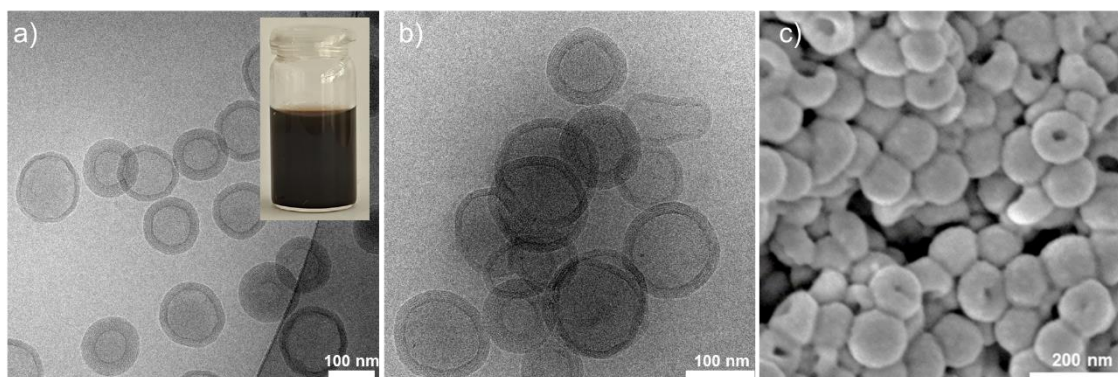


**Figure 5.3** (a) Cryo-TEM image of the PDA@PILs (Inset: the photo of the PDA@PILs dispersion in water). (b) Cryo-TEM image and (c) SEM image of the PDA@Fe-PILs particles.

pristine ones after the PDA coating process. Due to the dynamic feature of ionic bonds, ion exchange has been widely used to introduce alien metal atoms into the PILs matrix for further processing or applications.<sup>[195b, c]</sup> Here, as a typical anion of iron element, ferricyanide ions were applied to exchange with  $\text{Br}^-$  ions in the polyimidazolium-based vesicles. The elemental mapping images (Figure 5.4) of the PDA@PILs samples before and after the anion exchange process were collected by energy-dispersive X-ray spectroscopy (EDX). The PDA@Fe-PILs sample has a homogenous distribution of iron atoms with a low Br atom content, while the PDA@PILs sample shows a high Br atom content, indicating the successful introduction of ferricyanide ions into the PILs particles. As depicted in the cryo-TEM image (Figure 5.3b), PDA@Fe-PILs particles hold the same vesicle structure as PILs particles after anion exchange without noticeable change. In Figure 5.3c, spherical and bowl-like particles are found in the SEM image of the PDA@Fe-PILs sample, which is similar to the PILs particles. These results prove that the PDA coating and following anion-exchange process have little effect on the nanostructure of the PILs vesicles.

To obtain iron nitride, melamine powder was used as nitrogen source since it can easily produce ammonia during heat treatment. Initially, the effects of the nitridation temperature on the crystal phase of the PDA@Fe-PILs sample have been studied. The XRD patterns of the PDA@Fe-PILs sample after nitridation at different temperatures are shown in Figure 5.5a. It is revealed that the pure hexagonal phase of iron nitride ( $\text{Fe}_3\text{N}_{1.33}$ , PDF#01-070-7407) can be only achieved in the temperature range of 500-600 °C. With increasing the calcination temperature to 700 °C, the metal iron (Fe, PDF#06-0696) phase is appeared. Moreover, the TEM images in Figure 5.5b and 5c reveal that the iron nitride obtained at 600 °C exhibits a larger particle size of 20-70 nm than that at 500 °C. As shown in Figures 5.5d and 5e, for the PDA@Fe-PILs sample calcinated at 500 °C, the visible carbon nanocapsules with a diameter of ~50 nm and a

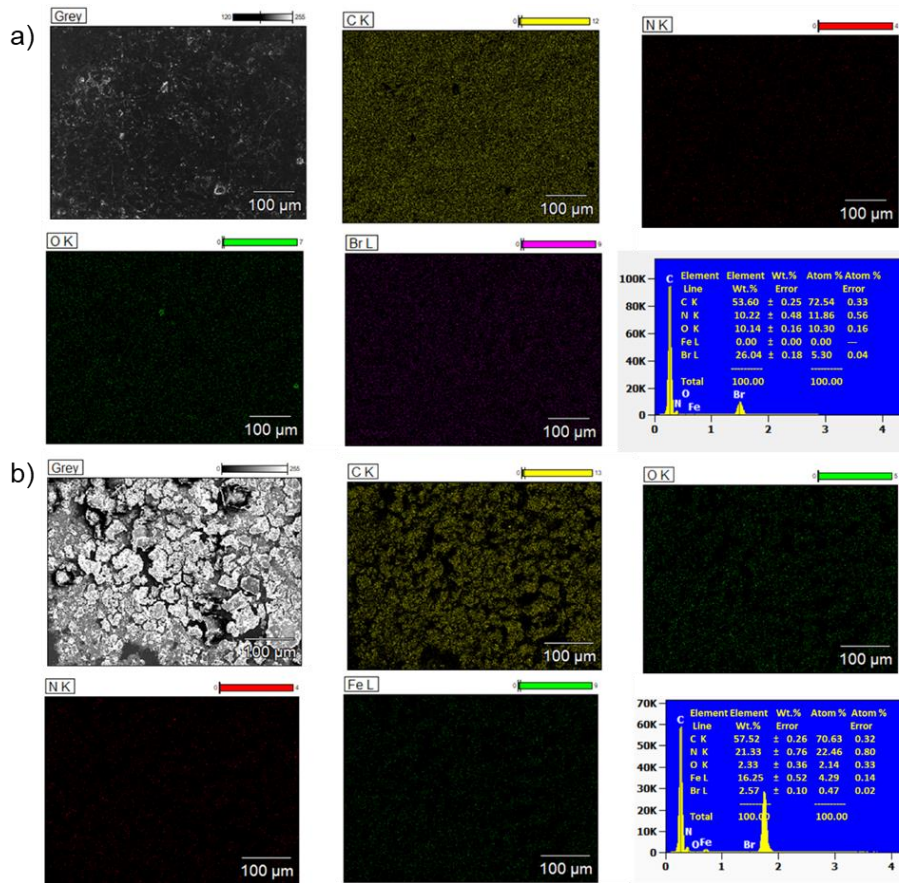


**Figure 5.4** EDX analysis with scanning electron microscope (SEM) images and corresponding element mappings of the PDA@PILs nanovesicles (a) and the PDA@Fe-PILs nanovesicles (b), respectively.

thickness of 15-25 nm are obtained, which inherent from the PILs vesicles. The large void space inside carbon nanocapsules is beneficial for a high sulfur loading and physical confinement of polysulfides. Moreover, fine iron nitride nanoparticles of 3-5 nm in size are observed and they are well-dispersed all over the hollow carbon shell. With a high specific surface area, metal-based compounds with fine particle size could promote their catalytic effects or interactions with LiPSs. The above results suggest that 500 °C is the optimal nitridation temperature for the PDA@Fe-PILs sample. From here on, only the iron nitride obtained at 500 °C was named as  $\text{Fe}_x\text{N}@C$  for further characterization and used as sulfur host for Li-S batteries in this chapter.

Furthermore, the HR-TEM and elemental mapping images of  $\text{Fe}_x\text{N}@C$  particles have been taken to investigate its crystal structure and distribution of different elements. In Figure 5.5f, the lattice fringes of the iron nitride particles are observed in the high-resolution TEM image. The interplanar distance is measured to be 0.31 nm, which is corresponding to the (101) facet of  $\text{Fe}_3\text{N}_{1.33}$ .<sup>[200]</sup> In addition, a STEM image of the  $\text{Fe}_x\text{N}@C$  sample with the corresponding EELS elemental mapping of Fe, C, and N elements is demonstrated in Figure 5.6a and 6b. The



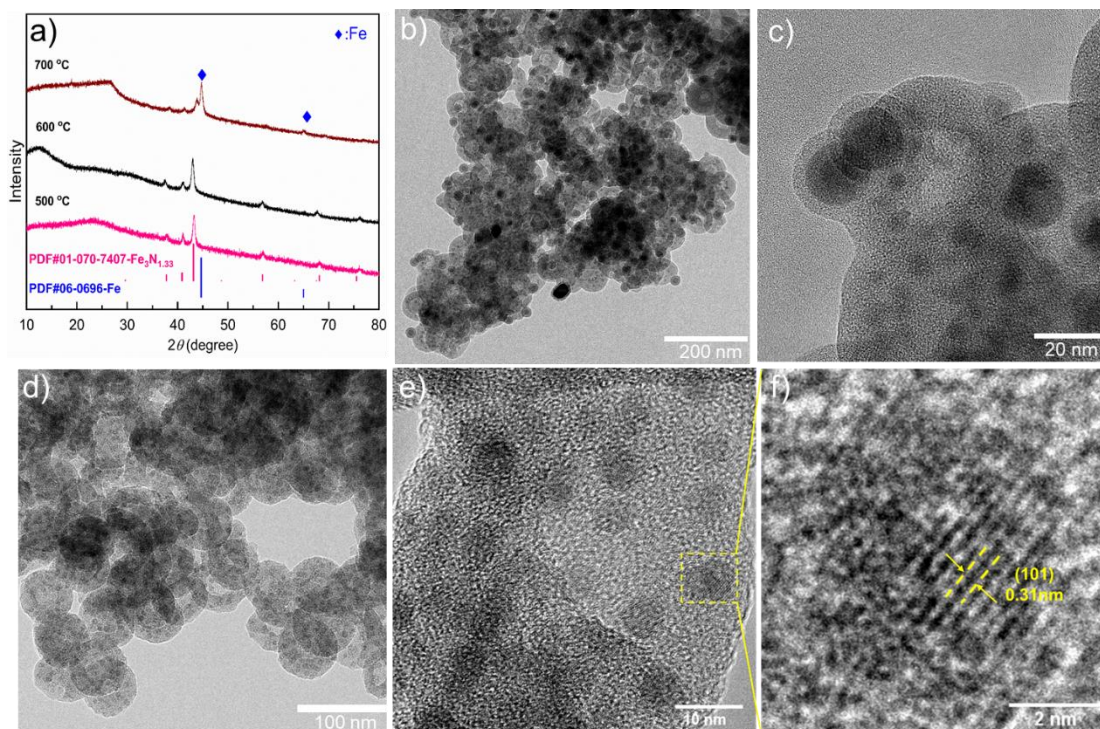


**Figure 5.5** (a) XRD patterns of the PDA@Fe-PILs after calcination at different temperatures (500, 600, and 700 °C) along with melamine under argon atmosphere; TEM images of the PDA@Fe-PILs after calcination at 600 °C (b and c) and 500 °C (d and e) with melamine as nitrogen source; (f) HR-TEM image of the  $\text{Fe}_x\text{N}@C$  nanocapsules.

existence of N element is originated from the polydopamine and imidazole-based PILs. Interestingly, it is found that the N-content near the carbon nanocapsule inner layer is higher than that of the outer layer. The reason for this observation is that the imidazole-based PILs as carbon source could preserve a higher N content than that of polydopamine under a mild carbonization condition. The presence of N atoms in carbon materials could increase their polarity, facilitating the interactions with polar LiPS molecules. SEM image of the  $\text{Fe}_x\text{N}@C$  particles is shown in Figure 5.6c. The particle size of carbon nanocapsules is much smaller than that of the soft template PILs vesicles due to the loss of the long alkyl chains during calcination. Additionally, the  $\text{Fe}_x\text{N}@C$  particles maintain the same morphologies as the dried PILs vesicles, i.e., spherical and bowl-like particles.

To measure the specific surface area and pore size distribution of  $\text{Fe}_x\text{N}@C$ ,  $\text{N}_2$  adsorption/desorption measurement at 77 K has been conducted. A characteristic hysteresis loop can be observed in Figure 5.7a, which is a typical type-III isotherm. The corresponding pore size distribution diagram (the inset of Figure 5.7a) shows that  $\text{Fe}_x\text{N}@C$  nanocapsules possess multiple mesopores. Their diameters are centered at 5, 17, and 22 nm, respectively. The 5 nm mesopores may be related to the pore inside the carbon shell, while the larger mesopores of 17 and 22 nm may stem from the hollow voids inside the carbon nanocapsules.

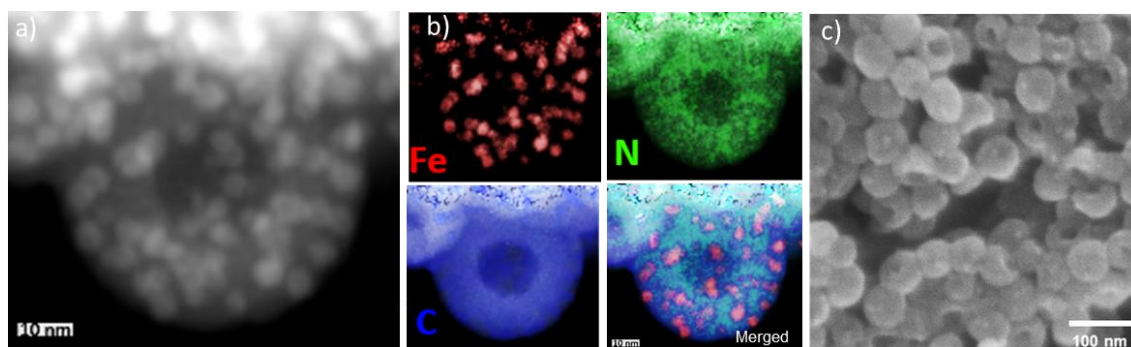


**Figure 5.6** (a) STEM image of the  $\text{Fe}_x\text{N}@C$  nanocapsules with (b) corresponding EELS mapping images of different elements (Fe, N, and C); (c) SEM image of the  $\text{Fe}_x\text{N}@C$  particles.

The existence of mesopores in the  $\text{Fe}_x\text{N}@C$  sample is favorable for sulfur loading and their surface can also serve as the physical adsorption reservoir for LiPSs, mitigating the shuttling effect. Based on the Brunauer-Emmett-Teller (BET) equation, the specific surface area of the  $\text{Fe}_x\text{N}@C$  sample is  $120 \text{ m}^2 \text{ g}^{-1}$ . To determine the iron content inside the composite  $\text{Fe}_x\text{N}@C$  sample, its TGA curve has been measured under synthetic air atmosphere. As shown in Figure 5.7b, the minor mass loss in the range of 50-150 °C is believed to be the evaporation of the adsorbed water and the mass increase around 300 °C is ascribed to the oxidation of iron nitrides. After the full oxidation of carbon above 500 °C, the mass of the  $\text{Fe}_2\text{O}_3$  residual is 32.4 wt.%. According to this result, the calculated iron content inside the  $\text{Fe}_x\text{N}@C$  nanocapsules is 22.7 wt.%.

X-ray photoelectron spectroscopy (XPS) has been applied to extract structure information of the surface composition and valence state of iron and nitrogen in the  $\text{Fe}_x\text{N}@C$  nanocapsules. The high-resolution Fe 2p and N 1s spectra of the  $\text{Fe}_x\text{N}@C$  sample are displayed in Figures 5.7c and 7d, respectively. For the Fe 2p spectrum, two peaks at 723.4 and 710.3 eV are found and assigned to Fe 2p<sub>1/2</sub> and Fe 2p<sub>3/2</sub> of  $\text{Fe}^{2+}$  states, respectively; the Fe 2p<sub>1/2</sub> and Fe 2p<sub>3/2</sub> of  $\text{Fe}^{3+}$  are found located at 724.8 eV and 711.8 eV, respectively.<sup>[152]</sup> In addition, the peaks at 713.4 and 726.5 eV are satellite peaks. The co-existence of  $\text{Fe}^{3+}/\text{Fe}^{2+}$  is due to the surface oxidation of the iron nitride nanoparticles when they are exposed to air. Nitrogen doping into the carbon material can provide multiple favorable effects here, *i.e.*, to enhance the electrical conductivity and offer more active sites for the chemical confinement of LiPSs.<sup>[151]</sup> The N1s spectrum in Figure 5.7d can be deconvoluted into four peaks at 398.1, 400.2, 401.1, and 403.2 eV, corresponding to the pyridinic, pyrrolic, graphitic, and oxidized N species, respectively.<sup>[150]</sup> It is worth noting that the peak of the pyridinic N includes the contribution of the Fe-N since the binding energy of N-Fe is close to that of the pyridinic N.<sup>[201]</sup>

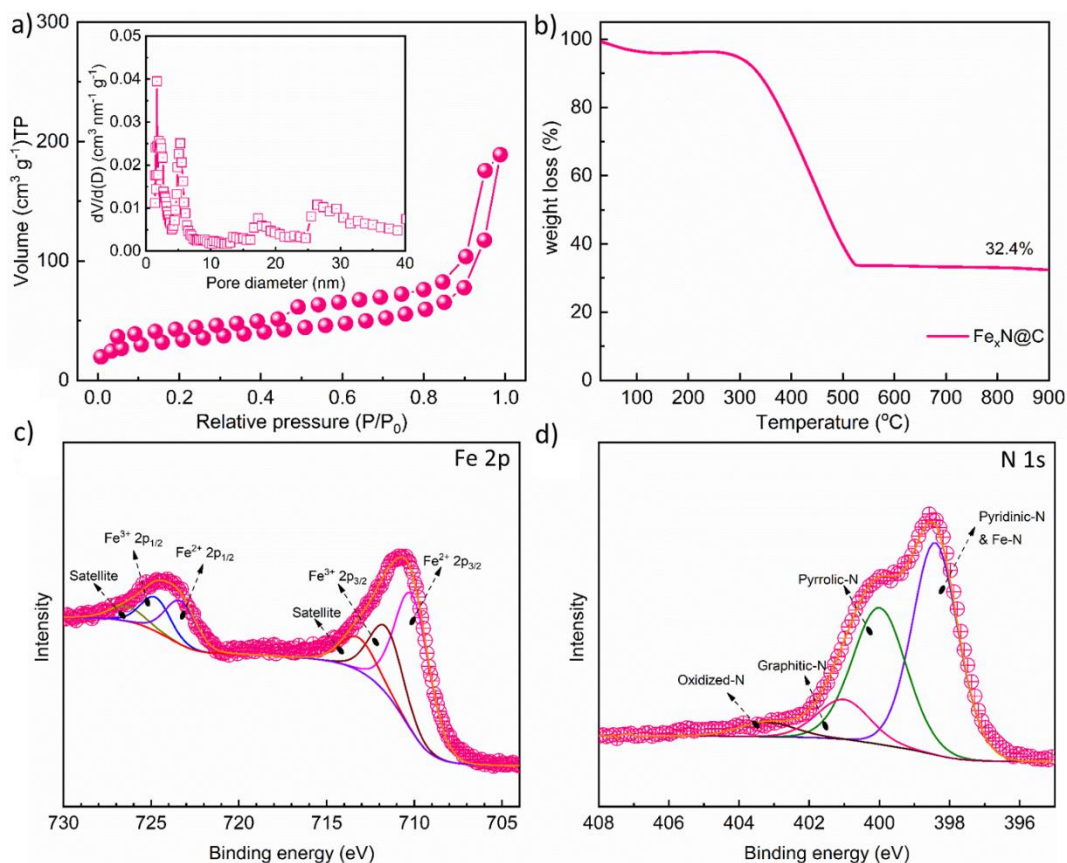


**Figure 5.7** (a) Nitrogen adsorption-desorption isotherms of the sample  $\text{Fe}_x\text{N}@C$  with the inset corresponding to the pore size distribution plot; (b) TGA curve of the sample  $\text{Fe}_x\text{N}@C$  in the synthetic air; XPS spectra of (c) Fe 2p and (d) N 1s of the sample  $\text{Fe}_x\text{N}@C$ .

Besides, the effects of PDA coating, ferricyanide anions, and melamine on the morphology of the PILs nanovesicles-derived carbon nanocapsules calcinated at  $500^\circ\text{C}$  have been also investigated systematically. Without a PDA coating, as shown in Figure 5.8a, the PILs vesicles are cross-linked with each other after the anion-exchange process because the ferricyanide anions with a charge of 3- could work as a cross-linker. After the heat treatment of anion-exchanged PILs particles at  $500^\circ\text{C}$ , only irregularly shaped bulk carbon embedded with metal-containing nanoparticles is obtained due to the presence of ferricyanide (Figure 5.8b). Similarly, the carbon bulk in Figure 5.8c is collected when calcinating the iron-free PDA@PILs nanovesicles under the same carbonization condition. Interestingly, the nanocapsule shape of carbon can be nicely obtained after the calcination of the PDA@Fe-PILs sample without the presence of melamine (Figure 5.8d). These results indicate that the co-existence of PDA and ferricyanide anions could hold the vesicular shape of PILs particles, preventing their convergence in a softened state at elevated temperatures. However, only a few large iron-based particles in size of 7-20 nm are embedded in carbon nanocapsules without the presence of melamine as a nitrogen source, suggesting that melamine is important for achieving the well-

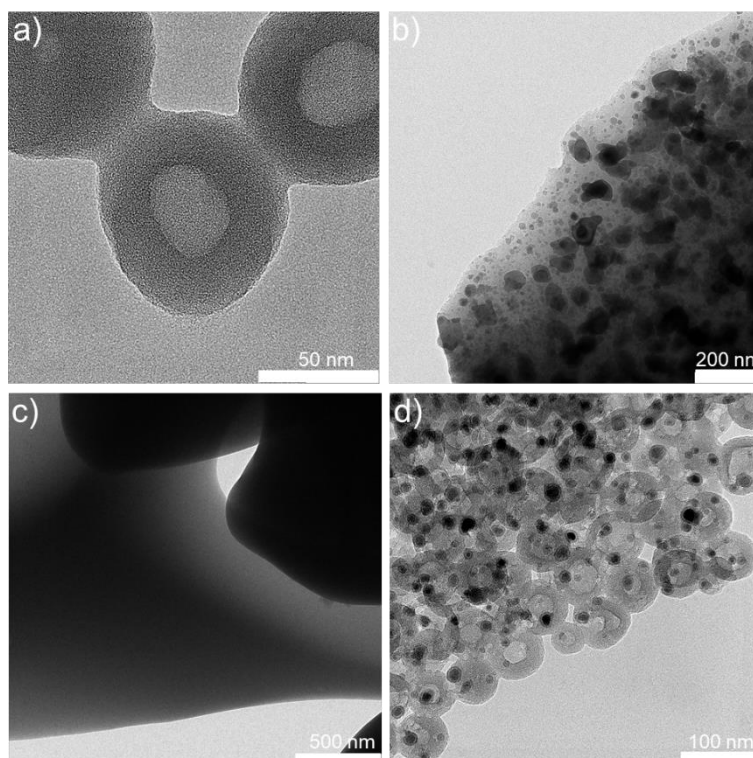


**Figure 5.8** TEM images of (a) the PILs particles after anion-exchange with ferricyanide, (b) anion-exchanged PILs sample after calcination at 500 °C, (c) PDA@PILs particle after calcination, which is without the anion-exchange process, and (d) PDA@Fe-PILs after calcination without melamine as nitrogen sources.

distributed iron nitride nanoparticles inside the carbon nanocapsules. According to a previous report, the good dispersity of iron nitride nanoparticles stems from the N species in the melamine and imidazole-ring that act as anchoring site points to the metallic species.<sup>[165c]</sup> Consequently, using the PILs vesicles as template, carbon nanocapsules embedded with small iron nitride particles can be synthesized with the co-existence of PDA, ferricyanide ions, and melamine as nitrogen source.

As a comparison sample, the metal-free carbon nanocapsules have been obtained by etching the iron nitride particles out of the composite  $\text{Fe}_x\text{N}@C$  sample via acid treatment. Figure 5.9a shows the TEM image of the carbon nanocapsules (N-Carbon), indicating that iron nitride particles are removed after the repeated acid etching process. Based on the TGA result of the N-Carbon sample (Figure 5.9b), only a tiny amount of iron remains in the carbon nanocapsules. Owing to the removal of iron nitride particles that has a higher density than carbon, the N-Carbon sample exhibits a higher specific surface area of  $233 \text{ m}^2 \text{ g}^{-1}$  based on the BET model (Figure 5.9c). Multiple pores with diameters of 1, 3, and 20 nm are found in the carbon nanocapsules.



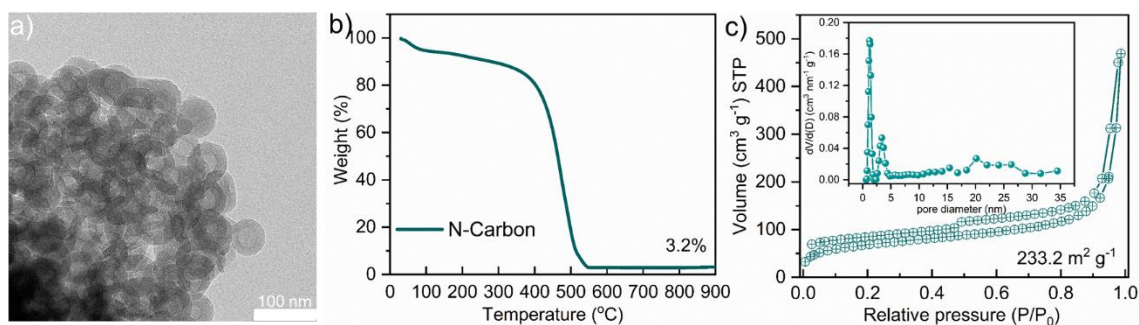


**Figure 5.9** (a) TEM image of the N-Carbon nanocapsules; (b) TGA curve of the N-Carbon nanocapsules under the synthetic air; (c)  $N_2$  adsorption-desorption isotherms of the N-Carbon nanocapsules with the corresponding pore size distribution (inset).

## 5.2 Interaction of $Fe_xN@C$ particles with polysulfides

### 5.2.1 LiPSs adsorption test

To reveal the adsorption capability of  $Fe_xN@C$  to the LiPSs, the adsorption tests have been conducted inside the glove box. According to  $N_2$  adsorption-desorption results, the same BET-specific surface area of  $2\text{ m}^2$  has been applied to study the affinity of each material to LiPSs. The inset of Figure 5.10a shows the visualized adsorption test result of the  $Fe_xN@C$  and N-Carbon particles to  $Li_2S_6$  solution. Firstly, 6 mL of  $Li_2S_6$  solution (1 mM) in a mixture solvent DME/DOL ( $v/v = 1/1$ ) was added into vials with different host materials (N-Carbon and  $Fe_xN@C$ ). After aging for 6 h in a glove box, the color of the supernatant in the vial with the  $Fe_xN@C$  sample turned from yellow to colorless. This indicates that  $Fe_xN@C$  nanocapsules have a strong adsorption capability to extract LiPSs from the solution to the surface of  $Fe_xN@C$  particles. By contrast, the color of the supernatant with metal-free carbon nanocapsules was light yellow, suggesting a weaker affinity to LiPSs. Moreover, UV-*vis* spectra of the two supernatant solutions in Figure 5.10a have been recorded and their comparison confirms that the  $Li_2S_6$  concentration in the vial with the  $Fe_xN@C$  sample is reduced notably.

To further analyze the interactions of  $Fe_xN@C$  to the LiPSs, high-resolution XPS analysis of the  $Fe_xN@C$  particles before and after the adsorption of  $Li_2S_6$  has been made, as shown in Figure 5.10b. An obvious blue shift can be observed in the  $Fe2p$  spectra after the adsorption of  $Li_2S_6$ , which is highlighted with the dotted lines to show the difference between the two XPS spectra. In addition, a weak shoulder peak at 708 eV in the  $Fe\ 2p_{3/2}$  region of  $Fe_xN@C-Li_2S_6$  can be distinguished and allocated to the Fe-S binding.<sup>[169]</sup> The blue shift in the  $Fe\ 2p$  spectrum of  $Fe_xN@C-Li_2S_6$  suggests that the iron nitride particles indeed provide a strong chemical interaction toward LiPSs.<sup>[202]</sup> The formation of Fe-S binding in the  $Fe_xN@C-Li_2S_6$  indicates

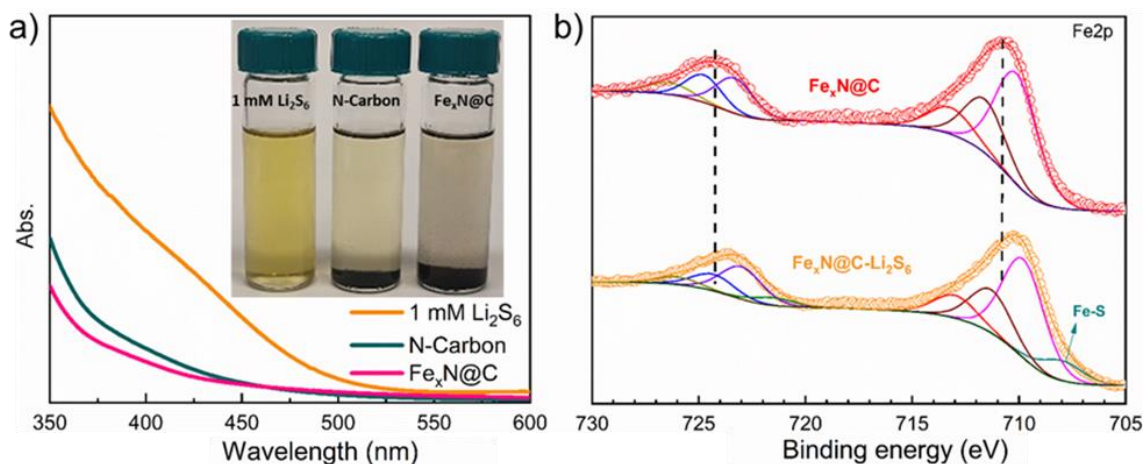


**Figure 5.10** (a) Static adsorption test for the  $\text{Li}_2\text{S}_6$  solution by the N-Carbon and  $\text{Fe}_x\text{N@C}$  with the UV-*vis* spectra of the corresponding supernatants, respectively; (b) the Fe 2p spectra of the  $\text{Fe}_x\text{N@C}$  particles before and after the adsorption test.

the electrons of sulfur atoms in the polysulfide molecules are transferred to the iron atoms, which could reduce the energy barrier for the conversion of LiPSs to  $\text{Li}_2\text{S}$ .<sup>[203]</sup>

### 5.2.2 Investigation of catalytic effects

The catalytic effects of  $\text{Fe}_x\text{N@C}$  on the conversion reaction of LiPSs to  $\text{Li}_2\text{S}$  were investigated in a symmetrical test cell by cyclic voltammetry method, as shown in Figure 5.11a. Since the  $\text{Li}_2\text{S}_6$ -free symmetrical cell only exhibits a minor contribution from the capacitive current, the polarization profiles of cells with the other two electrodes are assigned to the redox current of  $\text{Li}_2\text{S}_6$ . It can be observed that the current density significantly increases when  $\text{Fe}_x\text{N@C}$  and N-Carbon nanocapsules were used as the electrodes, demonstrating that both iron nitride and hollow carbon nanocapsules can significantly facilitate the electrochemical reactions of LiPSs. The larger area of the CV curves in the  $\text{Fe}_x\text{N@C}$  electrode than that of the carbon nanocapsules suggests considerable improvement in the redox kinetics of LiPSs conversion reactions in a liquid phase ( $\text{Li}_2\text{S}_8 \leftrightarrow \text{Li}_2\text{S}_6 \leftrightarrow \text{Li}_2\text{S}_4$ ) by introducing iron nitride nanoparticles into carbon nanocapsules.<sup>[153]</sup> To further explore the catalytic properties of the  $\text{Fe}_x\text{N@C}$  nanoparticles,  $\text{Li}_2\text{S}$  nucleation was investigated with the potentiostat discharging method.<sup>[22]</sup> As observed in Figure 5.11b and 11c, the presence of  $\text{Fe}_x\text{N@C}$  notably results in faster nucleation and growth and a higher discharging peak current during potentiostatic discharge at 2.05 V vs.  $\text{Li/Li}^+$ . Based on Faraday's law, the discharge capacity of the  $\text{Fe}_x\text{N@C}$  electrode was 816.0 mAh  $\text{g}^{-1}$ , which is higher than that of the N-Carbon electrode (610.1 mAh  $\text{g}^{-1}$ ). Apart from this observation, the current peak position during the  $\text{Li}_2\text{S}$  precipitation process at  $\text{Fe}_x\text{N@C}$  is located at 52 s, which is much earlier than that for the N-Carbon electrode. This result suggests

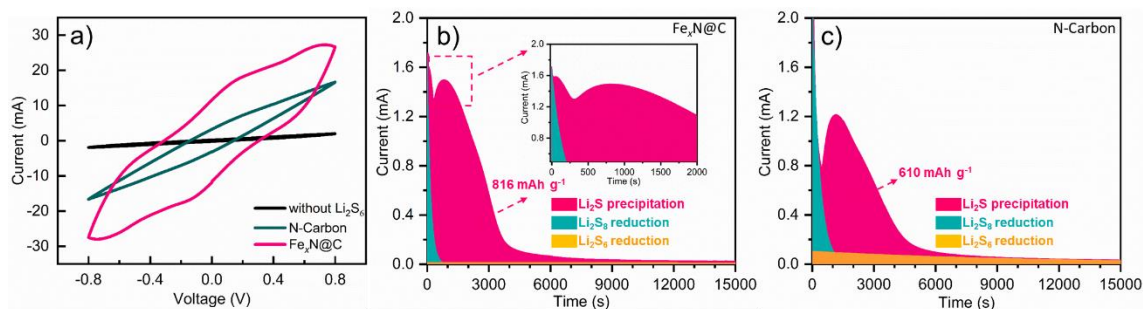


**Figure 5.11** (a) CV curves at a scan rate of  $10 \text{ mV s}^{-1}$  from  $-0.8$  to  $0.8 \text{ V}$  of the symmetric cells with different electrodes as noted in figure; the  $\text{Li}_2\text{S}$  precipitation test on different electrodes:  $\text{Fe}_x\text{N@C}$  (b) and N-Carbon (c).

that iron nitride nanoparticles can boost the kinetics of the  $\text{Li}_2\text{S}$  precipitation process during cycling.

### 5.3 Electrochemical performance

To demonstrate the structural merits of the  $\text{Fe}_x\text{N@C}$  nanocapsules, a sulfur-loaded composite of  $\text{Fe}_x\text{N@C/S}$  has been prepared by the melting diffusion method and used as cathode materials for Li-S batteries. The specific sulfur contents inside the composites are 72.1 wt.% and 72.6 wt.% for the  $\text{Fe}_x\text{N@C/S}$  and N-Carbon/S, respectively, which are determined by TGA (Figure 5.12a). The CV measurements have been conducted in a cell voltage range of 1.7–2.8 V vs.  $\text{Li/Li}^+$  at a scanning rate of  $0.1 \text{ mV s}^{-1}$ . Two representative sharp peaks are observed in the first cathodic scan as shown in Figure 5.12b. The first peak around 2.25 V corresponds to the reduction of sulfur to long-chain LiPSs ( $\text{Li}_2\text{S}_n$ ), and the other is ascribed to the reduction of LiPSs to lithium sulfides ( $\text{Li}_2\text{S}_2/\text{Li}_2\text{S}$ ). During the successive anodic scanning, the two oxidation peaks (2.39 and 2.44 V) can be assigned to the reversible conversion of  $\text{Li}_2\text{S}$  to LiPSs and finally to sulfur. To note, the peak position of  $\text{Fe}_x\text{N@C}$  in the cathodic scan is shifted to a higher electrode potential, while in the anodic scan, it moves to a lower electrode potential, indicating the lower polarization of the battery with  $\text{Fe}_x\text{N@C}$  as the host materials compared with the carbon nanocapsules. This could be ascribed to the high conductivity and the catalytic effect of the ultrafine iron nitride particles inside the carbon nanocapsules. The initial charging-discharging curves of these two electrodes at 0.1C are given in Figure 5.12c. The initial specific discharge capacity of the  $\text{Fe}_x\text{N@C/S}$  electrode is  $1481.5 \text{ mAh g}^{-1}$ , which is much higher than that of the N-Carbon/S ( $1345.0 \text{ mAh g}^{-1}$ ). Two characteristic plateaus in the discharge curve are observed at around 2.3 and 2.1 V for both studied electrodes, corresponding to the conversion reactions from sulfur to LiPSs and their further reduction to lithium sulfide, respectively. The cycling performance of Li-S batteries with different sulfur host materials was

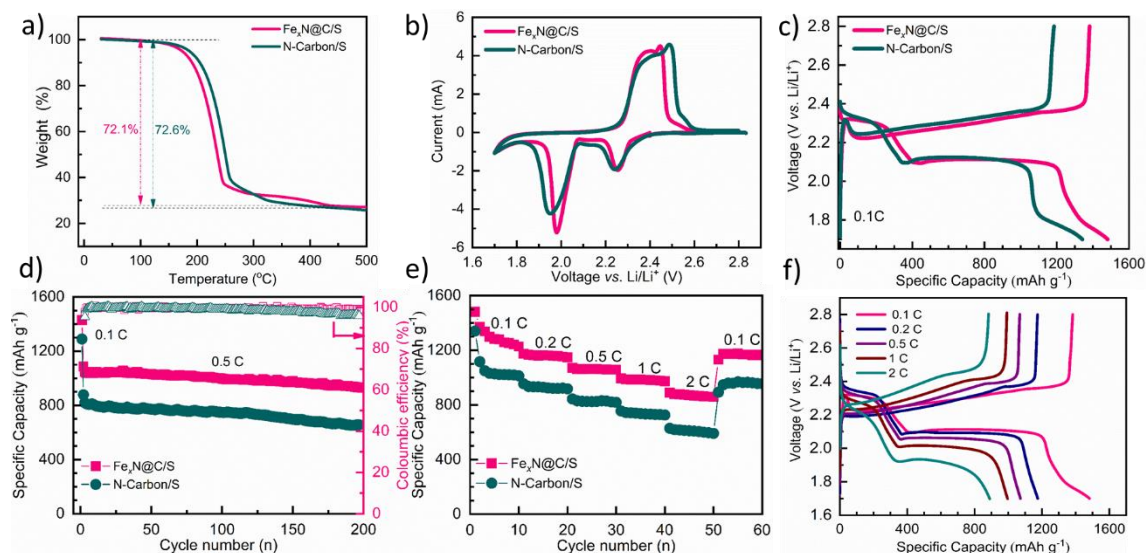


**Figure 5.12** (a) TGA curves of the  $\text{Fe}_x\text{N}@C/S$  and N-Carbon/S composites under nitrogen; (b) CV curves scanned at  $0.1 \text{ mV s}^{-1}$ , (c) discharge-charge curves at  $0.1 \text{ C}$  ( $1 \text{ C} = 1675 \text{ mA g}^{-1}$ ), (d) cycling stability at  $0.5 \text{ C}$ , (e) rate capability of the Li-S batteries with  $\text{Fe}_x\text{N}@C/S$  and N-Carbon/S as the cathode; (f) the charge/discharge profiles of the  $\text{Fe}_x\text{N}@C/S$  electrode at different C rates.

further measured at  $0.5 \text{ C}$  (Figure 5.12d). The initial discharge capacity of the N-Carbon/S electrode was  $878.9 \text{ mAh g}^{-1}$  at  $0.5 \text{ C}$ . After 100 cycles, it is still capable of delivering a capacity of  $748.8 \text{ mAh g}^{-1}$ , which is much higher than that of the previous carbon nanocapsule/sulfur composites.<sup>[178a]</sup> This could be ascribed to nitrogen-rich carbon derived from PDA and PILs, which can offer rich sites to chemically anchor LiPSs. Combined with the synergistic chemical adsorption and catalytic effect of iron nitride particles and the physical confinement of the carbon nanocapsules to suppress the shuttle effect, the  $\text{Fe}_x\text{N}@C/S$  electrode shows excellent cycling stability and delivers a high initial discharge capacity of  $1085.0 \text{ mAh g}^{-1}$  at  $0.5 \text{ C}$  with a remained value of  $930.0 \text{ mAh g}^{-1}$  after 200 cycles, which is much higher than its counterparts. To confirm the structural robustness of the nanocapsule particles, the  $\text{Fe}_x\text{N}@C/S$  electrode after cycling was washed with  $\text{CS}_2$  and ethanol and imaged with TEM. As shown in Figure 5.13, the  $\text{Fe}_x\text{N}@C$  particles still maintained nanocapsular morphology without breaking down, suggesting good structural robustness.

The rate capabilities of  $\text{Fe}_x\text{N}@C/S$  and N-Carbon/S electrodes were measured at different current densities and displayed in Figure 5.12e. After 10 cycles at each current, the retained discharge capacities of the  $\text{Fe}_x\text{N}@C/S$  electrode are  $1226.9$ ,  $1148.7$ ,  $1057.6$ ,  $973.8$ , and  $858.1 \text{ mAh g}^{-1}$  at  $0.1$ ,  $0.2$ ,  $0.5$ ,  $1$ , and  $2 \text{ C}$ , respectively. Under the same condition, the N-Carbon/S electrode delivers a remained capacity of  $1012.5$ ,  $918.0$ ,  $818.9$ ,  $725.4$ , and  $591.4 \text{ mAh g}^{-1}$  at  $0.1$ ,  $0.2$ ,  $0.5$ ,  $1$ , and  $2 \text{ C}$ , respectively. Since the iron nitride particles inside carbon nanocapsules can facilitate the conversion reaction from LiPSs to  $\text{Li}_2\text{S}$ , it is expected that the  $\text{Fe}_x\text{N}@C/S$

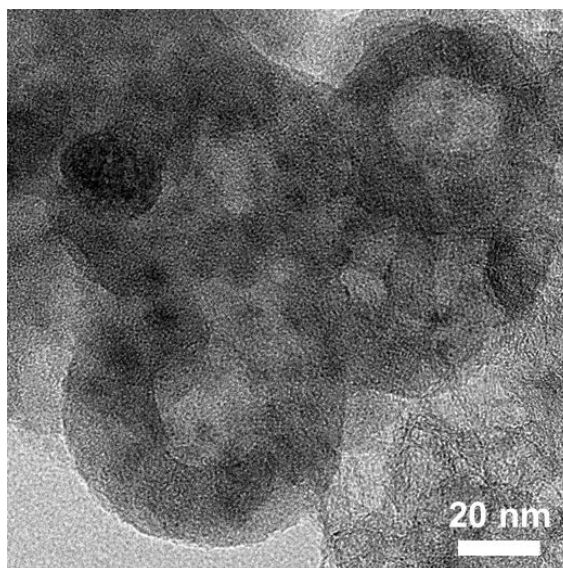


**Figure 5.13** TEM image of the  $\text{Fe}_x\text{N}@C$  particles after cycling for 100 cycles at 0.5C.

electrode exhibits a better rate capability than that of the N-Carbon/S electrode. Meanwhile, the EIS results in Figure 5.14a and 14b prove that the coin cell with  $\text{Fe}_x\text{N}@C/S$  electrode exhibits a lower charge transfer resistance than that with the N-Carbon/S cathode, which could be contributed to its better rate capability. From the charge/discharge voltage profiles of the  $\text{Fe}_x\text{N}@C/S$  electrode at different current densities (Figure 5.12f), the charge platforms shifted positively, and the discharge platforms shifted negatively with the increasing rate, which is attributed to the polarization. Moreover, the two typical discharge plateaus are present even when the current density increases to 2 C, suggesting the fast redox kinetics of the  $\text{Fe}_x\text{N}@C$  electrode due to the high conductivity and catalytic effect of iron nitride particles. Finally, the long-term cycling stability of the Li-S battery with the  $\text{Fe}_x\text{N}@C/S$  electrode has been tested and demonstrated in Figure 5.14c. After the activation at 0.1 C for one cycle, the  $\text{Fe}_x\text{N}@C/S$  electrode shows an initial discharge capacity of  $1061.0 \text{ mAh g}^{-1}$  at 1 C, suggesting the unique carbon nanocapsules embedded with fine iron nitride particles could improve the sulfur utilization efficiency even at a high C-rate. After 500 cycles, it continues to deliver a discharge capacity of  $556.5 \text{ mAh g}^{-1}$  with an average fading rate of 0.095% per cycle, indicating the potential of  $\text{Fe}_x\text{N}@C$  nanocapsules to promote the applications of Li-S batteries.

In this chapter, structurally exquisite carbon/iron nitride composite nanocapsules have been successfully templated from morphologically similar poly(ionic liquid)s nanovesicles after the PDA coating and ion exchange. Because of the unique hollow nanostructure, the obtained carbon nanocapsules embedded with ultrafine iron nitride nanoparticles can work as an efficient sulfur host material for Li-S batteries. The large voids in the nanocapsules allow to



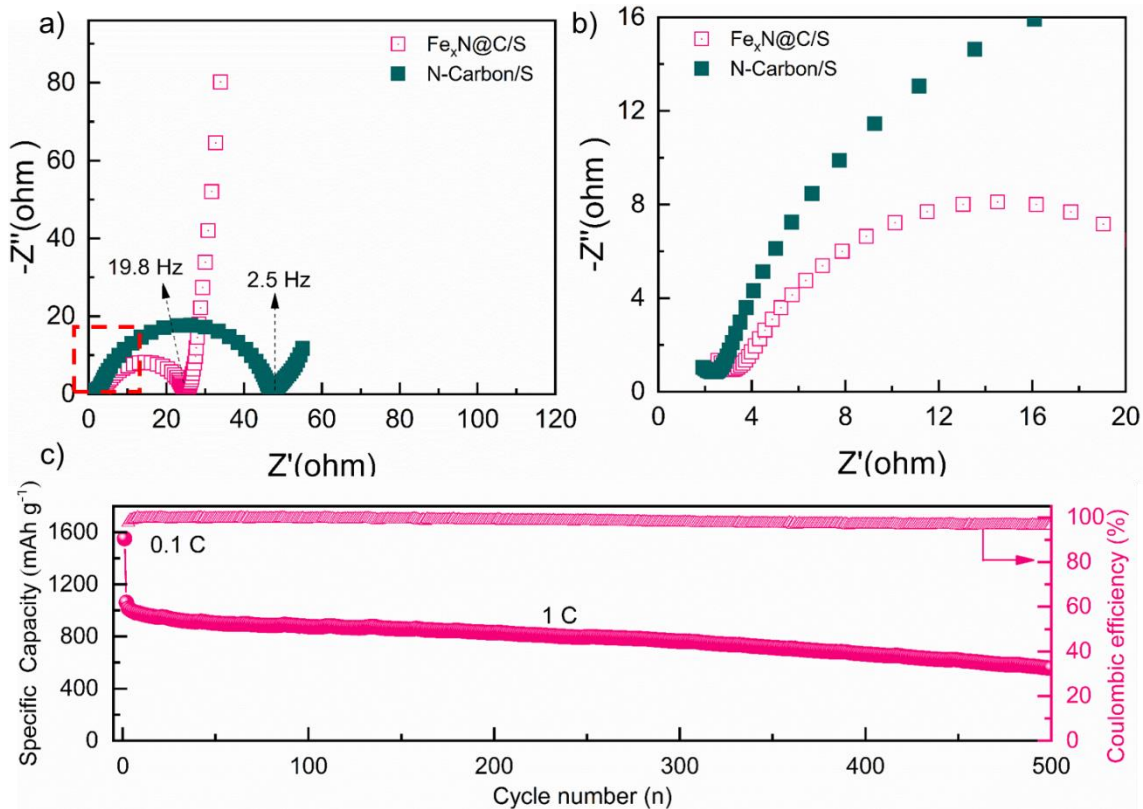


**Figure 5.14** (a) EIS spectra of the Li-S batteries with different cathodes (Fe<sub>x</sub>N@C/S and N-Carbon/S) and the corresponding enlarged red rectangle area (b); (c) long-term cycling performance at 1 C of the Li-S batteries with Fe<sub>x</sub>N@C/S as the cathode.

accommodate a high sulfur loading (70 wt.%) and mitigate the volumetric expansion during the cycling process. The iron nitride nanoparticles were found to significantly facilitate the LiPSs to Li<sub>2</sub>S conversion during the discharging process due to their high conductivity and catalytic activity. Based on the adsorption test, Fe<sub>x</sub>N@C nanocapsules exhibited a strong ability to confine LiPSs due to the chemical adsorption of iron nitride nanoparticles and the physical confinement of carbon nanocapsules. Benefiting from those advantages, the Fe<sub>x</sub>N@C/S electrode delivers a high initial discharge capacity of 1085.0 mAh g<sup>-1</sup> at 0.5 C with a remained value of 930.0 mAh g<sup>-1</sup> after 200 cycles; it also exhibits a high rate capability with the initial discharge capacity of 889.8 mAh g<sup>-1</sup> at 2 C. The synthetic route developed in this chapter can be used to obtain structurally well-defined porous carbon nanomaterials functionalized with metal-based compounds, and they are expected to meet electrochemical applications beyond batteries.

## 6. Summary and Outlook

This thesis presents the synthesis of nanostructured iron-based compounds (oxide, sulfide, and nitride) using the colloidal  $\beta$ -FeOOH nanospindles and poly(ionic liquid)s vesicles as hard and soft templates, respectively. Their morphologies, crystal structures, compositions, and adsorption capabilities to LiPSs have been systematically investigated. Moreover, the nanostructured iron-based compounds synthesized in this thesis have been applied as efficient sulfur host materials to suppress the shuttle effect of LiPSs in Li-S batteries with improved electrochemical performance.

Firstly, mesoporous C@M-Fe<sub>3</sub>O<sub>4</sub> nanospindles have been synthesized by using mesoporous Fe<sub>2</sub>O<sub>3</sub> nanospindles as precursors, which is derived from the pyrolysis of FeOOH nanospindles in a confined nanospace. The C@M-Fe<sub>3</sub>O<sub>4</sub> particles with abundant “triple-phase” sites could improve the sulfur reduction reaction from LiPSs to Li<sub>2</sub>S. Owing to the synergistic effects of the chemical binding and physical confinement to LiPSs, the C@M-Fe<sub>3</sub>O<sub>4</sub>/S electrode shows a high initial discharge capacity of 952.1 mAh g<sup>-1</sup> at 1 C with a retained capacity of 507.7 mAh g<sup>-1</sup> after 600 cycles.

Secondly, iron oxide/sulfide-based sulfur host materials with the same yolk-shell morphology have been designed and synthesized by using FeOOH nanoparticles as hard template to systematically investigate the effects of chemical composition on the electrochemical performance of Li-S batteries. It is found that the FeS<sub>2</sub> nanoparticles show the strongest adsorption ability to LiPSs than that of Fe<sub>3</sub>O<sub>4</sub> and FeS. Besides, the FeS<sub>2</sub> particles inside the carbon shell can significantly accelerate the conversion of LiPSs to Li<sub>2</sub>S. Benefiting from the chemical adsorption and catalytic effect of FeS<sub>2</sub> and the physical confinement of the carbon shell to suppress the shuttle effects, the constructed FeS<sub>2</sub>-C/S electrode delivers the highest discharge capacity and rate capability among three sulfur host materials.

Thirdly, carbon/iron nitride composite nanocapsules have been successfully synthesized using the PILs nanovesicles as soft template. It is revealed that the co-existence of PDA coating and ferricyanide anion is crucial for obtaining the carbon nanocapsules derived from the PILs vesicles. The presence of melamine as nitrogen source is beneficial for the good distribution of iron-based particles inside the carbon capsules. Because of the unique hollow nanostructure, the Fe<sub>x</sub>N@C particles can significantly facilitate the conversion reaction from LiPSs to Li<sub>2</sub>S during the discharging process. The Fe<sub>x</sub>N@C/S electrode shows a high initial discharge

capacity of 1085.0 mAh g<sup>-1</sup> at 0.5 C with excellent cycling stability.

In summary, this thesis presents the synthesis of nanostructured iron-based compounds by using low-cost and colloidal templates, and investigates the effects of different nanostructures and compositions of sulfur host materials on the electrochemical performance of Li-S batteries. The proposed colloidal synthesis routes show great potential in the development of cathode materials in Li-S batteries with improved electrochemical performance.



## 7. Experimental Part and Methods

### 7.1 Chemicals and materials

**Table 7.1** Chemicals and materials used in this thesis.

<i>Chemicals and materials</i>	<i>Purity</i>	<i>Company</i>
Ammonia solution (NH <sub>3</sub> ·H <sub>2</sub> O)	28 wt. %	Sigma-Aldrich
2, 2'-azobis[2-methyl-N-(2-hydroxyethyl) propionamide] (VA086)	N/A	Wako Chemicals
bis(trifluoromethane) sulfonimide lithium salt (LiTFSI)	anhydrous, 99.99%	Sigma-Aldrich
1-bromodecane	98%	Sigma-Aldrich
Carbon disulfide (CS <sub>2</sub> )	≥99.9%	Sigma-Aldrich
Carbon paper	N/A	Fuel Cell Store
Cetyltrimethylammonium bromide (CTAB)	≥98%	Sigma-Aldrich
Diethyl ether	≥99.5%	Sigma-Aldrich
1,2-dimethoxyethane (DME)	anhydrous, 99.5%	Sigma-Aldrich
1,3-dioxolane (DOL)	anhydrous, 99.8%	Sigma-Aldrich
Ethanol	anhydrous	Sigma-Aldrich
Hydrochloride acid (HCl)	37 wt. %	VWR International
Iron(III) chloride (FeCl <sub>3</sub> )	97%	Sigma-Aldrich
Lithium nitrate (LiNO <sub>3</sub> )	99.99%	Sigma-Aldrich
Lithium sulfide (Li <sub>2</sub> S)	99.98%	Sigma-Aldrich
Melamine	99%	Alfa Aesar
Methanol	anhydrous	Sigma-Aldrich
N-methyl-2-pyrrolidone (NMP)	anhydrous, 99.5%	Sigma-Aldrich
Polyvinylidene fluoride (PVDF)	N/A	Sigma-Aldrich
Potassium ferricyanide (III)	99.9%	Sigma-Aldrich
Sodium hydroxide (NaOH)	N/A	Sigma-Aldrich
Sublimed sulphur (S)	99.5%	Sigma-Aldrich
Tetraethyl orthosilicate (TEOS)	>99%	Sigma-Aldrich
Tris(hydroxymethyl) aminomethane (Tris)	>99.9%	Carl Roth
1-vinylimidazole	≥99%	Sigma-Aldrich
Carbon coated Aluminium foil (thickness:18 μm )	N/A	MTI Corporation
Coin cell case (CR20××)	N/A	MTI Corporation
Conductive Carbon Black	N/A	MTI Corporation
Lithium chips (diameter:14 mm, thickness:~300 μm)	99.95%	China Energy Lithium
Ketjenblack	N/A	Lion Specialty Chemicals

All chemicals and materials were used without any further purification and modification. The deionized water used for the synthesis was produced by Milli-Q with a resistivity of 18.2 MΩ·cm at room temperature.

## 7.2 Material synthesis procedure

### 7.2.1 Synthesis of FeOOH nanospindles

The synthesis of FeOOH nanospindles was based on the previous report with a minor modification.<sup>[144]</sup> Specifically, iron chloride (3.9 g) was firstly dissolved into 240 mL distilled water and 6.0 g CTAB powder was added. The whole mixture was stirred for 30 min at room temperature to form a homogeneous solution. Then, it was heated in an oil bath at 60 °C for 15 h. Afterwards, it was centrifuged and washed with deionized water for several times. Finally, the collected FeOOH particles were re-dispersed into the water *via* ultrasonication for 2 h to obtain the colloidal solution with a solid content of 30 mg mL<sup>-1</sup>.

### 7.2.2 Synthesis of polydopamine (PDA)-coated FeOOH nanospindles

2.4 mL FeOOH nanospindle colloidal aqueous solution (solid content of FeOOH: 12.6 g L<sup>-1</sup>) was dispersed into a 97.6 mL tris-buffer solution (pH = 8.5). After ultrasonication for 2 h, 20 mg dopamine hydrochloride was added to the mixture and stirred at room temperature for 15 h with a speed of 450 rpm. Then, the PDA-coated FeOOH nanospindles were purified by centrifuging at 7000 rpm for 10 min, followed by washing with deionized water for three times. Finally, the collected sample was collected by freeze-drying.

### 7.2.3 Synthesis of SiO<sub>2</sub>-coated FeOOH nanospindles

4 mL of the FeOOH colloidal solution was dispersed into the mixture solution of ethanol (240 mL) and water (41 mL) with ultrasonication for 2 h. After adding 2.4 mL of NH<sub>3</sub>·H<sub>2</sub>O (28 wt.%), 0.19 mL of TEOS was added dropwise into the solution within 20 min under ultrasonication. After stirring at room temperature overnight, it was centrifuged and washed with water three times. After the freeze-drying process, the SiO<sub>2</sub>@FeOOH powder was collected.

### 7.2.4 Synthesis of mesoporous Fe<sub>2</sub>O<sub>3</sub> nanospindles

The SiO<sub>2</sub>@FeOOH particles were heated using a muffle oven to 500 °C with a ramping rate of 2 °C min<sup>-1</sup>. The particles were kept at 500 °C in the ceramic crucible for 2 hours. Then, the obtained SiO<sub>2</sub>@Fe<sub>2</sub>O<sub>3</sub> powder was dispersed in 100 mL of NaOH solution (2 M). The dispersion was stirred overnight at 60 °C to remove the SiO<sub>2</sub> layer. Then, the particles were centrifuged and then re-dispersed into water for two cycles. Afterward, it was dispersed into water *via* ultrasonication to obtain the colloidal solution with a solid content of ~8 mg mL<sup>-1</sup>.

Finally, the mesoporous Fe<sub>2</sub>O<sub>3</sub> nanospindle powder was collected after the freeze-drying process, named as M-Fe<sub>2</sub>O<sub>3</sub> in the text.

### 7.2.5 Synthesis of carbon-coated mesoporous Fe<sub>3</sub>O<sub>4</sub> nanospindles and mesoporous carbon nanospindles

15 mL of the colloidal Fe<sub>2</sub>O<sub>3</sub> solution (solid content: ~8 mg mL<sup>-1</sup>) was dispersed into 300 mL Tris-buffer solution (pH = 8.5) via ultrasonication for 30 min. After adding dopamine hydrochloride (60 mg) into the solution, it was stirred for overnight at room temperature. Then, it was centrifuged and washed with water three times. Finally, it was freeze-dried to obtain the polydopamine-coated M-Fe<sub>2</sub>O<sub>3</sub> powder (PDA@M-Fe<sub>2</sub>O<sub>3</sub>). Afterwards, the PDA@M-Fe<sub>2</sub>O<sub>3</sub> powder was calcinated at 550 °C for 2 h under argon with a ramping rate of 3 °C min<sup>-1</sup>. The collected black powder was named as C@M-Fe<sub>3</sub>O<sub>4</sub>. For the mesoporous carbon nanospindle sample, the C@M-Fe<sub>3</sub>O<sub>4</sub> powder (300 mg) was added in 150 mL of HCl solution (2 M) and stirred at 80 °C overnight. Finally, it was filtered and washed with ethanol three times. After drying at 60 °C under a vacuum oven, the mesoporous carbon nanospindle powder was collected and labelled as M-Carbon.

### 7.2.6 Synthesis of Fe<sub>3</sub>O<sub>4</sub>-C yolk-shell nanoparticles

150 mg of the obtained PDA-coated FeOOH particles was put in an alumina crucible and calcinated at 550 °C for 2 h at a ramping rate of 1 °C min<sup>-1</sup> under argon. Then, 300 mg of the calcinated sample was immersed into the HCl solution (2 M) at room temperature to partially remove the iron oxide particles. After etching for 2 h, the mixture was centrifuged at 8000 rpm for 10 min and washed with deionized water for several times. Then, it was dried at 80 °C under vacuum. The obtained powder was denoted as yolk-shell Fe<sub>3</sub>O<sub>4</sub>-C.

### 7.2.7 Synthesis of FeS<sub>2</sub>-C and FeS-C yolk-shell nanoparticles

100 mg of Fe<sub>3</sub>O<sub>4</sub>-C particles was mixed with 300 mg of elemental sulfur in 3 mL carbon disulfide (CS<sub>2</sub>) solution under stirring. After the evaporation of the solvent, the mixture was ground in a mortar for 15 min before the sulfidation process. Then, the mixture was calcined in an alumina crucible at 400 °C and 800 °C for 2 h under argon at a ramping rate of 5 °C per min to get FeS<sub>2</sub>-C and FeS-C nanoparticles, respectively. After calcination, the obtained sample was washed with carbon disulfide and ethanol for several times to remove the residual sulfur. Then, it was dried at room temperature under vacuum.

### 7.2.8 Synthesis of hollow PILs nanocapsules

According to the previous report,<sup>[141d]</sup> the monomer 3-*n*-decyl-1-vinylimidazolium bromide (ILM-10) was synthesized by dissolving 0.1 mol of 1-vinylimidazole and 0.1 mol of decyl bromide into 30 mL of methanol. Then, the mixture was stirred at 60 °C for 15 h. After cooling down, the reaction mixture was added dropwise into 1 L of diethyl ether. The white precipitate was filtered off and dried under vacuum at room temperature. The polymerization of ILM-10 monomer to form hollow PILs nanovesicles was based on the previous report with minor changes.<sup>[204]</sup> Specifically, 1 g of the monomer ILM-10 and 150 mg of water-soluble initiator VA086 were dissolved in 100 mL deionized water inside a 250 mL Schlenk flask. The air inside the Schlenk flask was replaced with argon by three freeze-pump-thaw cycles. Afterward, the flask was put into an oil bath and stirred at 75 °C for 24 h. After cooling down to room temperature, a stable translucent dispersion was obtained. The stable dispersion was then purified *via* dialysis against deionized water (>10-fold volume) for 3 days, replacing the water every 12 h.

### 7.2.9 Synthesis of polydopamine-coated PILs nanovesicles (PDA@PILs)

Firstly, 41.2 mL of the colloidal PIL solution (solid content: 9.7 mg mL<sup>-1</sup>) was diluted into 158.8 mL water under sonication in 15 min. Then, 0.21g of Tris powder was added into the solution above, and the pH value was adjusted to ~8.5 with the desired amount of the concentrated HCl solution (37 wt.%). After that, 100 mg of dopamine hydrochloride was added to the solution. During the initial dopamine polymerization process, the solution was treated by sonication for 2 h at room temperature. Afterwards, it was magnetically stirred at room temperature for 15 h. Finally, the colloidal dispersion of the PDA-coated PILs (PDA@PILs) nanovesicles was purified *via* dialysis.

### 7.2.10 Synthesis of carbon nanocapsules functionalized with iron nitride nanoparticles

After dialysis, the volume of the above-mentioned PDA@PILs nanovesicle dispersion was adjusted to 300 mL in a round-bottom flask. After a sonication treatment for 15 min, 0.494 g of potassium ferricyanide (K<sub>3</sub>[Fe(CN)<sub>6</sub>]) was added into the dispersion. Along with sonication treatment for 1 h, the flask was sealed and put into an oil bath at 60 °C for the ion exchange for 24 h. After cooling down to room temperature, it was vacuum filtered off and washed with water three times. The obtained sample was freeze-dried and termed as PDA@Fe-PILs. 200 mg of PDA@Fe-PILs powder was placed in an alumina crucible at the centre of the tube furnace and 3 g of melamine powder was placed in another alumina crucible, which was

positioned upstream of PDA@Fe-PILs powder. The sample PDA@Fe-PILs was calcinated at 500 °C at a heating rate of 5 °C min<sup>-1</sup> for 2 h and then naturally cooled down to room temperature under Ar flow. The obtained sample is termed as Fe<sub>x</sub>N@C.

### 7.2.11 Synthesis of nanovesicle-templated hollow carbon nanocapsules and bulk carbon particles

The hollow carbon nanocapsule sample was synthesized by etching off the iron nitride nanoparticles with a hydrochloride solution (4 M) at 60 °C for 15 h. After washing with deionized water and ethanol three times, the etching process was repeated twice to ensure no iron nitride particles were left. Then, the collected hollow carbon nanocapsules were dried at 60 °C under vacuum, termed as “N-Carbon”. The bulk carbon particles (Bulk-Carbon) were obtained by calcination of the PDA@PILs powder under the same condition as that of the Fe<sub>x</sub>N@C nanocapsules.

### 7.2.12 LiPSs adsorption tests

A Li<sub>2</sub>S<sub>n</sub> solution was prepared by adding the desired amount of S and Li<sub>2</sub>S powder in a molar ratio of (n-1)/1 into the solution of DME and DOL (v/v = 1:1) followed with stirring at 80 °C for 48 h in the glove box. The host material nanoparticles with the same surface area (based on their BET results) were added into the Li<sub>2</sub>S<sub>n</sub> solution, respectively. After aging for a given time in the glove box, the supernatant liquid was centrifuged and sealed in cylinder quartz for a UV-vis spectroscopy test.

## 7.3 Electrochemical Measurement

### 7.3.1 Preparation of the sulfur/host material composites

The sulfur/host material composites were prepared by the conventional solid diffusion method. Firstly, the sublimed sulfur powder was mixed with the host materials in a mass ratio of 6:4 or 7:3. After grinding for 30 min, the mixture was sealed into a Teflon container under an argon atmosphere. Then, it was heated at 155 °C for 12 h to incorporate sulfur into the host materials.

### 7.3.2 Electrode preparation and coin cell assembly

The electrode preparation procedures in Chapter 4 are listed as following: the sulfur/host material composite, PVDF, and carbon black were mixed in a mass ratio of 8:1:1 in NMP to make a slurry. After grinding for 30 min, the slurry was coated onto a carbon-coated Al foil via the doctor blade method. Then, the electrode was dried at 50 °C under vacuum for 12 h.

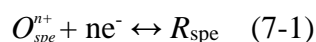
After that, the electrode was cut into wafers with a diameter of 14 mm. The areal loading of sulfur was around 1.0-1.1 mg cm<sup>-2</sup>.

The electrode preparation procedures in chapter 3 and chapter 5 are listed as following: the PVDF, Katjenblack, and sulfur/host material composite were uniformly mixed with a mass ratio of 1:2:7 in a mortar with NMP solution to make a slurry. Then, the cathode slurry was cast on carbon paper and the areal mass loading of S inside the electrode was controlled to be around 1.5 mg cm<sup>-2</sup>. After baking at 60 °C overnight under vacuum, the prepared electrode was cut into disks (diameter: 14 mm) as cathode.

The Li-S coin cells used in thesis were assembled with Li foil as anode and a piece of Celgard 2700 membrane as the separator in an Ar-filled glove box (UNIlab plus, M. BRAUN) with H<sub>2</sub>O content < 0.5 ppm and O<sub>2</sub> content < 0.5 ppm. 1 M LiTFSI in DME/DOL (v/v = 1:1) with 2 wt.% of LiNO<sub>3</sub> was used as the electrolyte. The volume of the electrolyte for each cell was 40 μL. Before electrochemical testing, all the cells were aged at room temperature for 12 h to let the electrolyte wet the electrode.

### 7.3.3 Cyclic voltammetry, galvanostatic charge-discharge, and electrochemical impedance spectroscopy

*Cyclic voltammetry(CV)* based on the Nernst equation is a widely applied potentiodynamic electrochemical technique in electrochemical fields. It can be used to acquire qualitative and quantitative information about electrochemical redox reactions, such as electrochemical kinetics, the reversibility of reactions, reaction mechanisms, and electrocatalytic processes. Linear scan's weep CV is the most typical mode. Figure 7.1 shows a representative CV curve of a simple reversible electrochemical reaction:



where  $O_{spe}$  represents the oxidized species and  $R_{spe}$  is the reduced species. During the cathodic scan, the reduction of species at the electrode starts as the voltage approaches the reduction potential. The cathodic current is proportional to the concentration gradient between the electrode surface and the bulk solution. The anodic scan involves the oxidation of species and thus the anodic peak current and oxidation potential are obtained. CV curves can provide information on the redox behavior and kinetics of redox reactions at the electrode surface. The CV curves of Li-S batteries and symmetrical cells were measured with a Biologic VMP3 electrochemical workstation at room temperature.

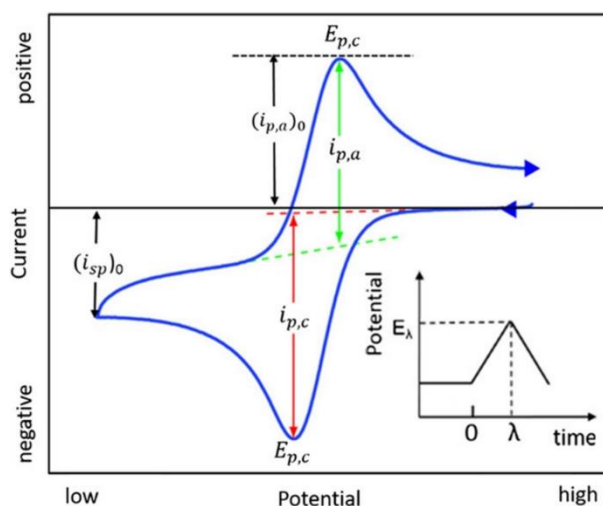


**Figure 7.1** A schematic CV curve for a simple reversible electrochemical reaction, where the inset is the voltage change during the CV scan.<sup>[205]</sup>

*Galvanostatic charge-discharge (GCD)* measurements record the voltage response under the constant applied current, which is widely used to investigate the capacity, cycling stability, and rate capability of electrode material. Depending on whether gravimetric or areal capacity is emphasized, the current in GCD measurement is usually normalized to the mass of electrode active materials or the area of electrodes. In this thesis, the gravimetric capacity ( $\text{mAh g}^{-1}$ ) is used in all measured coin cells and the current density is normalized to be specific C-rate current, where 1 C is defined as the current required to reach the theoretical capacity of an electrode material. The calculation of Coulombic efficiency in this thesis is the ratio of the discharge capacity to the charge capacity. Because rechargeable batteries are expected to have a very long service life, lifespan is one important parameter. Economically, the longer the service life, the lower the time-averaged cost and the more competitive the batteries will be in the market. The cycle life of a battery is investigated by measuring its capacity fading along the cycle number with repeatedly charging-discharging. Cycling stability is generally determined by the intrinsic properties of electrode materials. Simply adjusting the current in a suitable range can be used to assess the rate capability. As the current rate increases, the capacity decreases due to the increased polarization. The applied current density of  $1675 \text{ mA g}_{\text{sulfur}}^{-1}$  is defined as 1 C in this thesis. The specific capacity of Li-S batteries is calculated based on the mass of sulfur inside the cathodes. The cycling stability and rate capability of Li-S batteries were evaluated by galvanostatically charging and discharging with a Neware battery testing system at room temperature.



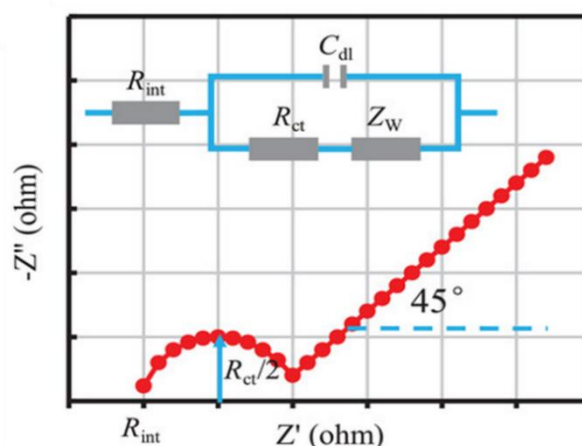


Figure 7.2 EIS with corresponding Randles circuit.<sup>[206]</sup>

*Electrochemical impedance spectroscopy (EIS)* is usually measured by applying an alternating current (AC) potential to an electrochemical cell and simultaneously measuring the current through the cell. The small amplitude of the AC signal ensures that the system can be treated as a combination of physical components, allowing for linear analysis and interpretation of the impedance data. In battery research, the most common technique is to measure the impedance under an applied sinusoidal voltage which has a low amplitude (a few mV *vs.* open-circuit voltage) over a wide frequency range. EIS is usually presented in two forms: Nyquist plot and Bode plot. The Nyquist plot plots the real part of impedance *vs.* the inverse imaginary part. It is more commonly used because of its simplicity in identifying the internal resistance ( $R_{int}$ ) and charge transfer resistance ( $R_{ct}$ ), as shown in Figure 7.2. The Nyquist plot can also be used to construct the equivalent electrical circuit, known as the Randles circuit, which comprises  $R_{int}$ , double layer capacitance ( $C_{dl}$ ),  $R_{ct}$ , and Warburg impedance ( $Z_w$ ). On the other hand, the Bode plot shows the magnitude and phase of impedance *vs.* frequency, leading to difficulty in the data interpretation. In this thesis, the electrochemical impedance spectra of Li-S batteries were recorded on GAMRY Interface 1000 within a frequency range from 100 kHz to 0.01 Hz.

### 7.3.4 Kinetics of $\text{Li}_2\text{S}$ precipitation and dissolution in the host materials

Initially, the host materials were mixed with conductive carbon and PVDF with a weight ratio of 8:1:1 in NMP for forming a mixed slurry. The slurry was coated onto a carbon-coated Al foil and subsequently dried at 60 °C under vacuum overnight. The areal loading of host materials is around 0.8 mg cm<sup>-2</sup> and the diameter of the electrode is 14 mm. Finally, the obtained electrodes were assembled into CR2032 coin cells as cathode with Li foil as the counter electrode. 20  $\mu\text{L}$   $\text{Li}_2\text{S}_8$  (0.25 M) solution with 1.0 M LiTFSI in the solvent of DOL and

DME (v/v = 1:1) was applied as catholyte, and 20  $\mu\text{L}$  control electrolyte without  $\text{Li}_2\text{S}_8$  was used as anolyte. For  $\text{Li}_2\text{S}$  precipitation, the assembled cells were first discharged galvanostatically at 0.1 C to 2.12 V and then discharged potentiostatically at 2.05 V for  $\text{Li}_2\text{S}$  nucleation and growth. The current vs. time curve of potentiostatic discharge at 2.05 V was fitted as the sum of two exponential functions:

$$I = a e^{bt} \quad (7-2)$$

where  $a$  and  $b$  are constants,  $I$  is current, and  $t$  is time. For  $\text{Li}_2\text{S}$  dissolution, the assembled batteries were first galvanostatically discharged at 0.1 C to 1.7 V, and subsequently galvanostatically discharged at 0.05 C to 1.7 V for the complete transformation of liquid LiPSs to solid  $\text{Li}_2\text{S}$ . Then, the cells were potentiostatically charged at 2.4 V for the oxidization of  $\text{Li}_2\text{S}$  to soluble polysulfides. The potentiostatic discharge/charge processes were recorded with a Biologic VMP3 electrochemical workstation and terminated after 65000 s.

### 7.3.5 Kinetic evaluation of polysulfide conversion

Two identical electrodes, the same as the one for the  $\text{Li}_2\text{S}$  precipitation test, were used as the working and the counter electrode, respectively, in the symmetric cell. 40  $\mu\text{L}$   $\text{Li}_2\text{S}_6$  (0.417 M, or 2.5 M of sulfur) solution with 1.0 M LiTFSI in the solvent of DOL and DME (v/v = 1:1) was used as electrolyte. The CV curves of assembled symmetric cells were measured with a Biologic VMP3 electrochemical workstation at a scan rate of 10  $\text{mV s}^{-1}$  between -0.8 and 0.8 V.

## 7.4 Material Characterization

### 7.4.1 Powder X-ray diffraction (PXRD)

The principle of XRD is based on the diffraction of X-rays by periodic atomic planes along with recording the diffracted signal by angle.<sup>[207]</sup> Bragg's law revealed the geometrical explanation of the XRD phenomenon, given in the following equation:

$$n\lambda = 2d_{hkl}\sin(\theta) \quad (7-3)$$

where  $n$  is the diffraction order,  $d_{hkl}$  represents the lattice spacing,  $\lambda$  is the incident beam wavelength, and  $\theta$  is the angle of the diffracted beam in degrees. The sum of the intensity scattered from the individual atoms describes the total intensity diffracted by a considered unit cell. The diffracted intensities  $I_{(hkl)}$  are related to the crystallographic structure factor  $F_{(hkl)}$ ,

$$F_{(hkl)} = \sum_{j=1}^N f_j \times \exp(2\pi i(hx_j + ky_j + lz_j)) \quad (7-4)$$

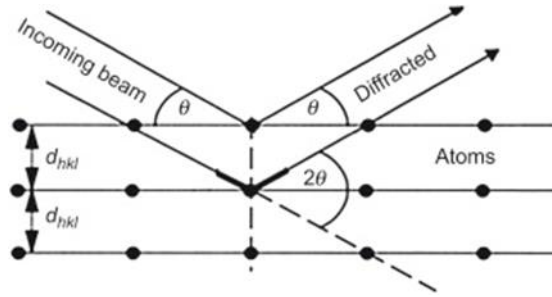


**Figure 7.3** Diffraction of an incoming X-ray beam from the lattice planes.<sup>[207]</sup>

where  $hkl$  is the Miller indices of the diffracting planes,  $f_j$  is the atomic scattering factor of atom  $j$ , and  $xyz$  represents the relative atomic position in the unit cell.<sup>[208]</sup> Several factors determine the total diffracted intensity for a lattice plan family ( $hkl$ ). These factors are merged to form a formula, which describes the whole intensity at a given  $2\theta$  position:

$$I_{(b)} = K \times |F_{(hkl)}|^2 \times f_a e^{\frac{-B \sin^2(\theta)}{\lambda^2}} \times A \times L(\theta) \times P(\theta) \times m \quad (7-5)$$

where  $K$  is a constant,  $f_a e^{\frac{-B \sin^2(\theta)}{\lambda^2}}$  represents the temperature factor describing the average displacement of atoms,  $L(\theta)$  is the Lorentz factor,  $A$  is the absorption factor,  $P(\theta)$  is the polarization factor, and  $m$  represents the multiplicity, describing equivalent crystal plane number.<sup>[209]</sup>

For XRD patterns collected in this thesis, the sample preparation is as follows: firstly, the sample powder was uniformly spread inside the pot of a sample holder and pressed with a glass plate to make the sample surface flat and have the same height as the sample holder. Then, it was positioned at a Bruker D8 diffractometer with  $\text{Cu } K\alpha$  ( $1.5406 \text{ \AA}$ ) radiation. The filament current is 40 mA and the acceleration voltage is 40 kV. The XRD patterns were collected in the  $2\theta$  range of  $10\text{-}80^\circ$  for 2 hours.

#### 7.4.2 X-ray photoelectron spectroscopy (XPS)

In XPS, the sample is irradiated with soft X-rays (less than  $\sim 6 \text{ keV}$ ) and the kinetic energy of the emitted electrons is measured. The usage of soft X-ray makes it a surface-sensitive analytical method to investigate chemical state information of the elements in the sample.<sup>[210]</sup>

The emitted photoelectron is the result of the complete transfer of the X-ray energy to a core-level electron, which can be expressed mathematically in the following equation:

$$h\nu = BE + KE + \Phi_{spec} \quad (7-6)$$

where  $h\nu$  represents the energy of the X-ray,  $BE$  is the binding energy of the electrons bound to the atom,  $KE$  stands for the kinetic energy of the electron that is emitted, and  $\Phi_{spec}$  is the spectrometer work function, which is a constant value. The binding energy of an electron is

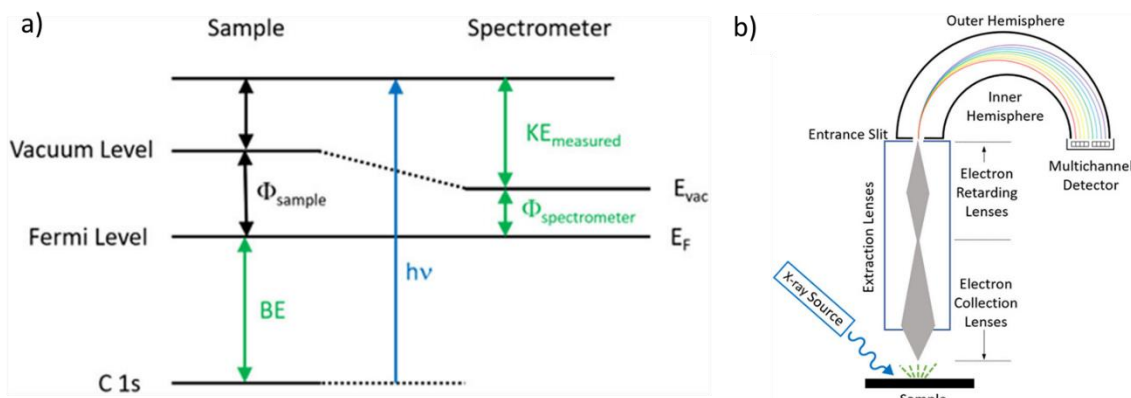


**Figure 7.4** (a) The energy level diagram illustrates schematically the basic XPS equation; (b) schematic diagrams show the major components of an XPS instrument.<sup>[210]</sup>

amaterial property and is independent of the X-ray source used to eject it. As demonstrated in Figure 7.4a, to determine the binding energy of an electron, the above equation can be rearranged as follows,

$$BE = hv - KE - \Phi_{spec} \quad (7-7)$$

where  $hv$  and  $\Phi_{spec}$  are known,  $KE$  can be measured in the XPS experiment. It is worth noting that the BE of the photoelectron is measured with respect to the sample's Fermi level other than the vacuum level, which is the reason that  $\Phi_{spec}$  is included.

As shown in Figure 7.4b, an XPS instrument typically consists of an X-ray source, sample stage, extraction lenses, analyzer, and detector, which are all set in an ultra-high vacuum environment. Photoelectron peaks in the spectroscopy are labeled by the elements and orbitals from which they were ejected. For instance, "C1s" describes electrons emitted from the 1s orbital of a carbon atom. The XPS spectra of samples in this thesis were characterized by an ESCA-Lab-220i-XL X-ray Photoelectron Spectrometer (Thermo Fisher Scientific) with Al K $\alpha$  sources ( $hv = 1486.6$  eV).

### 7.4.3 Raman spectroscopy

The interaction of light with matter can lead to several different processes (such as reflection, radiation, absorption, and scattering). There are three different types of scattering: the first one, called Rayleigh scattering, is unshifted in frequency ( $\nu_0$ ) and corresponds to an elastic dispersion of light because the system returns to its initial state after being excited to the "virtual state".<sup>[211]</sup> The other two types of scattering are Stokes scattering and anti-Stokes scattering. The incident photons in the Stokes scattering scenario move the system from the ground state to a "virtual state" and provide it with a finite amount of energy as the system

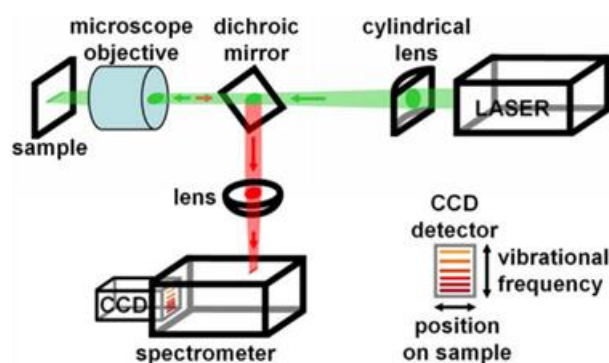


Figure 7.5 Scheme of a Raman spectrometer.<sup>[212]</sup>

descends to a higher energy vibrational state in the ground state.<sup>[213]</sup> In contrast, when anti-Stokes scattering occurs, the system loses energy by leaving an excited vibrational state and then returning to a lower energy vibrational state in the ground state.<sup>[213]</sup> Raman scattering is a phenomenon contributed by the above two processes, involving a net energy transfer between the system and the incident light. The Raman spectra of the sample powders in Chapter 4 were obtained using a LabRAM HR Evolution Raman spectrometer with a HeNe laser as the excitation line at  $\lambda = 633$  nm. The scheme of a Raman spectrometer is shown in Figure 7.5.

#### 7.4.4 Ultraviolet-visible (UV-vis) spectroscopy

UV-vis spectroscopy is used to measure the absorption or reflectance properties of materials in the UV-vis spectral region. It is a qualitative and nondestructive technique. The light wavelength ( $\lambda$ ) required for electronic transitions is typically in the ultraviolet (200-390 nm) and visible (390-780 nm) regions of the electromagnetic radiation spectrum.<sup>[214]</sup> When the light beam passes through a solution, a part of the light may be absorbed, while the rest is transmitted through the solution. In UV-vis spectroscopy, the light intensity through the sample is measured. For the light entering the sample at a fixed wavelength, the ratio of the transmitted light intensity ( $I$ ) to the incident light intensity ( $I_0$ ) is called transmittance ( $T$ ), while the negative logarithm of transmittance is called absorbance ( $A$ ) ( $A = -\log T$ ). UV-vis spectroscopy follows the Beer-Lambert law given by the following equation:

$$A = \log (I_0/I) = \epsilon l C \quad (7-8)$$

where  $\epsilon$  is the molar absorption or extinction coefficient that is characteristic of a given compound under defined conditions (wavelength, solvent, and temperature),  $l$  is the path length, and  $C$  is the concentration.<sup>[214-215]</sup> It shows that the absorbance ( $A$ ) is directly proportional to the concentration ( $C$ ) of the absorbing substance and the path length ( $l$ ) when a monochromatic light beam passes through a sample solution. The schematic diagram of the UV-vis

spectrometer used in this thesis is shown in Figure 7.6 and it consists of a deuterium (for the wavelengths in the ultraviolet region) and tungsten lamp (for the wavelengths in the visible region) as light source, a sample cell, a reference cell, a detector, and a monochromator.<sup>[216]</sup> The sample preparation process of UV-vis spectra in this thesis is as follows: after LiPS adsorption tests, the supernatants in the vials were centrifuged for five minutes inside the glove box to remove the residual particles. Afterwards, the supernatants were placed in a quartz sample cell with a 1.0 cm cell path length and sealed airtight in case of the oxidation of LiPSs. Finally, UV-vis spectra were recorded in the range of 200-1000 nm by using Lambda 650 spectrometer supplied by Perkin-Elmer at room temperature and the mixed solution of DOL/DME ( $v/v = 1/1$ ) is used as the reference.

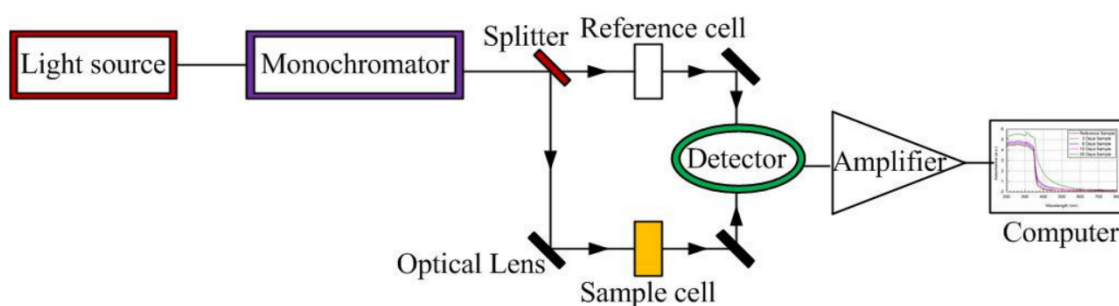


**Figure 7.6** Schematic diagram of a UV-vis spectrometer.<sup>[216]</sup>

#### 7.4.5 Electron microscopy (EM)

*Scanning electron microscopy (SEM):* In SEM, the electron beam is focused on a spot and is scanned sequentially across the specimen as shown in Figure 7.7a. The SEM produces images by probing the specimen with a focused electron beam that is scanned across a rectangular area of the specimen.<sup>[217]</sup> When the electron beam interacts with the specimen, it loses energy by a variety of mechanisms. The lost energy is converted into alternative forms such as heat, emission of low-energy secondary electrons and high-energy backscattered electrons, light emission or X-ray emission, providing information about the specimen surface, such as its topography and composition. For the SEM analysis, 20  $\mu\text{L}$  of the concentrated sample dispersion was dropped on the silicon wafer and dried at room temperature in a fume hood. Then, the silicon wafer was stick to an SEM sample holder and sputtered with a thin-layer carbon. Finally, SEM images along with the EDX elemental mapping were performed using an LEO 1530 field emission SEM equipped with an EDX attachment (Zeiss) measurement in secondary electron mode at 2 kV.

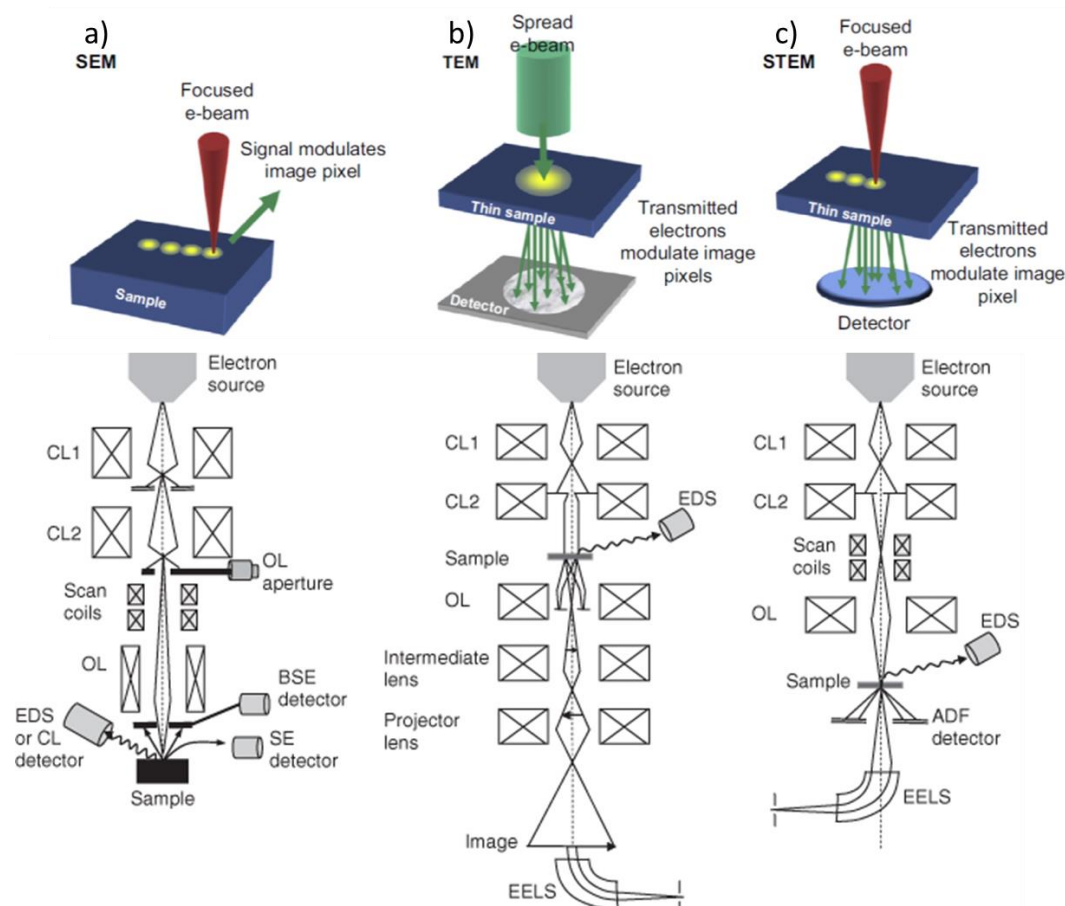


**Figure 7.7** Schematic illustration of the imaging methodology for different EMs: (a) SEM, serial collection of data points; (b) TEM, parallel image acquisition; (c) STEM, serial collection of transmitted electrons along with the corresponding schematic of their main components.<sup>[217-218]</sup>

*Transmission electron microscopy (TEM):* the TEM works by producing an electron beam from an electron gun and accelerating it towards a specimen as shown in Figure 7.7b. The electrons interact with the specimen, creating an image, which is magnified by the objective lens system of the microscope. The electron source is usually a tungsten or LaB<sub>6</sub> filament cathode and the electron beam is accelerated by an anode at a voltage range of 100 keV-400 keV. The electron beam is then focused by electrostatic and electromagnetic lenses and transmitted through the specimen before being captured to create the image.

To prepare the TEM specimens, sample dispersions (0.05-0.1 wt.%) were ultrasonicated for 0.5 h. Then 5  $\mu$ L of the dispersion was dropped onto the carbon-coated copper TEM grids (200 mesh, Science Services, Germany), which TEM grids were pre-treated with a glow discharge for 20 s under vacuum. After drying in a fume hood at room temperature, the specimen was put in the sample holder and then transferred to a JEOL JEM-2100 with a LaB<sub>6</sub> cathode (JEOL GmbH, Eching, Germany). It was operated at a 200 kV acceleration voltage and all images



were recorded by a bottom-mounted 4k CMOS camera system (TemCam-F416, TVIPS, Germany) and proceeded with a digital imaging processing system (EM-Menu 4.0, TVIPS, Germany).

*Scanning transmission electron microscopy (STEM):* a typical STEM is a conventional transmission electron microscope equipped with additional scanning coils, detectors, and necessary circuitry, which permits a fine electron probe to be scanned across the specimen as demonstrated in Figure 7.7c. The STEM image and electron energy-loss spectroscopy (EELS) in Chapter 5 were performed using a Nion HERMES microscope (Nion Co., Kirkland, WA, USA). Samples for STEM-EELS analysis were prepared by depositing a drop of sample solution on lacey carbon-coated copper TEM grids (200 mesh, Electron Microscopy Sciences, Hatfield, PA) and letting them dry at room temperature.

*Cryogenic transmission electron microscopy (Cryo-TEM):* Cryogenic electron microscopy (cryo-EM) was developed in 1974 by Glaeser and Taylor.<sup>[219]</sup> Since then, it has been widely used to investigate the structure of biological materials in life sciences. The method involves cooling the specimen to cryogenic temperatures, which helps to preserve its original morphology and structure. This has allowed researchers to gain a better understanding of the structure of biological materials. In recent years, cryo-EM has also been applied to other types of materials, such as micelles, polymers, and lithium dendrite, and has proven useful in the investigation of electron beam and/or air-sensitive materials.<sup>[220]</sup>

Cryo-TEM in Chapter 5 was performed with a JEOL JEM-2100 transmission electron microscope (JEOL GmbH, Eching, Germany). Cryo-TEM specimens were vitrified by plunging the samples into liquid ethane using an automated plunge freezer (Vitrobot Mark IV, FEI) set at 4 °C and 95 % humidity. The sample preparation process is demonstrated in Figure 7.8. Firstly, approximately 5  $\mu\text{L}$  of 0.025 wt.% solution was deposited on a lacey carbon-coated copper grid (200 meshes, Electron Microscopy Sciences, Hatfield, PA) and equilibrated at the adjusted temperature and humidity for 2 min. After blotting the liquid, the specimens were vitrified, inserted into a pre-cooled cryo-transfer holder (Gatan 914, Gatan, Munich, Germany), and finally transferred into TEM which was operated at 200 kV. A defocus of the objective lens of about 0.5  $\mu\text{m}$  was used to increase the contrast. Cryo-TEM micrographs were recorded with a bottom-mounted 4\*4k CMOS camera (TemCam-F416, TVIPS, Gauting, Germany). The total electron dose in each micrograph was kept below 20  $\text{e}^- \text{\AA}^{-2}$ .

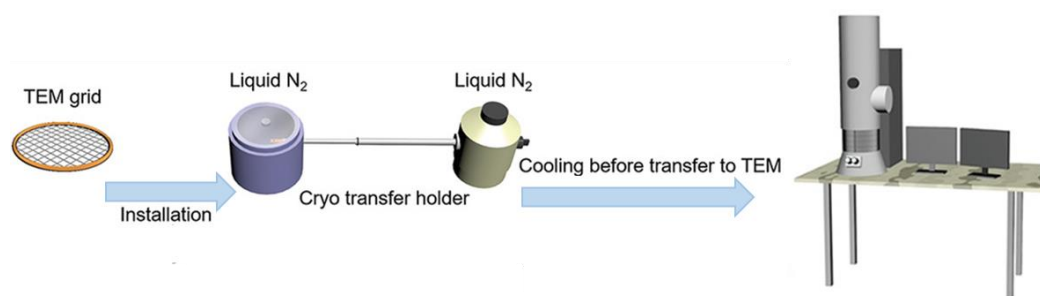


**Figure 7.8** Scheme of sample preparation route for cryo-TEM measurement.<sup>[220a]</sup>

#### 7.4.6 Electron tomography

The structural and morphological properties of nanostructured materials have been explored using electron microscopy methods like TEM and SEM. However, these methods have restrictions and can only furnish limited 2D information, making it challenging to obtain a true representation of the 3D structures, especially for nanostructures with intricate shapes.<sup>[221]</sup> SEM can only provide surface information while TEM can only provide projected three-dimensional information on a two-dimensional image. To overcome these limitations, electron tomography (ET) has been developed to visualize and analyze three-dimensional structural information of hollow or porous nanostructures.<sup>[222]</sup> ET gathers a series of two-dimensional images by tilting the specimen in the electron beam and taking a picture at each tilt step, as shown in Figure 7.9.<sup>[220b]</sup> The nanostructure is then represented in three dimensions by aligning and reconstructing these images using numerical algorithms.

For the sample preparation of ET images in Chapter 3, the M-Fe<sub>2</sub>O<sub>3</sub> nanoparticles suspended in ethanol were dried on lacey carbon-coated copper TEM grids (200 mesh, Science Services). Tomographic data were collected on a JEM-2100 (JEOL GmbH, Eching, Germany) operated at 200 kV and equipped with a 4k × 4k CMOS digital camera (TVIPS TemCam-F416). Using the Serial-EM acquisition software package,<sup>[223]</sup> tilt series were acquired with a tilt range of ± 60° and a 2° angular increment at a magnification of 100,000×, corresponding to a pixel size of 1.2 Å at the specimen level. Tilt series were aligned using patch tracking and then reconstructed using weighted back-projection with the IMOD software package.<sup>[224]</sup> Surface segmentations were performed manually using Amira (FEI Company, Eindhoven, The Netherlands). Three-dimensional surface renderings and movies were generated with UCSF Chimera.<sup>[225]</sup>

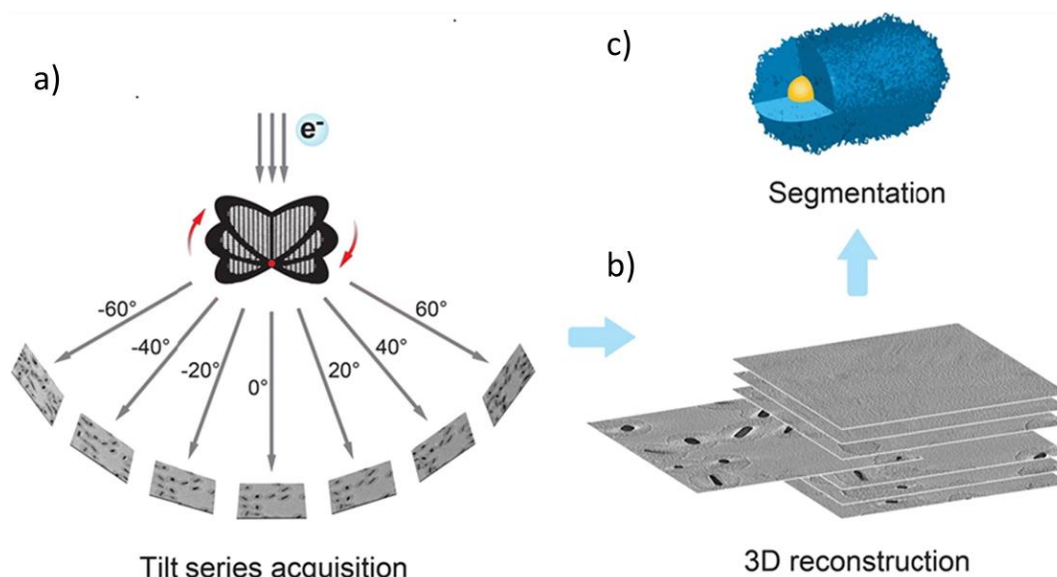


Figure 7.9 General electron tomography workflow.<sup>[220b]</sup>

#### 7.4.7 N<sub>2</sub> adsorption/desorption test

Gas physisorption is a technique for determining the specific surface area, pore size distribution, and pore volume of solids and powders. It is based on the equilibrium of Van der Waals interactions between gas molecules and solid particles. According to IUPAC, there are six different types of nitrogen adsorption-desorption isotherms. These isotherms can be either microporous (type I), nonporous or macroporous (types II, III, and VI), or mesoporous (types IV and V).<sup>[226]</sup> Usually, the adsorption isotherm curve can be divided into three stages: single-layer adsorption, multi-layer adsorption, and capillary condensation.<sup>[227]</sup>

The Brunauer-Emmett-Teller (BET) theory is based on two assumptions: firstly, the adsorption energy is independent of the adsorption sites; secondly, gas molecules interact only in the vertical direction, while the lateral interactions between adjacent adsorbed molecules are negligible.<sup>[147]</sup> Physisorption of the first adsorbate layer is as follows:

$$\frac{x}{W(1-x)} = \frac{1}{C \times W_{ml}} + \frac{C-1}{C \times W_{ml}} x \quad (7-9)$$

where  $W$  is the mass adsorbed at relative vapor pressure,  $x$  is  $P/P_0$ , where  $P$  is the actual vapor pressures of adsorbate and  $P_0$  is saturated one,  $W_{ml}$  is the required mass of adsorbate forming a complete monolayer adsorbed on a given sample, and  $C$  is a constant, which expresses the differences in the heat of adsorption of the first and second or higher layers. The  $C$  value depends on the temperature and the heat of adsorption of the first layer  $E_1$ . For higher layers,  $E_n$  equals the latent heat of condensation:

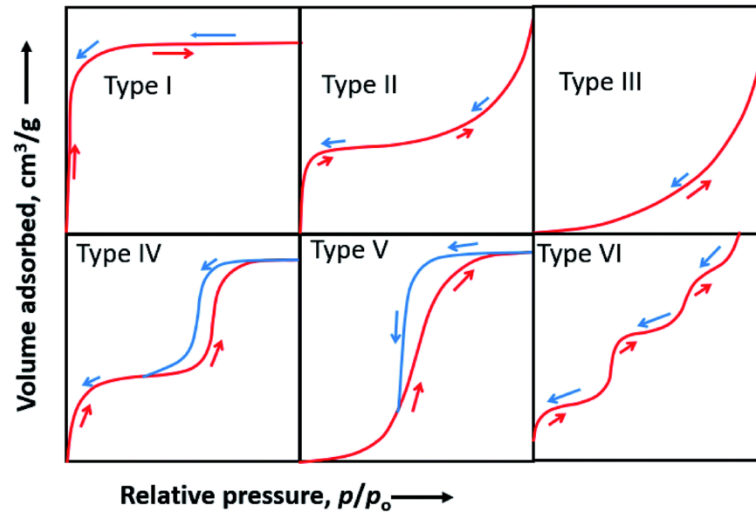


Figure 7.10 Different types of adsorption isotherms classified by IUPAC.<sup>[226]</sup>

$$C = \exp\left(\frac{E_1 - E_n}{RT}\right) \quad (7-10)$$

According to Equation (7-10), a plot of the function  $y = x/W(1-x)$  gives a straight line with an intercept at  $\beta_0 = 1/(C \times W_{ml})$  and a slope of  $\beta_1 = (C - 1)/(C \times W_{ml})$ . The mass of gas that forms a monolayer,  $W_{ml}$ , is obtained from the sum of the intercept and slope:

$$\frac{1}{W_{ml}} = \beta_0 + \beta_1 \quad (7-11)$$

The specific surface area (SSA) is calculated by

$$SSA = \frac{W_{ml}}{M \times m} \times N \times A \quad (7-12)$$

where  $M$  is the molar mass of nitrogen,  $m$  is the sample mass,  $A$  represents the nitrogen molecular cross-sectional area ( $0.162 \text{ nm}^2$ ), and  $N$  is Avogadro's number.

The Barrett, Joyner, and Halenda (BJH) method is a technique used to estimate the pore size distribution (PSD) from gas physisorption equilibrium isotherms. It is based on two assumptions: first, the shape of the pores is cylindrical; second, the adsorbed amount results from both physical adsorption on the pore walls and capillary condensation in mesopores.<sup>[146]</sup> According to BJH, the pore size is calculated as the sum of the multilayer thickness ( $t$ ) and the meniscus radius obtained from the Kelvin equation.

$$\ln \frac{P}{P_0} = \frac{2\gamma V_M}{rRT} \quad (7-13)$$

where  $P/P_0$  is the relative pressure in equilibrium with a meniscus,  $\gamma$  is the surface tension of the adsorbate in the liquid form,  $V_M$  is the molar volume of the liquid,  $R$  is the universal gas constant,  $r$  is the radius of the meniscus formed in the mesopore, and  $T$  is temperature. This method provides information about the distribution of pore sizes in a sample.

For the nitrogen adsorption-desorption measurement in this thesis, the sample preparation is as follows: firstly, the sample powder was dried in an oven at 80 °C under vacuum for overnight. Then, 30-40 mg of the sample powder was loaded into the glass sample holder. Afterwards, the outgassing process was conducted at 120 °C under vacuum for 20 h in the Quantachrome Autosorb-1 systems. Finally, the sample holder was immersed in the liquid N<sub>2</sub> of a Dewars. The N<sub>2</sub> adsorption/desorption isotherms were collected by using Quantachrome Autosorb-1 systems at 77 K. Specific surface areas were calculated by using the BET method based on a multipoint analysis and the pore size distribution of sample powder is based on the BJH model.

#### 7.4.8 Thermogravimetric analysis (TGA)

Thermogravimetric analysis (TGA) is a method for determining the mass of a sample as a function of temperature, time, and surrounding atmosphere. It is widely used for determining the thermal stability and decomposition behavior of a wide range of materials, including polymers, ceramics, and chemicals. In a TGA measurement, a small amount of the sample is weighed in the aluminum oxide or platinum crucible. Then, the crucible loaded with the sample is subjected to a controlled temperature program under different atmospheres. Finally, the sample mass changes with increasing temperature are continuously recorded by a microbalance. The information obtained from TGA is useful for the optimization of processing conditions, quality control, and product development.

In this thesis, TGA curves were applied to determine the specific contents of the sulfur or iron content inside the composites. Generally, around 10 mg of the measured sample was loaded in an alumina crucible and the TGA curves were collected on PerkinElmer (TGA 8000) in the temperature range of 30-900 °C at a heating rate of 10 °C min<sup>-1</sup>. For sulfur content, the measurement was conducted under N<sub>2</sub> atmosphere. After the temperature reaches over 350 °C, the sulfur will fully evaporate from the composite and the sulfur ratio is the difference of the weight loss in the temperature range of 100°C to 500 °C. For the iron content, the measurement procedure is the same but the atmosphere is synthetic air. The specific iron content is calculated based on the remained weight ratio contributed by the residual Fe<sub>2</sub>O<sub>3</sub>.



## Bibliography

- [1] S. Zhang, K. Ueno, K. Dokko and M. Watanabe, *Adv. Energy Mater.* **2015**, *5*, 1500117.
- [2] J. B. Goodenough and K.-S. Park, *J. Am. Chem. Soc.* **2013**, *135*, 1167-1176.
- [3] A. K. Padhi, K. S. Nanjundaswamy and J. B. Goodenough, *J. Electrochem. Soc.* **1997**, *144*, 1188.
- [4] K. Amine, H. Tukamoto, H. Yasuda and Y. Fujita, *J. Electrochem. Soc.* **1996**, *143*, 1607.
- [5] a) T. Ohzuku, T. Yanagawa, M. Kouguchi and A. Ueda, *J. Power Sources* **1997**, *68*, 131-134; b) F. Zhang, X. a. Zhou, X. Fu, C. Wang, B. Wang, W. Liang, P. Wang, J. Huang and S. Li, *Mater. Today Energy* **2021**, *22*, 100873.
- [6] Y.-K. Sun, S.-T. Myung, B.-C. Park, J. Prakash, I. Belharouak and K. Amine, *Nat. Mater.* **2009**, *8*, 320-324.
- [7] a) A. Vezzini, *Bulletin SEV/VSE* **2009**, *100*, 19; b) R. Spotnitz and J. Franklin, *J. Power Sources* **2003**, *113*, 81-100.
- [8] M. Johnson-Groh in *Advances in lithium sulfur batteries pave the way for their commercial use*, Vol. AIP Publishing LLC, **2019**.
- [9] Z. W. Seh, Y. Sun, Q. Zhang and Y. Cui, *Chem. Soc. Rev.* **2016**, *45*, 5605-5634.
- [10] M. Zhao, B.-Q. Li, H.-J. Peng, H. Yuan, J.-Y. Wei and J.-Q. Huang, *Angew. Chem. Int. Ed.* **2020**, *59*, 12636-12652.
- [11] A. Manthiram, Y. Fu, S. H. Chung, C. Zu and Y. S. Su, *Chem. Rev.* **2014**, *114*, 11751-11787.
- [12] Y. Yang, G. Zheng and Y. Cui, *Chem. Soc. Rev.* **2013**, *42*, 3018-3032.
- [13] K. Fan and H. Huang, *Energy Storage Mater.* **2022**, *50*, 696-717.
- [14] a) A. Fu, C. Wang, F. Pei, J. Cui, X. Fang and N. Zheng, *Small* **2019**, *15*, 1804786; b) J. Xu, T. Lawson, H. Fan, D. Su and G. Wang, *Adv. Energy Mater.* **2018**, *8*, 1702607; c) X.-B. Cheng, R. Zhang, C.-Z. Zhao and Q. Zhang, *Chem. Rev.* **2017**, *117*, 10403-10473.
- [15] M. Klimpel, M. V. Kovalenko and K. V. Kravchyk, *Commun. Chem.* **2022**, *5*, 77.
- [16] M. Helen, M. A. Reddy, T. Diemant, U. Golla-Schindler, R. J. Behm, U. Kaiser and M. Fichtner, *Sci. Rep.* **2015**, *5*, 12146.
- [17] Z. Lin, Z. Liu, N. J. Dudney and C. Liang, *ACS Nano* **2013**, *7*, 2829-2833.
- [18] A. Gupta and S. Sivaram, *Energy Technol.* **2019**, *7*, 1800819.
- [19] X. Tang, Z. Xu, Z. Sun, J. Zhou, X. Wu, H. Lin, J. Rong, S. Zhuo and F. Li, *Energy Technol.* **2019**, *7*, 1900574.



- [20] L. Qie, C. Zu and A. Manthiram, *Adv. Energy Mater.* **2016**, *6*, 1502459.
- [21] P. Wang, B. Xi, M. Huang, W. Chen, J. Feng and S. Xiong, *Adv. Energy Mater.* **2021**, *11*, 2002893.
- [22] F. Y. Fan, W. C. Carter and Y. M. Chiang, *Adv. Mater.* **2015**, *27*, 5203-5209.
- [23] R. Deng, M. Wang, H. Yu, S. Luo, J. Li, F. Chu, B. Liu and F. Wu, *Energy Environ. Sci.* **2022**, *5*, 777-799.
- [24] D. Geng, N. Ding, T. S. A. Hor, S. W. Chien, Z. Liu, D. Wu, X. Sun and Y. Zong, *Adv. Energy Mater.* **2016**, *6*, 1502164.
- [25] C. Sun, J. Liu, Y. Gong, D. P. Wilkinson and J. Zhang, *Nano Energy* **2017**, *33*, 363-386.
- [26] X.-B. Cheng, H.-J. Peng, J.-Q. Huang, F. Wei and Q. Zhang, *Small* **2014**, *10*, 4257-4263.
- [27] X. Xu, S. Wang, H. Wang, B. Xu, C. Hu, Y. Jin, J. Liu and H. Yan, *J. Energy Storage* **2017**, *13*, 387-400.
- [28] X.-R. Chen, C. Yan, J.-F. Ding, H.-J. Peng and Q. Zhang, *J. Energy Chem.* **2021**, *62*, 289-294.
- [29] H. Hong, N. A. R. Che Mohamad, K. Chae, F. Marques Mota and D. H. Kim, *J. Mater. Chem. A* **2021**, *9*, 10012-10038.
- [30] G. Ma, Z. Wen, M. Wu, C. Shen, Q. Wang, J. Jin and X. Wu, *Chem. Commun.* **2014**, *50*, 14209-14212.
- [31] Q. Yun, Y.-B. He, W. Lv, Y. Zhao, B. Li, F. Kang and Q.-H. Yang, *Adv. Mater.* **2016**, *28*, 6932-6939.
- [32] M. Arakawa, S.-i. Tobishima, Y. Nemoto, M. Ichimura and J.-i. Yamaki, *J. Power Sources* **1993**, *43*, 27-35.
- [33] B. Moorthy, R. Ponraj, J. H. Yun, J. E. Wang, D. J. Kim and D. K. Kim, *ACS Appl. Energy Mater.* **2020**, *3*, 11053-11060.
- [34] G.-D. Yang, B. Li, Y.-H. Song, L. Ding, S.-G. Gong, X.-L. Wu, J.-P. Zhang, Y.-F. Li and H.-Z. Sun, *Electrochim. Acta* **2022**, *430*, 141035.
- [35] K. Huang, Z. Li, Q. Xu, H. Liu, H. Li and Y. Wang, *Adv. Energy Mater.* **2019**, *9*, 1900853.
- [36] a) J. Gao, M. A. Lowe, Y. Kiya and H. D. Abruña, *J. Phys. Chem. C* **2011**, *115*, 25132-25137; b) S. Yun, S. H. Park, J. S. Yeon, J. Park, M. Jana, J. Suk and H. S. Park, *Adv. Funct. Mater.* **2018**, *28*, 1707593.
- [37] E. Peled, Y. Sternberg, A. Gorenshtein and Y. Lavi, *J. Electrochem. Soc.* **1989**, *136*, 1621.

- [38] G. Liu, Q. Sun, Q. Li, J. Zhang and J. Ming, *Energy & Fuels* **2021**, *35*, 10405-10427.
- [39] S. S. Zhang, *J. Power Sources* **2013**, *231*, 153-162.
- [40] M. Armand, *Solid State Ion.* **1994**, *69*, 309-319.
- [41] R. Cao, J. Chen, K. S. Han, W. Xu, D. Mei, P. Bhattacharya, M. H. Engelhard, K. T. Mueller, J. Liu and J. G. Zhang, *Adv. Funct. Mater.* **2016**, *26*, 3059-3066.
- [42] H. Zhang, G. G. Eshetu, X. Judez, C. Li, L. M. Rodriguez-Martínez and M. Armand, *Angew. Chem. Int. Ed.* **2018**, *57*, 15002-15027.
- [43] a) S. S. Zhang, *Electrochim. Acta* **2012**, *70*, 344-348; b) D. Aurbach, E. Pollak, R. Elazari, G. Salitra, C. S. Kelley and J. Affinito, *J. Electrochem. Soc.* **2009**, *156*, A694.
- [44] X. Liu, J. Q. Huang, Q. Zhang and L. Mai, *Adv. Mater.* **2017**, *29*, 1601759.
- [45] S. Li, W. Zhang, J. Zheng, M. Lv, H. Song and L. Du, *Adv. Energy Mater.* **2021**, *11*, 2000779.
- [46] T. Jeon and S. C. Jung, *J. Mater. Chem. A* **2021**, *9*, 23929-23940.
- [47] Q. Wang, J. Zheng, E. Walter, H. Pan, D. Lv, P. Zuo, H. Chen, Z. D. Deng, B. Y. Liaw, X. Yu, X. Yang, J.-G. Zhang, J. Liu and J. Xiao, *J. Electrochem. Soc.* **2015**, *162*, A474.
- [48] W. J. Chung, J. J. Griebel, E. T. Kim, H. Yoon, A. G. Simmonds, H. J. Ji, P. T. Dirlam, R. S. Glass, J. J. Wie, N. A. Nguyen, B. W. Guralnick, J. Park, Á. Somogyi, P. Theato, M. E. Mackay, Y.-E. Sung, K. Char and J. Pyun, *Nat. Chem.* **2013**, *5*, 518-524.
- [49] S. Li, S. Yang, D. Shen, W. Sun, X. Shan, W. Dong, Y. Chen, X. Zhang, Y. Mao and S. Tang, *Phys. Chem. Chem. Phys.* **2017**, *19*, 32708-32714.
- [50] L. Borchardt, M. Oschatz and S. Kaskel, *Chem. Eur. J* **2016**, *22*, 7324-7351.
- [51] B. Meyer, J. M. Austin and D. Jensen, *J. Chem. Eng. Data* **1971**, *16*, 364-366.
- [52] R. Steudel, *Chem. Rev.* **2002**, *102*, 3905-3946.
- [53] G. Li, S. Wang, Y. Zhang, M. Li, Z. Chen and J. Lu, *Adv. Mater.* **2018**, *30*, 1705590.
- [54] R. Steudel, G. Holdt and T. Göbel, *J. Chromatogr. A* **1989**, *475*, 442-446.
- [55] P. L. Cloke, *Geochim. Cosmochim. Acta* **1963**, *27*, 1265-1298.
- [56] R. S. Assary, L. A. Curtiss and J. S. Moore, *J. Phys. Chem. C* **2014**, *118*, 11545-11558.
- [57] S. Li, B. Jin, X. Zhai, H. Li and Q. Jiang, *ChemistrySelect* **2018**, *3*, 2245-2260.
- [58] X. Ji, K. T. Lee and L. F. Nazar, *Nat. Mater.* **2009**, *8*, 500-506.
- [59] M. Helen, T. Diemant, S. Schindler, R. J. Behm, M. Danzer, U. Kaiser, M. Fichtner and M. Anji Reddy, *ACS Omega* **2018**, *3*, 11290-11299.
- [60] C. Qi, Z. Li, G. Wang, H. Yuan, C. Chen, J. Jin and Z. Wen, *Adv. Energy Mater.* **2021**, *11*, 2102024.

- [61] S. Xin, L. Gu, N.-H. Zhao, Y.-X. Yin, L.-J. Zhou, Y.-G. Guo and L.-J. Wan, *J. Am. Chem. Soc.* **2012**, *134*, 18510-18513.
- [62] Z. Zeng and X. Liu, *Adv. Mater. Interfaces* **2018**, *5*, 1701274.
- [63] H.-J. Peng and Q. Zhang, *Angew. Chem. Int. Ed.* **2015**, *54*, 11018-11020.
- [64] H.-J. Peng, G. Zhang, X. Chen, Z.-W. Zhang, W.-T. Xu, J.-Q. Huang and Q. Zhang, *Angew. Chem. Int. Ed.* **2016**, *55*, 12990-12995.
- [65] M. Winter and R. J. Brodd, *Chem. Rev.* **2004**, *104*, 4245-4270.
- [66] a) S. Wenzel, H. Metelmann, C. Raiß, A. K. Dürr, J. Janek and P. Adelhelm, *J. Power Sources* **2013**, *243*, 758-765; b) J. Zhang, C. Wang and A. J. Leothand, *Energy Environ. Sci.* **2022**, *15*, 5415-5420.
- [67] A. Van der Ven, J. Bhattacharya and A. A. Belak, *Acc. Chem. Res.* **2013**, *46*, 1216-1225.
- [68] Y. X. Yin, S. Xin, Y. G. Guo and L. J. Wan, *Angew. Chem. Int. Ed.* **2013**, *52*, 13186-13200.
- [69] Y. Tang, Y. Zhang, W. Li, B. Ma and X. Chen, *Chem. Soc. Rev.* **2015**, *44*, 5926-5940.
- [70] H. Mehrer, *Diffusion in solids: fundamentals, methods, materials, diffusion-controlled processes*, Springer Science & Business Media, **2007**, p.
- [71] L. Kong, J.-X. Chen, H.-J. Peng, J.-Q. Huang, W. Zhu, Q. Jin, B.-Q. Li, X.-T. Zhang and Q. Zhang, *Energy Environ. Sci.* **2019**.
- [72] L. Zhou, D. L. Danilov, F. Qiao, J. Wang, H. Li, R.-A. Eichel and P. H. L. Notten, *Adv. Energy Mater.* **2022**, *12*, 2202094.
- [73] F. Y. Fan and Y.-M. Chiang, *J. Electrochem. Soc.* **2017**, *164*, A917.
- [74] X. Gao, D. Zhou, Y. Chen, W. Wu, D. Su, B. Li and G. Wang, *Commun. Chem.* **2019**, *2*, 66.
- [75] Z. Wei Seh, W. Li, J. J. Cha, G. Zheng, Y. Yang, M. T. McDowell, P. C. Hsu and Y. Cui, *Nat. Commun.* **2013**, *4*, 1331.
- [76] Z. Li, J. Zhang, B. Guan, D. Wang, L. M. Liu and X. W. Lou, *Nat Commun* **2016**, *7*, 13065.
- [77] C. Hoffmann, S. Thieme, J. Brückner, M. Oschatz, T. Biemelt, G. Mondin, H. Althues and S. Kaskel, *ACS Nano* **2014**, *8*, 12130-12140.
- [78] S. Mei, X. Xu, R. D. Priestley and Y. Lu, *Chemical science* **2020**, *11*, 12269-12281.
- [79] F. Li, L. Xie, G. Sun, Q. Kong, F. Su, Y. Cao, J. Wei, A. Ahmad, X. Guo and C.-M. Chen, *Microporous Mesoporous Mater.* **2019**, *279*, 293-315.
- [80] S. Reghunath, D. Pinheiro and S. D. KR, *Appl. Surf. Sci. Adv.* **2021**, *3*, 100063.

- [81] a) L. Ni, Z. Wu, G. Zhao, C. Sun, C. Zhou, X. Gong and G. Diao, *Small* **2017**, *13*, 1603466; b) C. Nan, Z. Lin, H. Liao, M.-K. Song, Y. Li and E. J. Cairns, *J. Am. Chem. Soc.* **2014**, *136*, 4659-4663.
- [82] H. Kim and M. S. Lah, *Dalton Trans.* **2017**, *46*, 6146-6158.
- [83] S. Mei, C. J. Jafta, I. Lauermann, Q. Ran, M. Kärgell, M. Ballauff and Y. Lu, *Adv. Funct. Mater.* **2017**, *27*, 1701176.
- [84] a) L. Xie, Z. Jin, Z. Dai, Y. Chang, X. Jiang and H. Wang, *Carbon* **2020**, *170*, 100-118; b) R. R. Poolakkandy and M. M. Menampambath, *Nanoscale Adv.* **2020**, *2*, 5015-5045.
- [85] X. Wang, J. Feng, Y. Bai, Q. Zhang and Y. Yin, *Chem. Rev.* **2016**, *116*, 10983-11060.
- [86] C. Rupp, H. Steckel and B. W. Müller, *Int. J. Pharm.* **2010**, *387*, 120-128.
- [87] S. Liu, C. Zhang, W. Yue, X. Chen and X. Yang, *ACS Appl. Energy Mater.* **2019**, *2*, 5009-5018.
- [88] Y. Zhou, Z. Wei, W. Lei, J. You, T. Liang, Q. Zhang and D. Shi, *ACS Appl. Energy Mater.* **2022**, *5*, 7432-7442.
- [89] N. D. Petkovich and A. Stein, *Chem. Soc. Rev.* **2013**, *42*, 3721-3739.
- [90] P. Qiu, Y. Yao, W. Li, Y. Sun, Z. Jiang, B. Mei, L. Gu, Q. Zhang, T. Shang, X. Yu, J. Yang, Y. Fang, G. Zhu, Z. Zhang, X. Zhu, T. Zhao, W. Jiang, Y. Fan, L. Wang, B. Ma, L. Liu, Y. Yu and W. Luo, *Nano Lett.* **2021**, *21*, 700-708.
- [91] P. Walstra, *Chem. Eng. Sci.* **1993**, *48*, 333-349.
- [92] A. D. Roberts, X. Li and H. Zhang, *Chem. Soc. Rev.* **2014**, *43*, 4341-4356.
- [93] B. A. Armitage, *Biopolymers, liquid crystalline polymers, phase emulsion*, Springer, **1996**, p.
- [94] A. Feinle, M. S. Elsaesser and N. Hüsing, *Chem. Soc. Rev.* **2016**, *45*, 3377-3399.
- [95] a) W. Sun, S. Liu, Y. Li, D. Wang, Q. Guo, X. Hong, K. Xie, Z. Ma, C. Zheng and S. Xiong, *Adv. Funct. Mater.* **2022**, *32*, 2205471; b) K. Xi, D. He, C. Harris, Y. Wang, C. Lai, H. Li, P. R. Coxon, S. Ding, C. Wang and R. V. Kumar, *Adv. Sci.* **2019**, *6*, 1800815.
- [96] Z. Cao, J. Jia, S. Chen, H. Li, M. Sang, M. Yang, X. Wang and S. Yang, *ACS Appl. Mater. Interfaces* **2019**, *11*, 39772-39781.
- [97] C. Ma, Y. Zhang, Y. Feng, N. Wang, L. Zhou, C. Liang, L. Chen, Y. Lai, X. Ji, C. Yan and W. Wei, *Adv. Mater.* **2021**, *33*, 2100171.
- [98] J. Li, Z. Xiong, Y. Wu, H. Li, X. Liu, H. Peng, Y. Zheng, Q. Zhang and Q. Liu, *J. Energy Chem.* **2022**, *73*, 513-532.
- [99] E. P. Kamphaus and P. B. Balbuena, *J. Phys. Chem. C* **2016**, *120*, 4296-4305.

- [100] K. Lv, P. Wang, C. Wang, Z. Shen, Z. Lu, H. Zhang, M. Zheng, P. He and H. Zhou, *Small* **2020**, *16*, 2000870.
- [101] S. Ju, T.-Y. Cai, H.-S. Lu and C.-D. Gong, *J. Am. Chem. Soc.* **2012**, *134*, 13780-13786.
- [102] W. Sun, C. Liu, Y. Li, S. Luo, S. Liu, X. Hong, K. Xie, Y. Liu, X. Tan and C. Zheng, *ACS Nano* **2019**, *13*, 12137-12147.
- [103] B. Jiang, D. Tian, Y. Qiu, X. Song, Y. Zhang, X. Sun, H. Huang, C. Zhao, Z. Guo, L. Fan and N. Zhang, *Nano-Micro Lett.* **2021**, *14*, 40.
- [104] C. Zheng, S. Niu, W. Lv, G. Zhou, J. Li, S. Fan, Y. Deng, Z. Pan, B. Li, F. Kang and Q.-H. Yang, *Nano Energy* **2017**, *33*, 306-312.
- [105] T. Yamanaka, H. Shimazu and K. Ota, *Phys. Chem. Miner.* **2001**, *28*, 110-118.
- [106] J. He, L. Luo, Y. Chen and A. Manthiram, *Adv. Mater.* **2017**, *29*, 1702707.
- [107] N. Zhang, B. D. Levin, Y. Yang, D. A. Muller and H. D. Abruña, *J. Electrochem. Soc.* **2018**, *165*, A1656.
- [108] X. Chen, H.-J. Peng, R. Zhang, T.-Z. Hou, J.-Q. Huang, B. Li and Q. Zhang, *ACS Energy Lett.* **2017**, *2*, 795-801.
- [109] G. Babu, N. Masurkar, H. Al Salem and L. M. R. Arava, *J. Am. Chem. Soc.* **2017**, *139*, 171-178.
- [110] S. S. Zhang and D. T. Tran, *J. Mater. Chem. A* **2016**, *4*, 4371-4374.
- [111] A. Douglas, R. Carter, L. Oakes, K. Share, A. P. Cohn and C. L. Pint, *ACS Nano* **2015**, *9*, 11156-11165.
- [112] X. Rui, H. Tan and Q. Yan, *Nanoscale* **2014**, *6*, 9889-9924.
- [113] W. M. Skinner, H. W. Nesbitt and A. R. Pratt, *Geochim. Cosmochim. Acta* **2004**, *68*, 2259-2263.
- [114] G. Zhou, H. Tian, Y. Jin, X. Tao, B. Liu, R. Zhang, Z. W. Seh, D. Zhuo, Y. Liu, J. Sun, J. Zhao, C. Zu, D. S. Wu, Q. Zhang and Y. Cui, *Proc. Natl. Acad. Sci. U. S. A.* **2017**, *114*, 840-845.
- [115] Z. Chen, A. Liao, Z. Guo, F. Yu, T. Mei, Z. Zhang, M. S. Irshad, C. Liu, L. Yu and X. Wang, *Electrochim. Acta* **2020**, *353*, 136561.
- [116] W. Li, Z. Gong, X. Yan, D. Wang, J. Liu, X. Guo, Z. Zhang and G. Li, *J. Mater. Chem. A* **2020**, *8*, 433-442.
- [117] D. Liu, C. Zhang, G. Zhou, W. Lv, G. Ling, L. Zhi and Q. H. Yang, *Adv. Sci.* **2018**, *5*, 1700270.
- [118] N. Mosavati, S. O. Salley and K. Y. S. Ng, *J. Power Sources* **2017**, *340*, 210-216.

- [119] J. Wu, T. Ye, Y. Wang, P. Yang, Q. Wang, W. Kuang, X. Chen, G. Duan, L. Yu, Z. Jin, J. Qin and Y. Lei, *ACS Nano* **2022**, *16*, 15734-15759.
- [120] Y. Li, D. Pan, Y. Zhou, Q. Kuang, C. Wang, B. Li, B. Zhang, J. Park, D. Li, C. Choi and Z. Zhang, *Nanoscale* **2020**, *12*, 10834-10841.
- [121] T. Liapina, A. Leineweber, E. J. Mittemeijer and W. Kockelmann, *Acta Mater.* **2004**, *52*, 173-180.
- [122] T. T. Nguyen, J. Balamurugan, H. W. Go, Q. P. Ngo, N. H. Kim and J. H. Lee, *Chem. Eng. J.* **2022**, *427*, 131774.
- [123] C. Giordano, C. Erpen, W. Yao, B. Milke and M. Antonietti, *Chemistry of Materials* **2009**, *21*, 5136-5144.
- [124] H. Zhao, M. Lei, X. Chen and W. Tang, *Journal of Materials Chemistry* **2006**, *16*, 4407-4412.
- [125] Y.-S. Jun, W. H. Hong, M. Antonietti and A. Thomas, *Advanced Materials* **2009**, *21*, 4270-4274.
- [126] Z. Li, Y. Fang, J. Zhang and X. W. Lou, *Adv. Mater.* **2018**, *30*, 1800525.
- [127] a) H. Wang, W. Zhang, J. Xu and Z. Guo, *Adv. Funct. Mater.* **2018**, *28*, 1707520; b) Q. Pang, D. Kundu, M. Cuisinier and L. F. Nazar, *Nat. Commun.* **2014**, *5*, 4759.
- [128] D. S. Wu, F. Shi, G. Zhou, C. Zu, C. Liu, K. Liu, Y. Liu, J. Wang, Y. Peng and Y. Cui, *Energy Storage Mater.* **2018**, *13*, 241-246.
- [129] a) W. Liu, C. Luo, S. Zhang, B. Zhang, J. Ma, X. Wang, W. Liu, Z. Li, Q.-H. Yang and W. Lv, *ACS Nano* **2021**, *15*, 7491-7499; b) H. Lin, S. Zhang, T. Zhang, H. Ye, Q. Yao, G. W. Zheng and J. Y. Lee, *Adv. Energy Mater.* **2019**, *9*, 1902096; c) W. Bao, L. Liu, C. Wang, S. Choi, D. Wang and G. Wang, *Adv. Energy Mater.* **2018**, *8*, 1702485; d) Z. Cheng, Y. Wang, W. Zhang and M. Xu, *ACS Appl. Energy Mater.* **2020**, *3*, 4523-4530.
- [130] a) R. Sun, Y. Bai, Z. Bai, L. Peng, M. Luo, M. Qu, Y. Gao, Z. Wang, W. Sun and K. Sun, *Adv. Energy Mater.* **2022**, *12*, 2102739; b) L. Xu, H. Zhao, M. Sun, B. Huang, J. Wang, J. Xia, N. Li, D. Yin, M. Luo and F. Luo, *Angew. Chem.* **2019**, *131*, 11615-11620; c) H.-J. Li, Y.-H. Song, K. Xi, W. Wang, S. Liu, G.-R. Li and X.-P. Gao, *J. Mater. Chem. A* **2021**, *9*, 10704-10713.
- [131] a) B. Zhang, C. Luo, Y. Deng, Z. Huang, G. Zhou, W. Lv, Y.-B. He, Y. Wan, F. Kang and Q.-H. Yang, *Adv. Energy Mater.* **2020**, *10*, 2000091; b) S. Huang, Z. Wang, Y. Von Lim, Y. Wang, Y. Li, D. Zhang and H. Y. Yang, *Adv. Energy Mater.* **2021**, *11*, 2003689; c) C. Ye, Y. Jiao, H. Jin, A. D. Slattery, K. Davey, H. Wang and S.-Z. Qiao, *Angew. Chem. Int. Ed.*

- 2018, 57, 16703-16707; d) W. Yao, W. Zheng, J. Xu, C. Tian, K. Han, W. Sun and S. Xiao, *ACS Nano* **2021**, 15, 7114-7130.
- [132] S. Evers, T. Yim and L. F. Nazar, *J. Phys. Chem. C* **2012**, 116, 19653-19658.
- [133] a) D. Xie, S. Mei, Y. Xu, T. Quan, E. Härk, Z. Kochovski and Y. Lu, *ChemSusChem* **2021**, 14, 1404-1413; b) P. Xu, H. Liu, Q. Zeng, X. Li, Q. Li, K. Pei, Y. Zhang, X. Yu, J. Zhang, X. Qian and R. Che, *Small* **2021**, 17, 2005227.
- [134] a) Z. Li, J. Zhang, B. Guan, D. Wang, L.-M. Liu and X. W. Lou, *Nat. Commun.* **2016**, 7, 13065; b) X. Huang, T. Qiu, X. Zhang, L. Wang, B. Luo and L. Wang, *Mater. Chem. Front.* **2020**, 4, 2517-2547; c) S. Mei, A. Siebert, Y. Xu, T. Quan, R. Garcia-Diez, M. Bär, P. Härtel, T. Abendroth, S. Dörfler, S. Kaskel and Y. Lu, *Batter. Supercaps* **2022**, 5, e202100398.
- [135] a) Z. Shen, Z. Zhang, M. Li, Y. Yuan, Y. Zhao, S. Zhang, C. Zhong, J. Zhu, J. Lu and H. Zhang, *ACS Nano* **2020**, 14, 6673-6682; b) S. Rehman, T. Tang, Z. Ali, X. Huang and Y. Hou, *Small* **2017**, 13, 1700087.
- [136] a) J. Wang, Y. Zhao, G. Li, D. Luo, J. Liu, Y. Zhang, X. Wang, L. Shui and Z. Chen, *Nano Energy* **2021**, 84, 105891; b) Y. Li, T. Jiang, H. Yang, D. Lei, X. Deng, C. Hao, F. Zhang and J. Guo, *Electrochim. Acta* **2020**, 330, 135311; c) J. Shen, X. Xu, J. Liu, Z. Liu, F. Li, R. Hu, J. Liu, X. Hou, Y. Feng, Y. Yu and M. Zhu, *ACS Nano* **2019**, 13, 8986-8996; d) S. Chen, J. Zhang, Z. Wang, L. Nie, X. Hu, Y. Yu and W. Liu, *Nano Lett.* **2021**, 21, 5285-5292; e) M. Liu, N. Deng, J. Ju, L. Fan, L. Wang, Z. Li, H. Zhao, G. Yang, W. Kang and J. Yan, *Adv. Funct. Mater.* **2019**, 29, 1905467.
- [137] J. Zhang, Z. Li, Y. Chen, S. Gao and X. W. Lou, *Angew. Chem.* **2018**, 130, 11110-11114.
- [138] a) D. Gu and F. Schüth, *Chem. Soc. Rev.* **2014**, 43, 313-344; b) Y. Ren, Z. Ma and P. G. Bruce, *Chem. Soc. Rev.* **2012**, 41, 4909-4927.
- [139] a) C. K. Tsung, J. Fan, N. Zheng, Q. Shi, A. J. Forman, J. Wang and G. D. Stucky, *Angew. Chem.* **2008**, 120, 8810-8814; b) H. Xu and W. Wang, *Angew. Chem.* **2007**, 119, 1511-1514.
- [140] a) L. Hou, L. Lian, L. Zhang, G. Pang, C. Yuan and X. Zhang, *Adv. Funct. Mater.* **2015**, 25, 238-246; b) X. Zhang, C. Y. Chuah, P. Dong, Y.-H. Cha, T.-H. Bae and M.-K. Song, *ACS Appl. Mater. Interfaces* **2018**, 10, 43316-43322; c) X. Xu, F. Li, D. Zhang, Z. Liu, S. Zuo, Z. Zeng and J. Liu, *Adv. Sci.* **2022**, 9, 2200247; d) S. Zhang, W. Wu, X. Xiao, J. Zhou, F. Ren and C. Jiang, *Nanoscale Res. Lett.* **2011**, 6, 89.



- [141] a) R.-P. Zhang, W.-C. Li, G.-P. Hao and A.-H. Lu, *Nano Research* **2021**, *14*, 3159-3173; b) M. Cai, Z. Wu, Z. Li, L. Wang, W. Sun, A. A. Tountas, C. Li, S. Wang, K. Feng, A.-B. Xu, S. Tang, A. Tavasoli, M. Peng, W. Liu, A. S. Helmy, L. He, G. A. Ozin and X. Zhang, *Nat. Energy* **2021**, *6*, 807-814; c) Y. Piao, J. Kim, H. B. Na, D. Kim, J. S. Baek, M. K. Ko, J. H. Lee, M. Shokouhimehr and T. Hyeon, *Nat. Mater.* **2008**, *7*, 242-247; d) S. Soll, T.-P. Fellingner, X. Wang, Q. Zhao, M. Antonietti and J. Yuan, *Small* **2013**, *9*, 4135-4141; e) S. Xuan, F. Wang, J. M. Y. Lai, K. W. Y. Sham, Y.-X. J. Wang, S.-F. Lee, J. C. Yu, C. H. K. Cheng and K. C.-F. Leung, *ACS Appl. Mater. Interfaces* **2011**, *3*, 237-244.
- [142] Y. Huang, Z. Li, T. Zhu, X. Gao, X. Lv, M. Ling, Z. Wan and Y. Xia, *ACS Appl. Energy Mater.* **2021**, *4*, 3921-3927.
- [143] S. Xin, J. Li, H. Cui, Y. Liu, H. Wei, y. Zhong and M. Wang, *Chem. Eng. J.* **2021**, *410*, 128153.
- [144] X. Wang, X. Chen, L. Gao, H. Zheng, M. Ji, C. Tang, T. Shen and Z. Zhang, *J. Mater. Chem.* **2004**, *14*, 905-907.
- [145] P. A. Midgley and R. E. Dunin-Borkowski, *Nat. Mater.* **2009**, *8*, 271-280.
- [146] E. P. Barrett, L. G. Joyner and P. P. Halenda, *J. Am. Chem. Soc.* **1951**, *73*, 373-380.
- [147] G. Pickett, *J. Am. Chem. Soc.* **1945**, *67*, 1958-1962.
- [148] E. Liu, H. Yuan, Z. Kou, X. Wu, Q. Xu, Y. Zhai, Y. Sui, B. You, J. Du and H. Zhai, *Sci. Rep.* **2015**, *5*, 11164.
- [149] Y. Xie, J. Cao, X. Wang, W. Li, L. Deng, S. Ma, H. Zhang, C. Guan and W. Huang, *Nano Lett.* **2021**, *21*, 8579-8586.
- [150] J. Xie, B.-Q. Li, H.-J. Peng, Y.-W. Song, M. Zhao, X. Chen, Q. Zhang and J.-Q. Huang, *Adv. Mater.* **2019**, *31*, 1903813.
- [151] J. Song, T. Xu, M. L. Gordin, P. Zhu, D. Lv, Y.-B. Jiang, Y. Chen, Y. Duan and D. Wang, *Adv. Funct. Mater.* **2014**, *24*, 1243-1250.
- [152] X. Chen, S. Zeng, H. Muheiyati, Y. Zhai, C. Li, X. Ding, L. Wang, D. Wang, L. Xu, Y. He and Y. Qian, *ACS Energy Lett.* **2019**, *4*, 1496-1504.
- [153] Z. Yuan, H. J. Peng, T. Z. Hou, J. Q. Huang, C. M. Chen, D. W. Wang, X. B. Cheng, F. Wei and Q. Zhang, *Nano Lett* **2016**, *16*, 519-527.
- [154] H. Yuan, H.-J. Peng, B.-Q. Li, J. Xie, L. Kong, M. Zhao, X. Chen, J.-Q. Huang and Q. Zhang, *Adv. Energy Mater.* **2019**, *9*, 1802768.
- [155] Q. Lin, L. Huang, W. Liu, Z. Li, R. Fang, D.-W. Wang, Q.-H. Yang and W. Lv, *Phys. Chem. Chem. Phys.* **2021**, *23*, 21385-21398.

- [156] a) Z. Li, Y. Zhou, Y. Wang and Y.-C. Lu, *Adv. Energy Mater.* **2019**, *9*, 1802207; b) A. Bewick, M. Fleischmann and H. Thirsk, *Trans. Faraday Soc.* **1962**, *58*, 2200-2216; c) B. Scharifker and G. Hills, *Electrochim. Acta* **1983**, *28*, 879-889.
- [157] J.-L. Yang, D.-Q. Cai, X.-G. Hao, L. Huang, Q. Lin, X.-T. Zeng, S.-X. Zhao and W. Lv, *ACS Nano* **2021**, *15*, 11491-11500.
- [158] B. Wang, L. Wang, B. Zhang, S. Zeng, F. Tian, J. Dou, Y. Qian and L. Xu, *ACS Nano* **2022**, *16*, 4947-4960.
- [159] a) Z. Cheng, Z. Xiao, H. Pan, S. Wang and R. Wang, *Adv. Energy Mater.* **2018**, *8*, 1702337; b) S. Liu, J. Li, X. Yan, Q. Su, Y. Lu, J. Qiu, Z. Wang, X. Lin, J. Huang, R. Liu, B. Zheng, L. Chen, R. Fu and D. Wu, *Adv. Mater.* **2018**, *30*, e1706895.
- [160] C. Zhang, R. Du, J. J. Biendicho, M. Yi, K. Xiao, D. Yang, T. Zhang, X. Wang, J. Arbiol and J. Llorca, *Adv. Energy Mater.* **2021**, *11*, 2100432.
- [161] a) W. Ren, W. Ma, S. Zhang and B. Tang, *Energy Storage Mater.* **2019**, *23*, 707-732; b) A. Manthiram, S. H. Chung and C. Zu, *Adv. Mater.* **2015**, *27*, 1980-2006.
- [162] Y. Zhang, G. Li, J. Wang, G. Cui, X. Wei, L. Shui, K. Kempa, G. Zhou, X. Wang and Z. Chen, *Nat. Commun.* **2020**, *30*, 2001165.
- [163] J. Shen, X. Xu, J. Liu, Z. Liu, F. Li, R. Hu, J. Liu, X. Hou, Y. Feng, Y. Yu and M. Zhu, *ACS Nano* **2019**, *13*, 8986-8996.
- [164] Y. Chen, W. Zhang, D. Zhou, H. Tian, D. Su, C. Wang, D. Stockdale, F. Kang, B. Li and G. Wang, *ACS Nano* **2019**, *13*, 4731-4741.
- [165] a) Y. Zhang, R. Gu, S. Zheng, K. Liao, P. Shi, J. Fan, Q. Xu and Y. Min, *J. Mater. Chem. A* **2019**, *7*, 21747-21758; b) W. Li, Z. Chen, D. Wang, Z. Gong, C. Mao, J. Liu, H. Peng, Z. Zhang and G. Li, *J. Power Sources* **2019**, *435*, 226778; c) Y. Boyjoo, H. Shi, E. Olsson, Q. Cai, Z.-S. Wu, J. Liu and G. Q. Lu, *Adv. Energy Mater.* **2020**, *10*, 2000651; d) P. Jiang, S. Chen, C. Wang, D. Wang, J. Diao, Z. Cao, Z. Lin, Q. Luo, J. Lu, H. Huang, C. Zong, L. Hu and Q. Chen, *Mater. Today Sustain.* **2020**, *9*, 100039.
- [166] J. Zhou, X. Liu, L. Zhu, J. Zhou, Y. Guan, L. Chen, S. Niu, J. Cai, D. Sun, Y. Zhu, J. Du, G. Wang and Y. Qian, *Joule* **2018**, *2*, 2681-2693.
- [167] Z. Liu, T. Lu, T. Song, X.-Y. Yu, X. W. Lou and U. Paik, *Energy Environ. Sci.* **2017**, *10*, 1576-1580.
- [168] a) Q. Wang, W. Zhang, C. Guo, Y. Liu, C. Wang and Z. Guo, *Adv. Funct. Mater.* **2017**, *27*, 1703390; b) Y. Zhao, J. Zhu, S. J. H. Ong, Q. Yao, X. Shi, K. Hou, Z. J. Xu and L. Guan, *Adv. Energy Mater.* **2018**, *8*, 1802565.

- [169] Y. Xi, X. Ye, S. Duan, T. Li, J. Zhang, L. Jia, J. Yang, J. Wang, H. Liu and Q. Xiao, *J. Mater. Chem. A* **2020**, *8*, 14769-14777.
- [170] L. Wu, N. Y. Dzade, L. Gao, D. O. Scanlon, Z. Öztürk, N. Hollingsworth, B. M. Weckhuysen, E. J. Hensen, N. H. De Leeuw and J. P. Hofmann, *Adv. Mater.* **2016**, *28*, 9602-9607.
- [171] A. Matamoros-Veloza, O. Cespedes, B. R. Johnson, T. M. Stawski, U. Terranova, N. H. de Leeuw and L. G. Benning, *Nat. Commun.* **2018**, *9*, 1-7.
- [172] Z. Yang, K. Qian, J. Lv, W. Yan, J. Liu, J. Ai, Y. Zhang, T. Guo, X. Zhou and S. Xu, *Sci. Rep.* **2016**, *6*, 1-10.
- [173] D. Zhang, S. Wang, R. Hu, J. Gu, Y. Cui, B. Li, W. Chen, C. Liu, J. Shang and S. Yang, *Adv. Funct. Mater.* **2020**, *30*, 2002471.
- [174] Y. Wang, D. Adekoya, J. Sun, T. Tang, H. Qiu, L. Xu, S. Zhang and Y. Hou, *Adv. Funct. Mater.* **2018**, *29*, 1807485.
- [175] a) M. Wagemaker and F. M. Mulder, *Acc. Chem. Res.* **2013**, *46*, 1206-1215; b) H. Chen, C. Wang, W. Dong, W. Lu, Z. Du and L. Chen, *Nano Lett.* **2015**, *15*, 798-802.
- [176] a) H. Yuan, X. Chen, G. Zhou, W. Zhang, J. Luo, H. Huang, Y. Gan, C. Liang, Y. Xia, J. Zhang, J. Wang and X. Tao, *ACS Energy Lett.* **2017**, *2*, 1711-1719; b) M. Zhao, H.-J. Peng, Z.-W. Zhang, B.-Q. Li, X. Chen, J. Xie, X. Chen, J.-Y. Wei, Q. Zhang and J.-Q. Huang, *Angew. Chem. Int. Ed.* **2019**, *58*, 3779-3783.
- [177] a) G. He, S. Evers, X. Liang, M. Cuisinier, A. Garsuch and L. F. Nazar, *ACS Nano* **2013**, *7*, 10920-10930; b) W. Zhou, C. Wang, Q. Zhang, H. D. Abruña, Y. He, J. Wang, S. X. Mao and X. Xiao, *Adv. Energy Mater.* **2015**, *5*, 1401752.
- [178] a) S.-K. Park, J. Lee, T. Hwang and Y. Piao, *J. Mater. Chem. A* **2017**, *5*, 975-981; b) G. Tan, R. Xu, Z. Xing, Y. Yuan, J. Lu, J. Wen, C. Liu, L. Ma, C. Zhan, Q. Liu, T. Wu, Z. Jian, R. Shahbazian-Yassar, Y. Ren, D. J. Miller, L. A. Curtiss, X. Ji and K. Amine, *Nat. Energy* **2017**, *2*, 17090.
- [179] a) K. Jin, X. Zhou, L. Zhang, X. Xin, G. Wang and Z. Liu, *J. Phys. Chem. C* **2013**, *117*, 21112-21119; b) S. Dörfler, M. Hagen, H. Althues, J. Tübke, S. Kaskel and M. J. Hoffmann, *Chem. Commun.* **2012**, *48*, 4097-4099.
- [180] a) Z. Lyu, D. Xu, L. Yang, R. Che, R. Feng, J. Zhao, Y. Li, Q. Wu, X. Wang and Z. Hu, *Nano Energy* **2015**, *12*, 657-665; b) J. Zhang, C.-P. Yang, Y.-X. Yin, L.-J. Wan and Y.-G. Guo, *Adv. Mater.* **2016**, *28*, 9539-9544; c) C. Ma, Z. Zheng, X. Jia, X. Liu, J. Wang, W. Qiao and L. Ling, *J. Power Sources* **2021**, *486*, 229358.

- [181] a) X. Liang, C. Y. Kwok, F. Lodi-Marzano, Q. Pang, M. Cuisinier, H. Huang, C. J. Hart, D. Houtarde, K. Kaup, H. Sommer, T. Brezesinski, J. Janek and L. F. Nazar, *Adv. Energy Mater.* **2016**, *6*, 1501636; b) X. Tao, J. Wang, C. Liu, H. Wang, H. Yao, G. Zheng, Z. W. Seh, Q. Cai, W. Li, G. Zhou, C. Zu and Y. Cui, *Nat. Commun.* **2016**, *7*, 11203.
- [182] Z. Sun, J. Zhang, L. Yin, G. Hu, R. Fang, H. M. Cheng and F. Li, *Nat Commun* **2017**, *8*, 14627.
- [183] F. Zhou, Z. Li, X. Luo, T. Wu, B. Jiang, L. L. Lu, H. B. Yao, M. Antonietti and S. H. Yu, *Nano Lett.* **2018**, *18*, 1035-1043.
- [184] a) M. Wang, L. Fan, X. Sun, B. Guan, B. Jiang, X. Wu, D. Tian, K. Sun, Y. Qiu, X. Yin, Y. Zhang and N. Zhang, *ACS Energy Lett.* **2020**, *5*, 3041-3050; b) W. Tian, B. Xi, Z. Feng, H. Li, J. Feng and S. Xiong, *Adv. Energy Mater.* **2019**, *9*, 1901896.
- [185] H. Wang, J. Li, K. Li, Y. Lin, J. Chen, L. Gao, V. Nicolosi, X. Xiao and J.-M. Lee, *Chem. Soc. Rev.* **2021**, *50*, 1354-1390.
- [186] a) Z. Li, Q. He, X. Xu, Y. Zhao, X. Liu, C. Zhou, D. Ai, L. Xia and L. Mai, *Adv. Mater.* **2018**, *30*, 1804089; b) Z. Cui, C. Zu, W. Zhou, A. Manthiram and J. B. Goodenough, *Adv. Mater.* **2016**, *28*, 6926-6931.
- [187] a) R. Liu, W. Liu, Y. Bu, W. Yang, C. Wang, C. Priest, Z. Liu, Y. Wang, J. Chen, Y. Wang, J. Cheng, X. Lin, X. Feng, G. Wu, Y. Ma and W. Huang, *ACS Nano* **2020**, *14*, 17308-17320; b) Y. Zhong, D. Chao, S. Deng, J. Zhan, R. Fang, Y. Xia, Y. Wang, X. Wang, X. Xia and J. Tu, *Adv. Funct. Mater.* **2018**, *28*, 1706391.
- [188] L. Zhang, X. Chen, F. Wan, Z. Niu, Y. Wang, Q. Zhang and J. Chen, *ACS Nano* **2018**, *12*, 9578-9586.
- [189] a) Z. Sun, S. Vijay, H. H. Heenen, A. Y. S. Eng, W. Tu, Y. Zhao, S. W. Koh, P. Gao, Z. W. Seh, K. Chan and H. Li, *Adv. Energy Mater.* **2020**, *10*, 1904010; b) D.-R. Deng, F. Xue, Y.-J. Jia, J.-C. Ye, C.-D. Bai, M.-S. Zheng and Q.-F. Dong, *ACS Nano* **2017**, *11*, 6031-6039; c) K. Xiao, J. Wang, Z. Chen, Y. Qian, Z. Liu, L. Zhang, X. Chen, J. Liu, X. Fan and Z. X. Shen, *Small* **2019**, *15*, 1901454.
- [190] R. Li, H. Peng, Q. Wu, X. Zhou, J. He, H. Shen, M. Yang and C. Li, *Angew. Chem. Int. Ed.* **2020**, *59*, 12129-12138.
- [191] H. Liu, H. Shen, R. Li, S. Liu, A. Turak and M. Yang, *ChemElectroChem* **2019**, *6*, 2074-2079.
- [192] M. Zhang, L. Wang, B. Wang, B. Zhang, X. Sun, D. Wang, Z. Kong and L. Xu, *J. Mater. Chem. A* **2021**, *9*, 6538-6546.

- [193] F. Xu, B. Ding, Y. Qiu, R. Dong, W. Zhuang, X. Xu, H. Han, J. Yang, B. Wei, H. Wang and S. Kaskel, *Matter* **2020**, *3*, 246-260.
- [194] H. Wang, Y. Shao, S. Mei, Y. Lu, M. Zhang, J.-k. Sun, K. Matyjaszewski, M. Antonietti and J. Yuan, *Chem. Rev.* **2020**, *120*, 9363-9419.
- [195] a) H. Pan, Z. Cheng, Z. Xiao, X. Li and R. Wang, *Adv. Funct. Mater.* **2017**, *27*, 1703936; b) Z. Cheng, H. Pan, J. Chen, X. Meng and R. Wang, *Adv. Energy Mater.* **2019**, *9*, 1901609; c) H. Wang, S. Min, Q. Wang, D. Li, G. Casillas, C. Ma, Y. Li, Z. Liu, L.-J. Li, J. Yuan, M. Antonietti and T. Wu, *ACS Nano* **2017**, *11*, 4358-4364.
- [196] a) J. Balach, H. Wu, F. Polzer, H. Kirmse, Q. Zhao, Z. Wei and J. Yuan, *RSC Advances* **2013**, *3*, 7979-7986; b) Z. Li, Z. Xiao, P. Li, X. Meng and R. Wang, *Small* **2020**, *16*, 1906114.
- [197] W. Zhang, Z. Kochovski, Y. Lu, B. V. Schmidt, M. Antonietti and J. Yuan, *ACS Nano* **2016**, *10*, 7731-7737.
- [198] a) R. Fei, H. Wang, Q. Wang, R. Qiu, S. Tang, R. Wang, B. He, Y. Gong and H. J. Fan, *Adv. Energy Mater.* **2020**, *10*, 2002741; b) J. Gao, Y. Li, B. Peng, G. Wang and G. Zhang, *J. Mater. Chem. A* **2019**, *7*, 24199-24204.
- [199] M. Einert, C. Wessel, F. Badaczewski, T. Leichtweiß, C. Eufinger, J. Janek, J. Yuan, M. Antonietti and B. M. Smarsly, *Macromol. Chem. Phys.* **2015**, *216*, 1930-1944.
- [200] A. Leineweber, H. Jacobs, F. Hüning, H. Lueken and W. Kockelmann, *J. Alloys Compd.* **2001**, *316*, 21-38.
- [201] a) Q. Cheng, K. Mao, L. Ma, L. Yang, L. Zou, Z. Zou, Z. Hu and H. Yang, *ACS Energy Lett.* **2018**, *3*, 1205-1211; b) J. Xiao, Y. Xu, Y. Xia, J. Xi and S. Wang, *Nano Energy* **2016**, *24*, 121-129.
- [202] J. He, A. Bhargav and A. Manthiram, *ACS Nano* **2021**, *15*, 8583-8591.
- [203] a) H.-J. Peng, Z.-W. Zhang, J.-Q. Huang, G. Zhang, J. Xie, W.-T. Xu, J.-L. Shi, X. Chen, X.-B. Cheng and Q. Zhang, *Adv. Mater.* **2016**, *28*, 9551-9558; b) P. Zeng, C. Liu, X. Zhao, C. Yuan, Y. Chen, H. Lin and L. Zhang, *ACS Nano* **2020**, *14*, 11558-11569.
- [204] J.-K. Sun, Z. Kochovski, W.-Y. Zhang, H. Kirmse, Y. Lu, M. Antonietti and J. Yuan, *J. Am. Chem. Soc.* **2017**, *139*, 8971-8976.
- [205] X. Huang, Z. Wang, R. Knibbe, B. Luo, S. A. Ahad, D. Sun and L. Wang, *Energy Technol.* **2019**, *7*, 1801001.
- [206] X. Yang and A. L. Rogach, *Adv. Energy Mater.* **2019**, *9*, 1900747.

- [207] J. Epp in *4 - X-ray diffraction (XRD) techniques for materials characterization*, Eds.: G. Hübschen, I. Altpeter, R. Tschuncky and H.-G. Herrmann), Woodhead Publishing, **2016**, pp. 81-124.
- [208] G. Will, *Powder diffraction: The Rietveld method and the two stage method to determine and refine crystal structures from powder diffraction data*, Springer Science & Business Media, **2006**, p.
- [209] L. Spieß, H. Behnken, C. Genzel, R. Schwarzer and G. Teichert, *Moderne röntgenbeugung*, Springer, **2009**, p.
- [210] F. A. Stevie and C. L. Donley, *J. Vac. Sci. Technol. A: Vacuum, Surfaces, and Films* **2020**, 38, 063204.
- [211] S. Mosca, C. Conti, N. Stone and P. Matousek, *Nat. Rev. Methods Primers* **2021**, 1, 21.
- [212] A. Downes and A. Elfick, *Sensors* **2010**, 10, 1871-1889.
- [213] M. Testa-Anta, M. A. Ramos-Docampo, M. Comesaña-Hermo, B. Rivas-Murias and V. Salgueiriño, *Nanoscale Adv.* **2019**, 1, 2086-2103.
- [214] M. R. Sharpe, *Anal. Chem.* **1984**, 56, 339A-356A.
- [215] M. Picollo, M. Aceto and T. Vitorino, *Phys. Sci. Rev.* **2019**, 4.
- [216] A. M. Alshehawy, D.-E. A. Mansour, M. Ghali, M. Lehtonen and M. M. Darwish, *Processes* **2021**, 9, 732.
- [217] B. J. Inkson in *2 - Scanning electron microscopy (SEM) and transmission electron microscopy (TEM) for materials characterization*, Eds.: G. Hübschen, I. Altpeter, R. Tschuncky and H.-G. Herrmann), Woodhead Publishing, **2016**, pp. 17-43.
- [218] D. C. Bell and N. Erdman, *Low voltage electron microscopy: principles and applications*, John Wiley & Sons, **2012**, p.
- [219] K. A. Taylor and R. M. Glaeser, *Science* **1974**, 186, 1036-1037.
- [220] a) X.-C. Ren, X.-Q. Zhang, R. Xu, J.-Q. Huang and Q. Zhang, *Adv. Mater.* **2020**, 32, 1908293; b) Z. Kochovski, G. Chen, J. Yuan and Y. Lu, *Colloid. Polym. Sci.* **2020**, 298, 707-717.
- [221] S. Carencu, S. Moldovan, L. Roiban, I. Florea, D. Portehault, K. Vallé, P. Belleville, C. Boissière, L. Rozes, N. Mézailles, M. Drillon, C. Sanchez and O. Ersen, *Nanoscale* **2016**, 8, 1260-1279.
- [222] a) H. Friedrich, P. E. de Jongh, A. J. Verkleij and K. P. de Jong, *Chem. Rev.* **2009**, 109, 1613-1629; b) H. Song, Y. Yang, J. Geng, Z. Gu, J. Zou and C. Yu, *Adv. Mater.* **2019**, 31, 1801564.

- [223] D. N. Mastronarde, *J. Struct. Biol.* **2005**, *152*, 36-51.
- [224] J. R. Kremer, D. N. Mastronarde and J. R. McIntosh, *J. Struct. Biol.* **1996**, *116*, 71-76.
- [225] E. F. Pettersen, T. D. Goddard, C. C. Huang, G. S. Couch, D. M. Greenblatt, E. C. Meng and T. E. Ferrin, *J. Comput. Chem.* **2004**, *25*, 1605-1612.
- [226] M. Thommes, K. Kaneko, A. V. Neimark, J. P. Olivier, F. Rodriguez-Reinoso, J. Rouquerol and K. S. W. Sing, *Pure Appl. Chem.* **2015**, *87*, 1051-1069.
- [227] Y. Zhang, D. Shao, J. Yan, X. Jia, Y. Li, P. Yu and T. Zhang, *J. Nat. Gas Eng.* **2016**, *1*, 213-220.





## List of Figures

<b>Figure 1.1</b> (a) Comparison of the components in Li-ion and Li-S batteries; <sup>[2, 8]</sup> (b) theoretical energy densities of Li-S and Li-ion batteries, respectively. <sup>[9]</sup> .....	1
<b>Figure 1.2</b> (a) Polysulfide shuttle effect in a Li-S battery; <sup>[18]</sup> (b) typical voltage profile of a Li-S battery during the discharge-charge process. <sup>[19]</sup> .....	3
<b>Figure 1.3</b> (a) The schematization of the intertwined phenomena inducing the degradation of the Li metal anode during cycling; <sup>[29]</sup> (b) Li-S batteries without/with the Li <sub>3</sub> N layer; <sup>[30]</sup> (c) Li deposition in a conventional 2D planar current collector and a 3D porous current collector, respectively. <sup>[31]</sup> .....	5
<b>Figure 1.4</b> Relative energies of the electrolyte window $E_g$ and the electrode electrochemical potentials $\mu_A$ and $\mu_C$ . <sup>[2]</sup> .....	7
<b>Figure 1.5</b> (a) The structures of S <sub>8</sub> and Li <sub>2</sub> S <sub>n</sub> (n = 8, 6, 4, 2, and 1), where the green and yellow balls represent the Li and S atoms, respectively; <sup>[46]</sup> (b) different Li <sub>2</sub> S <sub>n</sub> dissolved in DOL/DME solvents. <sup>[47]</sup> .....	9
<b>Figure 1.6</b> (a) A schematic diagram of the sulfur (yellow) confined in CMK-3 with the melting impregnation and lithium/delithiation process; <sup>[58]</sup> (b) illustration of the difference in solvent accessibility by sulfur in carbon pores of varying size (ultramicroporous carbon (UMC), microporous and mesoporous carbon) in carbon/sulfur composites. <sup>[59]</sup> .....	11
<b>Figure 1.7</b> Illustration of the working mechanism of the different conductors. <sup>[64]</sup> .....	13
<b>Figure 2.1</b> The influence of the various types of polarization on the discharge curve of a battery. <sup>[65]</sup> .....	22
<b>Figure 2.2</b> (a) Schematic illustration for the fabrication of TiN-O-OMC particles; <sup>[74]</sup> (b) schematic lithiation process of sulfur-TiO <sub>2</sub> core-shell and sulfur-TiO <sub>2</sub> yolk-shell spherical particles; <sup>[75]</sup> .....	25
<b>Figure 2.3</b> (a) Schematic representation of different-shaped micelles ranging from spherical micelles ( $g \leq 1/3$ ) to bilayer lamellar micelles ( $g = 1$ ); <sup>[84b]</sup> (b) illustration of synthesis routes for G-mSnO <sub>2</sub> and G-mSnO <sub>2</sub> @S composites with the micelles of CTAB as template; <sup>[87]</sup> (c) schematic illustration of the fabrication of S@polyvinyl alcohol (PVA) particles. <sup>[88]</sup> .....	27
<b>Figure 2.4</b> (a) Crystal structure of hematite Fe <sub>3</sub> O <sub>4</sub> ; <sup>[101]</sup> (b) the calculated binding energy and optimized configurations of Li <sub>2</sub> S <sub>8</sub> and Li <sub>2</sub> S <sub>6</sub> on Fe <sub>3</sub> O <sub>4</sub> (311). <sup>[102]</sup> .....	29
<b>Figure 2.5</b> Crystalline structures of (a) pyrite FeS <sub>2</sub> and (b) troilite FeS; <sup>[112]</sup> the optimized geometries and binding energies of Li <sub>2</sub> S <sub>6</sub> and Li <sub>2</sub> S <sub>8</sub> on the surfaces of (c) FeS <sub>2</sub> and (d) FeS. <sup>[95b]</sup> .....	31
<b>Figure 2.6</b> (a) Phase diagram of the Fe-N binary system, where the red arrow show the stoichiometric $\epsilon$ -Fe <sub>3</sub> N; <sup>[120]</sup> (b) Crystal structure of the stoichiometric $\epsilon$ -Fe <sub>3</sub> N. <sup>[120]</sup> .....	33
<b>Figure 3.1</b> Schematic synthesis route of the C@M-Fe <sub>3</sub> O <sub>4</sub> nanospindles.....	36
<b>Figure 3.2</b> (a) TEM image and (b) XRD pattern of $\beta$ -FeOOH particles.....	37

<b>Figure 3.3</b> TEM images of (a) SiO <sub>2</sub> @FeOOH, (b) SiO <sub>2</sub> @M-Fe <sub>2</sub> O <sub>3</sub> , (c) FeOOH after calcination at 500 °C, and (d) mesoporous Fe <sub>2</sub> O <sub>3</sub> nanospindles; TEM images of a single Fe <sub>2</sub> O <sub>3</sub> particle with the insets of the cross-sectional views in the parallel (e) and perpendicular directions (f), respectively.....	38
<b>Figure 3.4</b> (a) N <sub>2</sub> adsorption-desorption isotherms of M-Fe <sub>2</sub> O <sub>3</sub> particles with the corresponding pore size distribution (inset); (b) XRD pattern of M-Fe <sub>2</sub> O <sub>3</sub> particles.....	39
<b>Figure 3.5</b> TEM images of the PDA@M-Fe <sub>2</sub> O <sub>3</sub> (a) and C@M-Fe <sub>3</sub> O <sub>4</sub> (b, c) nanospindles; (d) HR-TEM image of a randomly selected C@M-Fe <sub>3</sub> O <sub>4</sub> particle.....	40
<b>Figure 3.6</b> (a) XRD pattern and (b) SEM image of C@M-Fe <sub>3</sub> O <sub>4</sub> particles; (c) TGA curve of the C@M-Fe <sub>3</sub> O <sub>4</sub> particles under synthetic air; (d) N <sub>2</sub> adsorption-desorption isotherms of the C@M-Fe <sub>3</sub> O <sub>4</sub> particles with the inset of the corresponding pore size distribution.....	41
<b>Figure 3.7</b> The high-resolution XPS spectra of (a) C 1s, (b) N 1s, and (c) Fe 2p regions for the C@M-Fe <sub>3</sub> O <sub>4</sub> nanospindles.....	42
<b>Figure 3.8</b> (a) TEM image of the M-Carbon particles; (b) N <sub>2</sub> adsorption-desorption isotherms of the M-Carbon particles with corresponding pore size distribution.....	43
<b>Figure 3.9</b> (a) Static adsorption of Li <sub>2</sub> S <sub>8</sub> solution (2 mM) with different host materials (M-Carbon, M-Fe <sub>2</sub> O <sub>3</sub> , and C@M-Fe <sub>3</sub> O <sub>4</sub> ) with the corresponding UV-vis spectra (b) of the supernatants in the vials.....	44
<b>Figure 3.10</b> CV curves of the symmetrical cells with different electrodes (M-Carbon, M-Fe <sub>2</sub> O <sub>3</sub> , and C@M-Fe <sub>3</sub> O <sub>4</sub> ) scanned at 10 mV s <sup>-1</sup> in the range of -0.8 to 0.8 V.....	45
<b>Figure 3.11</b> Current-time plots of catholyte Li <sub>2</sub> S <sub>8</sub> potentiostatic discharged at 2.05 V (vs. Li/Li <sup>+</sup> ) on different host materials (M-Carbon (a), M-Fe <sub>2</sub> O <sub>3</sub> (b), and C@M-Fe <sub>3</sub> O <sub>4</sub> (c)); (d-f) the dimensionless transient of Li <sub>2</sub> S deposition in comparison with theoretical 2D and 3D electroplating models; i: current, i <sub>m</sub> : peak current; t: time, t <sub>m</sub> : time needed to achieve the peak current.....	46
<b>Figure 3.12</b> TGA curves of the M-Carbon/S, M-Fe <sub>2</sub> O <sub>3</sub> /S, and C@M-Fe <sub>3</sub> O <sub>4</sub> /S under nitrogen atmosphere.....	48
<b>Figure 3.13</b> CV profiles of Li-S cells with C@M-Fe <sub>3</sub> O <sub>4</sub> /S, M-Fe <sub>2</sub> O <sub>3</sub> /S, and M-Carbon/S cathodes at 0.1 mV s <sup>-1</sup> in the range of 1.7-2.8 V vs. Li/Li <sup>+</sup> ; (b) initial charge-discharge curves and (c) cycling performances of Li-S cell with different cathodes at 0.1 C (1 C = 1675 mA g <sup>-1</sup> ).....	49
<b>Figure 3.14</b> (a) Cycling performance of Li-S batteries with different cathodes (M-Carbon/S, M-Fe <sub>2</sub> O <sub>3</sub> /S, and C@Fe <sub>3</sub> O <sub>4</sub> /S) at 0.2 C; (b) rate capability of Li-S batteries with different host materials; (c) the initial charge-discharge curves of the C@M-Fe <sub>3</sub> O <sub>4</sub> /S electrode at different C rates; (d) the long-term cycling performance of Li-S cell with C@M-Fe <sub>3</sub> O <sub>4</sub> /S cathode at 1 C.....	50
<b>Figure 3.15</b> EIS spectra of the Li-S batteries with different cathodes before cycling.....	51
<b>Figure 4.1</b> Illustration of the synthetic routes of yolk-shell Fe <sub>3</sub> O <sub>4</sub> -C, FeS-C, and FeS <sub>2</sub> -C nanospindles.....	54
<b>Figure 4.2</b> SEM image of the FeOOH particles with the photograph of the FeOOH particles dispersed in water (a); (b, c) TEM images of the PDA-coated FeOOH (PDA@FeOOH) with the photograph of its dispersion in water;	

TEM images of the PDA@FeOOH particles after calcination at different temperatures (550 °C (c), 600 °C (d), and 700 °C (e)) under argon.....	55
<b>Figure 4.3</b> XRD patterns of the PDA@FeOOH nanoparticles after calcination at different temperatures under argon.....	56
<b>Figure 4.4</b> TEM images of the yolk-shell Fe <sub>3</sub> O <sub>4</sub> -C nanospindles after etching with HCl solution for different durations (1(a), 2 (b), and 3 h (c)) under a mild mechanical stirring; SEM images of yolk-shell Fe <sub>3</sub> O <sub>4</sub> -C particles before (d) and after etching for 2 h (e); XRD patterns of yolk-shell Fe <sub>3</sub> O <sub>4</sub> -C particles before and after etching for 2 h.....	57
<b>Figure 4.5</b> N <sub>2</sub> adsorption-desorption isotherms of the yolk-shell Fe <sub>3</sub> O <sub>4</sub> -C particles before (a) and after etching for 2h (b) with the insets of the corresponding pore size distribution.....	58
<b>Figure 4.6</b> TEM images of yolk-shell FeS-C (a) and FeS <sub>2</sub> -C (b) nanoparticles; SEM images of yolk-shell FeS-C (c) and FeS <sub>2</sub> -C (d) nanoparticles.....	59
<b>Figure 4.7</b> (a) XRD patterns of Fe <sub>3</sub> O <sub>4</sub> -C, FeS-C, and FeS <sub>2</sub> -C; (b) crystal structures of magnetite Fe <sub>3</sub> O <sub>4</sub> , troilite FeS, and pyrite FeS <sub>2</sub> , respectively.....	60
<b>Figure 4.8</b> XPS spectra of Fe 2p (a) and S 2p (b) in the Fe <sub>3</sub> O <sub>4</sub> -C, FeS-C, and FeS <sub>2</sub> -C nanoparticles; (c) Raman spectra of Fe <sub>3</sub> O <sub>4</sub> -C, FeS-C, and FeS <sub>2</sub> -C nanoparticles.....	61
<b>Figure 4.9</b> Nitrogen adsorption/desorption isotherms of FeS-C (a), and FeS <sub>2</sub> -C (b) nanoparticles and corresponding pore size distribution curves as insets.....	61
<b>Figure 4.10</b> UV- <i>vis</i> spectroscopy of 2 mM Li <sub>2</sub> S <sub>8</sub> in DOL/DME (v/v = 1/1) and the solutions after the addition of Fe <sub>3</sub> O <sub>4</sub> -C, FeS-C, and FeS <sub>2</sub> -C for 2 h with the same surface area of 2 m <sup>2</sup> based on their BET results. Inset: photographs of the vials with Li <sub>2</sub> S <sub>8</sub> solution and host materials. ....	62
<b>Figure 4.11</b> The current-time curves of Li <sub>2</sub> S <sub>8</sub> solution potentiostatically discharged at 2.05 V ( <i>vs.</i> Li/Li <sup>+</sup> ) on different host materials: Fe <sub>3</sub> O <sub>4</sub> -C (a), FeS-C (b), and FeS <sub>2</sub> -C (c).....	63
<b>Figure 4.12</b> (a) Potentiostatic charge curves of Li <sub>2</sub> S <sub>8</sub> solution at 2.4 V <i>vs.</i> Li/Li <sup>+</sup> on different electrodes; CV curves (b) of symmetric cells with Li <sub>2</sub> S <sub>6</sub> solution as electrolyte scanned at 10 mV s <sup>-1</sup> between -0.8 and 0.8 V.....	64
<b>Figure 4.13</b> (a) TGA curves of the composites (Fe <sub>3</sub> O <sub>4</sub> -C/S, FeS-C/S, and FeS <sub>2</sub> -C/S) under argon; (b) CV curves scanned at 0.1 mV s <sup>-1</sup> , galvanostatic charge/discharge profiles at 0.1 C (c), the enlarged rectangle region (d) of Li-S batteries with the Fe <sub>3</sub> O <sub>4</sub> -C/S, FeS-C/S, and FeS <sub>2</sub> -C/S as cathode in the range of 1.7-2.8 V <i>vs.</i> Li/Li <sup>+</sup> .....	65
<b>Figure 4.14</b> Cycling performance at 0.2 C (a) and 0.5 C (c) and rate capability (b) of Li-S batteries with different cathodes (Fe <sub>3</sub> O <sub>4</sub> -C/S, FeS-C/S, and FeS <sub>2</sub> -C/S) in the range of 1.7-2.8 V <i>vs.</i> Li/Li <sup>+</sup> at room temperature.....	66
<b>Figure 4.15</b> Electrochemical impedance spectroscopy of Li-S batteries with the Fe <sub>3</sub> O <sub>4</sub> -C/S, FeS-C/S, and FeS <sub>2</sub> -C/S as cathode before cycling.....	68
<b>Figure 5.1</b> Schematic illustration of the synthetic route to Fe <sub>x</sub> N@C nanocapsules.....	71

<b>Figure 5.2</b> (a) Photo of the dispersion of the PILs vesicles in water. (b) Cryo-TEM image and (c) SEM image of PILs vesicles.....	72
<b>Figure 5.3</b> (a) Cryo-TEM image of the PDA@PILs (Inset: the photo of the PDA@PILs dispersion in water. (b) Cryo-TEM image and (c) SEM image of the PDA@Fe-PILs particles.....	73
<b>Figure 5.4</b> EDX analysis with scanning electron microscope (SEM) images and corresponding element mappings of the PDA@PILs nanovesicles (a) and the PDA@Fe-PILs nanovesicles (b), respectively.....	74
<b>Figure 5.5</b> (a) XRD patterns of the PDA@Fe-PILs after calcination at different temperatures (500, 600, and 700 °C) along with melamine under argon atmosphere; TEM images of PDA@Fe-PILs after calcination at 600 °C (b and c) and 500 °C (d and e) with melamine as nitrogen source; (f) HR-TEM images of the Fe <sub>x</sub> N@C nanocapsules.....	75
<b>Figure 5.6</b> (a) STEM image of the Fe <sub>x</sub> N@C nanocapsules with (b) corresponding EELS mapping images of different elements (Fe, N, and C); (c) SEM image of the Fe <sub>x</sub> N@C particles.....	76
<b>Figure 5.7</b> (a) Nitrogen adsorption-desorption isotherms of the sample Fe <sub>x</sub> N@C with the inset corresponding to the pore size distribution plot; (b) TGA curve of the sample Fe <sub>x</sub> N@C in the synthetic air; XPS spectra of (c) Fe 2p and (d) N 1s of the sample Fe <sub>x</sub> N@C.....	77
<b>Figure 5.8</b> TEM images of (a) the PILs particles after anion-exchange with ferricyanide, (b) anion-exchanged PILs sample after calcination at 500 °C, (c) PDA@PILs particles after calcination, which is without the anion-exchange process, (d) PDA@Fe-PILs after calcination without melamine as nitrogen sources.....	78
<b>Figure 5.9</b> (a)TEM image of the N-Carbon nanocapsules; (b) TGA curve of the N-Carbon nanocapsules in the synthetic air; (c) N <sub>2</sub> adsorption-desorption isotherms of N-Carbon nanocapsules with the corresponding pore size distribution (inset).....	79
<b>Figure 5.10</b> (a) Static adsorption test for the Li <sub>2</sub> S <sub>6</sub> solution by the N-Carbon and Fe <sub>x</sub> N@C with the UV-vis spectra of the corresponding supernatants, respectively; (b) the Fe 2p spectra of the Fe <sub>x</sub> N@C particles before and after the adsorption test.....	80
<b>Figure 5.11</b> (b) CV curves at a scan rate of 10 mV s <sup>-1</sup> from -0.8 to 0.8 V of the symmetric batteries with different electrodes as noted in figure; the Li <sub>2</sub> S precipitation test on different electrodes: Fe <sub>x</sub> N@C (b) and N-Carbon (c).....	81
<b>Figure 5.12</b> (a) TGA curves of the Fe <sub>x</sub> N@C/S and N-Carbon/S composites under nitrogen; (b) CV curves scanned at 0.1 mV s <sup>-1</sup> , (c) discharge-charge curves at 0.1 C (1 C = 1675 mA g <sup>-1</sup> ), (d) cycling stability at 0.5 C, rate capability (e) of the Li-S batteries with Fe <sub>x</sub> N@C/S and N-Carbon/S as the cathode; (f) the charge/discharge profiles of the Fe <sub>x</sub> N@C/S electrode at different C rates.....	82
<b>Figure 5.13</b> TEM image of the Fe <sub>x</sub> N@C particles after cycling for 100 cycles at 0.5C.....	83
<b>Figure 5.14</b> (a) EIS spectra of the Li-S batteries with different cathodes (Fe <sub>x</sub> N@C/S and N-Carbon/S) and the corresponding enlarged red rectangle area (b); (c) long-term cycling performance at 1 C of the Li-S batteries with Fe <sub>x</sub> N@C/S as the cathode.....	84

<b>Figure 7.1</b> A schematic CV curve for a simple reversible electrochemical reaction, where the inset is the voltage change during the CV scan. <sup>[202]</sup> .....	93
<b>Figure 7.2</b> EIS with corresponding Randles circuit. <sup>[203]</sup> .....	94
<b>Figure 7.3</b> Diffraction of an incoming X-ray beam from the lattice planes. <sup>[204]</sup> .....	96
<b>Figure 7.4</b> (a) The energy level diagram illustrates schematically the basic XPS equation; (b) schematic diagrams show the major components of an XPS instrument. <sup>[207]</sup> .....	97
<b>Figure 7.5</b> Scheme of a Raman spectrometer. <sup>[210]</sup> .....	98
<b>Figure 7.6</b> Schematic diagram of UV-vis spectrometer. <sup>[213]</sup> .....	99
<b>Figure 7.7</b> Schematic of the imaging methodology for different Ems: (a) SEM, serial collection of data points; (b) TEM, parallel image acquisition; (c) STEM, serial collection of transmitted electrons along with the corresponding schematic of their main components. <sup>[214-215]</sup> .....	100
<b>Figure 7.8</b> Schematic route of sample preparation for cryo-TEM measurement. <sup>[217a]</sup> .....	102
<b>Figure 7.9</b> General electron tomography workflow. <sup>[217b]</sup> .....	103
<b>Figure 7.10</b> Different types of adsorption isotherms as classified by IUPAC. <sup>[223]</sup> .....	104



## List of Tables

<b>Table 3.1</b> The equations corresponding to the four classic electrochemical models, respectively. <sup>[152b, c]</sup> .....	47
<b>Table 7.2</b> Chemicals and materials used in this thesis.....	87





## List of Abbreviations

$a_e$	The equilibrium area of the head group
AC	Alternating current
BE	Binding energy
BET	Brunauer-Emmett-Teller
BFT	Bewick-Fleischman-Thirsk
BJH	Barett-Joyner-Halenda
$C$	Concentration of active species
$C_{dl}$	Double layer capacitance
CS <sub>2</sub>	Carbon disulfide
CF	Carbon flake
CMC	Critical micelle concentration
CMK-3	Conductive mesoporous carbon framework
CNT	Carbon nanotube
CNFs	Carbon nanofibers
Cryo-TEM	Cryogenic transmission electron microscopy
CTAB	Hexadecyltrimethylammonium bromide
CV	Cyclic voltammetry
$d_{hkl}$	Lattice spacing
$D_i$	Diffusivity
DFT	Density functional theory
DOL	1,3-dioxolane
DME	1,2-dimethoxyethane
DMSO	Dimethyl sulfoxide
$E$	Cell potential
E/S	Electrolyte/sulfur
$E_H$	The cell potential high plateau
$E_H^\ominus$	The standard cell potential
$E_L$	Cell potential at low plateau
$E_L^\ominus$	The standard cell potential at the low plateau
EELS	Electron energy-loss spectroscopy
EDX	Energy-dispersive X-ray spectroscopy
EIS	Electrochemical impedance spectroscopy
ET	Electron tomography
$f_j$	The atomic scattering factor of atom j
$F$	Faraday constant
$g$	Packing parameter
$\Delta G$	Gibbs free energy

GCD	Galvanostatic charge-discharge
HIPE	High internal phase emulsion
HUMO	Highest occupied molecular orbital
$I$	Current
ILM-10	3- <i>n</i> -decyl-1-vinylimidazolium bromide
$k_0$	The reaction rate constant
KB	Ketjenblack
KE	Kinetic energy
$l_0$	The tail length of the surfactant
$L(\Theta)$	Lorentz factor
Li-S batteries	Lithium-Sulfur batteries
Li-ion batteries	Lithium-ion batteries
LUMO	Lowest unoccupied molecular orbital
LiPSs	Lithium polysulfides
LiPF <sub>6</sub>	Lithium hexafluorophosphate
LiTFSI	Bis(trifluoromethane) sulfonimide lithium salt
Li <sub>2</sub> SO <sub>x</sub>	Lithium sulfate
$M_w$	Molecular weight
$N$	Avogadro's number
NCA	LiNi <sub>0.80</sub> Co <sub>0.15</sub> Al <sub>0.05</sub> O <sub>2</sub>
NMC	LiNi <sub>x</sub> Mn <sub>y</sub> Co <sub>z</sub> O <sub>2</sub>
NMP	N-methyl-2-pyrrolidone
O <sub>spe</sub>	The oxidized species
Oh	Octahedral
OMC	Ordered mesoporous carbon
O/W	Oil-in-water
P	Pressure
$P_{batt}$	Power density of battery
$P(\Theta)$	Polarization factor
PEO- <i>b</i> -PS	Di-block poly(ethylene oxide)- <i>b</i> -poly(styrene)
PDA	Polydopamine
PILs	Poly(ionic liquid)s
PVA	Polyvinyl alcohol
PVDF	Polyvinylidene fluoride
R	The universal gas constant
$R_{ct}$	Charge transfer resistance
$R_{int}$	The internal resistance
$R_{ohm}$	Ohmic resistance
R <sub>spe</sub>	The reduced species

ROP	Ring-opening polymerization
S	Sulfur
[S <sub>8(t)</sub> ]	Sulfur concentration dissolved in the electrolyte
[S <sub>4</sub> <sup>2-</sup> ]	S <sub>4</sub> <sup>2-</sup> concentration dissolved in the electrolyte
[S <sup>2-</sup> ]	Li <sub>2</sub> S concentration in the electrolyte
[S <sub>2</sub> <sup>2-</sup> ]	Li <sub>2</sub> S <sub>2</sub> concentration in the electrolyte
SEM	Scanning electron microscopy
SH	Scharifer-Hills
SRR	Sulfur reduction reaction
SSA	Specific surface area
STEM	Scanning transmission electron microscopy
<i>T</i>	Kelvin temperature
TEOS	Tetraethyl orthosilicate
TEM	Transmission electron microscopy
Td	Tetrahedral
TGA	Thermogravimetric analysis
TM	Transition metal
TMNs	Transition metal nitrides
Tris	Tris(hydroxymethyl) aminomethane
UMC	Ultramicroporous carbon
UV- <i>vis</i>	Ultraviolet-visible
<i>v</i> <sub>0</sub>	The hydrophobic tail volume of the surfactant
<i>V</i> <sub>op</sub>	Operating voltage
<i>V</i> <sub>ocv</sub>	Open circuit voltage
VA086	2, 2'-azobis[2-methyl- <i>N</i> -(2-hydroxyethyl)propionamide]
<i>W</i> <sub>ml</sub>	The mass of gas that forms a monolayer
XPS	X-ray photoelectron spectroscopy
XRD	X-ray diffraction
<i>Z</i> <sub>w</sub>	Warburg impedance
<i>η</i>	Voltage polarization
<i>τ</i>	Diffusion time
<i>λ</i>	Diffusion length
<i>Θ</i>	The angle of the diffracted beam
<i>Φ</i> <sub>spec</sub>	The spectrometer work function
<i>μ</i> <sub>A</sub>	The electrochemical potential of anode
<i>μ</i> <sub>C</sub>	The electrochemical potential of cathode
2DP	2D progressive nucleation
2DI	2D instantaneous nucleation
3DP	3D progressive nucleation

3DI


3D instantaneous nucleation

## List of Publications

### Peer-reviewed journal publications

- [1] **Dongjiu Xie**, Yaolin Xu, Yonglei Wang, Xuefeng Pan, Eneli Härk, Zdravko Kochovski, Alberto Eljarrat, Johannes Müller, Christoph T Koch, Jiayin Yuan, Yan Lu, Poly(ionic liquid) Nanovesicle-Templated Carbon Nanocapsules Functionalized with Uniform Iron Nitride Nanoparticles as Catalytic Sulfur Host for Li-S Batteries, *ACS Nano*, 2022, 16, 7, 10554-10565.
- [2] **Dongjiu Xie**, Oumeima Jouini, Shilin Mei, Ting Quan, Yaolin Xu, Zdravko Kochovski, Yan Lu, *ChemNanoMat*, 2022, 8, e202100455.
- [3] **Dongjiu Xie**, Shilin Mei, Yaolin Xu, Ting Quan, Eneli Härk, Zdravko Kochovski, Yan Lu, Efficient Sulfur Host Based on Yolk-Shell Iron Oxide/Sulfide-Carbon Nanospindles for Lithium-Sulfur Batteries, *ChemSusChem*, 2021, 14, 1404.
- [4] **Dongjiu Xie**, Yaolin Xu, Eneli Härk, Zdravko Kochovski, Xuefeng Pan, Xia Zhang, Johannes Schmidt, and Yan Lu, Carbon-coated Mesoporous Fe<sub>3</sub>O<sub>4</sub> Nanospindles with Interconnected Porosities as Polysulfide Mediators for Li-S Batteries, *Materials Today Energy*, 2023, 36, 101344.
- [5] Sadaf Saeedi Garakani, **Dongjiu Xie**, Atefeh Khorsand Kheirabad, Yan Lu, and Jiayin Yuan, Template-synthesis of a poly(ionic liquid)-derived Fe<sub>1-x</sub>S/nitrogen-doped porous carbon membrane and its electrode application in lithium-sulfur batteries *Mater. Adv.*, 2021, 2, 5203-5212.
- [6] Atefeh KhorsandKheirabad, Xianjing Zhou, **Dongjiu Xie**, Hong Wang, Jiayin Yuan, Hydrazine-Enabled One-Step Synthesis of Metal Nanoparticle-Functionalized Gradient Porous Poly(ionic liquid) Membranes, *Macromol. Rapid Commun.*, 2021, 42, 2000143.
- [7] Zehan Chen, He Jia, Stephanie Hoepfner, Christian Friebe, Jiande Wang, Géraldine Chanteux, **Dongjiu Xie**, Yan Lu, Alexandru Vlad, Ulrich S. Schubert, Jean-François Gohy, Hollow porous silicon nanospheres with 3D SiC@C coating as high-performance anodes, *Materials & Design*, 2023, 226, 111624.
- [8] Sadaf Saeedi Garakani, Anirban Sikdar, Miao Zhang, Kanglei Pang, **Dongjiu Xie**, Jiayin Yuan, Intrinsic peroxidase-like catalytic activity of wood-derived porous Fe<sub>3</sub>C/nitrogen-doped carbon membrane for colorimetric sensing of ascorbic acid, submitted to *Nanomaterials*, under review.

- [9] Meltem Karaismailoglu Elibol, Lihong Jiang, **Dongjiu Xie**, Sijia Cao, Xuefeng Pan, Eneli Härk, Yan Lu, Nickel oxide decorated halloysite nanotubes as sulfur host materials for lithium-sulfur batteries, submitted to *Global Challenges*, 2023, 7, 2300005.

 **Oral presentation as the presenting author**

- [1] March 9-11, 2020, *The 16th Zsigmondy Colloquium*, Düsseldorf, Germany


Title: Iron Sulfide (FeS) Nanoparticle Encapsulated into Hollow Carbon Nanospindle as Sulfur Host for Lithium-Sulfur Batteries, **Dongjiu Xie**, Shilin Mei, Zdravko Kochovski, and Yan Lu

- [2] October 11-13, 2021, *Polymer Brushes: New Development and Perspectives in Experiment, Theory and Applications*, held virtually

Title: Spherical Polyelectrolyte Brushes Templated Hollow C@MnO Spheres as Sulfur Host Materials for Li-S batteries, **Dongjiu Xie**, Oumeima Jouini, Shilin Mei, Ting Quan, and Yan Lu

- [3] August 30-31, 2022, *Battery Retreat*, Dessau, Germany

Title: Nanostructured Iron-based Compounds For Li-S batteries, **Dongjiu Xie**, Yan Lu

 **Poster presentation as the presenting author**

- [1] September 23-25, 2019, *49th Conference of the German Colloid Society (Kolloid-Tagung 2019)*, Stuttgart, Germany

Title: Iron Oxide Nanoparticles Encapsulated into Hollow Carbon Nanospindles as Sulfur Host for Lithium-Sulfur Batteries, **Dongjiu Xie**, Shilin Mei, Zdravko Kochovski, and Yan Lu

- [2] June 28-July 1, 2021, *The International Conference on Lithium-Sulfur Batteries*, held virtually

Title: Efficient Sulfur Host Based on Yolk-Shelled Iron Oxide/Sulfide-Carbon Nanospindles for Lithium-Sulfur Batteries, **Dongjiu Xie**, Shilin Mei, Yaolin Xu, Ting Quan, Eneli Härk, Zdravko Kochovski, and Yan Lu

- [3] May 30-31, 2022, *Helmholtz Energy Young Scientist Workshop 2022*, Frankfurt Maintal, Germany

Title: Poly(ionic liquid) Nanovesicle-Templated Carbon Nanocapsules Functionalized with Uniform Iron Nitride Nanoparticles as Catalytic Sulfur Host for Li-S Batteries,

**Dongjiu Xie**, Yaolin Xu, Yonglei Wang, Xuefeng Pan, Eneli Härk, Zdravko Kochovski, Alberto Eljarrat, Johannes Müller, Christoph T Koch, Jiayin Yuan, and Yan Lu

[4] September 27-30, *Electrochemistry 2022*, Berlin, Germany

Title: Poly(ionic liquid) Nanovesicle-Templated Carbon Nanocapsules Functionalized with Uniform Iron Nitride Nanoparticles as Catalytic Sulfur Host for Li-S Batteries,

**Dongjiu Xie**, Yaolin Xu, Yonglei Wang, Xuefeng Pan, Eneli Härk, Zdravko Kochovski, Alberto Eljarrat, Johannes Müller, Christoph T Koch, Jiayin Yuan, and Yan Lu





## Acknowledgement

First of all, I express my deepest acknowledgement to my supervisor Prof. Yan Lu for offering me the opportunity to work as a doctoral researcher in her group at Helmholtz-Zentrum Berlin für Materialien und Energie and for showing me the beauty and fun of colloidal chemistry. Over the last five years, her patient guidance, rich knowledge, and great encouragement greatly helped and enlightened me to synthesize the nanomaterials for Li-S batteries using colloidal methods. I appreciate her financial and spiritual support in my research work and life in German.

I would like to acknowledge my collaborator Prof. Jiayin Yuan, at the Department of Materials and Environmental Chemistry, Stockholm University for guiding me to explore the potential application of poly(ionic liquid)s in Li-S batteries and revising my manuscript. I am also in debt to Dr. Shilin Mei, Dr. Ting Quan, and Dr. Yaolin Xu for their great help in my research work.

My sincere thanks also go to Dr. Eneli Monerjan (HZB) for her support in the TGA measurement, fruitful discussions, and revising of my manuscripts. I would like to thank Dr. Zdrovko Kochovski (HZB), who made the Cryo-TEM and electron tomography measurement in this thesis, and Dr. Dirk Wallacher (WI-ASE, HZB) who taught me how to measure the N<sub>2</sub> adsorption-desorption isotherms. My appreciations also go to Dr. Jing Yang (TU Berlin) and Dr. Johannes Schmidt (TU Berlin) for the XPS measurement, Dr. Alberto Eljarrat (HU Berlin) for the STEM measurement, Mr. Johannes Müller (HU Berlin) for taking the SEM images, and Dr. Chenxu Sheng (HU Berlin) for collecting the Raman spectra.

I also would like to thank Mrs. Linda Schmalz (HZB) for her administrative help and spiritual support. Many thanks to my friends, and current and former colleagues at Department of electrochemical energy storage, HZB for their kind help and support.

Last but not least, I am extremely grateful to my parents for their unconditional love, encouragement, and support.



## **Declaration**

Die vorliegende Dissertation entstand im Zeitraum zwischen June 2018 und March 2023 am Helmholtz-Zentrum Berlin für Materialien und Energie von Prof. Yan Lu.

Hiermit erkläre ich, dass die vorliegende Arbeit selbstständig angefertigt wurde und keine anderen als die angegebenen Hilfsmittel und Quellen verwendet wurden.

The present work was carried out during the period from June 2018 to March 2023 at Helmholtz-Zentrum Berlin für Materialien und Energie under the supervision of Prof. Yan Lu

I declare that I have written this work on my own and used no other than the named aids and references.

Dongjiu Xie

Berlin, March 2023

